U.PORTO

FEUP FACULDADE DE ENGENHARIA
UNIVERSIDADE DO PORTO

Computational Framework for Multi-Scale Analysis of Heterogeneous Materials using Digital Image Recognition

Miguel Vieira de Carvalho

Master's Degree in Mechanical Engineering

Supervisor:
Prof. Francisco Manuel Andrade Pires

Second Supervisors:
Eng. Igor André Rodrigues Lopes
Dr. Shengua Wu

October 13, 2016

Abstract

Computational Framework for Multi-Scale Analysis of Heterogeneous Materials using Digital Image Recognition

With the advent of increasingly more complex heterogeneous materials, new methodologies are being developed to accurately predict their mechanical behaviour. At the microscale, a material is usually composed of multiple heterogeneities that, by interacting with the surroundings, may influence the macroscopic performance of the component.

During this thesis, a *Digital Image Based* (DIB) microstructure recognition technique was employed to model the microstructure of heterogeneous materials. This method enables the use of any given real 2D or 3D micrograph to identify different constituents, create a *Representative Volume Element* (RVE) and generate a finite element mesh that correctly fits these singularities. Following this, *Multi-Scale* models take advantage of RVEs generated with this approach to study the homogenized elastic properties of heterogeneous materials, such as the acquisition of the full stiffness tensor for orthotropic cases.

In addition, a study on the RVE and mesh size is performed for two- and three-phase materials. The influence of different stiffness ratios between fiber and matrix materials on the RVE size and on the homogenized properties is analysed and compared with analytical models, such as the *Hashin-Hill* bounds and the *Mori-Tanaka* method. Moreover, the insertion of an interface material in-between, changes the overall behaviour of a composite material, hence, a study of this factor is presented. Analytical expressions with extremely high accuracy against the numerical results were deduced to estimate the homogenized plane Young's modulus under these circumstances.

Finally, this method does not consider simplifications at the microscale, being able to model any constituent with arbitrary shapes or constitutive behaviours. Therefore the micrograph recognition technique is an inspiring and breakthrough method that aims to develop and characterize new and more elaborated heterogeneous materials.

Keywords: Micromechanics; Multi-Scale models; Homogenization; Effective properties; Heterogeneous materials; OOFEM; DIB.

Resumo

Modelo Computacional para Análise Multi-Escala de Materiais Heterogéneos com base em Reconhecimento Digital de Imagem

Devido ao aparecimento de materiais cada vez mais complexos, novas metodologias estão a ser desenvolvidas de forma a prever o comportamento mecânico destes. À microescala, as múltiplas heterogeneidades presentes num material interagem entre si e tendem a influenciar o seu comportamento macroscópico.

Ao longo desta tese foi utilizada uma técnica de reconhecimento de imagem ("Digital Image Based (DIB) microstructure recognition") para modelar a microestrutura do material. Esta permite identificar os seus constituintes, criar um *Elemento Representativo de Volume* (RVE) e gerar uma malha de elementos finitos, recorrendo a micrografias reais, com duas ou três dimensões. De seguida, e utilizando os RVEs gerados por este método, são utilizados modelos *Multi-Escala* para estudar as propriedades elásticas homogeneizadas de materiais heterogéneos, através do cálculo do tensor de rigidez para casos ortotrópicos.

Além disso, é estudado o tamanho do RVE e da malha de elementos finitos em materiais com duas e três fases. A influência do rácio entre a rigidez da fibra e da matriz no tamanho do RVE e nas propriedades elásticas homogeneizadas também é analisada e comparada com os métodos analíticos, como é o caso dos limites de *Hashin-Hill* e do modelo de *Mori-Tanaka*. A introdução de um novo material na interface entre a fibra e a matriz altera o comportamento do compósito e, como tal, este parâmetro é igualmente investigado. No caso apresentado, são também deduzidas expressões analíticas para estimar o módulo de Young homogeneizado no plano que estão em concordância com os resultados obtidos numericamente.

Por último, o método aqui referido não considera simplificações à escala microscópica e permite modelar qualquer constituinte, independentemente da sua forma e do tipo de comportamento constitutivo que possui. Assim sendo, pode-se concluir que a modelação de microestruturas através do reconhecimento de micrografias perfaz um método inspirador e revolucionário no desenvolvimento e caracterização de novos materiais heterogéneos.

Palavras-chave: Micro-mecânica; Modelos Multi-Escala, Homogeneização, Propriedades efetivas; Materiais heterogéneos; OOFEM; DIB.

Acknowledgements

First of all, I would like to thank my supervisor, Professor Francisco Pires, for all the support given while structuring and documenting this thesis. The advices were truly helpful and set the course in the most difficult moments. The level of effort and devotion are inspiring and, thanks to that, the whole process has been as smooth as it could be.

Moreover, it is impossible to forget all the assistance given by the Engineer Igor Lopes that, being the person that I worked more closely with, shared his knowledge on the more technical matter, and had unlimited patience for all my questions and doubts. To Dr. Shengua Wu, for proposing this challenging and interesting topic and for all the advices given during this project.

To the Board of European Students of Technology (BEST), and specifically, to the members and friends that are part of it, I would like to say that it was with you that I spent most of my time during this last four years, and it was with your help that I developed and became the person that I am today. Thank you for the sincere, sometimes stressful but, above all, enjoyable memories that we spent together and that I will keep for the rest of my life.

A special word to my girlfriend, Joana Silva, for the companionship and nights spent waken while working on this and other projects and for the time spent by my side on the most difficult moments. There were times when most of the things were not going as they should be and the encouragement words that she provided always helped me to keep the focus on what really matters. Not forgetting the friend that I spent the Erasmus experience with, João Sousa, that stood with me the past two months also working on his thesis, making this last stressful moments more bearable. To Luís Varandas, who shared my academic life since grade school until the end of college, for the advices given and enjoyable moments spent together and to Tomás Chuaqui that made the studying moments more cheerful and energetic. At last, a thank you to Miguel Ezcurdia Royo and Tiago Pinto for being awesome.

Finally, but not least, I would like to give my sincere words to my family, specially to my parents and sister for providing everything that I needed, and for always supporting my decisions, in particular during the last two years, while I was absent the majority of time due to other responsibilities.

My sincere gratitude to all,
Miguel Vieira de Carvalho

Contents

List of Figures

List of Tables

Nomenclature

Notation

a	Scalar value
$\boldsymbol{a}$	Vector
$\boldsymbol{A}$	Second-order tensor
$\mathbf{a}$, $\mathbf{A}$	Finite elements' related array (vector and tensor)
A	Fourth-order tensor
$\mathcal{A}$	Space

Acronyms

2D	Two dimensional;
3D	Three dimensional;
RVE	Representative Volume Element;
MSP	Micro-Scale Problem;
DIB	Digital Image Based;
OOF2	Object Oriented Finite-Elements, version 2;
OOF3D	Object Oriented Finite-Elements, 3D version;
CT	Computed Tomography;
SEM	Scanning Electron Microscope;
DOF	Degrees of Freedom;
nGP	Number of Gauss Points;

Indices

$(\cdot)_t$	Time dependent; Transversal direction;
$(\cdot)_{\text{iso}}$	Isochoric component;
$(\cdot)_{\text{v}}$	Volumetric component;
$\bar{(\cdot)}$	Reference configuration; Normalized scalar value;
$(\cdot)^d$	Discretized domain;

$(\cdot)^e$	Element domain;
$(\cdot)^g$	Global domain;
$(\cdot)^{(j)}$	Generic iterative step of the Newton-Raphson method;
$(\cdot)_\mu$	Reference configuration;
$(\cdot)^{+/-}$	Positive/negative part of the periodic boundary of the RVE;
$(\cdot)_p$	Reference to the plane;
$(\cdot)^*$	Homogenized (Effective) property;
$(\cdot)_f$	Reference to the fiber material;
$(\cdot)_c$	Reference to the inclusion material;
$(\cdot)_m$	Reference to the matrix material;
$(\cdot)_{\text{inter}}$	Reference to the interface material;
$(\cdot)_L$	Reference to the lower boundary;
$(\cdot)_H$	Reference to the upper boundary;

Operators

$\dot{(\cdot)}$	Time derivative;
$\ddot{(\cdot)}$	Second time derivative;
$\partial(\cdot)$	Boundary domain;
$\partial(\cdot)/\partial a$	Derivative with respect to a;
$\nabla(\cdot)$	Gradient;
$\nabla^s(\cdot)$	Symmetric gradient;
$\nabla^x(\cdot)$	Spatial gradient;
$\nabla^X(\cdot)$	Material gradient;
$\text{tr}(\cdot)$	Trace;
$\det(\cdot)$	Determinant;
$\mid (\cdot) \mid$	Scalar norm (absolute value);
$\parallel (\cdot) \parallel$	Euclidean norm of vectors or tensors;
$\ln(\cdot)$	Natural logarithm;
$\text{div}_x(\cdot)$	Spatial divergence;
$\text{div}_x(\cdot)$	Material divergence;
$(\cdot) : (\cdot)$	Double contraction of tensors;
$(\cdot) \cdot (\cdot)$	Simple contraction of tensors;
$(\cdot) \times (\cdot)$	Vector product;
$(\cdot) \otimes (\cdot)$	Tensor product;
$\bigcup(\cdot)$	Union operator;
$\mathsf{A}(\cdot)$	Assemblage of finite elements;

Chapter 1

Introduction

For many years, the so called homogeneous materials have been used in a wide range of applications. Since the mid-19th century, new processes have been developed and steel started to be mass-produced, being, since then, one of the most popular structural materials that exists, even nowadays. Other alloys, like aluminium, copper, nickel, titanium, are also widely used on everyday engineering components due to their good mechanical properties. From the point of view of a mechanical engineer, these materials are well studied and documented in terms of their properties (elastic, thermal, electrical, and so on). For example, steel, as an isotropic material, exhibits the same properties regardless the direction it has been loaded. However, when considering heterogeneous materials, these assumptions are not valid and a deeper analysis is needed to fully understand their properties and to be able to correctly choose a material regarding the final application.

Over the last years, a significant focus is being placed on the development of new heterogeneous materials. The high specific stiffness (stiffness to weight ratio) is one of their major attributes, making high-end fields like aeronautics and naval industries interested in such materials. Ceramic-metal composites also have great potential in various technological fields, due to their increased thermal, mechanical and electrical properties. In the framework of this thesis, the elastic properties of heterogeneous materials are analysed, taking into account that their behaviour is highly dependent on the material microstructure.

Several experimental procedures can be performed to find the elastic properties of a given material, but these analyses are very expensive and time-consuming. Since the late 19-century with *Woldemar Voigt*, analytical methods are being developed to estimate the overall elastic properties of composite materials, taking into account the elastic properties of the constituents. The *Voigt* model (Voigt, 1889), also known as the *rule of mixtures* is a simple linear method but, more recently, other authors have been creating more complex and meaningful models, as the *Mori-Tanaka* method (Mori and Tanaka, 1973) that also aims to predict the effective properties of heterogeneous materials.

Following the high evolution of computational power, numerical methods, like the *Finite Element Method*, are being widely used to solve the mathematical equations that govern the behaviour of the materials when a load or deformation is applied. However, conventional macroscopic constitutive models do not take into consideration complex phenomena that occur at the microstructure level and may influence the global behaviour. A new approach that considers both macro and microscales is being developed: *Multi-Scale* models. Instead of using constitutive models to characterize the behaviour of a solid, this method is based on the analysis of a *Representative Volume Element* (RVE), which is a model of the microstruscture of the material. The RVE contains information about the constituents properties and geometry. *Homogenization* techniques are employed to obtain macroscopic properties from microscopic scales.

More recently, *Digital Image Based* (DIB) microstructure recognition is under development, aiming to generate a model of the microstructure according to a real micrograph of the considered material. With this technique, it is possible to create a finite element mesh for the RVE based on an micrograph of the material at the microscale. After the solution of the micro-equilibrium equations of the RVE, the homogenized stress and strain are computed and an estimation of the effective elastic properties of the material can be obtained. This estimation is more accurate than those made by the analytical methods, since it takes into account the geometry of the microstructure and not only the properties of the phases.

1.1 Goals

The main goal of this thesis is to investigate and explore recent developments in image acquisition and non linear finite element models to estimate the effective elastic properties of heterogeneous materials based on a DIB microstructure recognition technique.

In order to accomplish this, a basic knowledge of *Continuum Mechanics*, *Micromechanics* and *Multi-Scale* models is required to better understand the concepts behind the program used to solve the equilibrium equations, *Micro-Scale Problem* (MSP).

The DIB microstructure recognition is developed with the Linux® open-source program OOF2 ("Object Oriented Finite-Elements", version 2), hence, understanding this program is essential and is deemed as the first step to accomplish the goal of this thesis. A Matlab® script has to be made to convert the output information of OOF2 to the required information of MSP, and later, another Matlab® script needs to be created to compute the effective elastic properties from the output information of the MSP. The program OOF3D ("Object Oriented Finite-Elements", 3D version), that creates finite element meshes from 3D RVEs like CT scans, is also going to be explored.

To correctly estimate these properties, several studies have to be made *a-priori*. A study about the RVE size needs to be done to find the smallest size that still correctly represents the microstructure. The influence of different parameters in the RVE size is going to be analysed (e.g. the ratio between the fiber and matrix stiffness). The dependency of the overall elastic

properties with a change in the stiffness ratio and the influence of an interface material in these properties are also set as a goals.

1.2 Main Procedure

To achieve the final result that estimates the overall elastic properties of a heterogeneous material based on its micrograph, a general procedure must be followed (Figure 1.1). The main structure of this procedure is explained in the next chapters.

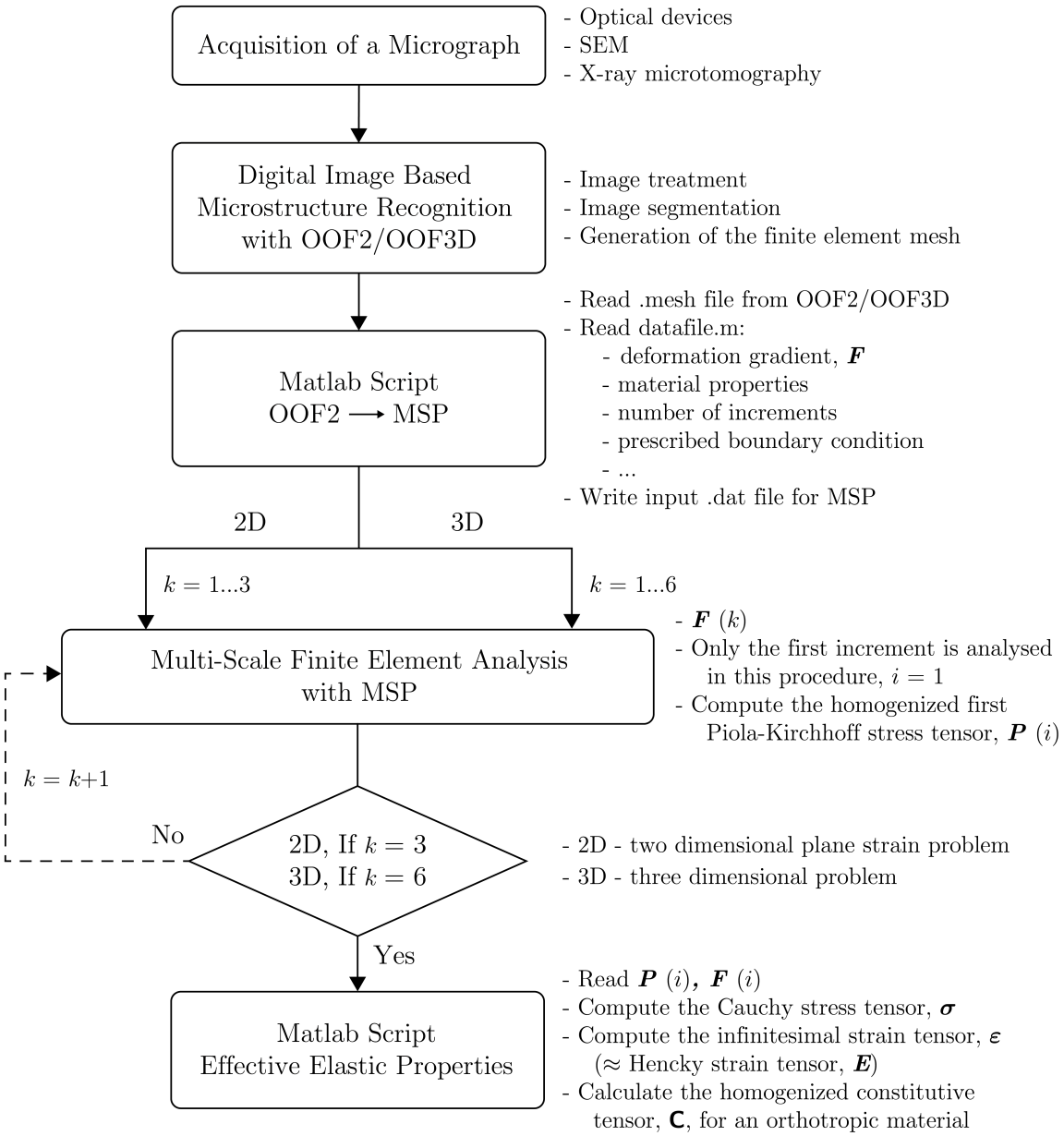

Figure 1.1: Scheme that represents the process to estimate the effective elastic properties of a heterogeneous material.

In Figure 1.1, the variable k represents an iteration. For the case of a two dimensional plane strain problem, pure normal strains in the $x-$ and $y-$direction and pure shear strain in the $x-y$ plane must be applied to the RVE to calculate all the components of the constitutive tensor, hence, $k = 3$. In the case of a three dimensional problem, the number of unknown coefficients is higher, thus, $x-$, $y-$ and $z-$direction pure normal strains and $x-y$, $x-z$ and $y-z$ plane pure shear strains must be applied to the RVE and, therefore, $k = 6$.

1.3 Structure of the Document

In this section, the overall structure of the document is going to be addressed. This thesis is divided into several chapters and, in the end of the document, a set of annexes and the references are compiled. Furthermore, a brief introduction to the chapters is, hereinafter, made.

Chapter 2

In this chapter, the concepts regarding *Continuum Mechanics and Finite Element Method* are presented. In the beginning, the theories that lead to the equations that govern the behaviour of a material under deformation are denoted. The whole formulation is made under the assumption of *large deformation* theory. Later, the numerical implementation of such equations is explained.

Chapter 3

In this chapter, basic concepts about *Micromechanics* and *Multi-Scale* models are presented. The notion of *Representative Volume Element* (RVE) is introduced, along with the admissible kinematical boundary conditions that can be applied to it. The numerical implementation of this procedure is also briefly described.

Chapter 4

In order to generate RVEs that can correctly characterize the microstructure, the *Digital Image Based* (DIB) microstructure recognition is introduced in this chapter. It uses real micrographs of materials to extract the constituents' information and to generate a finite element mesh that can model its behaviour. The detailed procedure is followed by an example to facilitate the understanding of this technique.

Chapter 5

Here, the *Hooke's Law* is presented, along with several analytical methods that aim to estimate the homogenized elastic properties of heterogeneous materials. Furthermore, a numerical approach based on the DIB microstructure recognition technique is introduced, followed by an example that validates the code used to compute these homogenized properties.

Chapter 6

In this chapter, the size of the RVE is studied, considering the effect of the stiffness ratio between the fiber and matrix materials, along with the mesh size that correctly models the microstructure. A comparison between the numerical and analytical models is performed and the influence of the stiffness ratio on the homogenized elastic properties is presented.

Chapter 7

Following the study done for two-phase materials, in this chapter, the insertion of an interface material in-between is analysed. The influence of this new material on the RVE size and on the mesh refinement is presented to validate the numerical results. Moreover, mathematical equations that express the homogenized plane Young's modulus for an unidirectional fiber composite are deduced, achieving good approximations with the numerical results.

Chapter 8

Finally, in this chapter, a conclusion note about the work performed in this thesis is presented, along with suggestions to keep developing this technique in future works.

Chapter 2

Continuum Mechanics and Finite Element Method

In order to be able to discuss *Multi-Scale Models*, there are some concepts that should be introduced first. *Continuum Mechanics* establishes the theory, the entities and the physical relations that are required to create a model capable of describing the behaviour of a solid. This was first formulated by the French mathematician *Augustin-Louis Cauchy* and it is a branch of mechanics that deals with the kinematics and the mechanical behaviour of the materials while assuming that they are modelled as a continuum medium instead of discrete particles. In reality, matter does not completely fill the space it occupies, it is formed by molecules which are composed by atoms and subatomic particles, and consequentially it is not continuous. However, on length scales much greater than that of the inter-atomic distance, such assumptions can be made. Within this theory, the term "particles", refer to an infinitesimal volume of material which the totality forms a body.

Due to the complexity of problems within the field of solid mechanics, various numerical techniques were developed. One of the most popular techniques is the *Finite Element Method*. In a simple way, this method is able to approximate solutions for boundary value problems governed by a set of differential equations through the discretization of the domain of the problem in sub-domains called *finite elements* where variable fields are interpolated. The simple equations that are used in each finite element are then assembled into a larger system of equations that model the entire problem. It is regarded as one of the most powerful numerical tools, given its high flexibility and the ability to be easily implemented on a computational level.

In this chapter, some fundamental topics about this matter are explained in order to simplify the concepts further presented. These are based on the textbooks of Neto et al. (2008) and Lai et al. (2010) and for a more detailed study, one should read the aforementioned references.

2.1 Kinematics of Deformation

In continuum mechanics two approaches of the theory can be found: the *infinitesimal strain theory* and *finite strain theory* (or *large strain/deformation theory*). The latest, deals with large deformations of the material, which makes it important to clearly distinguish between the undeformed and deformed configurations of the solid, invalidating the assumptions made in the infinitesimal strain theory.

Let $\mathscr{B}$ be a body which, in its reference configuration, occupies a region Ω of the three-dimensional Euclidean space $\mathscr{E}$ with a regular boundary $\partial\Omega$.

The displacement of this body can be separated in two components:

- **Rigid-body displacement**, that consists of a translation and/or rotation of the body without changing its shape. The relative displacement between particles is null.
- **Deformation**, that implies the change of shape and/or size of the body from the initial or undeformed configuration to the current or deformed one.

The deformation of $\mathscr{B}$ is deemed as a smooth one-to-one function that exists inside the three-dimensional Euclidean space

$$\varphi : \Omega \to \mathscr{E},$$

which describes the position $\boldsymbol{x}$ of each material particle $\boldsymbol{X}$ of $\mathscr{B}$ into a point of the deformed configuration $\varphi(\mathscr{B})$,

$$\boldsymbol{x} = \varphi(\boldsymbol{X}). \tag{2.1}$$

A body motion can be defined as a time-dependent deformation, so for each time t the position of the particle is given by:

$$\boldsymbol{x} = \varphi(\boldsymbol{X}, t), \tag{2.2}$$

which throughout the document will also be denoted as φ_t.

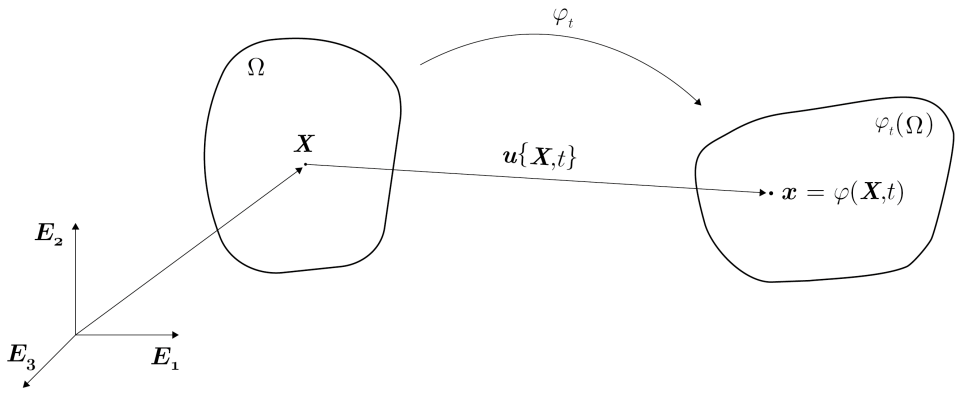

Figure 2.1: Deformation of a body.

In Figure 2.1, it is possible to see that the displacement vector field is defined by the difference between the position of the particle at time t and its initial configuration,

$$\boldsymbol{u}\{\boldsymbol{X}, t\} = \varphi(\boldsymbol{X}, t) - \boldsymbol{X}, \tag{2.3}$$

enabling the position of the particle $\boldsymbol{X}$ in the deformed configuration of the solid $\varphi(\mathscr{B})$ to be expressed as:

$$\boldsymbol{x} = \boldsymbol{X} + \boldsymbol{u}\{\boldsymbol{X}, t\}. \tag{2.4}$$

The velocity of a material particle $\boldsymbol{X}$ is defined as the derivative of the motion φ with respect to time,

$$\dot{\boldsymbol{x}}\{\boldsymbol{X}, t\} = \frac{\partial \varphi(\boldsymbol{X}, t)}{\partial t}. \tag{2.5}$$

With the assumption that $\varphi(\boldsymbol{X}, t)$ is invertible (at each time t, the map function is an one-to-one function) one can express the material points, $\boldsymbol{X}$, in terms of the place they occupy in the deformed configuration,

$$\boldsymbol{X} = \varphi^{-1}(\boldsymbol{x}, t) = \boldsymbol{x} - \boldsymbol{u}\{\varphi^{-1}(\boldsymbol{x}, t), t\}, \tag{2.6}$$

where $\varphi^{-1}(\boldsymbol{x}, t)$ is the map function for the initial configuration or the reference map. Based on this function it is possible to define:

$$\boldsymbol{v}\{\boldsymbol{x}, t\} \equiv \dot{\boldsymbol{x}}\{\varphi^{-1}(\boldsymbol{x}, t), t\}, \tag{2.7}$$

as the spatial velocity that gives the velocity of the material particle positioned at $\boldsymbol{x}$ at time t.

2.1.1 Material and Spatial Fields

Both fields $\dot{\boldsymbol{x}}$ and $\boldsymbol{v}$ represent the velocity of the material particles during the deformation but are related to different arguments and consequentially to different references. Both of them have time as an argument but while $\dot{\boldsymbol{x}}$ has the material particle $\boldsymbol{X}$ as the other argument, $\boldsymbol{v}$ is a function of the spatial position $\boldsymbol{x}$. Based on this two different types of analyses, two descriptions of the body motion can be made: the material description and the spatial description.

The first one, also known as *Lagrangian* formulation, consists on the evolution of the variables in a fixed material point $\boldsymbol{X}$ of the body $\mathscr{B}$ as it deforms.

The spatial description, or *Eulerian* formulation, is based on the analysis of the variables in a fixed point of space $\boldsymbol{x}$.

2.1.2 Deformation Gradient

It is possible to define the deformation gradient, $\boldsymbol{F}$, as the second-order tensor of the motion φ (based on material description),

$$\boldsymbol{F}\{\boldsymbol{X}, t\} = \nabla_X \, \varphi(\boldsymbol{X}, t) = \frac{\partial \boldsymbol{x}_t}{\partial \boldsymbol{X}}, \tag{2.8}$$

and taking into account the relation in (2.4), the last expression can be defined as:

$$\boldsymbol{F}\{\boldsymbol{X},t\} \equiv \boldsymbol{I} + \nabla_X\ \boldsymbol{u}, \tag{2.9}$$

where $\boldsymbol{I}$ is the second-order identity tensor.

Taking the spatial description, the deformation gradient is written as:

$$\boldsymbol{F}\{\boldsymbol{x},t\} \equiv [\nabla_x\ \varphi(\boldsymbol{x},t)]^{-1} \equiv [\boldsymbol{I} - \nabla_x\ \boldsymbol{u}]^{-1}. \tag{2.10}$$

In the previous equations, the operators ∇_X and ∇_x define, respectively, the gradient operator in material and spatial description. In order to understand the concept of deformation gradient, one material fiber should be considered. This infinitesimal fiber, $\mathrm{d}\boldsymbol{X}$, connects two neighbouring material particles: $\boldsymbol{X}$ and $\boldsymbol{X}+\mathrm{d}\boldsymbol{X}$ (Figure 2.2). After the deformation φ_t, this particles are moved to their new and deformed positions, $\boldsymbol{x}$ and $\boldsymbol{x}+\mathrm{d}\boldsymbol{x}$. The deformation gradient is the linear operator that relates the infinitesimal material fibers $\mathrm{d}\boldsymbol{X}$ with the deformed ones $\mathrm{d}\boldsymbol{x}$,

$$\mathrm{d}\boldsymbol{x} = \boldsymbol{F}\mathrm{d}\boldsymbol{X}. \tag{2.11}$$

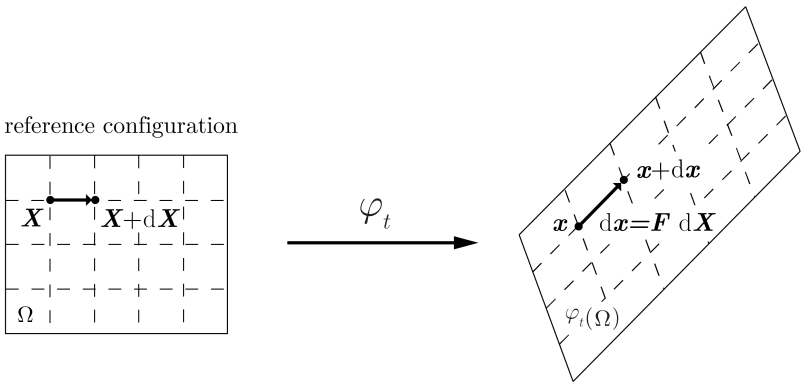

Figure 2.2: Deformation Gradient.

If the deformation gradient applied to $\mathscr{B}$ is uniform, the deformation is called homogeneous deformation. This happens if and only if it admits the representation,

$$\varphi(\boldsymbol{p}) = \varphi(\boldsymbol{q}) + \boldsymbol{F}(\boldsymbol{p} - \boldsymbol{q}), \tag{2.12}$$

for all points $\boldsymbol{p}, \boldsymbol{q} \in \mathscr{B}$, with $\boldsymbol{F}$ being a positive definite tensor.

Isochoric and Volumetric Decomposition of the Deformation Gradient

In order to introduce the concept of isochoric and volumetric deformation, it is important to define the determinant of the deformation gradient,

$$J = \det \boldsymbol{F}, \tag{2.13}$$

as the change of volume after deformation per unit of the initial volume (reference configuration),

$$J = \frac{\mathrm{d}v}{\mathrm{d}v_0}. \tag{2.14}$$

Basically, it represents the volume change ratio of the body $\mathscr{B}$. The determinant of the gradient must always satisfy $J > 0$ because the infinitesimal volume cannot collapse into a single material particle.

Now that the determinant of the deformation gradient is explained, one can define the following types of deformations:

Isochoric deformation - In an isochoric deformation, the change of volume is null (isochoric means conservation of volume) and so, taking into account Expression (2.14), it can be denoted by the following mathematical equation:

$$J = 1. \tag{2.15}$$

Volumetric deformation - A volumetric deformation consists of a purely uniform contraction/dilation of the body $\mathscr{B}$ in all directions and, consequently, the deformation gradient of any volumetric deformation can be expressed by the following tensor:

$$\boldsymbol{F} = \alpha \boldsymbol{I}, \tag{2.16}$$

where the scalar α is the deformation ratio. This deformation ratio can be obtained by dividing l with l_0, which are the deformed and undeformed lengths of a material fiber.

To take into account this two types of deformations, it is important to note that any deformation that is imposed to the body $\mathscr{B}$ can be decomposed as a purely isochoric deformation followed by a volumetric deformation or, conversely, as a volumetric deformation followed by an isochoric one,

$$\boldsymbol{F} = \boldsymbol{F}_{\mathrm{iso}}\boldsymbol{F}_{\mathrm{v}} = \boldsymbol{F}_{\mathrm{v}}\boldsymbol{F}_{\mathrm{iso}}, \tag{2.17}$$

where $\boldsymbol{F}_{\mathrm{iso}}$ and $\boldsymbol{F}_{\mathrm{v}}$ are, respectively, the isochoric and the volumetric components of the deformation gradient. This two types of deformations can be expressed as a function of $\boldsymbol{F}$,

$$\boldsymbol{F}_{\mathrm{iso}} \equiv J^{-\frac{1}{3}}\boldsymbol{F}, \tag{2.18a}$$

$$\boldsymbol{F}_{\mathrm{v}} \equiv J^{\frac{1}{3}}\boldsymbol{I}. \tag{2.18b}$$

It is important to note that, as expressed by the following expression:

$$\det \boldsymbol{F}_{\mathrm{v}} = [J^{\frac{1}{3}}]^3 \det \boldsymbol{I} = J, \tag{2.19}$$

the volumetric component $\boldsymbol{F}_{\mathrm{v}}$, produces the same volume change as $\boldsymbol{F}$.

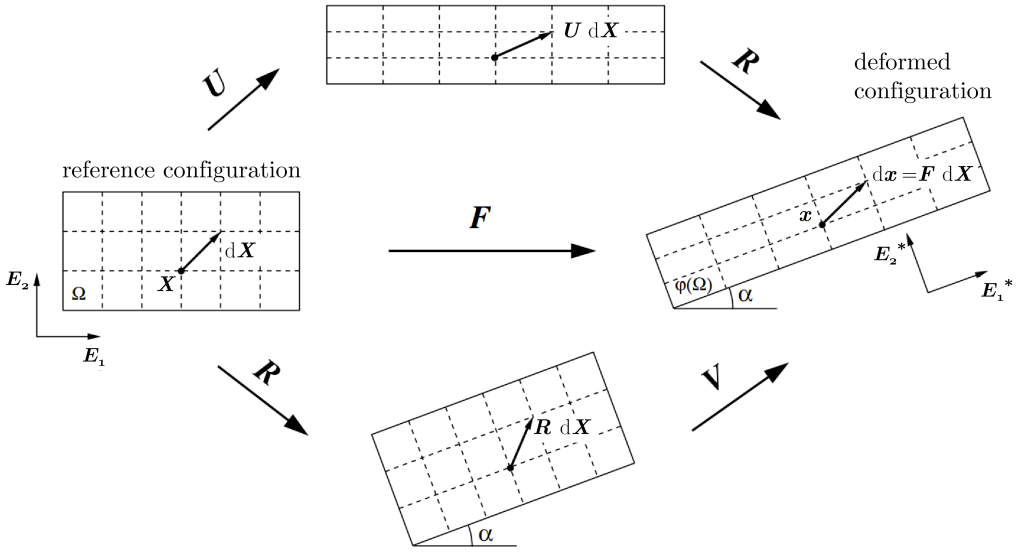

Figure 2.3: Representation of left and right polar decomposition of $\boldsymbol{F}$.

Polar Decomposition of the Deformation Gradient

The deformation gradient can also be decomposed by a set of pure rotations or elongations. By applying the polar decomposition to this tensor, one obtains:

$$\boldsymbol{F} = \boldsymbol{R}\boldsymbol{U} = \boldsymbol{V}\boldsymbol{R}, \tag{2.20}$$

where the orthogonal tensor $\boldsymbol{R}$ denotes the local rotation tensor and the symmetric positive definite tensors $\boldsymbol{U}$ and $\boldsymbol{V}$ are, respectively, the right and left stretch tensors, which are related by the rotation tensor,

$$\boldsymbol{V} = \boldsymbol{R}\boldsymbol{U}\boldsymbol{R}^T. \tag{2.21}$$

As shown in Figure 2.3, in the right polar decomposition $\boldsymbol{F} = \boldsymbol{R}\boldsymbol{U}$, first the stretches are mapped by $\boldsymbol{U}$ and then the rotation is applied, contrariwise, if one considers the left polar decomposition $\boldsymbol{F} = \boldsymbol{V}\boldsymbol{R}$, the rotation is mapped before the stretches. Considering the spectral decomposition of the stretch tensors, these can be denoted as:

$$\boldsymbol{U} = \sum_{i=1}^{3} \lambda_i \boldsymbol{l}_i \otimes \boldsymbol{l}_i, \tag{2.22a}$$

$$\boldsymbol{V} = \sum_{i=1}^{3} \lambda_i \boldsymbol{e}_i \otimes \boldsymbol{e}_i, \tag{2.22b}$$

in which the eigenvalues, λ_i, shared by both tensors, are the principal stretches and the eigenvectors define the Lagrangian ($\boldsymbol{l}_i$) and Eulerian ($\boldsymbol{e}_i$) principal directions, which are related through:

$$\boldsymbol{l}_i = \boldsymbol{R}\boldsymbol{e}_i. \tag{2.23}$$

The right and left stretch tensors can be expressed by:

$$\boldsymbol{U} = \sqrt{\boldsymbol{C}}, \tag{2.24a}$$

$$\boldsymbol{V} = \sqrt{\boldsymbol{B}}, \tag{2.24b}$$

where the tensors $\boldsymbol{C}$ and $\boldsymbol{B}$, named, respectively, right and left Cauchy-Green strain tensors, are a function of the deformation gradient:

$$\boldsymbol{C} = \boldsymbol{F}^T\boldsymbol{F}, \tag{2.25a}$$

$$\boldsymbol{B} = \boldsymbol{F}\boldsymbol{F}^T. \tag{2.25b}$$

2.2 Strain Measures

Aiming to describe the deformation of a body $\mathscr{B}$, several tensors have been proposed. Furthermore, all of them derive from the deformation gradient and characterize the same physical phenomenon. The selection process is related with the commitment between the phenomenon and the mathematical framework.

The two main families to quantify the strain of a solid are the *Lagrange* and the *Euler* strain tensors. The Lagrange strain tensor is a function of the right stretch tensor and it is defined by:

$$\boldsymbol{E}^{(m)} = \begin{cases} \frac{1}{m}(\boldsymbol{U}^m - \boldsymbol{I}) & , \text{ if } m \neq 0, \\ \ln[\boldsymbol{U}] & , \text{ if } m = 0, \end{cases} \tag{2.26}$$

and the Euler strain tensor is a function of the left stretch tensor,

$$\boldsymbol{\varepsilon}^{(m)} = \begin{cases} \frac{1}{m}(\boldsymbol{V}^m - \boldsymbol{I}) & , \text{ if } m \neq 0, \\ \ln[\boldsymbol{V}] & , \text{ if } m = 0. \end{cases} \tag{2.27}$$

In this expressions, m is a real value and $\ln[\cdot]$ denotes the tensor logarithm of $[\cdot]$. The value of this tensors is null if the motion of the body $\mathscr{B}$ is a rigid-body displacement. The Lagrangian and Eulerian strain tensors only differ by the local rotation $\boldsymbol{R}$ and are related by the next expression:

$$\boldsymbol{\varepsilon}^{(m)} = \boldsymbol{R}\boldsymbol{E}^{(m)}\boldsymbol{R}^T. \tag{2.28}$$

The program used during the project takes into account large deformations and has the logarithmic Lagrange strain tensor ($m = 0$) implemented. This tensor is also called *Hencky* tensor and is defined as:

$$\boldsymbol{E} = \ln[\boldsymbol{U}] \equiv \ln\left[\sqrt{\boldsymbol{F}^T\boldsymbol{F}}\right]. \tag{2.29}$$

In the case of infinitesimal deformations, the reference and the deformed configurations coincide, and the tensors of both families can be approximated by the infinitesimal strain

tensor:

$$\boldsymbol{\varepsilon} = \nabla^s \boldsymbol{u} = \frac{1}{2}\left[\nabla \boldsymbol{u} + (\nabla \boldsymbol{u})^T\right]. \tag{2.30}$$

2.3 Stress Measures

The deformation of a solid is directly related with the applied forces. These forces can be divided into two categories: boundary forces and body forces. Body or volume forces exist on the interior of the body and are measured in force per unit volume (e.g. magnetic and gravitational forces). The boundary or surface forces are measured in force per unit area and, as the name implies, are applied on the boundary of the body and are transmitted across its interior. Internal interaction forces arise from the action of one part of the body upon an adjacent part and are transmitted across the surface that separates them. The concept of stress, whose units are force per unit area, exists to quantify these surface forces mathematically and, as the strain measures, there are several stress tensors to define it in different ways. In this section the *Cauchy* and the first *Piola-Kirchhoff* stress tensors are presented.

2.3.1 Cauchy Stress Tensor

The Cauchy stress tensor, $\boldsymbol{\sigma}$, is a spatial description of the stresses since it refers to the deformed configuration. In the literature it is often referred as the true stress tensor or, simply, stress tensor and it is defined by:

$$\boldsymbol{t}\{\boldsymbol{x}, \boldsymbol{n}\} = \boldsymbol{\sigma}\{\boldsymbol{x}\}\boldsymbol{n}. \tag{2.31}$$

In this Expression, $\boldsymbol{t}$ is the resulting surface traction and $\boldsymbol{n}$ is the unit outward vector normal to the considered surface of the deformed configuration of the solid $\varphi(\mathscr{B})$. As a result of the balance of angular momentum, the Cauchy tensor is symmetric,

$$\boldsymbol{\sigma} = \boldsymbol{\sigma}^T. \tag{2.32}$$

This symmetric stress tensor can also be split into a spherical and traceless component:

$$\boldsymbol{\sigma} = \boldsymbol{s} + p\boldsymbol{I}, \tag{2.33}$$

where the invariant,

$$p \equiv \frac{1}{3}\mathrm{tr}\boldsymbol{\sigma} \tag{2.34}$$

is the hydrostatic pressure and $\boldsymbol{s}$ denotes the deviatoric stress tensor.

2.3.2 First Piola-Kirchhoff Stress Tensor

The first Piola-Kirchhoff stress tensor, $\boldsymbol{P}$, is a material description of the stresses, therefore it is related with the undeformed (reference) configuration of the body $\mathscr{B}$. It can be related with

the Cauchy tensor by:

$$\boldsymbol{P} = J\boldsymbol{\sigma}\boldsymbol{F}^{-T}. \tag{2.35}$$

Unlike the Cauchy tensor, the first Piola-Kirchhoff tensor is not necessarily symmetric.

2.4 Governing Equations and Balance Laws

Until this section, some of the variables that characterize the motion and deformation of a solid were introduced, along with the relevant strain and stress measures. However, continuum mechanics deals with the behaviour of materials that can be approximated to a continuum media for certain lengths and time scales, and, in order for this model to be accurate, several fundamental laws must be complied. Besides the thermodynamic principles, like the *Second Law of Thermodynamics*, that are not stated here, the *Conservation of Mass* and the *Momentum Balance Principle* govern the deformation of a solid and are further discussed.

2.4.1 Conservation of Mass

The postulate of conservation of mass requires that,

$$\dot{\rho} + \rho \, \mathrm{div}_x \dot{\boldsymbol{u}} = 0, \tag{2.36}$$

where ρ is the density of the solid and $\mathrm{div}_x(\cdot)$ denotes the spatial divergence operator.

2.4.2 Momentum Balance

The *Cauchy's theorem* denotes that the balance of momentum for $\mathscr{B}$ in terms of the Cauchy stress tensor (Section 2.3.1) can be expressed by the following partial equations with boundary conditions:

$$\begin{cases} \mathrm{div}_x \, \boldsymbol{\sigma} + \boldsymbol{b} = \rho\ddot{\boldsymbol{u}} & \text{, in } \varphi(\Omega), \\ \boldsymbol{t} = \boldsymbol{\sigma}\boldsymbol{n} & \text{, on } \varphi(\partial\Omega), \end{cases} \tag{2.37}$$

where $\boldsymbol{b}$ represents the volume (or body) forces in the deformed configuration, $\boldsymbol{t}$ is the applied boundary traction vector field and $\boldsymbol{n}$ is the outward unit vector normal to the deformed boundary, both of them on $\partial\Omega$. Equation (2.37) is known as *Cauchy's equation of motion* and it is formulated in the spatial description.

This principle may also be expressed in the material description (reference configuration of $\mathscr{B}$) in terms of the first Piola-Kirchhoff stress tensor,

$$\begin{cases} \mathrm{div}_X \, \boldsymbol{P} + \bar{\boldsymbol{b}} = \bar{\rho}\ddot{\boldsymbol{u}} & \text{, in } \Omega, \\ \bar{\boldsymbol{t}} = \boldsymbol{P}\bar{\boldsymbol{n}} & \text{, on } \partial\Omega, \end{cases} \tag{2.38}$$

where $\bar{\boldsymbol{b}}$ is the volume force in the reference configuration,

$$\bar{\boldsymbol{b}} = J\boldsymbol{b}, \tag{2.39}$$

$\bar{\rho}$ is the reference density (mass per unit of volume in the undeformed configuration),

$$\bar{\rho} = J\rho, \tag{2.40}$$

and $\bar{\boldsymbol{t}}$ represents the traction field on the undeformed boundary with normal outward unit vector $\bar{\boldsymbol{n}}$.

In both cases, these equations define the *Strong Equilibrium Equations*.

2.5 Weak Equilibrium Equations

Implementing the solution of the strong equilibrium equations in a numerical framework is difficult and not desirable, hence, the *Integral* or *Weak Equilibrium Equations* are formulated. They are the basis of the finite element methods and are obtained from the application of a variational principle to the equilibrium equations. In this section the weak formulation is obtained after the implementation of the *Virtual Work Principle* (subjugated to the *Principle of Least Action*).

Considering a *quasi-static* deformation, in which the inertia effects of the solid are neglected (e.g. application of a force in a slow and incremental way), the weak formulation can be expressed in both the spatial and material descriptions.

2.5.1 Spatial Description

In the Eulerian description, the equilibrium is related to the deformed configuration and it is stated in terms of the Cauchy stress tensor:

$$\int_{\varphi(\Omega)} [\boldsymbol{\sigma} : \nabla_x \boldsymbol{\eta} - \boldsymbol{b} \cdot \boldsymbol{\eta}] \, \mathrm{d}V - \int_{\varphi(\partial\Omega)} \boldsymbol{t} \cdot \boldsymbol{\eta} \, \mathrm{d}A = 0, \qquad \forall \boldsymbol{\eta} \in \mathcal{V}, \tag{2.41}$$

where $\boldsymbol{\eta}$ denotes the virtual displacements that belong to the space of admissible virtual displacements $\mathcal{V}$.

2.5.2 Material Description

The *quasi-static* Lagrangian description is associated with the first Piola-Kirchhoff stress tensor and with the reference configuration. It is expressed as:

$$\int_{\Omega} \left[\boldsymbol{P} : \nabla_X \boldsymbol{\eta} - \bar{\boldsymbol{b}} \cdot \boldsymbol{\eta}\right] \mathrm{d}V - \int_{\partial\Omega} \bar{\boldsymbol{t}} \cdot \boldsymbol{\eta} \, \mathrm{d}A = 0, \qquad \forall \boldsymbol{\eta} \in \mathcal{V}. \tag{2.42}$$

2.6 Finite Element Method

The weak equilibrium equations shown in Section 2.5 present a high degree of complexity, making it impossible to obtain solutions in an analytic way for solids with complex geometries or constitutive models. In order to solve this problem, one resorts to the numerical methods, being the *Finite Element Method* the most widespread numerical tool to predict the mechanical behaviour of a solid, in both scientific and industrial environments. Although the solution is not exact, provided that the error associated with the approximated solution is negligible, the result can be taken into consideration.

In this section, it is presented a summary of the application of the finite element method to *quasi-static* non linear solid mechanics.

To use the finite element method some steps must be fulfilled a priori:

1. Integral formulation of the problem;
2. Spatial domain discretization;
3. Time domain discretization;
4. Resolution of the system of equations that arises from the previously mentioned steps.

All of this stages are addressed hereafter.

2.6.1 Integral Formulation of the Problem

The integral formulation (weak formulation) of the problem was already presented in Section 2.5.1 and 2.5.2 for the spatial and material description, respectively. This was established using the *Virtual Work Principle* but it can also be reached through different methods, like the *Hamilton's Principle* and the *Method of Mean Weighted Residuals*.

2.6.2 Spatial Discretization

The spatial domain refers to the solid under analysis and its discretization is the basis of the finite element method. The spatial domain is divided into a finite number of subdomains, n_e, called finite elements (being the spatial domain of each element represented by Ω^e). The set of all finite element domains defines the discretized solid domain, Ω^d:

$$\Omega \approx \Omega^d = \bigcup_{e=1}^{n_e} \Omega^e \tag{2.43}$$

where $\bigcup$ refers to the union operation.

Interpolation of Variables

Each element is defined by a number of nodes, n_n, and the variables of interest are evaluated in these nodes. All relevant fields are then obtained through interpolation inside each element.

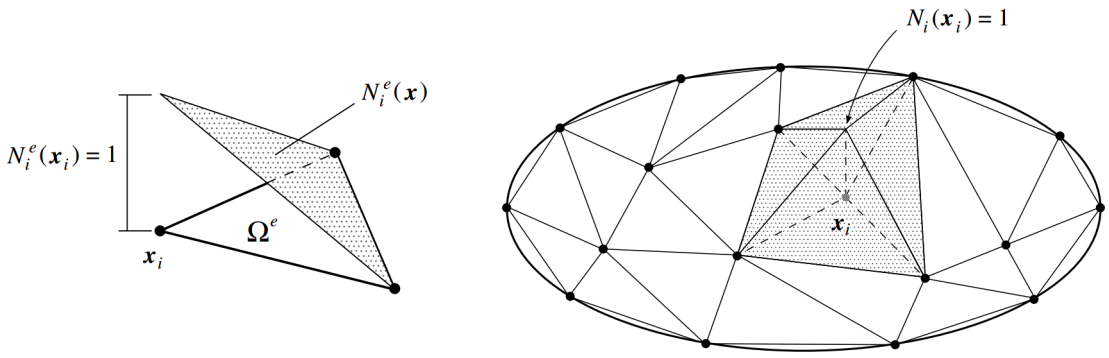

Figure 2.4: Finite element interpolation. The element and global shape function.

Considering a generic vectorial field $\boldsymbol{a}\{\boldsymbol{x}\}$, this interpolation process can be represented by:

$$\boldsymbol{a}\{\boldsymbol{x}\} = \sum_{i=1}^{n_n} N_i^e(\boldsymbol{x})\ \boldsymbol{a}\{\boldsymbol{x_i}\}, \qquad \boldsymbol{x} \in \Omega^e, \tag{2.44}$$

in which $\boldsymbol{a}\{\boldsymbol{x_i}\}$ denotes the nodal value of the vectorial field and $N_i^e(\boldsymbol{x})$ the interpolation function, also named as shape function, evaluated at a point $\boldsymbol{x}$ inside the element.

The shape functions depend on the type of element and have, among others, the *Kronecker delta* characteristic (Figure 2.4),

$$N_i^e(\boldsymbol{x_j}) = \delta_{ij}, \tag{2.45}$$

where δ_{ij} is the *Kronecker delta* function,

$$\begin{cases} \delta_{ij} = 1 & \text{, if } i = j, \\ \delta_{ij} = 0 & \text{, if } i \neq j. \end{cases} \tag{2.46}$$

Taking into consideration the whole discretized domain Ω^d, the global interpolation is defined in the same way. This approximation is given by:

$$\boldsymbol{a}\{\boldsymbol{x}\} = \sum_{i=1}^{n_p} N_i(\boldsymbol{x})\ \boldsymbol{a}\{\boldsymbol{x_i}\}, \qquad \boldsymbol{x} \in \Omega^d, \tag{2.47}$$

where n_p is the number of nodes of the whole domain (since adjacent elements share nodes, n_p is smaller than $n_n \times n_e$) and $N_i(\boldsymbol{x})$ is the global shape function, represented in Figure 2.4 and zero-valued outside the adjacent elements.

In order to find the vector field in a generic point $\boldsymbol{x}$ of the discretized domain Ω^d, it is convenient to introduce the following standard matrix notation. Let n_{dof} be the number of degrees of freedom for each node n_p, such that the global shape function matrix can be defined as:

$$\mathbf{N}(\boldsymbol{x}) = \left[\ \text{diag}\left[N_1(\boldsymbol{x})\right] \ \middle|\ \text{diag}[N_2(\boldsymbol{x})] \ \middle|\ \ldots \ \middle|\ \text{diag}[N_{n_p}(\boldsymbol{x})]\ \right], \tag{2.48}$$

where $\text{diag}\,[N_i(\boldsymbol{x})]$ denotes the $n_{\text{dof}} \times n_{\text{dof}}$ diagonal matrix,

$$\text{diag}\,[N_i(\boldsymbol{x})] = \begin{bmatrix} N_i(\boldsymbol{x}) & 0 & \dots & 0 \\ 0 & N_i(\boldsymbol{x}) & \dots & 0 \\ \vdots & \vdots & \ddots & \vdots \\ 0 & 0 & \dots & N_i(\boldsymbol{x}) \end{bmatrix}, \tag{2.49}$$

and, if all the nodal values are rearranged in a global vector $\boldsymbol{u}^g$,

$$\boldsymbol{u}^g = \{u_1^1 \ , \ \dots \ , \ u_{n_{\text{dof}}}^1 \ , \ \dots \ , \ \dots \ , \ u_1^{n_p} \ , \ \dots \ , \ u_{n_{\text{dof}}}^{n_p}\}^T, \tag{2.50}$$

where the generic element u_i^j is the i-component of the displacement vector of the global node j, then the vectorial field in a point $\boldsymbol{x}$ can be expressed as:

$$\boldsymbol{a}\{\boldsymbol{x}\} = \mathbf{N}(\boldsymbol{x})\ \boldsymbol{u}^g. \tag{2.51}$$

In order to complete the spatial discretization, two operators must be introduced: the discrete gradient operator, $\mathbf{G}^g$, and the discrete symmetric gradient operator, $\mathbf{B}^g$. Both must be defined taking into account the type of problem that is going to be solved (i.e. 2 - dimensional or 3 - dimensional fields). For the 2 - dimensional problem, these operators, also named as deformation matrices, are denoted as:

$$\mathbf{B}^g = \left[\begin{array}{cc|cc|c|cc} \frac{\partial N_1}{\partial x} & 0 & \frac{\partial N_2}{\partial x} & 0 & \dots & \frac{\partial N_{n_p}}{\partial x} & 0 \\ 0 & \frac{\partial N_1}{\partial y} & 0 & \frac{\partial N_2}{\partial y} & \dots & 0 & \frac{\partial N_{n_p}}{\partial y} \\ \frac{\partial N_1}{\partial y} & \frac{\partial N_1}{\partial x} & \frac{\partial N_2}{\partial y} & \frac{\partial N_2}{\partial x} & \dots & \frac{\partial N_{n_p}}{\partial y} & \frac{\partial N_{n_p}}{\partial x} \end{array}\right], \tag{2.52a}$$

$$\mathbf{G}^g = \left[\begin{array}{cc|cc|c|cc} \frac{\partial N_1}{\partial x} & 0 & \frac{\partial N_2}{\partial x} & 0 & \dots & \frac{\partial N_{n_p}}{\partial x} & 0 \\ 0 & \frac{\partial N_1}{\partial x} & 0 & \frac{\partial N_2}{\partial x} & \dots & 0 & \frac{\partial N_{n_p}}{\partial x} \\ \frac{\partial N_1}{\partial y} & 0 & \frac{\partial N_2}{\partial y} & 0 & \dots & \frac{\partial N_{n_p}}{\partial y} & 0 \\ 0 & \frac{\partial N_1}{\partial y} & 0 & \frac{\partial N_2}{\partial y} & \dots & 0 & \frac{\partial N_{n_p}}{\partial y} \end{array}\right]. \tag{2.52b}$$

Spatial Discretization of the Equilibrium Equations

Regarding the deformation matrices that were presented in the last section, the weak equilibrium equations, concerning a finite strain framework, can be discretized and, assuming the spatial formulation, Equation (2.41) is given by:

$$\left\{ \int_{\varphi(\Omega^d)} \left[(\mathbf{B}^g)^T\, \boldsymbol{\sigma} - \mathbf{N}^T\ \mathbf{b} \right] \mathrm{d}V - \int_{\varphi(\partial\Omega^d)} \mathbf{N}^T\ \mathbf{t}\ \mathrm{d}A \right\}^T \cdot \boldsymbol{\eta} = 0, \qquad \forall \boldsymbol{\eta} \in \mathcal{V}^d, \tag{2.53}$$

where $\mathcal{V}^d$ represents the discretized virtual displacement space and $\boldsymbol{\sigma}$ is the vector representation of the Cauchy stress tensor $\boldsymbol{\sigma}$.

Taking into account the material formulation, the discretized version of Equation (2.42) is:

$$\left\{ \int_{\Omega^d} \left[(\mathbf{G}^g)^T \, \mathbf{P} - \mathbf{N}^T \, \bar{\mathbf{b}} \right] \mathrm{d}V - \int_{\partial\Omega^d} \mathbf{N}^T \, \bar{\mathbf{t}} \, \mathrm{d}A \right\}^T \cdot \boldsymbol{\eta} = 0, \qquad \forall \boldsymbol{\eta} \in \mathcal{V}^d, \tag{2.54}$$

in which $\mathbf{P}$ is the vector configuration of the first Piola-Kirchhoff stress tensor $\boldsymbol{P}$.

According to the virtual work principle, the equations above have to be satisfied for all virtual displacements $\boldsymbol{\eta}$. Therefore, the terms inside the brackets must be null. Thus, it is possible to rewrite them as:

$$\mathbf{f}^{\text{int}} - \mathbf{f}^{\text{ext}} = 0, \tag{2.55}$$

where $\mathbf{f}^{\text{int}}$ and $\mathbf{f}^{\text{ext}}$ are, respectively, the global internal and external force vectors, and in the spatial form are denoted by:

$$\mathbf{f}^{\text{int}} = \int_{\varphi(\Omega^d)} (\mathbf{B}^g)^T \, \boldsymbol{\sigma} \, \mathrm{d}V, \tag{2.56a}$$

$$\mathbf{f}^{\text{ext}} = \int_{\varphi(\Omega^d)} \mathbf{N}^T \, \mathbf{b} \, \mathrm{d}A + \int_{\varphi(\partial\Omega^d)} \mathbf{N}^T \, \mathbf{t} \, \mathrm{d}A. \tag{2.56b}$$

In the computational framework of the finite element method, these force vectors are analysed element by element, and are obtained by integration over its domain,

$$\mathbf{f}_e^{\text{int}} = \int_{\varphi(\Omega^e)} (\mathbf{B}^e)^T \, \boldsymbol{\sigma} \, \mathrm{d}V, \tag{2.57a}$$

$$\mathbf{f}_e^{\text{ext}} = \int_{\varphi(\Omega^e)} (\mathbf{N}^e)^T \, \mathbf{b} \, \mathrm{d}A + \int_{\varphi(\partial\Omega^e)} (\mathbf{N}^e)^T \, \mathbf{t} \, \mathrm{d}A, \tag{2.57b}$$

in the deformed configuration. In the material formulation the force vectors are given by:

$$\mathbf{f}_e^{\text{int}} = \int_{\Omega^e} (\mathbf{G}^e)^T \, \mathbf{P} \, \mathrm{d}V, \tag{2.58a}$$

$$\mathbf{f}_e^{\text{ext}} = \int_{\Omega^e} (\mathbf{N}^e)^T \, \mathbf{b} \, \mathrm{d}A + \int_{\partial\Omega^e} (\mathbf{N}^e)^T \, \mathbf{t} \, \mathrm{d}A, \tag{2.58b}$$

The element force vectors are assembled to the global force vectors,

$$\mathbf{f}^{\text{int}} = \mathop{\mathsf{A}}_{e=1}^{n_e} \mathbf{f}_e^{\text{int}}, \tag{2.59a}$$

$$\mathbf{f}^{\text{ext}} = \mathop{\mathsf{A}}_{e=1}^{n_e} \mathbf{f}_e^{\text{ext}}. \tag{2.59b}$$

Gaussian Quadrature

In order to obtain the solution of an integral in a numerical way, the *Gaussian Quadrature* is the most commonly used method. To facilitate the use of this method, the coordinates of the finite elements are, usually, converted to parametric coordinates $\boldsymbol{\zeta}$ (mapping from physical to natural space). This conversion allows to solve complex structures in a more easy and expedite

way. The transformation between coordinates is given by the Jacobian matrix:

$$\mathbf{J} = \frac{\partial \boldsymbol{x}}{\partial \boldsymbol{\zeta}}. \tag{2.60}$$

The Gaussian quadrature method states that, by employing the following equality:

$$\int_{\Omega} \boldsymbol{a}\{\boldsymbol{x}\}\ \mathrm{d}V = \int_{-1}^{1} \boldsymbol{a}\{\boldsymbol{\zeta}\}\ \det(\mathbf{J})\ \mathrm{d}\boldsymbol{\zeta} \equiv \sum_{i=1}^{\mathrm{nGP}} \boldsymbol{a}\{\boldsymbol{\zeta}_i\}\ W_i\ \det(\mathbf{J}_i), \tag{2.61}$$

it is possible to reach the solution of an integration of a non-linearity field $\boldsymbol{a}$ of degree n over the domain V, by replacing it with the weighted sum of the corresponding values, $\boldsymbol{a}\{\boldsymbol{\zeta}_i\}$, in the Gauss points (nGP), where W_i is the weight of each point. The number of Gauss points has to be chosen accordingly with the degree n and the expression that connect both is:

$$n = 2 \times \mathrm{nGP} - 1. \tag{2.62}$$

2.6.3 Time Discretization

Usually, materials exhibit a behaviour that is dependent on the deformation history (i.e. deformation rate or/and the loading path they were submitted to). In the finite element method this problem is solved through an incremental strategy, in which the time domain is discretized: the time interval, $[t_0, t]$, is divided in $n+1$ sub-intervals where the equilibrium equations must be satisfied. In order to make this possible, there must be an internal variable, θ, in the constitutive relations of the material to store the information due to the previous increment.

Taking this into consideration, the constitutive stress response at increment $n+1$ is obtained considering the new current deformation state and the internal variables of the previous increment,

$$\boldsymbol{\sigma}_{n+1} = \hat{\boldsymbol{\sigma}}\{\boldsymbol{F}_{n+1}, \boldsymbol{\theta}_n\}, \tag{2.63a}$$

$$\boldsymbol{P}_{n+1} = \hat{\boldsymbol{P}}\{\boldsymbol{F}_{n+1}, \boldsymbol{\theta}_n\}, \tag{2.63b}$$

for the spatial and material formulation, respectively, in which $\hat{\boldsymbol{\sigma}}\{\boldsymbol{F}_{n+1}, \boldsymbol{\theta}_n\}$ and $\hat{\boldsymbol{P}}\{\boldsymbol{F}_{n+1}, \boldsymbol{\theta}_n\}$ are the incremental constitutive functional for each configuration.

In the case of infinitesimal deformations, the current deformation is defined by the infinitesimal strain tensor described in Equation (2.30), thus:

$$\boldsymbol{\sigma}_{n+1} = \hat{\boldsymbol{\sigma}}\{\boldsymbol{\varepsilon}_{n+1}, \boldsymbol{\theta}_n\}. \tag{2.64}$$

Therefore, considering Equation (2.41), the *quasi-static* incremental boundary value problem (spatial configuration) is defined as follows:

Given the set of internal variables, $\boldsymbol{\theta}_n$, and the displacement field obtained in the previous increment, knowing the current applied forces $\boldsymbol{b}_{n+1}$ and $\boldsymbol{t}_{n+1}$, find the displacement field, $\boldsymbol{u}_{n+1}$,

that satisfies,

$$\int_{\varphi(\Omega)} [\hat{\boldsymbol{\sigma}}\{\boldsymbol{F}_{n+1}, \boldsymbol{\theta}_n\} : \nabla_x \boldsymbol{\eta} - \boldsymbol{b} \cdot \boldsymbol{\eta}] \, \mathrm{d}V - \int_{\varphi(\partial\Omega)} \boldsymbol{t} \cdot \boldsymbol{\eta} \, \mathrm{d}A = 0, \qquad \forall \boldsymbol{\eta} \in \mathcal{V}. \tag{2.65}$$

2.6.4 Incremental Finite Element Solution

If the finite element discretization is applied to the problem stated before, Equation (2.65), can be expressed as:

$$\mathbf{r}\{\mathbf{u}_{n+1}\} = \mathbf{f}^{\text{int}}\{\mathbf{u}_{n+1}\} - \mathbf{f}^{\text{ext}}_{n+1} \tag{2.66}$$

where the unknown variable is the nodal vector displacement $\mathbf{u}_{n+1}$ such that the residual $\mathbf{r}$ is null (or extremely small). The force vectors are rewritten to take into consideration the incremental constitutive functional and are assembled from their elemental counterparts,

$$\mathbf{f}^{\text{int}}_{e_{n+1}} = \int_{\varphi(\Omega^e)} (\mathbf{B}^e)^T \, \hat{\boldsymbol{\sigma}}\{\boldsymbol{F}_{n+1}, \boldsymbol{\theta}_n\} \, \mathrm{d}V, \tag{2.67a}$$

$$\mathbf{f}^{\text{ext}}_{e_{n+1}} = \int_{\varphi(\Omega^e)} (\mathbf{N}^e)^T \, \mathbf{b}_{n+1} \, \mathrm{d}A + \int_{\varphi(\partial\Omega^e)} (\mathbf{N}^e)^T \, \mathbf{t}_{n+1} \, \mathrm{d}A. \tag{2.67b}$$

Due to the possible non-linear material behaviour or to geometrical non-linearities, Equation (2.66) is non-linear and so, in order to solve it in a computational way, a sturdy and efficient method must be utilized. The iterative *Newton-Raphson* method (Figure 2.5) is one of the most popular numerical tools for this matter, as it has a quadratic rate of asymptotic convergence that allows to obtain the solution in a faster and easier way.

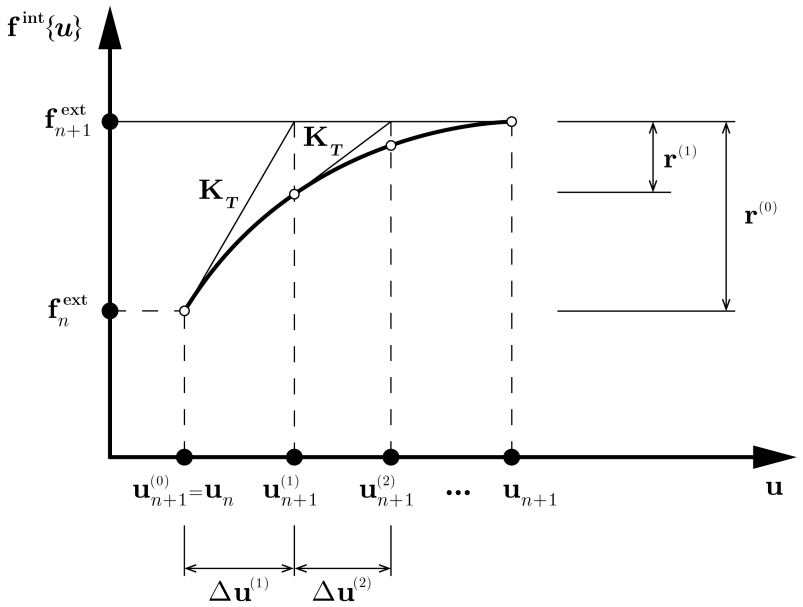

Figure 2.5: The Newton-Raphson algorithm for the incremental finite element solution.

For the increment $n+1$, the initial guess for the displacement fields is assumed to be the last converged value, $\mathbf{u}_{n+1}^{(0)} = \mathbf{u}_n$, and within iteration (j) it is updated as:

$$\mathbf{u}_{n+1}^{(j)} = \mathbf{u}_{n+1}^{(j-1)} + \Delta\mathbf{u}^{(j)}, \tag{2.68}$$

where $\Delta\mathbf{u}^{(j)}$ is obtained in each iteration (j) of the Newton-Raphson method through the resolution of the linearised version of the equilibrium equation:

$$\mathbf{K}_T^{(j-1)}\Delta\mathbf{u}^{(j)} = \mathbf{r}\{\mathbf{u}_{n+1}^{(j-1)}\}. \tag{2.69}$$

The global tangent stiffness matrix $\mathbf{K}_T$ is obtained as:

$$\mathbf{K}_T^{(j-1)} = \left.\frac{\partial\mathbf{r}}{\partial\mathbf{u}_{n+1}}\right|_{\mathbf{u}_{n+1}^{(j-1)}} = \mathop{\mathsf{A}}_{e=1}^{n_e}\int_{\varphi(\Omega^e)}(\mathbf{B}^e)^T\mathbf{D}\mathbf{B}^e\ \mathrm{d}V, \tag{2.70}$$

where $\mathbf{D}$ is the matrix representation of the spatial tangent modulus,

$$\mathbf{D} = \frac{\partial\boldsymbol{\sigma}}{\partial\boldsymbol{F}}. \tag{2.71}$$

This iterative process occurs until a convergence criterion, imposed *a priori*, has been achieved, i.e. $\dfrac{\parallel\mathbf{r}\parallel}{\parallel\mathbf{f}^{\mathrm{ext}}\parallel} < \mathrm{tol}.$

Chapter 3

Micromechanics and Multi-Scale Models

As previously explained, in continuum mechanics one considers that in an infinitesimal point the material can be classified as homogeneous. This leads to the assumption that the stresses and strains observed within the infinitesimal material neighbourhood that surrounds that infinitesimal point can be regarded as essentially uniform. Thus, the majority of the constitutive models (laws that define the relation between stress and strain) are based on these assumptions, considering the material as an homogeneous entity.

Although a large number of materials can be analysed in this manner, if one thinks of a more complex range of materials (e.g. composite materials) these assumptions are not valid because, at the microscale, this infinitesimal neighbourhood may be composed by different constituents and even cracks and voids. If a body with such complex microstructure is submitted to high levels of deformation, these microstructure constituents start to develop several mechanisms (e.g. plastic localization, void coalescence and micro-cracking) that will play a major role on the macroscopic behaviour of the material and, despite the fact that the traditional constitutive models are able to achieve accurate and reliable results, the need for models that can take into account these microstructural interactions is high, as it provides a good foundation for the analysis of multi-phase materials and for the design of new ones.

Therefore, a *Multi-Scale* approach is introduced in which two scales are considered: the *macroscale*, where macroscopic information such as the geometry of the body and the applied load are defined, and the *microscale*, where microscopic phenomena occurs with a great importance for the macroscopic behaviour.

A *Representative Volume Element* (RVE) is used to define the microscale of the problem as it should contain enough information about the microstructure of the material. The macroscopic deformation gradient, consequence of the macroscale properties, is applied to the RVE and a RVE equilibrium problem is solved, resulting in a microscopic stress field that is homogenized to obtain the macroscopic stress tensor. Furthermore, it is possible to assign a RVE to each integration point of the macroscopic finite element mesh in order to solve the microscale problem in all of them, giving rise to the *Coupled Multi-Scale Analysis*. This numerical tool is generic

and universal, as it is possible to properly analyse all kinds of microstructures presented in a material.

In this chapter, *Multi-Scale* models are described, the concept of *Representative Volume Element* is introduced and the theory for scale transition, homogenization and the classical boundary conditions are presented. The numerical approximation of these principles through the *Finite Element Method* is also briefly explained. For a more detailed study on these topics, the following references are suggested: Nemat-Nasser et al. (1993); Neto et al. (2008); Reis (2014).

3.1 Representative Volume Element

Despite the fact that a material can be considered homogeneous at the macroscale, when the microscale is taken into consideration, the microstrutcture is usually composed of multiple heterogeneities and singularities that influence the whole behaviour of the material. With that in mind, Hill (1963) suggested that it should exist a sub-region that would be statistically representative of the microstructure of the material and named it *Representative Volume Element* (RVE). In this geometrical microscale model, each phase, constituent or singularity is explicitly represented as it is demonstrated in Figure 3.1.

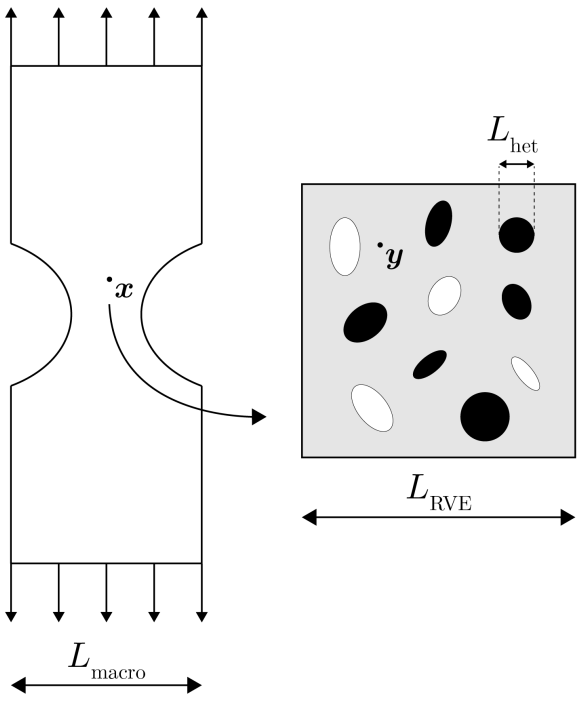

Figure 3.1: Macro and microscales and respective sizes.

Several authors have been proposing their definition of RVE (Hashin, 1983; Nemat-Nasser et al., 1993; Gitman et al., 2007) but the main idea is that the RVE should be large compared to the microstructural singularities, being statistically representative of them, but it must be

small enough so that it can be considered an infinitesimal point at the macroscale, allowing the application of the homogenization procedure. This concept leads to the so-called *scales separation principle* (Hashin, 1983) and is better understood through the following equation:

$$L_{\text{het}} \ll L_{\text{RVE}} \ll L_{\text{macro}}, \tag{3.1}$$

where L_{macro} is the macroscopic size of the structure, L_{RVE} is the size of the RVE and L_{het} is the typical size of the microstructural heterogeneities, as illustrated in Figure 3.1.

The definition of RVE size is the main scope of this work, as it is one of the most important features to take into account. It depends on the complexity of the microstructure and on the behaviour of its constituents, and it should be as small as possible while containing all of the information needed to be statistically representative of the microstructure. A large RVE requires a lot of computational power to be analysed, even more if it is included in a global macroscopic analysis, since in this type of simulation several RVEs' analyses are performed. Thus, it is important to find the right balance between a RVE that is statistically representative of the microscale singularities but is still affordable on a computational level. Several studies about this matter are presented on this thesis.

Nonetheless, there are some cases where the existence of a RVE is questionable. For instance, as shown in Gitman et al. (2007), when there is a material that shows strain localization with global softening behaviour, the possibility to find a RVE that is still statistically homogeneous vanishes.

It is important to note that, even if the traditional constitutive laws are not sufficiently accurate to predict the macroscopic behaviour of a material with complex microstructure, these models are used to successfully characterize the behaviour of each microstructural constituent, due to the fact that they are considered as continuum matter at the microscale.

3.2 Scale Transition Theory

For a better understanding of the subjects presented in the forthcoming sections, the notation used throughout the present document is introduced. As denoted in the previous chapter, $\boldsymbol{x}$ and $\boldsymbol{X}$ are the characters used to describe an infinitesimal point in the deformed and undeformed configurations at the macroscale, respectively. On the other hand, if one is referring to the microscale, $\boldsymbol{y}$ denotes the coordinates of the infinitesimal point in the deformed configuration and $\boldsymbol{Y}$ on the undeformed state.

The *scales separation principle*, that has already been introduced, states that the size of the RVE should be several times bigger than those of the micro heterogeneities but much smaller that the macro structure size. This principle must be satisfied to allow the homogenization of the stress and strain fields.

3.2.1 Numerical Homogenization

Primarily, it is important to introduce the numerical homogenization procedure since it is one of the core concepts of the multi-scale models. It enables the computation of macroscopic fields through a volumetric average of their microscopic counterparts over the RVE, in a material description.

To illustrate, let $\boldsymbol{A}\{\boldsymbol{y}\}$ be a generic tensorial field defined at the microscale, then its corresponding homogenized tensor, $\boldsymbol{A}\{\boldsymbol{x}\}$, is denoted by:

$$\boldsymbol{A}\{\boldsymbol{x}\} = \frac{1}{V_\mu} \int_{\Omega_\mu} \boldsymbol{A}\{\boldsymbol{y}\} \, \mathrm{d}V, \tag{3.2}$$

where Ω_μ is the undeformed domain of the RVE and V_μ is the volume on the reference configuration.

3.3 Microscale Equilibrium Problem

In this section, the procedure to find the microscopic stress field is introduced, being this the basis to the homogenized stress tensor. Furthermore, as the problem is formulated under the *large strain* theory, the deformation gradient, $\boldsymbol{F}$, is utilized to define the prescribed strains and, since the homogenization procedure is applied to the initial configuration, the homogenized first *Piola-Kirchhoff* stress tensor is obtained. This procedure is demonstrated in Figure 3.2.

Finally, this problem is going to be divided into the following steps:

1. Determination of the microscopic deformation gradient;
2. Definition of the admissible microscopic displacement field;
3. Description of the RVE equilibrium;
4. Presentation of the *Hill-Mandel* principle;
5. Homogenization of the first Piola-Kirchhoff stress tensor.

3.3.1 Microscopic Deformation Gradient

Considering a large deformation theory, the deformation applied to the RVE is characterized through a deformation gradient. As aforementioned, the homogenization procedure allows the determination of the macroscopic fields through their microscopic correspondence. Hence, for a generic macroscopic point $\boldsymbol{x}$ in an instant t, the macroscopic deformation gradient $\boldsymbol{F}\{\boldsymbol{x}, t\}$ is given by:

$$\boldsymbol{F}\{\boldsymbol{x}, t\} = \frac{1}{V_\mu} \int_{\Omega_\mu} \boldsymbol{F}\{\boldsymbol{y}, t\} \, \mathrm{d}V, \tag{3.3}$$

where the microscopic deformation gradient, $\boldsymbol{F}\{\boldsymbol{y}, t\}$, can be expressed as,

$$\boldsymbol{F}\{\boldsymbol{y}, t\} = \boldsymbol{I} + \nabla_X \, \boldsymbol{u}\{\boldsymbol{y}, t\}, \tag{3.4}$$

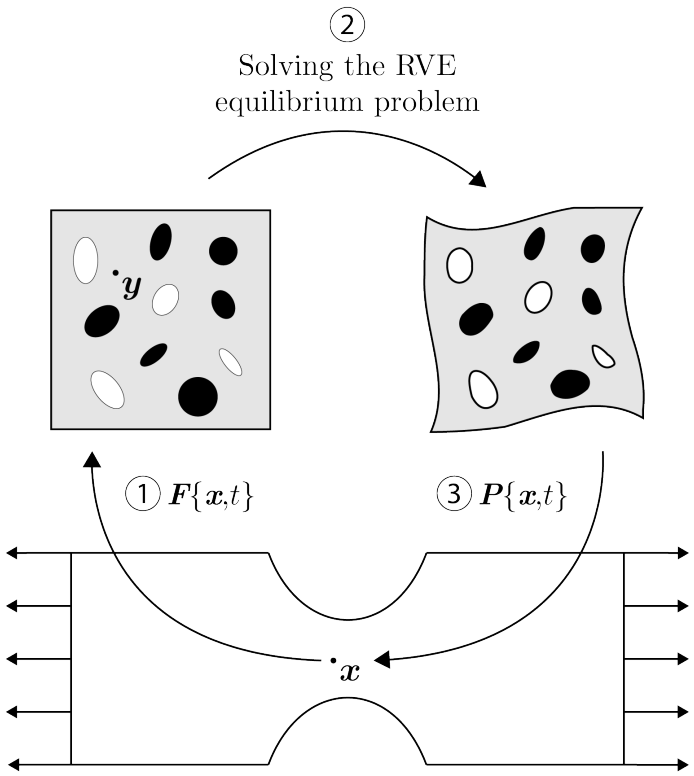

Figure 3.2: Representation of the procedure to solve a multi-scale problem.

where ∇_X is the gradient operator in material description. As a result, Expression (3.3) is rewritten as,

$$\boldsymbol{F}\{\boldsymbol{x},t\} = \boldsymbol{I} + \frac{1}{V_\mu}\int_{\Omega_\mu} \nabla_X\ \boldsymbol{u}\{\boldsymbol{y},t\}\ \mathrm{d}V. \tag{3.5}$$

Applying the macroscopic deformation gradient to the RVE generates a microscopic displacement field, $\boldsymbol{u}\{\boldsymbol{y},t\}$, and, without losing generality, this field can be decomposed as the sum of its linear part and the displacement fluctuation field,

$$\boldsymbol{u}\{\boldsymbol{y},t\} = (\boldsymbol{F}\{\boldsymbol{x},t\} - \boldsymbol{I})\,\boldsymbol{Y} + \tilde{\boldsymbol{u}}\{\boldsymbol{y},t\}, \tag{3.6}$$

where the linear part depends on the prescribed deformation gradient and the displacement fluctuation field, $\tilde{\boldsymbol{u}}\{\boldsymbol{y},t\}$, is the unknown variable of the microscopic equilibrium problem.

As a consequence, the microscopic deformation gradient can be defined in terms of its macroscopic counterpart and the displacement fluctuation field,

$$\begin{aligned}\boldsymbol{F}\{\boldsymbol{y},t\} &= \boldsymbol{I} + \nabla_X\ \boldsymbol{u}\{\boldsymbol{y},t\} \\ &= \boldsymbol{I} + \nabla_X\ [(\boldsymbol{F}\{\boldsymbol{x},t\} - \boldsymbol{I})\,\boldsymbol{Y} + \tilde{\boldsymbol{u}}\{\boldsymbol{y},t\}] \\ &= \boldsymbol{F}\{\boldsymbol{x},t\} + \nabla_X\ \tilde{\boldsymbol{u}}\{\boldsymbol{y},t\}.\end{aligned} \tag{3.7}$$

3.3.2 Admissible Microscopic Displacement Field

Having established the macroscopic deformation gradient (Equation (3.5)) and the microscopic displacement filed (Equation (3.6)), it is possible to obtain the following equation:

$$\boldsymbol{F}\{\boldsymbol{x},t\} = \boldsymbol{F}\{\boldsymbol{x},t\} + \frac{1}{V_\mu}\int_{\Omega_\mu} \nabla_X\ \tilde{\boldsymbol{u}}\{\boldsymbol{y},t\}\ \mathrm{d}V, \tag{3.8}$$

and, applying the *Gauss* theorem,

$$\int_{\Omega_\mu} \nabla_X\ \tilde{\boldsymbol{u}}\{\boldsymbol{y},t\}\ \mathrm{d}V = \int_{\partial\Omega_\mu} \tilde{\boldsymbol{u}}\{\boldsymbol{y},t\} \otimes \boldsymbol{N}\{\boldsymbol{Y}\}\ \mathrm{d}A = \boldsymbol{0}, \tag{3.9}$$

that defines the *minimal kinematical admissible constraint*, which defines the space of admissible displacement fluctuation,

$$\tilde{\mathcal{K}} \equiv \left\{ \tilde{\boldsymbol{u}},\ \text{sufficiently regular} \mid \int_{\partial\Omega_\mu} \tilde{\boldsymbol{u}}\{\boldsymbol{y},t\} \otimes \boldsymbol{N}\{\boldsymbol{Y}\}\ \mathrm{d}A = \boldsymbol{0} \right\}, \tag{3.10}$$

where $\boldsymbol{N}\{\boldsymbol{Y}\}$ is the outward unit vector normal to the boundary of the undeformed configuration of the RVE, $\partial\Omega_\mu$.

3.3.3 RVE Equilibrium

As pointed in Section 3.1, the RVE constituents are considered a continuum media, therefore the theory of *Continuum Mechanics*, presented in Chapter 2, is applied to model the microscale equilibrium problem.

The homogenization procedure is formulated under material description, nonetheless the microscopic equilibrium problem is solved considering a spatial description, thus the strong form of the equilibrium equations for the RVE is given by:

$$\begin{cases} \mathrm{div}_x\ \boldsymbol{\sigma}\{\boldsymbol{y},t\} + \boldsymbol{b}_\mu\{\boldsymbol{y},t\} = \boldsymbol{0} & ,\text{in } \varphi(\Omega_\mu), \\ \boldsymbol{t}_\mu\{\boldsymbol{y},t\} = \boldsymbol{\sigma}\{\boldsymbol{y},t\}\ \boldsymbol{n}\{\boldsymbol{y}\} & ,\text{on } \varphi(\partial\Omega_\mu), \end{cases} \tag{3.11}$$

where $\boldsymbol{b}_\mu\{\boldsymbol{y},t\}$ represents the volume forces in the deformed configuration of the RVE, $\boldsymbol{t}_\mu\{\boldsymbol{y},t\}$ the applied boundary traction vector field and $\boldsymbol{n}\{\boldsymbol{y}\}$ is the outward unit vector normal to the deformed boundary of the RVE, $\varphi(\partial\Omega_\mu)$.

The microscopic equilibrium problem is solved with the *Finite Element Method*. Accordingly, the *Virtual Work Principle* is employed to determine the *Weak Equilibrium Equations*, first in spatial description:

$$\int_{\varphi(\Omega_\mu)} [\boldsymbol{\sigma}\{\boldsymbol{y},t\} : \nabla_x\tilde{\boldsymbol{\eta}} - \boldsymbol{b}_\mu\{\boldsymbol{y},t\} \cdot \tilde{\boldsymbol{\eta}}]\ \mathrm{d}V - \int_{\varphi(\partial\Omega_\mu)} \boldsymbol{t}_\mu\{\boldsymbol{y},t\} \cdot \tilde{\boldsymbol{\eta}}\ \mathrm{d}A = 0, \qquad \forall\tilde{\boldsymbol{\eta}} \in \mathcal{V}, \tag{3.12}$$

and secondly, in material description:

$$\int_{\Omega_\mu} \left[\boldsymbol{P}\{\boldsymbol{y},t\} : \nabla_X \tilde{\boldsymbol{\eta}} - \bar{\boldsymbol{b}}_\mu\{\boldsymbol{y},t\} \cdot \tilde{\boldsymbol{\eta}}\right] \mathrm{d}V - \int_{\partial\Omega_\mu} \bar{\boldsymbol{t}}_\mu\{\boldsymbol{y},t\} \cdot \tilde{\boldsymbol{\eta}} \, \mathrm{d}A = 0, \qquad \forall \tilde{\boldsymbol{\eta}} \in \mathcal{V}, \tag{3.13}$$

with $\bar{\boldsymbol{b}}_\mu\{\boldsymbol{y},t\}$ and $\bar{\boldsymbol{t}}_\mu\{\boldsymbol{y},t\}$ representing the same as in Equation (3.11) but in the undeformed configuration of the RVE. In these expressions, $\tilde{\boldsymbol{\eta}}$ is the virtual displacement field and $\mathcal{V}$ is the space of virtual displacements that coincides with the space of admissible displacement fluctuation $\left(\mathcal{V} \equiv \tilde{\mathcal{K}}\right)$, since the virtual displacements are also admissible displacement variations.

3.3.4 Hill-Mandel Principle

This is one the major concepts in multi-scale models constitutive theories. The *Hill-Mandel* principle of *Macro-Homogeneity* uses an energetic balance to establish the connection between scales. It requires the macroscopic stress power to equal the average of its microscopic counterpart over the volume of the RVE. Considering a material formulation, the principle is expressed by:

$$\boldsymbol{P}\{\boldsymbol{x},t\} : \dot{\boldsymbol{F}}\{\boldsymbol{x},t\} = \frac{1}{V_\mu} \int_{\Omega_\mu} \boldsymbol{P}\{\boldsymbol{y},t\} : \dot{\boldsymbol{F}}\{\boldsymbol{y},t\} \, \mathrm{d}V. \tag{3.14}$$

where $\dot{\boldsymbol{F}}\{\cdot\}$ is the time derivative of the deformation gradient.

With Equation (3.7) in mind, it is possible to express that,

$$\dot{\boldsymbol{F}}\{\boldsymbol{y},t\} = \dot{\boldsymbol{F}}\{\boldsymbol{x},t\} + \nabla_X \, \dot{\tilde{\boldsymbol{u}}}\{\boldsymbol{y},t\}, \tag{3.15}$$

thus, combining Equation (3.14) with Equation (3.15), it is possible to rewrite the *Hill-Mandel* principle as:

$$\int_{\Omega_\mu} \boldsymbol{P}\{\boldsymbol{y},t\} : \nabla_X \, \dot{\tilde{\boldsymbol{u}}}\{\boldsymbol{y},t\} \, \mathrm{d}V = 0. \tag{3.16}$$

If one considers the hypothesis that $\dot{\tilde{\boldsymbol{u}}} \in \mathcal{V}$, Expression (3.13) results in the following conditions:

$$\int_{\Omega_\mu} \bar{\boldsymbol{b}}_\mu\{\boldsymbol{y},t\} \cdot \tilde{\boldsymbol{\eta}} \, \mathrm{d}V = 0, \qquad \forall \tilde{\boldsymbol{\eta}} \in \mathcal{V}, \tag{3.17}$$

$$\int_{\partial\Omega_\mu} \bar{\boldsymbol{t}}_\mu\{\boldsymbol{y},t\} \cdot \tilde{\boldsymbol{\eta}} \, \mathrm{d}A = 0, \qquad \forall \tilde{\boldsymbol{\eta}} \in \mathcal{V}. \tag{3.18}$$

Analysing these expressions, the main conclusion that can be drawn from the *Hill-Mandel* principle is that the body and traction forces are reactive forces related to the kinematical constraints applied to the displacement fluctuation field on the RVE. This enables the simplification of the equilibrium equation, being stated as:

$$\int_{\Omega_\mu} \boldsymbol{P}\{\boldsymbol{y},t\} : \nabla_X \tilde{\boldsymbol{\eta}} \, \mathrm{d}V = 0, \qquad \forall \tilde{\boldsymbol{\eta}} \in \mathcal{V}, \tag{3.19}$$

or, in spatial form,

$$\int_{\varphi(\Omega_\mu)} \boldsymbol{\sigma}\{\boldsymbol{y},t\} : \nabla_x \tilde{\boldsymbol{\eta}} \, \mathrm{d}V = 0, \qquad \forall \tilde{\boldsymbol{\eta}} \in \mathcal{V}. \tag{3.20}$$

3.3.5 Homogenized Stress Tensor

The homogenized first Piola-Kirchhoff stress tensor, $\boldsymbol{P}\{\boldsymbol{x},t\}$, is given by:

$$\begin{aligned} \boldsymbol{P}\{\boldsymbol{x},t\} &= \frac{1}{V_\mu} \int_{\Omega_\mu} \boldsymbol{P}\{\boldsymbol{y},t\} \, \mathrm{d}V \\ &= \frac{1}{V_\mu} \int_{\partial\Omega_\mu} \bar{\boldsymbol{t}}_\mu\{\boldsymbol{y},t\} \otimes \boldsymbol{Y} \mathrm{d}A - \frac{1}{V_\mu} \int_{\Omega_\mu} \bar{\boldsymbol{b}}_\mu\{\boldsymbol{y},t\} \otimes \boldsymbol{Y} \mathrm{d}V \end{aligned} \tag{3.21}$$

3.4 Admissible Kinematical Boundary Conditions

As mentioned in Section 3.3.1, the unknown variable in a microscopic equilibrium problem is the displacement fluctuation field $\tilde{\boldsymbol{u}}\{\boldsymbol{y},t\}$.

In order to simulate the behaviour of a RVE, it is necessary to impose a specific boundary condition and different choices may lead to different results. The type of material and the characteristics behind the heterogeneities distribution in the RVE are some of the key points that should be considered while choosing a boundary condition to the micromechanical problem.

The simplest boundary condition, named *Taylor* hypothesis (represented in Figure 3.3), assumes that the microscopic displacement field is a linear function of $\boldsymbol{Y}$,

$$\boldsymbol{u}\{\boldsymbol{y},t\} = (\boldsymbol{F}\{\boldsymbol{x},t\} - \boldsymbol{I})\, \boldsymbol{Y}, \tag{3.22}$$

implying that the displacement fluctuation field is null,

$$\tilde{\boldsymbol{u}}\{\boldsymbol{y},t\} = \boldsymbol{0}, \tag{3.23}$$

and, as a consequence, the microscopic deformation gradient is equivalent to the macroscopic counterpart,

$$\boldsymbol{F}\{\boldsymbol{y},t\} \equiv \boldsymbol{F}\{\boldsymbol{x},t\}. \tag{3.24}$$

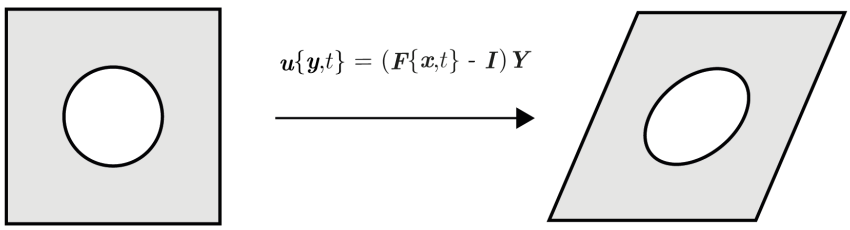

Figure 3.3: Scheme to represent the *Taylor* hypothesis.

It is a simple boundary condition and the most restrictive one. As a result, the stiffness of heterogeneous materials is overestimated - resembling the *rule of mistures*[1] (or *Voigt* model), an analytical method used to obtain the effective stiffness tensor of a composite material.

The three classical boundary conditions are presented next, along with a short review on an alternative version of the *Periodic* boundary condition, the *Mortar Periodic* boundary condition.

3.4.1 Linear Boundary Condition

This condition dictates that the displacement field on the RVE boundaries is equal to the prescribed one, leading to a null displacement fluctuation field on this boundary,

$$\tilde{\boldsymbol{u}}\{\boldsymbol{y}, t\} = \mathbf{0}, \qquad \forall \boldsymbol{y} \in \partial\Omega_\mu. \tag{3.25}$$

This satisfies expressions (3.9) and (3.18). However, expression (3.17) is only verified in the absence of body forces and accelerations.

3.4.2 Periodic Boundary Condition

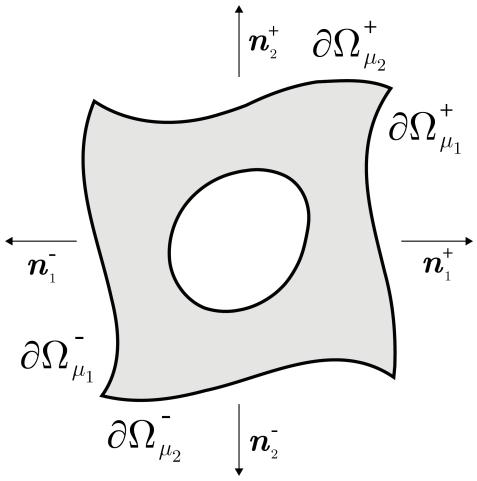

Figure 3.4: Boundaries of the RVE in the *Periodic* boundary condition.

The *Periodic* boundary condition is the most used kinematical constraint in micromechanics. With this boundary, the microstructure is seen as a periodic repeated pattern of the RVE, hence, displacements on opposite boundary sides must be compatible.

To implement this condition it is necessary to divide the boundaries of the RVE into a positive, $\partial\Omega_\mu^+$, and a negative, $\partial\Omega_\mu^-$, part (Figure 3.4), such that:

$$\partial\Omega_\mu = \partial\Omega_\mu^+ \cup \partial\Omega_\mu^-. \tag{3.26}$$

[1] Further addressed in Section 5.2.1

Furthermore, one must also consider the outward unit vectors $\boldsymbol{n}^+$, normal to $\partial\Omega_\mu^+$, and $\boldsymbol{n}^-$, normal to $\partial\Omega_\mu^-$, and that both have the following relation:

$$\boldsymbol{n}^- = -\boldsymbol{n}^+. \tag{3.27}$$

This boundary condition is expressed by a periodic displacement fluctuation field and an anti-periodic traction field and may be stated as:

$$\tilde{\boldsymbol{u}}\{\boldsymbol{y}^+, t\} = \tilde{\boldsymbol{u}}\{\boldsymbol{y}^-, t\}, \tag{3.28}$$

$$\bar{\boldsymbol{t}}_\mu\{\boldsymbol{y}^+, t\} = -\bar{\boldsymbol{t}}_\mu\{\boldsymbol{y}^-, t\}, \tag{3.29}$$

where $\boldsymbol{y}^+ \in \partial\Omega_\mu^+$ and $\boldsymbol{y}^- \in \partial\Omega_\mu^-$, correspond to similar points in opposite sides of the RVE.

Similarly to the *Linear* boundary condition, this condition satisfies expressions (3.9) and (3.18), but expression (3.17) is only verified in the absence of body forces and accelerations.

3.4.3 Uniform Traction Boundary Condition

The enforcement of the *minimal kinematical admissible constraint*, presented in Section 3.3.2, and denoted by:

$$\int_{\partial\Omega_\mu} \tilde{\boldsymbol{u}}\{\boldsymbol{y}, t\} \otimes \boldsymbol{N}\{\boldsymbol{Y}\} \, \mathrm{d}A = \boldsymbol{0}, \tag{3.30}$$

leads to an uniform traction field (hence the name of this condition) on the RVE boundaries.

Considering the *Hill-Mandel* principle, it is possible to conclude that this uniform traction field is driven by the macroscopic stress and equal to:

$$\boldsymbol{P}\{\boldsymbol{y}, t\}\boldsymbol{N}\{\boldsymbol{y}, t\} = \boldsymbol{P}\{\boldsymbol{x}, t\}\boldsymbol{N}\{\boldsymbol{x}, t\}. \tag{3.31}$$

3.4.4 Mortar Periodic Boundary Condition

The standard implementation of the *Periodic* boundary condition requires the RVE to be modelled by a conforming finite element mesh. The nodes on opposite boundary sides must be coincident, i.e. on the top and bottom boundaries the $x-$coordinate of the nodes must be the same and the same principle applies for the left and right boundaries but for the $y-$coordinate.

The main idea of this alternative version is that it enables the use of the *Periodic* boundary condition, while the finite element mesh in non-conform. Briefly, it uses *mortar* methods to discretize the boundary domain and combines the *Lagrange* multiplier method to enforce the accuracy of the solution. More information can be found in Reis and Andrade Pires (2014).

3.4.5 Remarks on the Different Boundary Conditions

After explaining the different boundary conditions that can be applied to the micro-scale problem, it is noteworthy to discuss these different approaches and withdraw some conclusions.

While the *Taylor* hypothesis is the most restrictive, the other conditions can be sorted according to the level of constraint that they enforce to the system. The *Uniform Traction* boundary condition is the less restrictive of them all, followed by the *Periodic* constraint (or *Mortar Periodic*) and, lastly, the *Linear* boundary condition is the most restrictive constraint (excluding the *Taylor* hypothesis). In Figure 3.5, a scheme that illustrates the differences between these three boundaries is presented.

During the work of this thesis, the RVEs were submitted to the *Linear*, *Uniform Traction* and *Mortar Periodic* boundary conditions. The *Mortar Periodic* boundary condition was used in place of the *Periodic* one, because the finite element mesh created with the OOF2 open-source program[2] creates a non-periodic mesh.

Furthermore, as it is demonstrated in Chapter 6, there are several authors that suggest that the *Periodic* constraint converges faster to the theoretical solution (Terada et al., 2000; Kanit et al., 2003). The *Uniform Traction* and the *Linear* boundary conditions are seen as the lower and upper bounds, respectively, for the effective elastic properties of the heterogeneous material. If the size of the RVE is large enough, all of the boundary conditions should converge for the same result. It is important to note that the *Linear* constraint is the one that requires less computational power.

Lastly, regarding the *Uniform Traction* boundary condition, there is a relevant aspect that must be mentioned: since this condition is based on the *minimal kinematical admissible constraint*, when large deformations are imposed on the RVE, *spurious* effects may appear (Coenen et al., 2012), which lead to unrealistic and meaningless results.

3.5 Numerical Implementation of the Microscale Problem

Having explained all the theoretical concepts that are necessary to solve the RVE equilibrium problem, the computational implementation is briefly introduced. The numerical tool used in this work is based on the *Finite Element Method* and the constraints that are associated with the microscopic problem are implemented using the *Condensation* method that eliminates the rows and columns related with the prescribed degrees of freedom, in the global system of equations. In the framework of this thesis, it is not important to fully detail the procedure to implement this on a computational level, and more information regarding this can be found on Reis (2014); Rodrigues Lopes (2016).

3.5.1 Micro-Scale Problem (MSP)

The computational program used during this thesis is named Micro-Scale Problem (MSP). It has been initially developed by Reis (2014) and, is currently being further developed by Rodrigues Lopes (2016). As the name implies, it solves the micro-scale problem under the hypothesis of *large stains* theory, within a generic non-linear finite element framework.

[2]OOF2 is the program utilized to create the finite element mesh based on a microstructure's image.

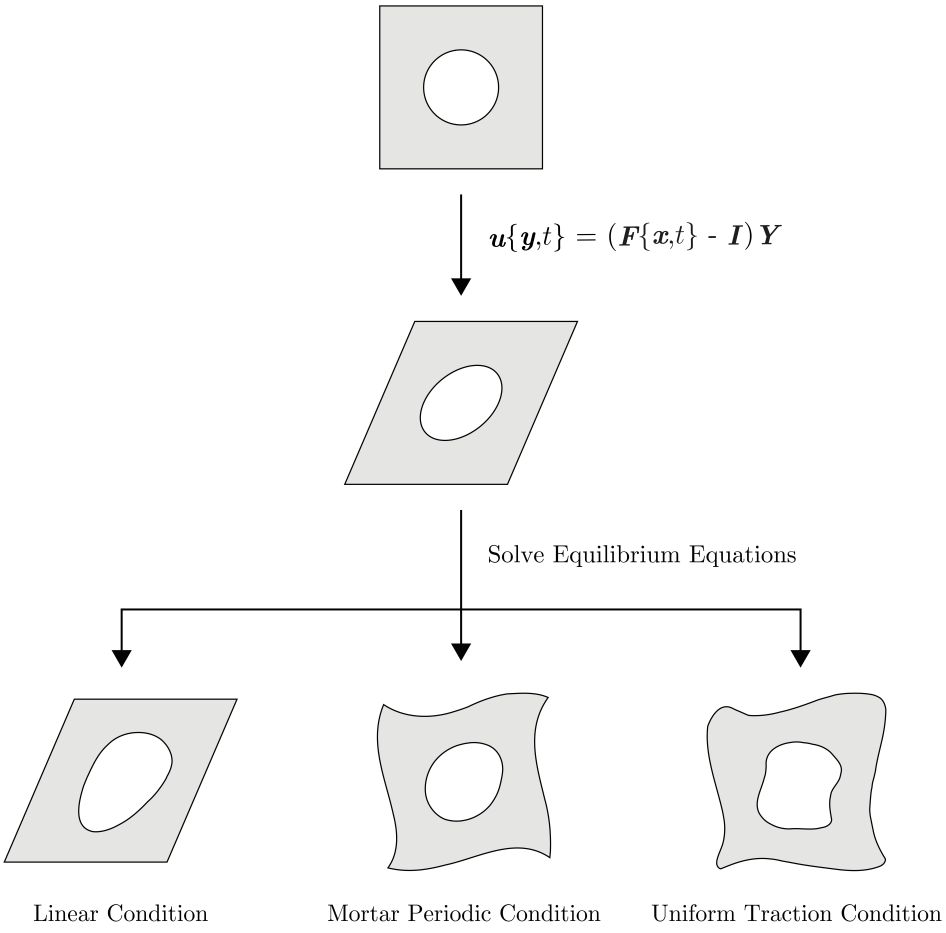

Figure 3.5: Scheme of the different boundary conditions.

Figure 3.6: Main input and output of the MSP program.

The source code of this program is written in Fortran® and it is necessary to provide a data file with the RVE model information and the macroscopic load. As shown in Figure 3.6, the main input is the macroscopic deformation gradient (and the chosen boundary condition) and, regarding the output, besides the deformed configuration of the RVE and some discrete values of the problem's variables, the homogenized first *Piola-Kirchhoff* stress tensor is returned.

In Chapter 4, the procedure to create a finite element mesh to be analysed with MSP is presented and, in Chapter 5, the numerical method utilized to compute the effective elastic properties of a composite material is detailed.

Chapter 4

Digital Image Based Microstructure Recognition

The main objective of this work is to estimate the effective elastic properties of any material from its the microscopic structure. Regarding only the phases' volume fractions and elastic properties, analytical methods, such as mean-field approaches and other spatial averaging techniques, can be used to determine these overall properties (further reviewed in Chapter 5). However, these methods usually do not take into account the geometry of the microstructure and so, in applications where its influence becomes critical, methods based on RVE analysis, where microscopic heterogeneities can be modelled, are better suited for a proper definition of the micro-macro relation.

There are several numerical procedures to generate RVEs based on microstructure informations (e.g. for a unidirectional fiber composite, a *Monte Carlo* randomness approach can be used to create a large number of RVEs, if the size of the RVE and fiber volume fraction are provided) but, if the material presents a microstructure that has heterogeneities with random and complex shapes, these methods are not sufficiently accurate.

Therefore, in order to overcome these difficulties, *Digital Image Based* (DIB) microstructure recognition techniques are used, enabling the construction of a finite element model based on a micrograph from a representative slice of the material. Therefore, the data obtained from this type of analysis can be related with the material that is going to be used in a project. Using this method, any type of complex shape can be modelled (even voids), but it is important to note that this method involves approximations from the beginning, since the finite element mesh is an approximation of an image that in turn is also a pixel discretization of the real structure.

In this chapter, the detailed procedure to obtain the 2D finite element mesh from an image using the Linux® open-source software package OOF2[1] (named for "Object Oriented Finite-Elements", version 2) (Technology, 2016) is explained.

[1] The version of the program used is OOF2 2.1.12.

In Waters et al. (2015), OOF is used to model porous copper and, studies of Ni-Al_2O_3 composites based on DIB microstructure recognition can be found in Sharma et al. (2012) and Sharma et al. (2014).

Finally, the DIB microstructure recognition is applied to 3D RVEs using the open-source software package OOF3D[2] (named for "Object Oriented Finite-Elements", version 3D).

4.1 Acquisition of a Micrograph

First of all, before having the image of the microstructure, one has to capture it. In spite of being beyond the scope of this work, a brief introduction on how to obtain a micrograph is given in this section.

Besides the usual optical devices such as light microscopes, one of the most used methods to obtain a micrograph is the *scanning electron microscopy* (SEM). It uses a beam of electrons to scan over a surface, enabling the user to get information about the sample's surface topography and composition. Depending on the instrument, the resolution range is from about 1 nm, up to 20 nm. During the process, the only variable that can change is the amount of electrons received by the detector in a x, y position, and so, only a single value can be attributed to each pixel of the captured image. This leads to a single gradient from black to white, and a gray scale image is created. Nonetheless, there are several ways to produce a color in a SEM image, such as replacing the gray level of each pixel with an arbitrary color, or by photo-editing the image with a specific software. *Transmission electron microscopy* (TEM) can also be used to generate images with resolution of the nanometre order. The main idea is that the beam of electrons is transmitted through an ultra-thin specimen of the material under analysis. An image is then formed from the interaction of this electrons with the specimen as they pass thorough it.

There are also methods that can be used to create a 3D model of the interior of a material without destroying the actual object. *X-ray microtomography*, uses X-rays to generate several images of the cross-section of the material and can perform with resolutions at the micrometre order (μm). Micro-CT (micro-computed tomography) scanners (Figure 4.1a) are used to capture these cross-section images.

4.2 Image-Based Finite Element Mesh

At this moment, with the micrograph of the material at hand, a finite element mesh that models its microstructure can be created, but several actions have to be completed before the final output is achieved. In this section, the overall procedure is described in detail and, at the end, an example is presented to ensure a better comprehension of the reader. This section was based on A.Langer et al. (2001) and Reid et al. (2008).

It is important to note that OOF2 permits the use of different images to represent a single microstructure - the main structure of the program. For instance, there may be cases where

[2]The version of the program used is OOF3D 3.0.1.

(a) Micro-CT scanner (Bergen, 2016). (b) SEM scanner (Hitachi, 2016).

Figure 4.1: Examples of SEM and a micro-CT scanners.

one image can represent well enough the majority of a microstructure but some singularities are represented with higher definition in another image and, in this case, the user just has to be sure that both images have the same pixel size (width and height) to be able to use them simultaneously. While creating the microstructure, OOF2 automatically interprets the size of the image as pixel dimensions, however, the user is advised to define the microstructure's size with physical dimensions[3], to facilitate the process of creating the finite element mesh.

To briefly introduce the whole process, in the first place a microstructure is created from an image file to further identify the different pixel groups that belong to specific materials, based on its different color values. Secondly, the material properties of interest to the definition of the problem (elastic, thermal, electric and so on) are attributed to these pixel groups. In the third place, a skeleton that contains the geometry of the finite element mesh is created and improved in order to minimize two elemental functionals, named *shape energy* and *homogeneity energy*, that quantify the skeleton quality, and as a result, the mesh quality. Finally, with the last version of the skeleton (that only contains the mesh geometry), the finite element mesh is created while attributing, respectively, triangular and quadrilateral elements (linear or quadratic order) to the triangles and quadrilaterals of the skeleton.

Summarizing, the user has to follow the steps presented below:

1. Create a microstructure based on an image (or several);
2. Segment the microstructure into different pixel groups;
3. Assign materials to these groups that represent the microstructure's constituents;
4. Generate a skeleton that correctly represents this microstructure;
5. Create the finite element mesh based on the final version of the skeleton;

[3]OOF2 has no built in system of units. The output data will be in the units that are given by the user. The *International System of Units* (SI) is recommended.

4.2.1 Image Treatment

Before the segmentation process of the micrograph can begin, there are cases where the boundaries of different materials are not well defined due to low image quality, and so, some image processing may be needed to better distinguish these singularities. Nonetheless, it is relevant to first define two concepts that are frequently used when addressing images in 2D and 3D:

Pixel - It stands for "picture element" and it is the smallest physical and controllable element of a picture that can be represented on a screen device.

An important note is made on the concept of image resolution as it stands for the capacity to observe or measure the smallest object clearly and with distinct boundaries, and it is basically the pixel count in a digital image. There are several ways to quantify the resolution of an image, being the number of pixels columns (width) and rows (height) one of the most common methods. One can simply multiply the number o pixel columns by pixel rows to obtain the amount of pixels contained in an image, usually given in megapixel [MP]. Finally, the concept of PPI (Pixel Per Inch) is also usually used as a quantifier of the image resolution.

Voxel - This word is based on the words "volume" and "element" and, similarly to the pixel, it represents a value on a regular grid that exists in the three dimensional space. With it, it is possible to represent an object in 3D and some volumetric displays describe their resolution in voxel dimensions (e.g. $1024 \times 1024 \times 1024$ voxels). The segmentation of a 3D RVE and the generation of a finite element mesh is, in all, similar to the procedure here explained for the 2D case, however, one must substitute the concept of pixel with voxel.

With this in mind, OOF2 contains almost 20 image modification algorithms that enable the user to improve the quality of the material boundaries and solve other problems that may exist.

Along the usual ones, such as negating, fading, dimming, enhancing the contrast or converting the image to gray scale, OOF2 can also utilize functions of higher complexity. Some utilize a *Gaussian* function[4], like *Blur* and *Sharpen*. *Despeckle* and *ReduceNoise* aim to reduce the noise of the image while preserving the material edges and *MedianFilter* reduces the noise by replacing each pixel color with the median over a local region with a user-defined pixel radius. The *Normalize* routine, normalizes the gray scale image to cover the full range of values, meaning that the color of lightest pixel is converted into white (i.e 0 in the gray scale range), the color of the darkest one is converted into black (i.e 255 in the gray scale range) and the rest of the pixels suffer the same scale transition.

An example is demonstrated in Figure 4.2. It can be noticed that the initial micrograph does not correctly represent the materials' boundaries. Firstly, the image is *Normalized* (Figure 4.2b). In the second place, the *Contrast* tool is applied 5 times (Figure 4.2c). Then, to reduce the noise, *MedianFilter* is used with a radius of 5 pixels for 10 consecutively iterations (Figure 4.2d).

[4]Function utilized in *statistics* to describe the *normal* distributions.

In Section 4.2.2, a comparison between a segmentation of the initial and final image is made in order to illustrate the importance of processing the original image (Figure 4.4).

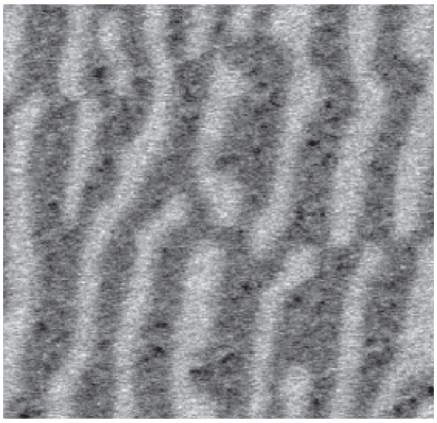

(a) Initial micrograph.

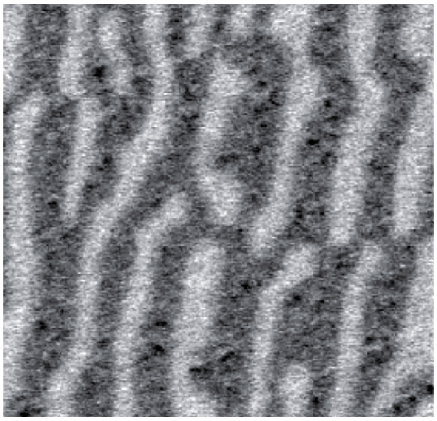

(b) Applying the *Normalize* tool.

(c) Applying the *Contrast* tool five times.

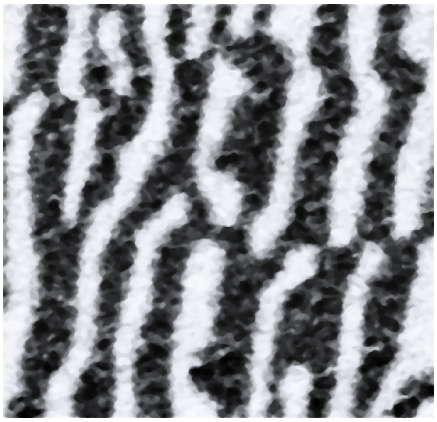

(d) Applying the *MedianFilter* tool ten times.

Figure 4.2: Demonstration of an image treatment of a micrograph of a lamellar directionally solidified eutectic of NiO (lighter phase) and yttria-stabilized ZrO_2 (darker phase) (A.Langer et al., 2001).

4.2.2 Image Segmentation

After the image treatment process, the boundaries between the different materials are expected to be more distinct and, therefore, the segmentation process can start. The main objective of this process is to select all the pixels that belong to a microstructure's feature and group them together so that the material properties can be attributed to these pixels simultaneously. These groups can be named and stored for later retrieval.

In addition to the usual selection methods, like user-manual selection tools (e.g. selecting individual pixels or pixels that are inside a rectangle or a circle), automatic tools are also available. There are two major tools to select pixels based on their colors:

Color/Demography Tool - With this tool, it is possible to select all the pixels that are within a color range of a previously targeted one, since it ignores this pixel's location. The color range value can be defined by a gray, RGB (Red, Blue and Green) or HSV code (Hue, Saturation and Value). All range values are defined by a decimal number between 0 and 1, except Hue that can be defined by any value between 0 and 360.

Burn Tool - Similar to the *Color/Demography* method, the *Burn* tool enables the selection of multiple pixels that are within a color range of the targeted one. However, the main difference is that it only selects contiguous pixels to the targeted one and not all of them. The selection spreads from the selected pixel and a *local* and *global flammability* value must be defined to determine if the selection continues from one pixel to another.

The *local flammability* is the maximum difference between two neighbouring pixel values, while the *global flammability* is the difference between the initial pixel value beyond which the selection will not occur. The difference can be computed either through the sum of the absolute values of the RGB differences (*L1*) or through the square root of the sum of the squares of the RGB differences (*L2*).

In Figure 4.3 the difference between the *Color* and *Burn* methods is presented. Taking into consideration the *Color* tool, the range difference is computed in gray scale values, with *delta gray*[5] = 0.3, while the target is any purely white pixel. Regarding the *Burn* tool, the *local* and *global flammability* are set to 0.15 and a light pixel from the middle grain is selected.

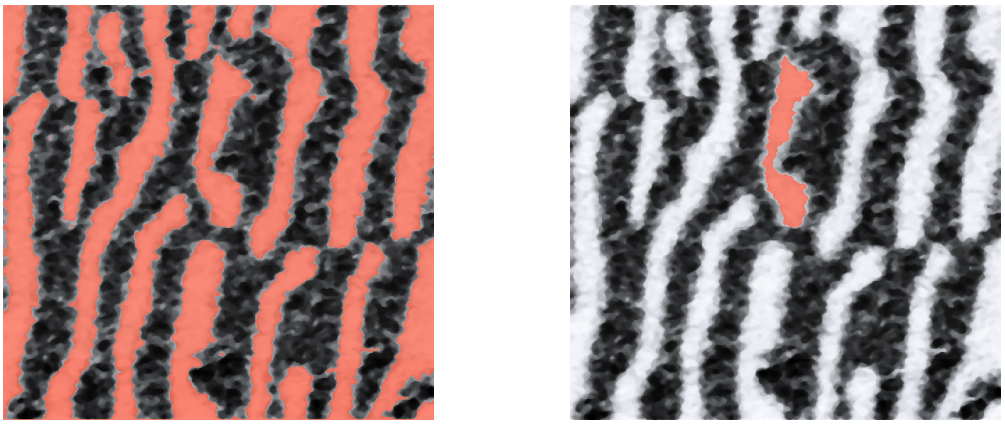

(a) *Color* tool. (b) *Burn* tool.

Figure 4.3: Comparission between the *Color* and *Burn* methods using the image in Figure 4.2d.

It is also noteworthy to demonstrate the difference between a segmentation on a low quality image (Figure 4.2a) and on an image that has already been treated (Figure 4.2d). The method chosen to select the pixels is the *Color* one and the parameters are equal to the ones used on the example of Figure 4.3a. The amount of pixels of this image is 695300 and the amount selected by the *Color* method on the first case is 523688, while on the second case is 301073.

[5] *Delta gray* is the parameter that defines the gray color range value in OOF2.

The difference in the volume fraction of the light material from one case to another is around 30%, which is high. The selection results are demonstrated in Figure 4.4.

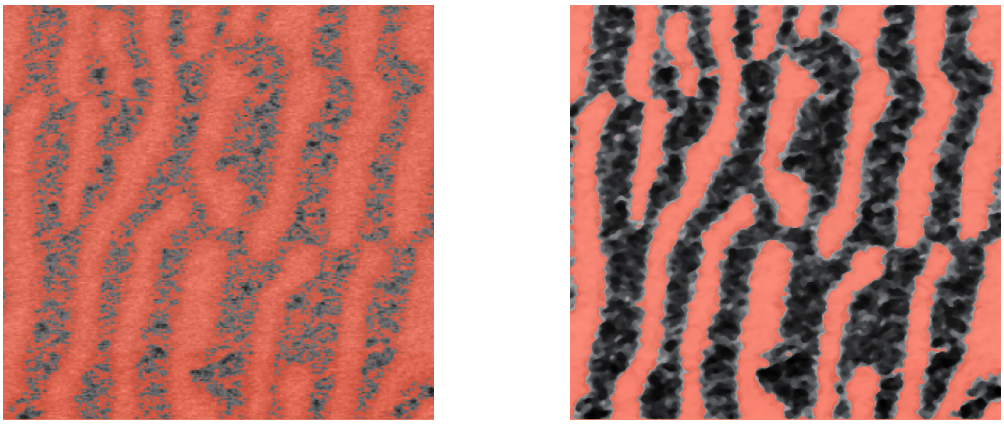

(a) Selection without any image treatment (Figure 4.2a).

(b) Selection after the image treatment (Figure 4.2d).

Figure 4.4: Comparison between the *Color* method on low and high qualty images.

Note: In cases where the selection of a specific feature is difficult, it is easier to select the opposite of it and then invert the selection.

Attribution of Material Properties

Regarding the attribution of a material to the different pixel groups, OOF2 has a large list of options. It is possible to assign elastic, thermal and electrical properties, and, within the elasticity options, there is the possibility to assign any 3D crystal symmetry and any 3D crystallographic orientation to a material (e.g. isotropic, orthotropic and anisotropic materials), since one can insert the full 3D stiffness tensor, but, in the framework of this project, only isotropic elasticity is relevant. Furthermore, since an isotropic material can be characterized by two elastic constants[6], the *Young's* modulus and the *Poisson's* ratio, or the *Lamé* parameters[7] are enough to correctly define it. At this moment, the values of these properties are not relevant, since they can be changed later on, during the migration of the final mesh output file to the MSP program.

Note: In OOF2, the material information can be saved on a data file with the extension ".material" for later retrieval.

Active Areas

It is also important to notice that there are cases where parts of the geometry are not supposed to be meshed, like in the study of microstructures with voids. Before the creation of the skeleton begins, the user can select these areas and inactivate them - these areas do not have any material attributed and can be selected via the same pixel selection methods.

[6] Later addressed in Chapter 5.

[7] Appendix A presents the relations between the most common elastic constants.

4.2.3 Skeleton and Mesh Quality

Before explaining the automated procedure to create a finite element mesh based on the already segmented image, it is important to have a quantitative measure of the quality of the mesh (or skeleton). This value affects the convergence behaviour of the results in the finite element solver (in this case, in the *Newton-Raphson* method) and also dictates if the finite element mesh correctly represents the microstructure or not. In OOF2, this quality is measured by an elemental potential energy, E, and most of the skeleton modification routines are designed to lower it.

The elemental potential energy is a weighted average of two elemental functionals (Reid et al., 2008):

Shape Energy - This energy function quantifies the shape of the finite element taking into account its aspect-ratio. Since high aspect-ratio elements are responsible for a slow convergence of the finite element solver, in this type of elements the *shape energy*, E_{shape}, has a high value. The minimization scheme of the potential energy promotes low aspect-ratio elements and so, squares and equilateral triangles have a null *shape energy* (Figure 4.5a, 4.5c).

For triangular elements it is denoted by:

$$E_{\text{shape}} = 1 - \frac{4\sqrt{3}A}{L_0^2 + L_1^2 + L_2^2}, \tag{4.1}$$

where A is the area of the element and L_i are the length of the element sides. In the case of quadrilateral (quad) elements, this energy is measured in each corner by the following equation:

$$q = \frac{2A_{\parallel}}{L_0^2 + L_1^2}, \tag{4.2}$$

where L_i are the length of the adjacent edges to the respective corner and $A_{\parallel}$ is the area of the parallelogram formed by these edges. So that this elemental functional is dependent on the position of all nodes, the *shape energy* of a quad is defined as a weighted average of the corner with the minimum energy, q_{min}, and the opposite corner, q_{op}, and it is given by:

$$E_{\text{shape}} = 1 - \left((1 - w_{\text{op}})\, q_{\text{min}} + w_{\text{op}} q_{\text{op}} \right), \tag{4.3}$$

in which w_{op} is a parameter[8] assuming the value of 10^{-5}.

Homogeneity Energy - On the other hand, this function is responsible to measure the degree of similarity between the skeleton (and later, the finite element mesh) and the microstructure's image. It is defined by a simple equation:

$$H = \frac{\max\{a_i\}}{A}, \tag{4.4}$$

[8]The value of w_{op} needs to be small enough so that E_{shape} is dominated by q_{min} but not too small to keep the importance of q_{op} in the equation.

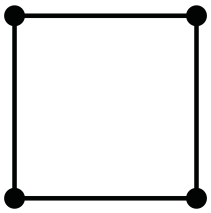

(a) Quadrilateral element with $E_{\text{shape}} = 0$.

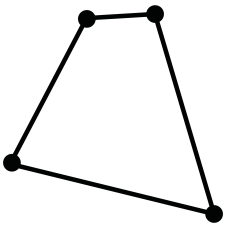

(b) Quadrilateral element with $E_{\text{shape}} > 0$.

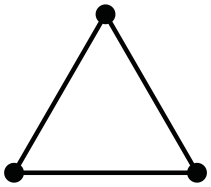

(c) Triangular element with $E_{\text{shape}} = 0$.

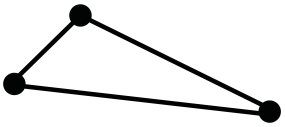

(d) Triangular element with $E_{\text{shape}} > 0$.

Figure 4.5: Perfect and badly shaped quadrilateral and triangular elements.

where a_i is the area of each material within the element (this expression takes into consideration the fractional area of the pixels that intersect the boundaries of the element, thus making this functional a continuous function) and A is the area of the element.

If an element is filled with only one material, its homogeneity is 1.0 (Figure 4.6a), but, due to the fact that the *homogeneity energy*, E_{hom}, should be defined as null for the perfect homogeneous element, this functional is expressed by:

$$E_{\text{hom}} = 1 - H. \tag{4.5}$$

As addressed earlier, the effective elemental energy, E, is a combination of both elemental functionals weighted by a tunable parameter, α, that defines if the priority is to lower the *shape energy* or the *homogeneity energy*,

$$E = \alpha E_{\text{hom}} + (1 - \alpha) E_{\text{shape}}. \tag{4.6}$$

This parameter has to be set for all the skeleton adaptive routines but, it is also possible to define other restrictions while using these methods. The priority is defined by choosing the parameter α, but additional restrictions may be set to the *shape* and *homogeneity energy* values, which is an important feature in several adaptive steps.

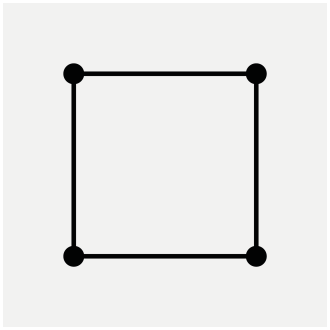

(a) Quadrilateral element with $H = 1.0$.

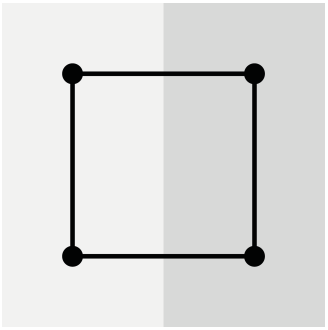

(b) Quadrilateral element with $H = 0.5$.

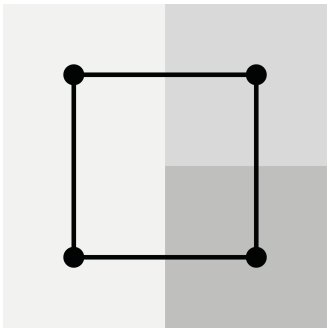

(c) Quadrilateral element with $H = 0.5$.

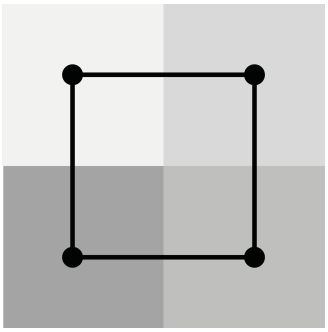

(d) Quadrilateral element with $H = 0.25$.

Figure 4.6: Scheme to represent the homogeneity on different cases.

4.2.4 Adaptive Methods to Generate and Refine a Mesh

Finally, considering the mesh quality parameters, the whole procedure to generate, refine and improve the finite element mesh build on a micrograph is described in this section.

Before reviewing the different mesh adaptive routines that are available in OOF2, it should be noted that this program enables the user to select the elements and nodes that are important to analyse, allowing for a shorter computational time.

Selection of Relevant Elements and Nodes

One can select elements either based on their type (triangular or quad), on their material, on their *homogeneity* and *shape energy* or on other characteristics. In addition, it is even possible to expand the element selection to better address a specific area. As far as the node selection is concerned, there are a couple of similar functions and one can also select the ones that belong to the already selected elements.

Furthermore, the user is also able to pin the internal boundary nodes that define the material boundaries to better adapt the mesh around a boundary without having these nodes moved from their coordinates.

Generation of the Finite Element Mesh Geometry

Regarding the microstructure's geometry, most of the usual mesh generator programs use mathematical functions to define the material boundaries and then create a mesh that fits to these boundaries. However, it is important to notice that during the image recognition of a micrograph, the problem's geometry is not so well defined and the boundaries can be somehow jagged due to the image pixelation.

There are three main approaches to create a finite element mesh based on an image, the simplest being the allocation of a quadrilateral or two triangular elements to each pixel (by clicking on the "Simple..." button in the *Skeleton* window of OOF2). This process raises two problems: first of all, it generates a number of elements far higher than the amount needed (large homogeneous regions can be discretized with a coarser mesh without loss of accuracy in the results), and secondly, it places the material boundaries of the mesh on the jagged pixelized representation of the boundaries presented in the image, leading to high stress concentration factors and to poor finite element convergence properties.

One can also simply create a grid of triangular or quadrilateral elements by defining the amount of elements in each dimension of the RVE, and later refine and improve it using the adaptive functions of OOF2 that take into account the mesh quality parameters addressed in Section 4.2.3.

Finally, after segmenting the image, OOF2 has an automated script (by selecting the "Auto..." button in the *Skeleton* window) to generate a first stage skeleton that attempts to model the micrograph. It incorporates a sequence of routines that refine and shape the skeleton to the material boundaries, requiring the user to define three parameters:

- Maxscale - an estimated size for the biggest elements in the initial skeleton;
- Minscale - an estimated size for the smallest elements in the final skeleton;
- Homogeneity threshold - this dictates which elements will be refined and which not.

During the process, all elements with *homogeneity* below the specified threshold are subdivided until their *homogeneity* is above the threshold or their size becomes smaller than the *minscale* parameter.

Before explaining this automated procedure, the skeleton adaptive routines must be elucidated and, to do so, it is important to first classify and divide them into two major aspects:

- Topology preserving routines - these methods move nodes while preserving the connectivity of the starting skeleton, improving it without increasing the number of elements;
- Topology non-preserving routines - these methods use algorithms that improve the skeleton by adding, removing or reconnecting nodes and elements.

All routines are presented and classified based on other characteristics in Table 4.1 and the most important ones are further discussed in this section.

Table 4.1: Classification of the OOF2 skeleton adaptive routines (Reid et al., 2008).

Routine	**Preserving**	**Homogeneity**	**Shape**	**MC**	**Snap**	**Fix**
Anneal	X	X	X	POT		
Fix Illegal Elements	X		X	O		X
Merge Triangles			X	O		
Rationalize		X	X	O		X
Refine		X	X			
Relax	X	X	X			
Smooth	X		X	OT		
Snap Anneal	X	X		OT	X	
Snap Nodes	X	X		O	X	
Snap Refine		X	X		X	
Split Quads		X		O		
Swap Edges		X	X	O		
Manual Node Motion	X	X	X		X	X

In this table header, *Preserving* indicates if the algorithm falls into a topology preserving routine, *Homogenity* and *Shape* specify if the primarily concern of the routine is to lower the *homogeneity* or *shape energy*, respectively. *Snap* shows that the new node position must lie on top of a material boundary and *Fix* means that the algorithm fixes badly shaped or illegal elements. *MC* stands for *Monte Carlo* methods and the letter P means that the new node positions are chosen randomly, O implies that the routine addresses nodes in a random order and T indicates that it accepts/rejects moves randomly based on a probability p given by a *Boltzmanm* distribution in which $p = \exp\left(\frac{-\Delta E}{T}\right)$, where ΔE is the change in *energy*.

Anneal - During the *Anneal* algorithm, the targeted nodes are moved to random positions within a specified radius, δ, and these new positions[9] are accepted or rejected according to a user-defined criterion: either accepting all moves or only the ones that decrease the effective energy of the system or only those that decrease this energy and simultaneously satisfy a *homogeneity* and *shape* condition.

This process usually requires several iterations to be successful since for each iteration, one node only attempts one move. The user can define a fixed number of iterations or set the process to stop after a certain condition is guaranteed (e.g the success rate of the process being lower than specified value). As mentioned in Table 4.1, the order in which the nodes are moved is random and changes in each iteration.

Before moving one node to a new position, OOF2 computes the total effective energy of the elements where it belongs and, afterwards, the chosen criterion defines if the move is either accepted or rejected (the moves that create illegal elements are automatically rejected). Table 4.1 also states that it is possible to accept a movement which initially was rejected, according to a probability given by a *Boltzmanm* distribution.

[9]Computed from a *Gaussian* distribution of width δ and mean 0.0

When the elements size is already good enough to resolve all the singularities of the micrograph, the *Anneal* routine is useful and can usually take into account both *homogeneity* and *shape energy*, depending on the parameter α.

Smooth - This algorithm is similar to the *Anneal* method but instead of moving a target node in a random way, it attempts to move it to the average position of the adjacent nodes (i.e nodes that share a common segment), without ever creating illegal elements.

The name is self-explanatory since this method aims to improve the elements shape by smoothing the node density gradients. It is usually employed on the last steps to create the final skeleton and, combined with the aforementioned *Pin Nodes* function, increases the quality of the elements around material boundaries without changing their homogeneity, improving the convergence behaviour of the finite element solver.

Snap Nodes - This routine main objective is to improve the *homogeneity energy* of an element by snapping its nodes to the material boundaries.

It scans the current skeleton selection to check if there are elements below a specified homogeneity and identifies the transition point for each segment of these elements. Afterwards, based on the arrangement of its transition points, assigns a priority to each situation (Reid et al., 2008) and, starting from the highest priority, attempts to move the nodes to these points. It can move one or two nodes from the same element simultaneously and, when the move is accepted according to a given criterion, OOF2 tries to snap the nodes from the surrounding elements to better adjust to a boundary.

Due to the nature of this process, *Snap Nodes* contributes to the creation of badly shaped elements when α is large, however, it is more efficient if this parameter favours homogeneity. Later, the user can use the *Rationalize* routine to eliminate these elements.

Refine - This is usually the first step to create a skeleton. The element's size needs to be small enough to correctly resolve the singularities of the microstructure and, on top of that and as explained in Chapter 2, the accuracy of the results given by the finite element method is related with the mesh refinement. However, *Refine* is usually not sufficient to generate an acceptable skeleton, and needs to be combined with other methods.

The user must define the elements that should be considered, namely, elements with an area smaller than a given value can be excluded from further refinement. It is also needed to specify the edges of the elements that should be refined and how these edges are refined (bisected or trisected). During the *Refine* method, OOF2 enables the possibility to keep the elements shape, i.e quadrilaterals can be refined into smaller quadrilaterals, and triangular elements likewise.

Snap Refine - Similar to *Refine* and *Snap Nodes*, this algorithm attempts to subdivide heterogeneous elements by spawning new nodes in the transition points that are located in the material boundaries, instead of just bisecting or trisecting the edges on a equal manner.

Snap Refine usually improves the *homogeneity energy* of the skeleton without creating as many nodes as *Refine* does, because it directly splits elements in the relevant points. However, it is important not to overuse this routine, since it tends to create badly shaped elements after a few iterations. The user is able to define a specific distance from an existing node, below which *Snap Refine* does not create a new one, preventing the aforementioned problem, although this solution is not always applicable.

The user should use *Refine* first and then, when the element's size is good enough, use *Snap Refine* to better resolve the singularities of the microstructure. *Rationalize* and *Smooth* after this routine has been proven to be a good methodology to prevent thin elements generated by *Snap Refine*.

Rationalize - As mentioned while explaining the other routines, *Rationalize* is the most powerful method to clean up badly shaped elements. It either removes them or simply modifies them and their surroundings to decrease the *shape energy*. When a previous routine generates elements with sharp angles or with high aspect-ratios, using *Rationalize* improves the skeleton quality.

This algorithm has three sub-algorithms:

1. Remove short sides - This sub-routine eliminates the shortest edge of a quad element by replacing it with a triangular one. The user defines a ratio and, if the fraction between the size of the shortest side and the second shortest side of the quadrilateral element is greater than this value, the nodes that belong to this edge are merged. If the element that shares these nodes is a quadrilateral, *Rationalize* transforms it into a triangle but it can also be eliminated if it was already a triangle;

2. Split wide quads - If a quadrilateral element has large interior angles (value specified by the user), this sub-routine divides it into two triangles and, consequently, improves the *shape energy* of the system;

3. Remove bad triangles - This sub-routine is probably the most important and relevant one. Thin elements are responsible for a bad convergence behaviour during the finite element analysis and, along the deformation process, they can degenerate into illegal elements and interrupt the analysis or produce incorrect information. The user can define an angular range, and all triangles with interior angles outside that range are either eliminated or have their surroundings replaced by a set of new ones.

It is important to note that this algorithm is applied with the order presented above and it is possible to select the target elements in order to get a lower computational time. The tunable parameter α also plays a major role on the results given by this routine, since it defines if the priority is the *shape* or *homogeneity energy*.

Merge Triangles - Linear triangular elements are known for presenting a constant strain inside its domain, which is a simplification of the real behaviour of a material. If it is possible, a quadrilateral element should be used instead of a triangular one.

As the name implies, *Merge Triangles* merges two triangular elements to form a quadrilateral one. It improves the *shape energy* of the system and reduces the total number of elements, decreasing the duration of the finite element analysis.

Split Quads and Swap Edges - These two routines are used when a skeleton is near its final version but there are some elements along the material boundaries that need to be improved to better represent the microstructure.

In the case of *Split Quads*, when a quadrilateral element has two of its opposite corners on top of a material boundary, this means that the material boundary passes thorough one of the diagonals of this element and so, by dividing the element into two triangles, the *homogeneity energy* is decreased.

Swap Edges takes into consideration both types of elements (triangular and quads) and, if a shared edge of a pair of elements crosses a material boundary, this routine tries to improve their *homogeneity* by merging two triangles into one quadrilateral and dividing it along its other diagonal. It can also improve the *shape energy* of two adjacent quadrilaterals by swapping its internal common edge.

Fix Illegal Elements - A skeleton cannot be converted into a finite element mesh if it contains illegal elements. Firstly, it is important to define an illegal element as an element that has corners with an angle greater than 180° or less than 0°. Non-convex shapes are also part of it.

Fix Illegal Elements routine does not take into account the *homogeneity* and *shape energy*. Similarly to *Smooth*, it attempts to move the node of the illegal corner to the average position of its surroundings and if it fails, it attempts to move the other nodes of the element to see if the illegal element is removed. To either accept or reject the attempted movement, this routine only verifies if the illegal elements in the vicinity of the node are removed or not.

It is advised to check if the skeleton continues to be a good representation of the microstructure after resorting to this routine.

As previously introduced, OOF2 has an automated procedure to generate a first version of a skeleton. It is possible to define the output skeleton as periodic, but, since the *Mortar Periodic* boundary condition (Section 3.4.4) is going to be used instead of the *Periodic* constraint, this condition is set to false. After having defined the parameters *maxscale*, *minscale* and *homogeneity threshold*, this automated script follows a specific sequence of routines.

Firstly, it creates a skeleton grid with quadrilaterals of size equal to *maxscale*. The *Refine* routine is then used to iteratively refine the initial grid, by bissecting the edges with $\alpha = 0.8$. As addressed earlier, all refinement operations are only applied to the elements with size greater than *minscale* or with *homogeneity* lower than the specified *homogeneity threshold*, and the

iterations are repeated until there is an element with linear dimensions smaller than the *minscale* parameter. Once the *Refine* routine is finished, the *Snap Refine* routine is applied once to place the nodes and edges on the boundaries of the materials. Since these routines usually generate badly shaped elements, the *Rationalize* routine is used twice to remove these elements. Lastly, using the *Pin Nodes* function, the internal boundary nodes are locked and a *Smooth* routine is applied for 5 iterations with $\alpha = 0.3$.

This procedure is able to create a sufficiently good first stage skeleton. Nevertheless, there are cases where several routines must be used to further improve the *shape* and *homogeneity energy* after this step.

4.2.5 Output Files of OOF2

As the name of the program suggests ("Object Oriented Finite Elements"), OOF2 is an objected oriented program since it works with classes and sub-classes. The main objects are *Microstructures*, *Images*, *Skeletons*, *Meshes* and *SubProblems*. OOF2 also runs finite element analysis, subdividing *Meshes* into *SubProblems* but this is not related with the scope of this thesis, since this analysis is going to be done in a different program - MSP.

While the user is generating the DIB finite element mesh, the user can can save different parts of the work for later retrieval. The main idea is that the file extension has to be the same as the object (or class) name that is going to be saved (e.g. ".skeleton" saves the *Skeleton* information, ".microstructure" saves the *Microstructure* information, ".material" saves the *Material* information, and so on).

If the ".microstructure" file is created, only the *Images*, the pixel groups and the *Material Map* (that contains the information of the material assigned to each pixel) are saved. The ".skeleton" file, besides the information contained in the *Microstructure* class, also contains the skeleton information. Lastly, the ".mesh" file contains the *Skeleton* class, but also the finite element mesh information. More information regarding OOF2 structure can be found on OOF2 Manual (Technology, 2016).

In the last sections, the procedure to obtain the final version of the skeleton that fits into the microstructure's geometry is explained. After that, the finite element mesh is created and built upon the skeleton's geometry.

Along the creation of the finite element mesh, OOF2 asks the order of the mapping and interpolating functions[10]. The mapping functions are responsible for mapping the coordinates of the finite elements from the physical to the natural space (parametric coordinates $\boldsymbol{\zeta}$) and vice versa and can either be linear or quadratic. The interpolation functions are used to interpolate the displacement field within elements and can also be linear or quadratic. The combination of different orders in these functions generate different possibilities and, in Table 4.2, the different options provided by OOF2 to create the finite element mesh are presented. Their definition is directly obtained from the OOF2 program:

[10] See Section 2.6.2 for more information.

- T3_3 - Isoparametric 3 noded triangle with linear interpolation for both fields and positions;
- Q4_4 - Isoparametric 4 noded quadrilateral with bilinear interpolation for both positions and fields;
- T3_6 - Subparametric 6 noded triangle with linear interpolation for positions and quadratic interpolation for fields;
- Q4_8 - Subparametric 8 noded quadrilateral with bilinear interpolation for positions and quadratic interpolation for fields;
- T6_6 - Isoparametric 6 noded triangle with quadratic interpolation for both positions and fields;
- Q8_8 - Isoparametric 8 noded quadrilateral with quadratic interpolation for both positions and fields;
- Q9_9 - Isoparametric 9 noded quadrilateral with quadratic interpolation for both positions and fields.

Table 4.2: Options provided by OOF2 to generate the finite element mesh based on the skeleton geometry.

Mapping	**Interpolating Order**	
Order	1	2
1	T3_3 Q4_4	T3_6 Q4_8
2	-	T6_6 Q8_8 Q9_9

In the MSP program, only the isoparametric elements are admissible, thus, the mapping order must be equal to the interpolating order.

Furthermore, it is possible to keep saving the progress on a couple of different formats:

- Script - This format saves a file that contains the OOF2 commands as a Python® script. This type of file can be edited to modify or insert new commands. It is important to note that, since this file is interpreted by a Python® interpreter, the security is low because any malicious Python® program can be disguised as an OOF2 script;
- Ascii - Similar to the script type file, the ascii file format contains the commands in Python® code but it is not processed by the Python® interpreter, and so, it does not present any security risk. The routines that read this type of file only understand OOF2 commands.

- Binary - The binary file format is faster to read and write and don't have any security problems. Since the whole data is saved in binary code, this type of files are more accurate. However, they cannot be edited in a text editor.

- Abaqus - Only skeletons and meshes can be stored in this type of format. As the name implies, this file allows the user to insert the data in the Abaqus® finite element program. The information regarding nodes and elements is stored in a tabular environment.

During the work of this thesis, the finite element mesh is saved in the *Abaqus* format file. Then, a MATLAB® script (described in Appendix B) is developed to read the information contained in this file and, write an output file to be read by the MSP program.

Note: It is advised to save the progress whenever is possible, since OOF2 tends to crash some times. If the user does not want to change anything on the save file, the *Binary* format is advised.

4.3 Example of a DIB Microstructure Recognition using OOF2

In this section, the whole procedure to create a finite element mesh with DIB microstructure recognition is reviewed with the help of a simple example. The micrograph that serves as base to this example is presented in Figure 4.7.

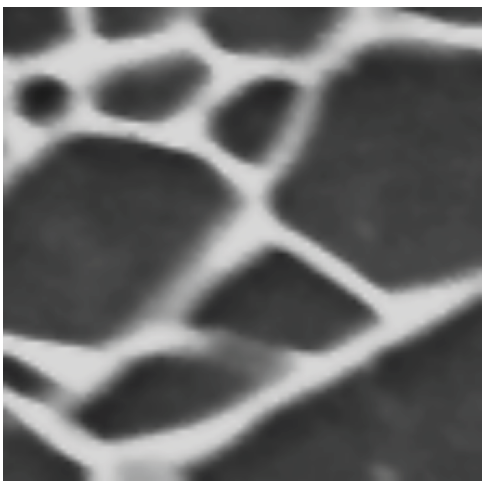

Figure 4.7: Image sample from a microstructure: A micrometer scale SEM image of plasma-etched Si_3Na_4 (Reid et al., 2008).

As demonstrated in Figure 4.8, by selecting the button "New from Image File", OOF2 enables the creation of a microstructure based on a rasterized image file[11]. By selecting this button, the menu displayed in Figure 4.9 appears and the selection of the image file occurs. In this step, a name and physical height and width dimensions can also be assigned to the

[11] An image that its represented by a grid of pixels, each of which has a number of bits to designate its color.

microstructure. It is noteworthy to mention that, if these characteristics are not user-defined, OOF2 will automatically create a name and assign pixel dimensions to the microstructure.

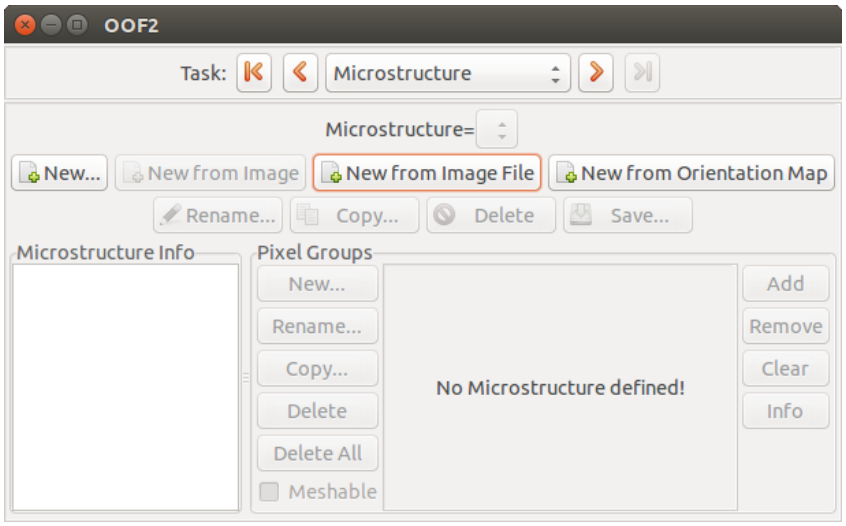

Figure 4.8: Creating a microstructure from an image file.

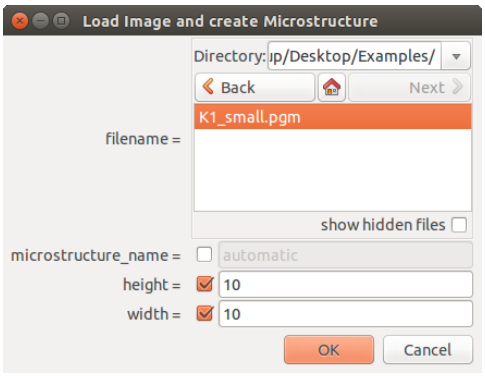

Figure 4.9: Selecting the image file and defining the physical dimensions of the RVE.

Finally, the microstructure is created and its information can be seen in the OOF2 *Microstructure* window (Figure 4.10). In this figure, it is also demonstrated that the pixel groups are not yet defined.

Therefore, as explained in Section 4.2.2, this image has to be segmented in two different materials: the *Black* and the *White* material. However, the material boundaries are blurry and the material parts are not well defined, and so, an image treatment is needed before the segmentation can begin.

The image treatment procedure hereafter explained is based on a tutorial provided by OOF2.

4.3.1 Image Treatment

By applying *Normalize*, the initial image is normalized, meaning that the gray code values fill the full range from black to white (0 to 255) and, the result is presented in Figure 4.11a. After

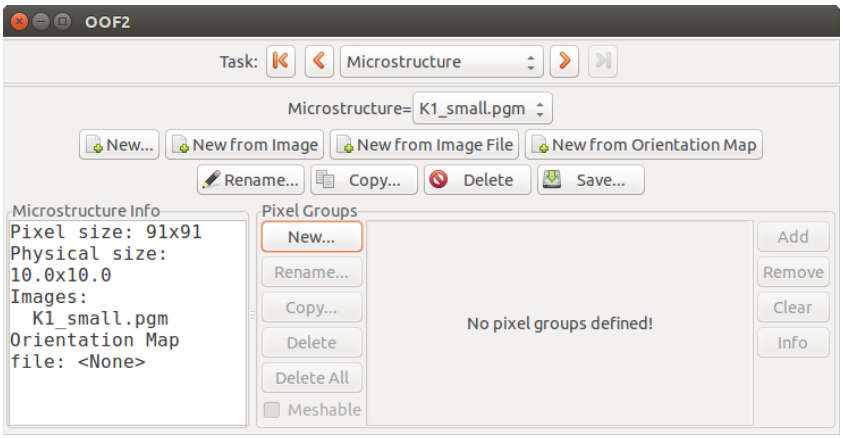

Figure 4.10: Information about the microstructure and pixel groups.

that, the *Contrast* function is used three times to improve the definition of both materials, as the darker and brighter regions get darker and brighter, respectively (Figure 4.11b).

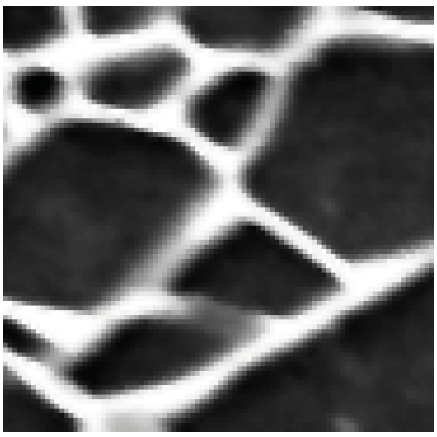

(a) Applying the *Normalize* tool.

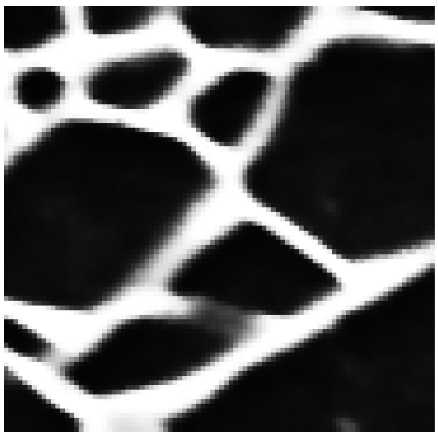

(b) Applying the *Contrast* tool three times.

Figure 4.11: Image treatment of Figure 4.7 to better define both materials.

In Figure 4.11b, both materials are well defined. However, there is a part of the microstructure where exists *White* material but, due to the *Contrast* tool, this part became darker. This minor problem will be solved during the pixel's selection step.

4.3.2 Image Segmentation

Since Figure 4.7 is a gray-scale image, the *Color* method is going to be used to segment it into two different pixel groups: *Black* and *White*. The color range value is given by a gray code parameter, *delta gray*, and it is set to 0.5 while the target pixel is any black pixel. Figure 4.12 shows the resulting selection in red.

In Figure 4.12 it can be noticed that there is a "path" connecting two black grains that is also selected. This "path" should belong to the *White* group and not to the *Black* one and,

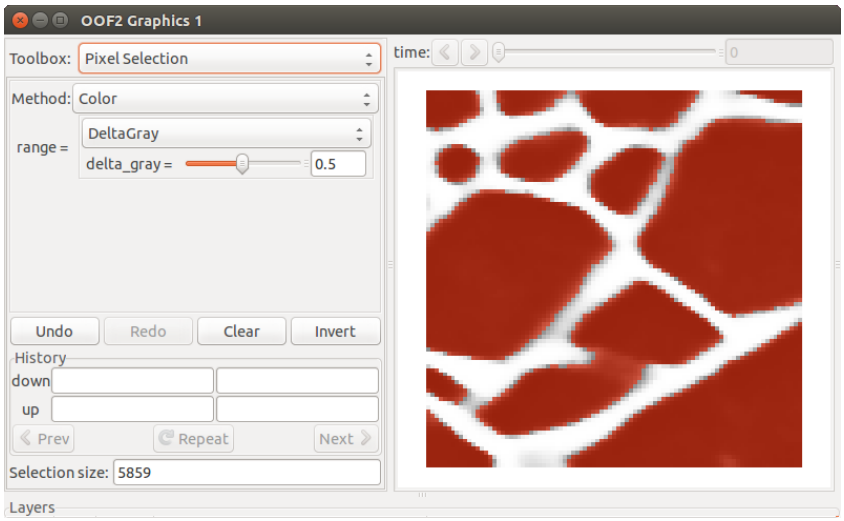

Figure 4.12: Selection of the black pixels using the *Color* method.

to solve this problem, the selection is inverted (Figure 4.13a) and the pixels in the "path" are selected using the *Brush* tool with a circle of radius[12] = 0.25 (Figure 4.13b).

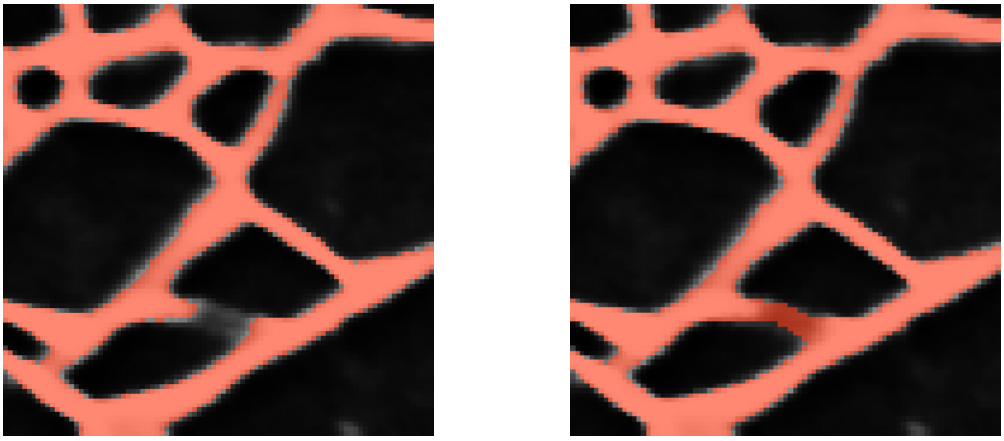

(a) The selection displayed in Figure 4.12 is inverted.

(b) Using the *Brush* tool, the "path" between the two black grains is selected.

Figure 4.13: Correction of the selection shown in Figure 4.12.

Now that the whole *White* material is selected, the user needs to create the *White* pixel group by clicking "New..." in the *Microstructure* window of OOF2 and then, add the selected pixels to the new pixel group by clicking "Add". After this, the selection is inverted again and the *Black* group is created in the same way. The pixel groups information can be seen in Figure 4.14.

[12]Defined in physical dimensions.

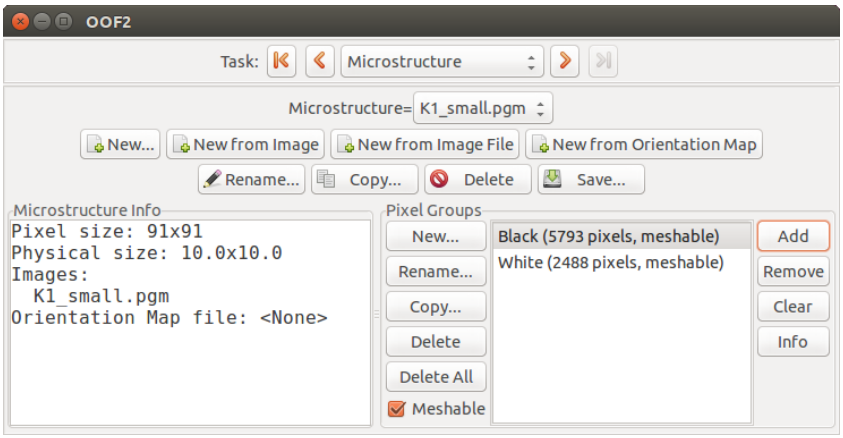

Figure 4.14: Information about the microstructure and pixel groups.

Attribution of the Material Properties

Once the pixel groups containing the *Black* and *White* materials are created, the user can attribute the material properties to them on the *Materials* window of OOF2.

Firstly, the materials have to be created by selecting the "New..." button. The materials are named *Black_mat* and *White_mat* for easier comprehension and, both of them are of *bulk* type. In this case, both materials are considered isotropic and their properties[13] are presented in Table 4.3. A color property is also added to better distinguish both materials and the skeleton lines.

Table 4.3: Material properties assigned in OOF2.

	Young's Modulus	**Poisson's Ratio**	**Color**
Black_mat	100 GPa	0.3	0.8
White_mat	10 GPa	0.3	0.4

Secondly, these properties are added on the same *Materials* window (Figure 4.15). To create them, one has to click in "Copy..." with "Isotropic" (inside the folder "Mechanical" and sub-folder "Elasticity") or "Color" selected. Following the same principle that was used to name both materials, the elastic properties are named *Black_elast* and *White_elast* and the color properties are named *Black_color* and *White_color*. The "Parametrize..." button sets the parameters for the selected property. Using the button "Add Property to Material", *Black_elast* and *Black_color* are added to *Black_mat* and *White_elast* and *White_color* are added to *White_mat*.

Finally, the materials have to be assigned to the pixel groups. By clicking on the button "Assign Material to Pixels..." the *Black_mat* and *White_mat* are attached to the *Black* and *White* groups, respectively.

[13] The assigned properties are not representative of the plasma-etched Si_3Na_4.

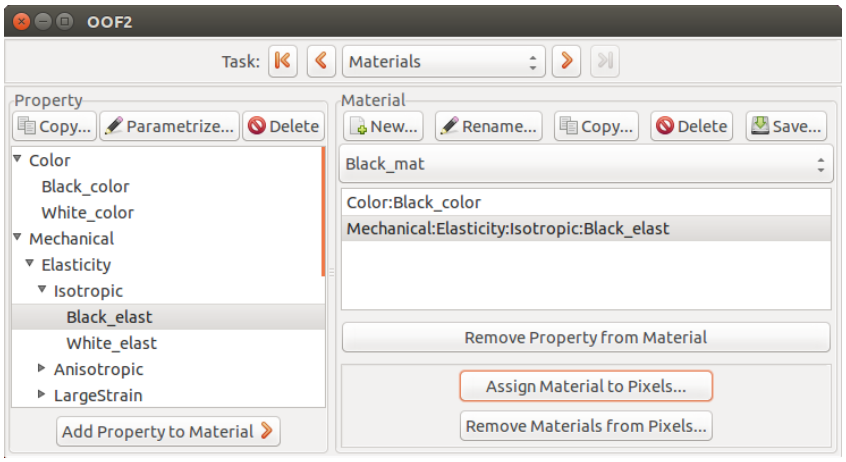

Figure 4.15: Material properties assigned in OOF2.

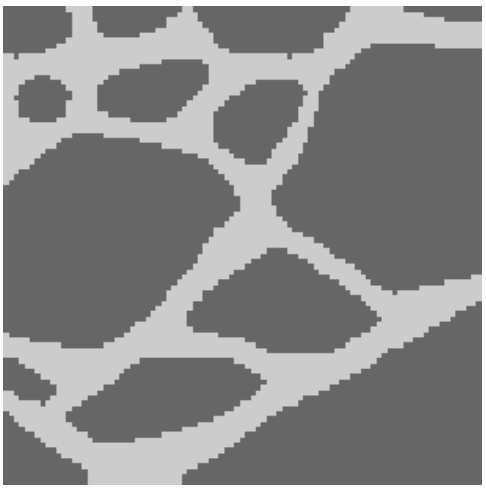

Figure 4.16: *Material image* of the already segmented microstructure.

The new segmented image can be seen on a new layer created in the *Graphics* window. This is known as a *material image* and its representation is displayed in Figure 4.16.

4.3.3 Generation of the Skeleton Geometry

After having completed the image segmentation process, the user can create the skeleton that will later be converted into the finite element mesh. As addressed in Section 4.2.4, OOF2 has an automated script that is available by clicking on the "Auto..." button of the *Skeleton* window.

For this case, the parameters[14] are set as $maxscale = 0.4$, $minscale = 0.3$ and *homogeneity threshold* $= 0.9$ and the result in presented in Figure 4.17.

As it can be seen from Figure 4.17, the automated script of OOF2 generates a fairly good skeleton but several elements need to be treated to better represent both materials.

[14] *Maxscale* and *minscale* are defined in physical dimensions. If, while creating the microstructure, the physical dimensions are not defined, these parameters have to be defined in pixel dimensions.

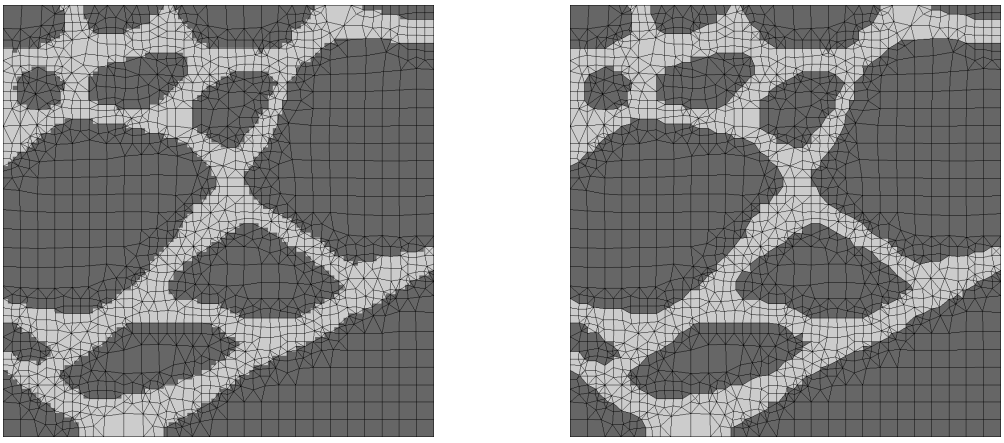

(a) Representation of the materials' color. (b) Representation of the elements' color.

Figure 4.17: Initial skeleton created by the automated script of OOF2.

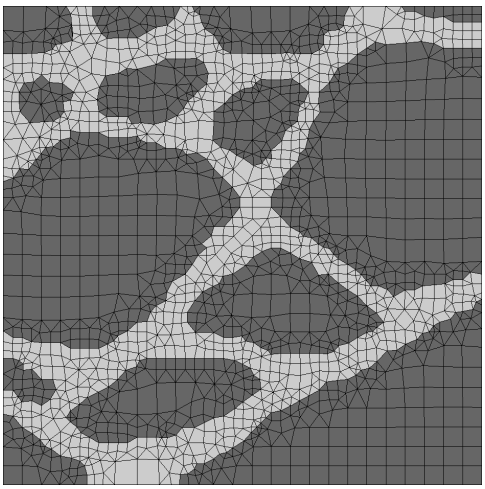

Figure 4.18: Final skeleton with the elements' color represented.

After running a couple of routines, like *Merge Triangles*, *Split Quads*, *Swap Edges*, *Rationalize* and *Smooth* (with the internal boundary nodes locked in their position), it is possible to achieve the final version of the skeleton, presented in Figure 4.18. The sub-algorithms of the *Rationalize* routine are applied with tighter constraints than those used in the automated script of OOF2. Therefore, triangular and quadrilateral elements that were tolerated during the initial procedure are replaced by elements with lower *shape energy*. Moreover, in Figure 4.17b, there are some defected elements presented in the boundaries of the interior clusters that are corrected in the final version of the skeleton.

4.3.4 Generation of the Finite Element Mesh

As addressed on Section 4.2.5, OOF2 enables the creation of isoparametric and subparametric elements of linear or quadratic order for both mapping and interpolation functions. In this

example, the elements chosen are of linear order for both functions (T3_3 and Q4_4) (Figure 4.19). The "2-cornered" elements are not addressed because, when saving the file in the *Abaqus* format, their information is not contained, only the quadrilateral and triangular elements matter in this case. The final numbers of elements and nodes are displayed in Table 4.4.

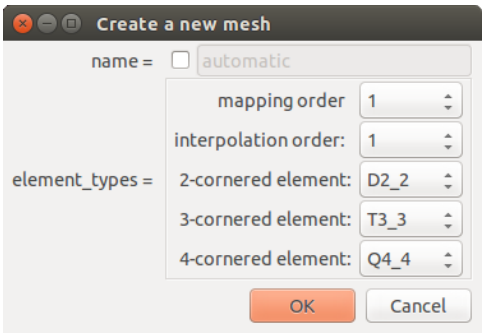

Figure 4.19: Selecting the order for both mapping and interpolation functions and creating the finite element mesh.

Table 4.4: Information about the final version of the finite element mesh.

Type	**Number**
Elements	2303
Quadrilateral	935
Triangular	1368
Nodes	1687
Homogeneity	0.9815

4.4 Example of a DIB Microstructure Recognition using OOF3D

As mentioned, the same developers of OOF2, have created a program that generates finite element meshes based on 3D RVEs - OOF3D. The procedure is in all similar as the one described for OOF2 with the replacement of the pixel concept for voxel.

Regarding 3D images, one has to think of them as a group of 2D images that may be interpreted as different layers. Therefore, if the 2D images that characterize the 3D RVE are equal, it is the same as considering that the RVE is an extruded version of the 2D RVE, as illustrated in Figure 4.20.

In this section, a brief example of the procedure followed to generate the finite element mesh of a 3D RVE is presented. The RVE chosen is given by OOF3D as an example file. It characterizes a bone structure and it is not an extruded image, meaning that each 2D layer is represented by a different image. Since it is only composed by voxels of two colors (black and white), the image segmentation is simple: it can be performed by the voxel selection *Color*

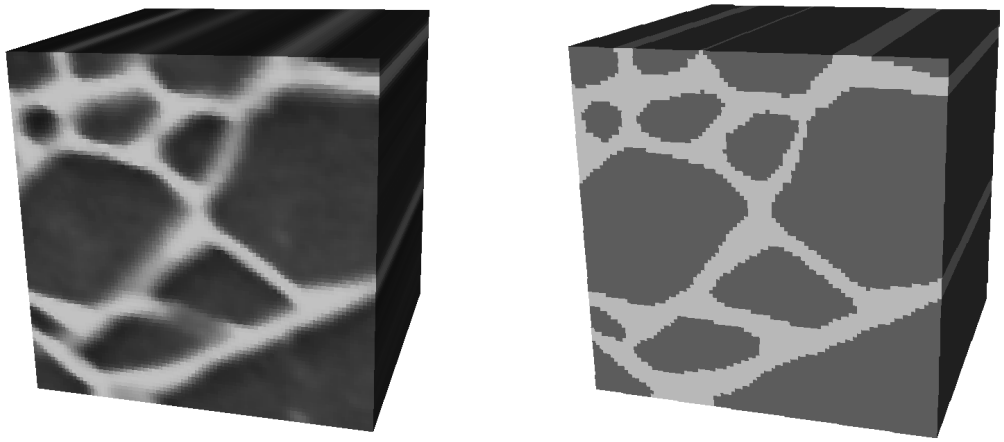

(a) 3D micrograph. (b) Material image.

Figure 4.20: Image segmentation of an extruded 3D RVE of the microstrucutre displayed in Figure 4.7.

method or through the "Group"[15] button in the *Image* window. The initial RVE and the material image are displayed in Figure 4.21.

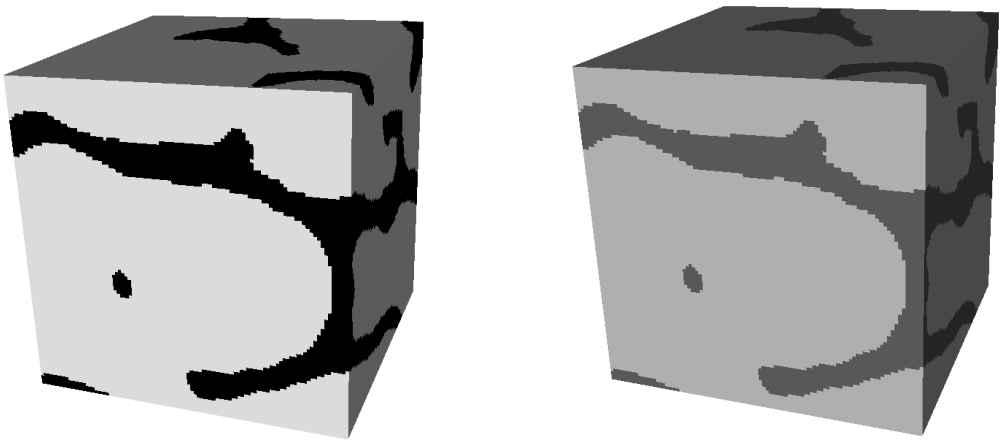

(a) 3D micrograph. (b) Material image.

Figure 4.21: Image segmentation of a 3D RVE that represents a bone structure. The lighter and the darker material represent the bone and porosity, respectively.

OOF3D does not have an automated script to create a first skeleton version like OOF2 does, thus, the initial skeleton is created as a grid of $10 \times 10 \times 10$ tetrahedral elements. After that, the *Refine* routine is applied ($\alpha = 0.8$) on the elements with homogeneity lower than 0.95 and the *Snap Nodes* tool is used to move the nodes to the material boundaries (homogeneity threshold $= 0.9$ and $\alpha = 0.9$). A higher refinement is performed on the darker part and the *Rationalize*

[15]This function groups pixels/voxels of different colors into different groups. It usually does not lead to a good result due to the pixels/voxels of different gray shades that may exist.

routine is used to lower the *shape energy* and to eliminate unneeded elements. To finalise, the *Smooth* routine is applied for 10 iterations with $\alpha = 0.15$ and with the internal boundary nodes locked on their positions. The final mesh version is presented in Figure 4.22.

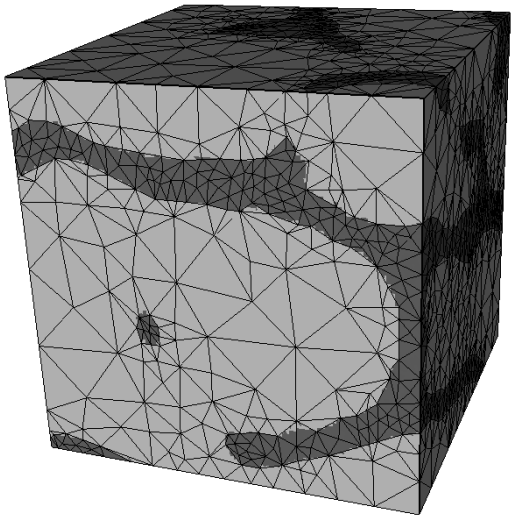

Figure 4.22: Finite element mesh that models the RVE displayed in Figure 4.21.

Finally, some problems occurred while exploring the functionalities of OOF3D. The program is an extended version of OOF2 for three dimensional problems but it is not as developed and tested as the 2D version. For instance, the number of adaptive methods to generate and refine the mesh is low and the type of elements that can be used is limited to tetrahedrons (the developers aim to introduce hexahedral elements in the future).

Furthermore, while saving the file that contains the finite element mesh data in *Abaqus* format to be later converted with MATLAB® and used in MSP, the program crashes, or does not save any file. Due to this problem, it was not possible to use OOF3D to perform a 3D finite element analysis. Even so, this section demonstrated the use of this program to generate a finite element mesh based on a 3D micrograph to reinforce that, in the future, this type of methodology may be available to use.

4.5 Special Notes

There is always a learning process that needs to be respected while getting in contact with a new program. In the first DIB microstructure recognitions with OOF2, there were several problems that, with the experience gained throughout the thesis, have been solved. In this section, special notes and tips are presented to avoid some errors, and to, overall be more efficient while working with OOF2 (and OOF3D).

- The adaptive methods used to generate and refine the finite element mesh should be used with the graphics window closed. This will decrease the time taken to complete the routines, since OOF2 prints the skeleton information (nodes, elements) in the graphics window every time a change is made. This greatly increases the time consumed per routine (probably doubling or more), and is even more severe as the amount of nodes/elements becomes bigger;

- When trying to zoom in/out or pan over the image in the graphics window, it is advised to uncheck the layers that contain the skeleton or mesh information, to again lower the time consumed by the operation;

- OOF2 tends to sometimes crash without warning, showing a "Segmentation Fault (Core Dumped)" error in the terminal window. This usually occurs when OOF2 tries to access data that is not allocated in memory. To prevent this error, the user must reselect the relevant nodes and elements targeted by a routine after a non-topology preserving routine is applied. For instance, in the case that the user selects the elements with *shape energy* higher than 0.8 to apply the *Rationalize* routine and, after that, it wants to apply, for example, the *Smooth* routine to the same type of elements, the selection must occur again because in the *Rationalize* routine several elements may have been eliminated and the *Smooth* function will try to access elements or nodes that don't exist. However, OOF2 saves a log file in the temp folder of the computer that can be loaded as a script file to recover the work lost;

- The user should save the skeleton in binary format after major operations. If possible, keeping two different versions and always saving the last step on a different one is a good practice to prevent losing all the information when OOF2 crashes while saving and overwriting the info, leading to a corrupt file;

- As mentioned in Section 4.2.5, OOF2 enables the user to load a Python® script (".py" file extension) that includes the command lines for the program to follow. With this, it is possible and advised to write the desired routines in advance and load the script to turn the procedure more automatic.

4.6 Conclusions

Despite the fact that the open-source programs used to generate the finite element mesh based on real micrographs are still under development regarding memory efficiency and debugging, the DIB microstructure recognition technique presents an innovation on how materials with complex microstructures are analysed. The possibility of creating a model that analyses and captures each given real microstructure and not only simplified representations of it, is inspiring and may be considered as a promising feature in the development of new materials.

Chapter 5

Methods for the Determination of Homogenized Elastic Properties

It is well known, the majority of materials tend to deform in the elastic domain before reaching plasticity. This means that a body that has only been strained in the elastic domain, returns to its initial configuration after being unloaded. If, on the other hand, during deformation plasticity has been reached, the material will stay with permanent deformation, which can be relieved by some heat treatments (e.g. annealing and tempering).

The set of equations that relates stress with strain (and possibly strain history, strain rate and other fields quantities) are called *constitutive equations* but, unlike the governing equations presented in Chapter 2, these cannot be usually calculated using fundamental physical relations. Instead, constitutive equations are related with experimental measurements. In this way, it is helpful to review the basic assumptions taken to develop the stress-strain laws:

- A small sample extracted from the solid has uniform properties;
- When the solid is deformed, lines that are initially straight in the solid are deformed into smooth curves (with continuous slope);
- Short segments of these lines (much shorter than the radius of curvature of the curves) are just stretched and rotated by deformation, implying that the deformation of a sufficiently small volume element can be characterized by a deformation gradient;
- The stress that occurs at point in the solid depends only in the change of shape of an extremely small volume element that surrounds it. Therefore, it must be a function of the deformation gradient or a strain measure that derives from it.

These assumptions are approximations because materials are not uniform at small scales, whether it is at the inter atomic or microstructural level. Therefore, the elastic range, well defined for the vast majority of homogeneous materials, is affected by materials with complex

microstructures. Thus, there is an high dependency between the elastic properties of porous and composite materials and their microstructures. Experimental procedures can be used to find out these properties but the monetary costs inherent to them are high, and so, in this chapter, several analytical methods that aim to solve this problem are introduced. Moreover, a numerical procedure that consists on applying different loads (pure strain and pure shear deformations) to an RVE that correctly represents a microstructure (created by the DIB microstructure recognition technique presented in Chapter 4) is described. This method improves the accuracy of the results since it takes into account the real microstructure's geometry.

In order to better understand the elasticity concept, the generalized *Hooke's Law* must be introduced, along with the elastic constants that are generally utilized. Greater attention will be given to orthotropic, transversely isotropic and isotropic materials. All of this information can be found on Lai et al. (2010), Bower (2010) and Hwu (2010).

5.1 Hooke's Law

To formulate the elastic behaviour of a material under small deformations, the 4th-order compliance tensor, $\mathbf{S}$, and the 4th-order stiffness tensor, $\mathbf{C}$, also named as elasticity tensor, must be introduced as the linear map between the 2nd-order strain and stress tensors. This is mathematically expressed by the generalized *Hooke's Law*,

$$\boldsymbol{\varepsilon} = \mathbf{S} : \boldsymbol{\sigma}, \tag{5.1a}$$

$$\boldsymbol{\sigma} = \mathbf{C} : \boldsymbol{\varepsilon}, \tag{5.1b}$$

being $\mathbf{C}$ the inverse tensor of $\mathbf{S}$,

$$\mathbf{C} = \mathbf{S}^{-1}. \tag{5.2}$$

A 4th-order tensor has 81 components but, in a linearly elastic body, due to symmetry relations that exist in the strain and stress tensors, $\boldsymbol{\sigma} = \boldsymbol{\sigma}^T$ and $\boldsymbol{\varepsilon} = \boldsymbol{\varepsilon}^T$, both constitutive tensors, $\mathbf{S}$ and $\mathbf{C}$, have minor symmetry,

$$(\cdot)_{ijkl} = (\cdot)_{jikl} = (\cdot)_{ijlk} \tag{5.3}$$

hence, the number of independent components is reduced to 36.

Furthermore, it is assumed that the concept of elasticity is related with the capacity of the materials to store energy which is denoted as *strain energy function*,

$$U = \frac{1}{2}\, \mathbf{C} : \boldsymbol{\varepsilon} : \boldsymbol{\varepsilon}, \tag{5.4}$$

which is a positive definite function of the strain components such that,

$$\boldsymbol{\sigma} = \frac{\partial U}{\partial \boldsymbol{\varepsilon}}. \tag{5.5}$$

With this assumption, it is possible to prove that the constitutive tensors also have major symmetry,

$$(\cdot)_{ijkl} = (\cdot)_{klij}, \tag{5.6}$$

and, consequently, the number of independent elastic constants decreases to 21, characteristic of a material with generalized anisotropic behaviour.

Considering these properties, it is possible to define the *Hooke's Law* in a matrix basis following the *Voigt* notation:

$$\begin{Bmatrix} \sigma_{11} \\ \sigma_{22} \\ \sigma_{33} \\ \sigma_{23} \\ \sigma_{13} \\ \sigma_{12} \end{Bmatrix} = \begin{bmatrix} C_{1111} & C_{1122} & C_{1133} & C_{1123} & C_{1113} & C_{1112} \\ & C_{2222} & C_{2233} & C_{2223} & C_{2213} & C_{2212} \\ & & C_{3333} & C_{3323} & C_{3313} & C_{3312} \\ & & & C_{2323} & C_{2313} & C_{2312} \\ & & & & C_{1313} & C_{1312} \\ \text{sym.} & & & & & C_{1212} \end{bmatrix} \begin{Bmatrix} \varepsilon_{11} \\ \varepsilon_{22} \\ \varepsilon_{33} \\ \gamma_{23} \\ \gamma_{13} \\ \gamma_{12} \end{Bmatrix}, \tag{5.7}$$

where,

$$\gamma_{23} = 2\varepsilon_{23} \qquad \gamma_{13} = 2\varepsilon_{13} \qquad \gamma_{12} = 2\varepsilon_{12} \tag{5.8}$$

are the *engineering shear strains*. In Expression (5.7), the indices are not very practical but demonstrate the tensorial character of the tensors $\boldsymbol{\sigma}$, $\boldsymbol{\varepsilon}$ and $\mathbf{C}$. Due to this complexity, one can also write it in the simplified or "contracted form",

$$\begin{Bmatrix} \sigma_1 \\ \sigma_2 \\ \sigma_3 \\ \sigma_4 \\ \sigma_5 \\ \sigma_6 \end{Bmatrix} = \begin{bmatrix} C_{11} & C_{12} & C_{13} & C_{14} & C_{15} & C_{16} \\ & C_{22} & C_{23} & C_{24} & C_{25} & C_{26} \\ & & C_{33} & C_{34} & C_{35} & C_{36} \\ & & & C_{44} & C_{45} & C_{46} \\ & & & & C_{55} & C_{56} \\ \text{sym.} & & & & & C_{66} \end{bmatrix} \begin{Bmatrix} \varepsilon_1 \\ \varepsilon_2 \\ \varepsilon_3 \\ \varepsilon_4 \\ \varepsilon_5 \\ \varepsilon_6 \end{Bmatrix}. \tag{5.9}$$

However, one must know that C_{ij}'s are not components of a 2nd-order tensor and $\boldsymbol{\sigma}_i$ and $\boldsymbol{\varepsilon}_j$ are not those of a vector.

It is usual for linear elastic solids to have at least one plane of symmetry, that can be described by the plane S_1 with unit normal vector $\boldsymbol{e}_1$. This phenomenon is known as *elastic symmetry*, and a material that has one plane of symmetry is called a *monoclinic material*. For such material, the number of independent elastic constants is reduced to 13,

$$\begin{Bmatrix} \sigma_1 \\ \sigma_2 \\ \sigma_3 \\ \sigma_4 \\ \sigma_5 \\ \sigma_6 \end{Bmatrix} = \begin{bmatrix} C_{11} & C_{12} & C_{13} & C_{14} & 0 & 0 \\ & C_{22} & C_{23} & C_{24} & 0 & 0 \\ & & C_{33} & C_{34} & 0 & 0 \\ & & & C_{44} & 0 & 0 \\ & & & & C_{55} & C_{56} \\ \text{sym.} & & & & & C_{66} \end{bmatrix} \begin{Bmatrix} \varepsilon_1 \\ \varepsilon_2 \\ \varepsilon_3 \\ \varepsilon_4 \\ \varepsilon_5 \\ \varepsilon_6 \end{Bmatrix}. \tag{5.10}$$

5.1.1 Orthotropic Material

In the case that a linearly elastic material has two perpendicular planes of material symmetry, S_1 plane with unit normal vector $\boldsymbol{e}_1$ and S_2 plane with unit normal vector $\boldsymbol{e}_2$, then automatically the plane S_3, mutually perpendicular to both, with the unit normal vector $\boldsymbol{e}_3$ is also a plane of material symmetry. This type of material is named *orthotropic elastic material* and has three different Young's modulus, E_1, E_2 and E_3 that are associated with the directions $\boldsymbol{e}_1, \boldsymbol{e}_2$ and $\boldsymbol{e}_3$.

For this solid, the number of independent coefficients decreases to 9 and the constitutive equations become:

$$\begin{Bmatrix} \sigma_1 \\ \sigma_2 \\ \sigma_3 \\ \sigma_4 \\ \sigma_5 \\ \sigma_6 \end{Bmatrix} = \begin{bmatrix} C_{11} & C_{12} & C_{13} & 0 & 0 & 0 \\ & C_{22} & C_{23} & 0 & 0 & 0 \\ & & C_{33} & 0 & 0 & 0 \\ & & & C_{44} & 0 & 0 \\ & & & & C_{55} & 0 \\ \text{sym.} & & & & & C_{66} \end{bmatrix} \begin{Bmatrix} \varepsilon_1 \\ \varepsilon_2 \\ \varepsilon_3 \\ \varepsilon_4 \\ \varepsilon_5 \\ \varepsilon_6 \end{Bmatrix}. \tag{5.11}$$

It is important to note that all the components of the stiffness matrix, C_{ij}, are related with the following elastic constants:

- **Young's Modulus,** E_i, describes the material's strain response to an uniaxial stress in the direction i of the load. It is the ratio of the stress (force per unit area) along an axis to the strain along the same axis in the range of stresses in which Hooke's law holds;

- **Poisson's Ratio,** ν_{ij}, also known as the coefficient of expansion on the transverse axis, describes the response of the material in the directions orthogonal to this uniaxial stress. It is set as the ratio that corresponds to a contraction in the direction j when an extension is applied in the direction i. It is dimensionless and typically ranges from 0.20 to 0.49, and is around 0.3 for most metals. If $\nu = 0.5$, the solid is incompressible - its volume remains constant, no matter how it is deformed;

- **Shear Modulus,** G_{ij}, expresses the material's response to shear stress and it is defined as the ratio of the shear stress σ_{ij} to the shear strain γ_{ij};

- **Bulk Modulus,** K, represents the resistance of the material to an uniform compression. It is defined by the ratio between an infinitesimal increase in the pressure that is submitted to the material and the relative decrease of its volume.

Therefore, the elasticity matrix can be rewritten as:

$$C_{ij} = \begin{bmatrix} \frac{1-\nu_{23}\nu_{32}}{E_2E_3\Delta} & \frac{\nu_{21}+\nu_{23}\nu_{31}}{E_2E_3\Delta} & \frac{\nu_{31}+\nu_{21}\nu_{32}}{E_2E_3\Delta} & 0 & 0 & 0 \\ & \frac{1-\nu_{13}\nu_{31}}{E_1E_3\Delta} & \frac{\nu_{32}+\nu_{12}\nu_{31}}{E_1E_3\Delta} & 0 & 0 & 0 \\ & & \frac{1-\nu_{12}\nu_{21}}{E_1E_2\Delta} & 0 & 0 & 0 \\ & & & G_{23} & 0 & 0 \\ & & & & G_{13} & 0 \\ \text{sym.} & & & & & G_{12} \end{bmatrix}, \tag{5.12}$$

where Δ denotes the determinant of the stiffness matrix, given by:

$$\Delta = \frac{1-\nu_{23}\nu_{32}-\nu_{13}\nu_{31}-\nu_{12}\nu_{21}-2\,\nu_{32}\nu_{13}\nu_{21}}{E_1E_2E_3}. \tag{5.13}$$

In order to derive a method to extract the elastic constants, it is necessary to express them as a function of the matrix components, C_{ij},

$$\begin{gathered} E_1 = \frac{\Theta}{C_{22}C_{33}-C_{23}^2}, \qquad E_2 = \frac{\Theta}{C_{11}C_{33}-C_{13}^2}, \qquad E_3 = \frac{\Theta}{C_{11}C_{22}-C_{12}^2}, \\ \nu_{12} = \frac{C_{12}C_{33}-C_{13}C_{23}}{C_{22}C_{33}-(C_{23})^2}, \qquad \nu_{13} = \frac{C_{13}C_{22}-C_{12}C_{23}}{C_{22}C_{33}-(C_{23})^2}, \qquad \nu_{23} = \frac{C_{23}C_{11}-C_{12}C_{13}}{C_{11}C_{33}-(C_{13})^2}, \\ G_{23} = C_{44}, \qquad G_{13} = C_{55}, \qquad G_{12} = C_{66}. \end{gathered} \tag{5.14}$$

where Θ is given by:

$$\Theta = C_{11}C_{22}C_{33} + 2\,C_{23}C_{13}C_{12} - C_{11}(C_{23})^2 - C_{22}(C_{13})^2 - C_{33}(C_{12})^2. \tag{5.15}$$

Based on the symmetry of the compliance matrix, it is also possible to find the following relation between the Poisson's ratio and the Young's modulus:

$$\frac{\nu_{ij}}{E_i} = \frac{\nu_{ji}}{E_j}, \qquad \text{for } i,j = 1,2,3, \quad i \neq j. \tag{5.16}$$

2D Plane Strain

In engineering components, stress (and strain) are tensor fields defined in three dimensions (Figure 5.1) but under some circumstances it is possible to simplify the problem into two dimensional studies. These are divided into two distinct physical types: *plane deformation* (or *plane strain*) and *plane stress*. The first one arises from the study of prismatic structures' deformations that have the axis length several times bigger than the cross section dimensions

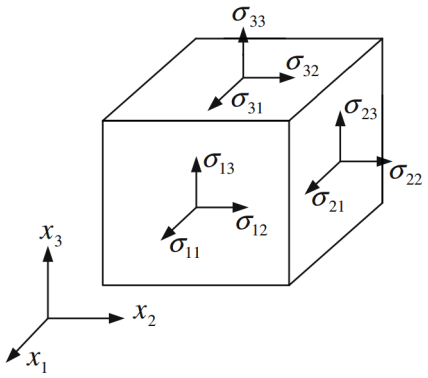

Figure 5.1: Components of stress in three dimensions.

(e.g. long metal billet, large cylindrical bodies). The external forces are distributed in a way, such that the deformation in the axis direction vanishes and the remaining components do not vary along the length of the prismatic structure. As an example, consider the cross section of a cylinder that is parallel to the x_1x_2-plane, the state of plane strain may be characterized by:

$$u_i = u_i(x_1, x_2), \quad i = 1, 2, \quad u_3 = 0, \tag{5.17}$$

where u_1, u_2 and u_3 are the displacements in the x_1, x_2 and x_3 directions. Furthermore, as the relation between displacement and strain is:

$$\begin{gathered} \varepsilon_{11} = \frac{\partial u_1}{\partial x_1}, \qquad \varepsilon_{22} = \frac{\partial u_2}{\partial x_2}, \qquad \varepsilon_{33} = \frac{\partial u_3}{\partial x_3}, \\ \gamma_{23} = \frac{\partial u_2}{\partial x_3} + \frac{\partial u_3}{\partial x_2}, \qquad \gamma_{13} = \frac{\partial u_1}{\partial x_3} + \frac{\partial u_3}{\partial x_1}, \qquad \gamma_{12} = \frac{\partial u_1}{\partial x_2} + \frac{\partial u_2}{\partial x_1}, \end{gathered} \tag{5.18}$$

Equation (5.17) leads to:

$$\varepsilon_{33} = \gamma_{13} = \gamma_{23} = 0. \tag{5.19}$$

and to the following Cauchy stress tensor:

$$\boldsymbol{\sigma} = \begin{bmatrix} \sigma_{11} & \sigma_{12} & 0 \\ \sigma_{12} & \sigma_{22} & 0 \\ 0 & 0 & \sigma_{33} \end{bmatrix}, \tag{5.20}$$

in which the non-zero σ_{33} is needed to maintain the constraint ε_{33}.

Finally, the constitutive law (Haboussa, 2012, p. 12) is expressed by:

$$\begin{Bmatrix} \sigma_{11} \\ \sigma_{22} \\ \sigma_{33} \\ \sigma_{12} \end{Bmatrix} = \begin{bmatrix} C_{11} & C_{12} & C_{13} & 0 \\ & C_{22} & C_{23} & 0 \\ & & C_{33} & 0 \\ \text{sym.} & & & C_{44} \end{bmatrix} \begin{Bmatrix} \varepsilon_{11} \\ \varepsilon_{22} \\ 0 \\ \gamma_{12} \end{Bmatrix}. \tag{5.21}$$

where the components, C_{ij} $(i,j=1,2,3)$, are defined in Equation (5.12) and $C_{44}=C_{66}=G_{12}$. The elastic constants are given by Expressions (5.14).

5.1.2 Transversely Isotropic Materials

A special case of an orthotropic material is one that contains a plane S_3 (plane of isotropy) with and unit normal vector $\boldsymbol{e}_3$ (axis of transverse isotropy), such that every perpendicular plane to it is a plane of symmetry. In this plane of symmetry, the elastic constants are independent of the direction, meaning that there is no distinction between the vectors $\boldsymbol{e}_1$ and $\boldsymbol{e}_2$. In this case the material is called a *Tranversely Isotropic Material* and the constitutive tensor is composed by 5 different independent components,

$$C_{ij}=\begin{bmatrix} C_{11} & C_{12} & C_{13} & 0 & 0 & 0 \\ & C_{11} & C_{13} & 0 & 0 & 0 \\ & & C_{33} & 0 & 0 & 0 \\ & & & C_{44} & 0 & 0 \\ & & & & C_{44} & 0 \\ \text{sym.} & & & & & \dfrac{(C_{11}-C_{12})}{2} \end{bmatrix}. \tag{5.22}$$

The engineering constants must satisfy:

$$\begin{gathered} E_1=E_2=E_p, \qquad E_3=E_t, \\ \nu_{13}=\nu_{23}=\nu_{pt}, \qquad \nu_{31}=\nu_{32}=\nu_{tp}, \qquad \nu_{12}=\nu_p, \\ G_{13}=G_{23}=G_{pt}, \qquad G_{12}=G_p, \end{gathered} \tag{5.23}$$

and the stiffness matrix is denoted by:

$$C_{ij}=\begin{bmatrix} \dfrac{1-\nu_{pt}\nu_{tp}}{E_pE_t\Delta} & \dfrac{\nu_p+\nu_{pt}\nu_{tp}}{E_pE_t\Delta} & \dfrac{\nu_{tp}+\nu_p\nu_{tp}}{E_pE_t\Delta} & 0 & 0 & 0 \\ & \dfrac{1-\nu_{pt}\nu_{tp}}{E_pE_t\Delta} & \dfrac{\nu_{tp}+\nu_p\nu_{tp}}{E_pE_t\Delta} & 0 & 0 & 0 \\ & & \dfrac{1-\nu_p^2}{E_p^2\Delta} & 0 & 0 & 0 \\ & & & G_{pt} & 0 & 0 \\ & & & & G_{pt} & 0 \\ \text{sym.} & & & & & G_p \end{bmatrix}. \tag{5.24}$$

Similar to the process done to obtain Equations (5.14), these elastic constants can be written

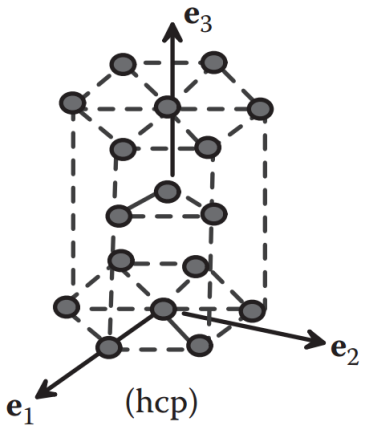

Figure 5.2: Atoms in a hexagonal close-packed solid.

as a function of tensor components,

$$E_p = \frac{\Theta}{C_{11}C_{33} - C_{13}^2}, \qquad E_t = \frac{\Theta}{(C_{11})^2 - C_{12}^2},$$

$$\nu_p = \frac{C_{12}C_{33} - (C_{13})^2}{C_{11}C_{33} - (C_{13})^2}, \qquad \nu_{pt} = \frac{C_{11}C_{13} - C_{12}C_{13}}{C_{11}C_{33} - (C_{13})^2}, \qquad \nu_{tp} = \frac{C_{11}C_{13} - C_{12}C_{13}}{(C_{11})^2 - (C_{12})^2}, \tag{5.25}$$

$$G_p = \frac{1}{2}(C_{11} - C_{12}), \qquad G_{pt} = C_{44},$$

where Θ is:

$$\Theta = C_{33}(C_{11})^2 + 2\ C_{12}(C_{13})^2 - 2\ C_{11}(C_{13})^2 - C_{33}(C_{12})^2. \tag{5.26}$$

Examples of transverse isotropic materials are the ones that have hexagonal close-packed (hcp) crystals at the microstructure. The $\boldsymbol{e}_3$ axis must be perpendicular to the basal plane of the crystal (Figure 5.2) because the planes perpendicular to $\boldsymbol{e}_3$ are isotropic planes. The orientation of $\boldsymbol{e}_1$ and $\boldsymbol{e}_2$ is arbitrary.

5.1.3 Isotropic Materials

In the case of isotropic materials, the constitutive law can be parametrized by only 2 independent constants. Examples are materials with cubic symmetry (e.g. face-centered cubic (fcc) and body-centered cubic (bcc) metals are shown in Figure 5.3) and for those, in addition to the axis of transverse isotropy $\boldsymbol{e}_3$, $\boldsymbol{e}_1$ is also an axis of transverse isotropy. Therefore,

$$C_{11} = C_{22} = C_{33}, \qquad C_{12} = C_{13}, \qquad C_{44} = \frac{(C_{11} - C_{12})}{2}. \tag{5.27}$$

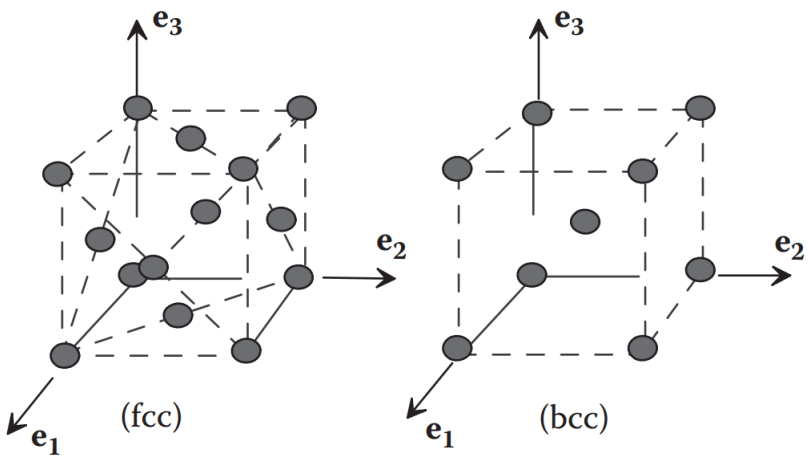

Figure 5.3: Atoms in face- and body-centered cubic materials.

The constitutive law can be written as:

$$C_{ij} = \begin{bmatrix} C_{11} & C_{12} & C_{12} & 0 & 0 & 0 \\ & C_{11} & C_{12} & 0 & 0 & 0 \\ & & C_{11} & 0 & 0 & 0 \\ & & & \frac{(C_{11}-C_{12})}{2} & 0 & 0 \\ & & & & \frac{(C_{11}-C_{12})}{2} & 0 \\ \text{sym.} & & & & & \frac{(C_{11}-C_{12})}{2} \end{bmatrix}. \tag{5.28}$$

The engineering constants always satisfy,

$$\begin{aligned} E &= E_1 = E_2 = E_3, \\ \nu &= \nu_{12} = \nu_{13} = \nu_{23}, \\ G &= G_{12} = G_{13} = G_{23}, \end{aligned} \tag{5.29}$$

and the shear modulus is dependent of the Young's modulus and Poisson's ratio through the following equation,

$$G = \frac{E}{2(1+\nu)}. \tag{5.30}$$

The two independent elastic constants are then defined as a function of tensor components, C_{ij},

$$\begin{aligned} E &= \frac{(C_{11})^2 + C_{12}C_{11} - 2\,(C_{12})^2}{C_{11} + C_{12}}, \\ \nu &= \frac{C_{12}}{C_{11} + C_{12}}, \end{aligned} \tag{5.31}$$

and the stiffness tensor, defined as a function of the elastic constants, is denoted by:

$$C_{ij} = \frac{E}{(1+\nu)(1-2\nu)} \begin{bmatrix} 1-\nu & \nu & \nu & 0 & 0 & 0 \\ & 1-\nu & \nu & 0 & 0 & 0 \\ & & 1-\nu & 0 & 0 & 0 \\ & & & \frac{1-2\nu}{2} & 0 & 0 \\ & & & & \frac{1-2\nu}{2} & 0 \\ \text{sym.} & & & & & \frac{1-2\nu}{2} \end{bmatrix}. \tag{5.32}$$

5.2 Analytical Methods

In the previous section, basic concepts of elasticity were introduced based on the assumption that the material was homogeneous. However, in the case of a heterogeneous material, the overall effective elastic properties are related with the elastic properties of the phases that form the composite and so, in order to obtain them, several analytical methods were developed throughout the years.

These methods are build upon *mean field approaches*, that aim to replace the complex elastic fields disturbed by a large number of inclusions by the average fields of a virtually homogenized composite, only considering the material properties of the phases which compose the material, and partly their geometry and localization.

In this section, some of the most common analytical methods to obtain the average properties of heterogeneous materials are presented.

5.2.1 Hill Bounds

Based on the uniform stress and strain trial function, the classical expressions for the minimum potential energy and the minimum complementary energy lead to the simplest and most extreme variational bounding expressions: the upper bound of *Voigt* (proposed in 1889) and the lower bound of *Reuss* (proposed in 1929).

These bounds are only related with the phase volume fractions and do not contain any information about the geometry of the inclusions in the inhomogeneous material. The simplicity of these equations implies that the results obtained with them are not of much practical use but, in contrast with higher-order bounds (e.g. *Hashin-Shtrikman Bounds*), they also hold for volume elements that are to small to be regarded RVEs. Nevertheless, neither of these models are correct, because the *Voigt* model violates equilibrium due to the implied traction across the phase boundaries and the *Reuss* model generates strains that would force the debounding of the phases. In tensorial form, *Hill Bounds* (Hill, 1952) can be expressed as:

$$\mathbf{C}_R^* = \left[\sum_{(i)} \phi_i \mathbf{S}_i\right]^{-1} \leq \mathbf{C}^* \leq \sum_{(i)} \phi_i \mathbf{C}_i = \mathbf{C}_V^* \tag{5.33}$$

where $\mathbf{C}^*$ is the homogenized (or effective) stiffness tensor, $\mathbf{C}_R^*$ and $\mathbf{C}_V^*$ are the estimated effective tensors given by the *Reuss* and *Voigt* models and ϕ_i is the volume fraction of phase i. More information about these models can be found on Berryman (2004) and Böhm (2016).

Voigt Model

The *Voigt* model, (also known as the *rule of mixtures*) is the upper boundary and takes into account that the applied load causes equal strains in both phases of the composite and so, the overall composite stress is the sum of the stresses carried out by each phase.

Thus, the composite effective stiffness tensor can be calculated by:

$$C_{ijkl}^* = \phi_f C_{ijkl}^f + \phi_m C_{ijkl}^m, \tag{5.34}$$

where ϕ_f and ϕ_m represent the fiber and matrix volume fraction, respectively.

Considering an isotropic composite material, an isotropic matrix with E_m and an isotropic fiber with E_f as Young's modulus, the overall Young's modulus, E^*, given by the *Voigt* model is the average of the constituents' moduli weighted by the volume fraction of each phase,

$$E^* = \phi_f E_f + \phi_m E_m, \tag{5.35}$$

where, usually, $\phi_f + \phi_m = 1$. Expression (5.35) assumes that the constituents have Poisson's ratios that lead to equal Poisson contractions.

Reuss Model

The *Reuss* model corresponds to the lower boundary and is known as the *inverse rule of mixtures* or the *rule of mixtures* for the compliance components. It formulates the case when each phase of the composite carries an equal stress. In this way, the compliance effective tensor for the composite is given by:

$$S_{ijkl}^* = \phi_f S_{ijkl}^f + \phi_m S_{ijkl}^m, \tag{5.36}$$

Consequently, in a isotropic material, the overall strain in the composite is the sum of the net strain carried out by each phase and the effective Young's modulus, E^*, given by the *Reuss* model is denoted as:

$$E^* = \left(\frac{\phi_f}{E_f} + \frac{\phi_m}{E_m} \right)^{-1}. \tag{5.37}$$

Expression (5.37) assumes that the constituents have Poisson's ratios that lead to equal Poisson contractions.

5.2.2 Modified Rule of Mixtures

The *Modified Rule of Mixtures* (Nakamura et al., 2000) is an alternative method to the *Voigt* and *Reuss* boundaries. If the composite is treated as isotropic, its uniaxial stress and strain

can be decomposed into:

$$\sigma = \phi_f \sigma_f + (1 - \phi_f)\sigma_m, \tag{5.38a}$$

$$\varepsilon = \phi_f \varepsilon_f + (1 - \phi_f)\varepsilon_m, \tag{5.38b}$$

where σ_f, σ_m and ε_f, ε_m are the stresses and strains of the fibers and matrix under uniaxial stress and strain conditions.

If one takes into consideration the dimensionless parameter q, that characterizes the normalized ratio of the stress to strain transfer, defined by:

$$q = \frac{1}{E_f} \frac{\sigma_f - \sigma_m}{\varepsilon_f - \varepsilon_m}, \quad q \in [0, \infty], \tag{5.39}$$

and combines Equation (5.38) with (5.39), while considering $E = \dfrac{\sigma}{\varepsilon}$, it is possible to obtain the following expression for the overall Young's modulus, E^*:

$$E^* = \frac{\phi_f E_f + (1 - \phi_f) E_m R}{\phi_f + (1 - \phi_f) R}, \tag{5.40}$$

where R is given by:

$$R = \frac{q + 1}{q + \dfrac{E_m}{E_f}}. \tag{5.41}$$

In Figure 5.4, the evolution of Equations (5.40) and (5.41) is presented and, it is possible to note that choosing a null value for the stress-strain transfer parameter, $q = 0$, the equation is equal to the *Reuss Model* and if $q \to \infty$, the equation refers to the *Voigt Model*.

The parameter q is empirical and depends on many factors, including composition, microstructure arrangement, internal constraints, and others.

The modified rule of mixtures can also be extended to elastic-plastic composites (Nakamura et al., 2000), but it is not included since it is out of the scope of this work.

5.2.3 Hashin and Shtrikman Bounds

Through a variational approach, *Hashin* and *Shtrickman* developed a set of tighter and more meaningful boundaries than those of *Hill Bounds* (*Voigt* and *Reuss*) for isotropic materials with arbitrary internal geometry (Hashin and Shtrikman, 1963). For two-phase materials the upper and lower bounds for the effective bulk modulus are defined by the following expressions:

$$K_L^* = K_1 + \frac{\phi_2}{\dfrac{1}{K_2 - K_1} + \dfrac{3\phi_1}{3K_1 + 4G_1}}, \tag{5.42a}$$

$$K_H^* = K_2 + \frac{\phi_1}{\dfrac{1}{K_1 - K_2} + \dfrac{3\phi_2}{3K_2 + 4G_2}}, \tag{5.42b}$$

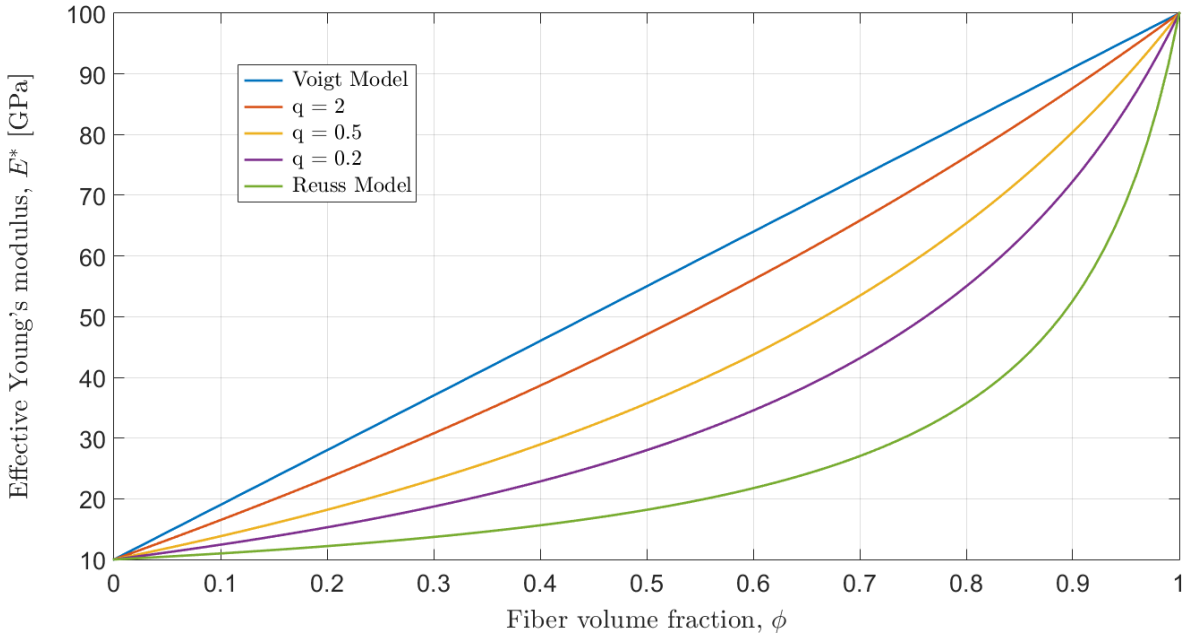

Figure 5.4: Comparison between the *Voigt*, *Reuss* and the *Modified Rule of Mixtures* models. In this example, $E_f = 100$ GPa and $E_m = 10$ GPa.

where K_L^* and K_H^* denotes the lower and upper bounds, respectively, for the effective bulk modulus of the composite, K_1, K_2 and ϕ_1, ϕ_2 are the bulk moduli and the volume fraction for phase 1 and 2, respectively. Here $K_2 \geq K_1$ and $G_2 \geq G_1$. In these expressions, it is assumed that both phases are made of an isotropic material. It has been shown in Hashin (1962) that Equation (5.42a) is the exact result for the bulk modulus of a certain composite material that has a matrix of phase 'one' material and spherical inclusions of phase 'two' material distributed in a particular way. Analogously, Expression (5.42b) gives the exact value for the bulk modulus if the matrix is of phase 'two' material and the spherical inclusions are of phase 'one' material. These are the most restrictive bounds that can be given in terms of phase volume fraction and phase moduli. It is also possible to note that if $G_1 = G_2$, both expressions are equal and predict an exact result for this particular case.

The expressions for the shear moduli are:

$$G_L^* = G_1 + \frac{\phi_2}{\dfrac{1}{G_2 - G_1} + \dfrac{6(K_1 + 2G_1)\phi_1}{5G_1(3K_1 + 4G_1)}}, \tag{5.43a}$$

$$G_H^* = G_2 + \frac{\phi_1}{\dfrac{1}{G_1 - G_2} + \dfrac{6(K_2 + 2G_2)\phi_2}{5G_2(3K_2 + 4G_2)}}, \tag{5.43b}$$

where G_L^* and G_H^* are the lower and upper bounds, respectively, for the effective shear modulus of the composite.

The bounds for the Young's modulus can also be obtained if one uses the following relation:

$$E_n^* = \frac{9K_n^* G_n^*}{3K_n^* + G_n^*}, \qquad n = L, H. \tag{5.44}$$

The dependency of the effective Young's modulus with the change of the volume fraction of phase 2, ϕ_2, (e.g. fiber material) is shown in Figure 5.5. This graphic also demonstrates that the distance between the boundaries increases while increasing the relative stiffness of one phase to others. To better demonstrated this, the effective Young's modulus has been normalized taking into account the respective phase properties. The scalar $\bar{E}^*$ is the normalized effective Young's modulus and is given by:

$$\bar{E}^* = \frac{E^* - E_1}{E_2 - E_1}. \tag{5.45}$$

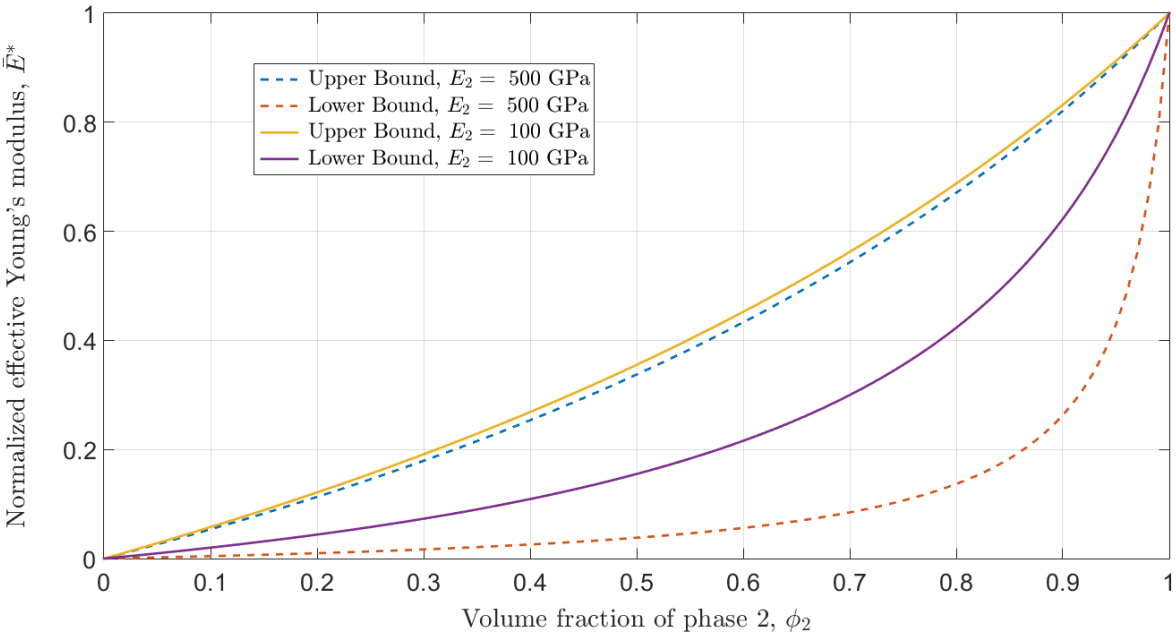

Figure 5.5: Representation of the *Hashin* and *Shtrikman* bounds for the effective Young's modulus and comparison between different relative stiffness values. Both cases have $E_m = 10$ GPa and $\nu_m = \nu_f = 0.3$.

Hill-Hashin Bounds

In references (Hill (1964); Hashin (1965)), the bounds for transversely isotropic composites with isotropic constituents were formulated. These bounds were deduced for the effective axial Young's modulus (E_t^*), effective axial (G_{pt}^*) and transverse shear moduli (G_p^*), effective axial Poisson's ratio (ν_{pt}^*) and effective plane strain bulk modulus (K_p^*) and are denoted as it follows:

$$\frac{\phi_m \phi_f}{\frac{\phi_f}{K_m} + \frac{\phi_m}{K_f} + \frac{1}{G_m}} \leq \frac{E_t^* - \phi_f E_f - \phi_m E_m}{4(\nu_f - \nu_m)^2} \leq \frac{\phi_f \phi_m}{\frac{\phi_f}{K_m} + \frac{\phi_m}{K_f} + \frac{1}{G_f}}, \tag{5.46a}$$

$$G_m + \frac{\phi_f}{\dfrac{1}{G_f - G_m} + \dfrac{\phi_m}{2G_m}} \leq G_{pt}^* \leq G_f + \frac{\phi_m}{\dfrac{1}{G_m - G_f} + \dfrac{\phi_f}{2G_f}}, \tag{5.46b}$$

$$G_m + \frac{\phi_f}{\dfrac{1}{G_f - G_m} + \dfrac{\phi_m(K_m + 2G_m)}{2G_m(K_m + G_m)}} \leq G_p^* \leq G_f + \frac{\phi_m}{\dfrac{1}{G_m - G_f} + \dfrac{\phi_f(K_f + 2G_f)}{2G_f(K_f + G_f)}}, \tag{5.46c}$$

$$K_m + \frac{\phi_f}{\dfrac{1}{K_f - K_m} + \dfrac{\phi_m}{K_m + G_m}} \leq K_p^* \leq K_f + \frac{\phi_m}{\dfrac{1}{K_m - K_f} + \dfrac{\phi_f}{K_f + G_f}}, \tag{5.46d}$$

$$\frac{\phi_m \phi_f}{\dfrac{\phi_f}{K_m} + \dfrac{\phi_m}{K_f} + \dfrac{1}{G_m}} \leq \frac{\nu_{pt}^* - \phi_f \nu_f - \phi_m \nu_m}{(\nu_f - \nu_m)\left(\dfrac{1}{K_m} - \dfrac{1}{K_f}\right)} \leq \frac{\phi_f \phi_m}{\dfrac{\phi_f}{K_m} + \dfrac{\phi_m}{K_f} + \dfrac{1}{G_f}}, \tag{5.46e}$$

and taking into account the following equation:

$$K_p^* = \frac{E_p^* G_p^*}{3(3G_p^* - E_p^*)}, \tag{5.47}$$

it is possible to define the bounds for the effective plane strain Young's modulus, E_p^*,

$$K_m + \frac{\phi_f}{\dfrac{1}{K_f - K_m} + \dfrac{\phi_m}{K_m + G_m}} \leq \frac{E_p^* G_p^*}{3(3G_p^* - E_p^*)} \leq K_f + \frac{\phi_m}{\dfrac{1}{K_m - K_f} + \dfrac{\phi_f}{K_f + G_f}}. \tag{5.48}$$

By modifying Inequation (5.48) and rewriting it in order to E_p^*, the following upper and lower boundaries are defined:

$$E_{p_L}^* = 9\left[\left(K_m + \frac{\phi_f}{\dfrac{1}{K_f - K_m} + \dfrac{\phi_m}{K_m + G_m}}\right)^{-1} + \frac{3}{G_{p_L}^*}\right]^{-1}, \tag{5.49a}$$

$$E_{p_H}^* = 9\left[\left(K_f + \frac{\phi_m}{\dfrac{1}{K_m - K_f} + \dfrac{\phi_f}{K_f + G_f}}\right)^{-1} + \frac{3}{G_{p_H}^*}\right]^{-1}, \tag{5.49b}$$

where $G_{p_H}^*$ and $G_{p_L}^*$ are, respectively, the right and left terms of Inequation (5.46c). Figure 5.6 demonstrates the dependency of $E_{p_H}^*$ and $E_{p_L}^*$ with the fiber volume fraction and compares it with the *Hashin* and *Shtrikman* boundaries.

5.2.4 Self-Consistent Method

Hill (1965) proposed a self consistent scheme and, as all models herein referred, have limitations when it comes to predict the overall properties of the composites. In reference Li and Wang

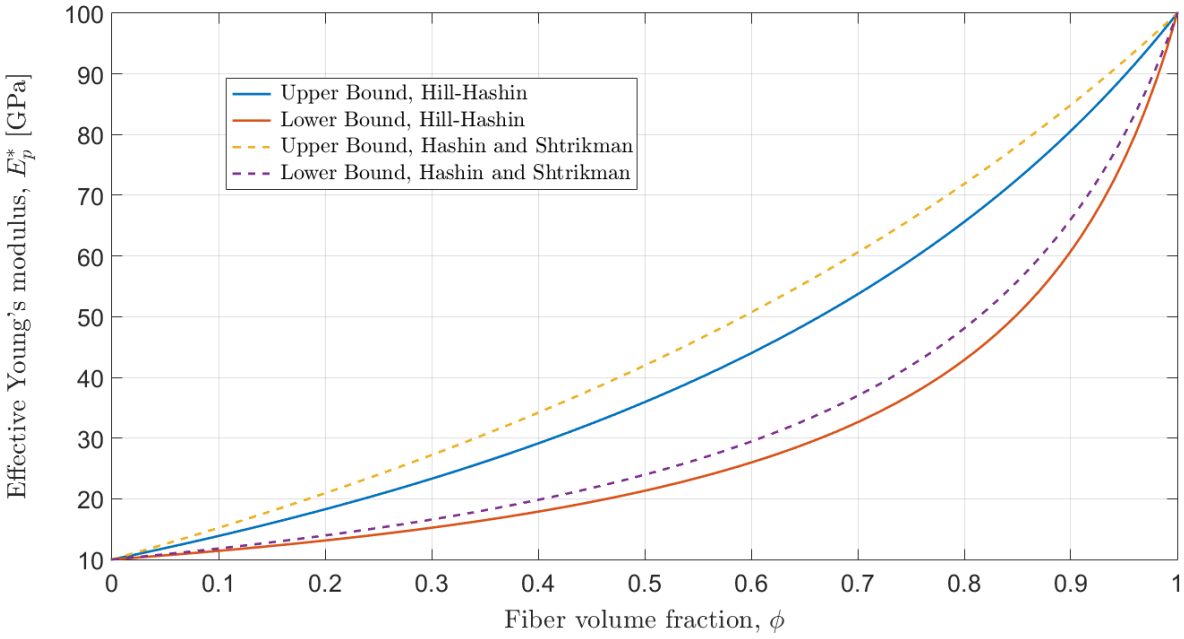

Figure 5.6: Representation of the *Hill-Hashin* bounds and comparison with the *Hashin* and *Shtrikman* bounds. Both cases have $E_f = 100$ GPa, $E_m = 10$ GPa and $\nu_m = \nu_f = 0.3$.

(2005) it is said that this scheme might fail to accurately predict the effective elastic properties, because it does not require any of the phases to be treated as a matrix, even though it includes the interaction between them.

The *Self-Consistent* method is based on the solution of an auxiliary problem where a single ellipsoidal inclusion is embedded in an infinite equivalent medium of the heterogeneous composite. The bounding between inclusion and the infinite medium is perfect, and so, there is displacement and traction continuity in the interface of the two phases. It has been shown in Eshelby (1957) that, in these type of problems, if one applies uniform stresses or strains to the system at infinity, the stress and strain fields in the inclusion are uniform, respectively, and so, the elastic properties can be determined by relating the far-field stresses and strains in the homogeneous medium with those found on the inclusion.

In order to find the effective properties of such system, Hill (1965) and Budiansky (1965) assume an initially homogeneous matrix into which inclusions of a different material have been placed, i.e. the inclusions can be considered embedded in the matrix, creating a fictitious matrix, and so the infinite medium is taken to be homogeneous with the same properties of the composite. For an elastic matrix, the Hill's *Self-Consistent* scheme is denoted by:

$$\boldsymbol{\sigma}^c - \boldsymbol{\sigma}^0 = -\mathbf{L}^* : (\boldsymbol{\varepsilon}^c - \boldsymbol{\varepsilon}^0), \tag{5.50}$$

where $\boldsymbol{\sigma}^0$ and $\boldsymbol{\varepsilon}^0$ define the far-field stress and strain that are applied in the fictitious matrix, $\boldsymbol{\sigma}^c$ and $\boldsymbol{\varepsilon}^c$ are the stress and strain tensors in the inclusion, respectively and $\mathbf{L}^*$ is the "constraint"

tensor defined by:

$$\mathsf{L}^* = \overline{\mathsf{L}} : (\mathbb{S} - \mathsf{I}), \tag{5.51}$$

in which $\mathbb{S}$ is the Eshelby tensor, I is the fourth-rank identity tensor,

$$\mathsf{I}_{ijkl} = \frac{\delta_{ik}\delta_{lj} + \delta_{il}\delta_{kj}}{2}, \tag{5.52}$$

where δ is the *Kronecker delta* function and $\overline{\mathsf{L}}$ is the elastic tensor that relates $\boldsymbol{\sigma}^0$ with $\boldsymbol{\varepsilon}^0$,

$$\boldsymbol{\sigma}^0 = \overline{\mathsf{L}} : \varepsilon^0, \tag{5.53a}$$

$$\overline{\mathsf{L}} = \phi_c \mathsf{L}_c : \mathsf{A}_c + (1 - \phi_c)\mathsf{L}_m : \mathsf{A}_m \tag{5.53b}$$

and,

$$\mathsf{A}_c = \left[\mathsf{L}^* + \mathsf{L}_c\right]^{-1} : \left[\mathsf{L}^* + \overline{\mathsf{L}}\right], \tag{5.54a}$$

$$\mathsf{A}_m = \left[\mathsf{L}^* + \mathsf{L}_m\right]^{-1} : \left[\mathsf{L}^* + \overline{\mathsf{L}}\right]. \tag{5.54b}$$

In Hill (1965) and Peng et al. (2009), the formulation for a case where it is assumed to have isotropic spherical inclusions and isotropic elastic composite is presented, and the following expressions are defined:

$$\frac{1}{K^*} = \frac{1}{K_m} + \frac{\phi_c \left(1 - \dfrac{K_c}{K_m}\right)}{K^* + \dfrac{1 + \nu^*}{3(1 - \nu^*)}(K_c - K^*)}, \tag{5.55a}$$

$$\frac{1}{G^*} = \frac{1}{G_m} + \frac{\phi_c \left(1 - \dfrac{G_c}{G_m}\right)}{G^* + \dfrac{2(4 - 5\nu^*)}{15(1 - \nu^*)}(G_c - G^*)}, \tag{5.55b}$$

where K_m, K_c, K^* and G_m, G_c, G^* are the bulk moduli and the shear moduli for the original matrix, the particle inclusion and the composite, respectively, ϕ_c is the volume fraction of the particle inclusions and ν^* is the Poisson's ratio of the composite which is given by:

$$\nu^* = \frac{3K^* - 2G^*}{6K^* + 2G^*}. \tag{5.56}$$

The expression for the effective Young's modulus is obtained by the following relation:

$$E^* = \frac{9K^*G^*}{3K^* + G^*}. \tag{5.57}$$

In Equations (5.55), K^* and G^* are dependent of their own values,

$$\frac{1}{K^*} = f(K^*, G^*, \dots), \tag{5.58a}$$

$$\frac{1}{G^*} = g(K^*, G^*, \dots), \tag{5.58b}$$

moreover, when computing them with MATLAB®, four different pairs of results were obtained for each volume fraction value. In the case of G^*, three out of four results were, consistently, negative, and so, there was only one pair that had both K^* and G^* positive, being this the only one that was physically admissible. The results demonstrated a good correlation with the bibliographic reference (Peng et al., 2009, Fig.2(b), Fig.4).

The representation of Equation (5.57) is displayed in Figure 5.7, as well as the *Hashin* and *Shtrikman* and the *Hill-Hashin* boundaries. The values obtained are within the *Hashin* and *Shtrikman* boundaries but, it can be noticed that this model is not within the *Hill-Hashin* bounds. This can be explained by the fact that Equations (5.55) are obtained under the assumption of an overall isotropic composite material and in the case of the *Hill-Hashin* bounds, the assumption is made for a transversely isotropic composite material. Therefore, both models can not be directly compared.

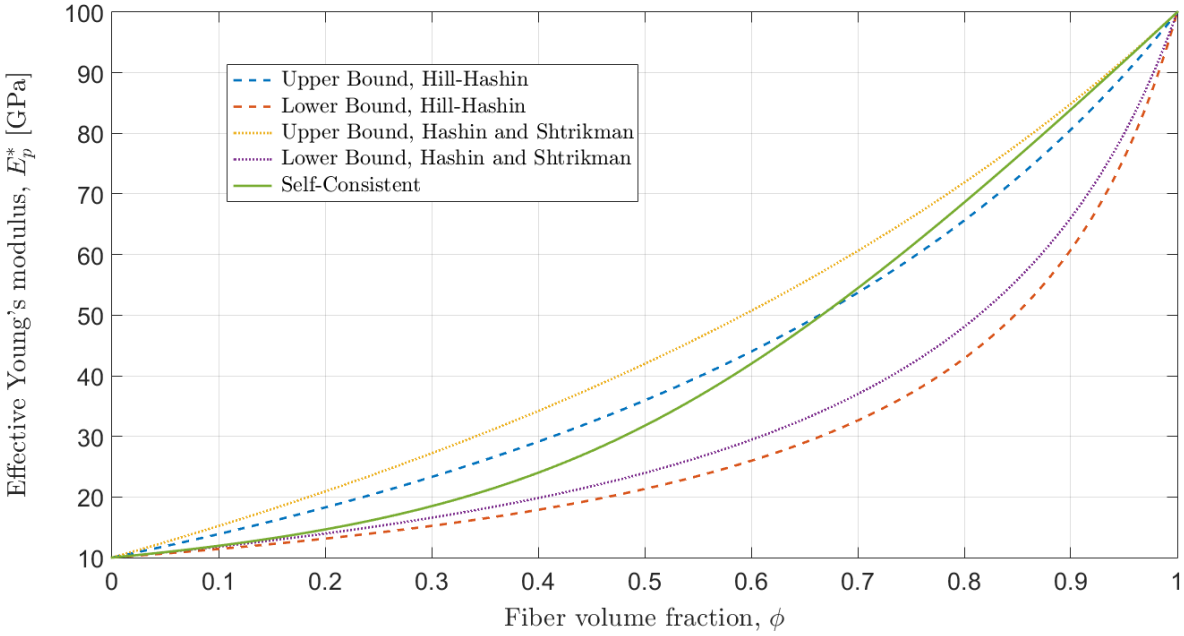

Figure 5.7: Representation of the *Self-Consistent* model and comparison with the *Hill-Hashin* and the *Hashin* and *Shtrikman* bounds. Both cases have $E_f = 100$ GPa, $E_m = 10$ GPa and $\nu_m = \nu_f = 0.3$.

5.2.5 Mori-Tanaka Methods

It is one of the most extensively used models to predict the effective elasticity tensor of heterogeneous materials and was originally proposed in Mori and Tanaka (1973). It was formulated under both traction and displacement - prescribed boundary conditions, and in Benveniste (1987) it was proved that the effective moduli under both conditions is the same, i.e. there is no duality gap, common to these types of boundaries.

The key difference in this method is the assumption that the average strain in an inclusion, $\boldsymbol{\varepsilon}_c$, (e.g. fiber) embedded in an all matrix material is related with the average strain in the matrix, $\boldsymbol{\varepsilon}_m$, by a fourth order tensor, $\tilde{\mathbf{A}}_c$,

$$\boldsymbol{\varepsilon}_c = \tilde{\mathbf{A}}_c : \boldsymbol{\varepsilon}_m, \tag{5.59}$$

where $\tilde{\mathbf{A}}_c$ is the strain concentration factor tensor given by:

$$\tilde{\mathbf{A}}_c = \left[\tilde{\mathbf{L}}^* + \mathbf{L}_c\right]^{-1} : \left[\tilde{\mathbf{L}}^* + \mathbf{L}_m\right], \tag{5.60}$$

and $\mathbf{L}_m$, $\mathbf{L}_c$ are the elasticity tensors for both matrix and inclusion, respectively and $\tilde{\mathbf{L}}^*$ is denoted by:

$$\tilde{\mathbf{L}}^* = \mathbf{L}_m : \left(\mathbb{S}^{-1} - \mathsf{I}\right), \tag{5.61}$$

hence, the constitutive relations for both phases can be defined as,

$$\boldsymbol{\sigma}_m = \mathbf{L}_m : \boldsymbol{\varepsilon}_m \tag{5.62a}$$

$$\boldsymbol{\sigma}_c = \mathbf{L}_c : \boldsymbol{\varepsilon}_c = \mathbf{L}_c : \tilde{\mathbf{A}}_c : (\mathbf{L}_m)^{-1} : \boldsymbol{\sigma}_m. \tag{5.62b}$$

It is shown in Weng (1984) that if one assumes an isotropic and elastic matrix and isotropic and elastic spherical inclusions, the effective properties of the composite material can be defined as:

$$K^* = K_m \left[1 + \frac{\phi_c \left(\frac{K_c}{K_m} - 1\right)}{1 + \alpha(1-\phi_c)\left(\frac{K_c}{K_m} - 1\right)}\right], \tag{5.63a}$$

$$G^* = G_m \left[1 + \frac{\phi_c \left(\frac{G_c}{G_m} - 1\right)}{1 + \beta(1-\phi_c)\left(\frac{G_c}{G_m} - 1\right)}\right], \tag{5.63b}$$

where,

$$\beta = \frac{2(4-5\nu_m)}{15(1-\nu_m)}, \tag{5.64a}$$

$$\alpha = \frac{1+\nu_m}{3(1-\nu_m)}, \tag{5.64b}$$

$$\nu_m = \frac{3K_m - 2G_m}{6K_m + 2G_m}. \tag{5.64c}$$

and ν_m is the Poisson's ratio of the matrix phase.

Expressions (5.63) in combination with Equation (5.57) were used to compute the effective Young's modulus given by the *Mori-Tanaka* model. Its representation and comparison with the *Hashin* and *Shtrikman* and the *Hill-Hashin* bounds is presented in Figure 5.8. It is noteworthy to mention that the *Mori-Tanaka* model is enclosed by the *Hill-Hashin* bounds, meaning that the effective plane strain Young's modulus, E_p^*, can be estimated by this model. Regarding the *Hashin* and *Shtrikman* boundaries, the *Mori-Tanaka* model is coincident with its lower boundary. In Section 5.2.3, it is mentioned that Expression (5.42a) is the exact result for the bulk modulus of a certain composite material that has a matrix of phase 'one' material and spherical inclusions of phase 'two' material distributed in a particular way. This expression of the *Mori-Tanaka* model was obtained under the assumption of spherical inclusions, and so, it is normal that both of them coincide, as it is mentioned in Hashin (1962) and Weng (1984). In Appendix C, after some algebraic modifications, it has been proved that Equations (5.63) are equal to Equation (5.42a) and (5.43a).

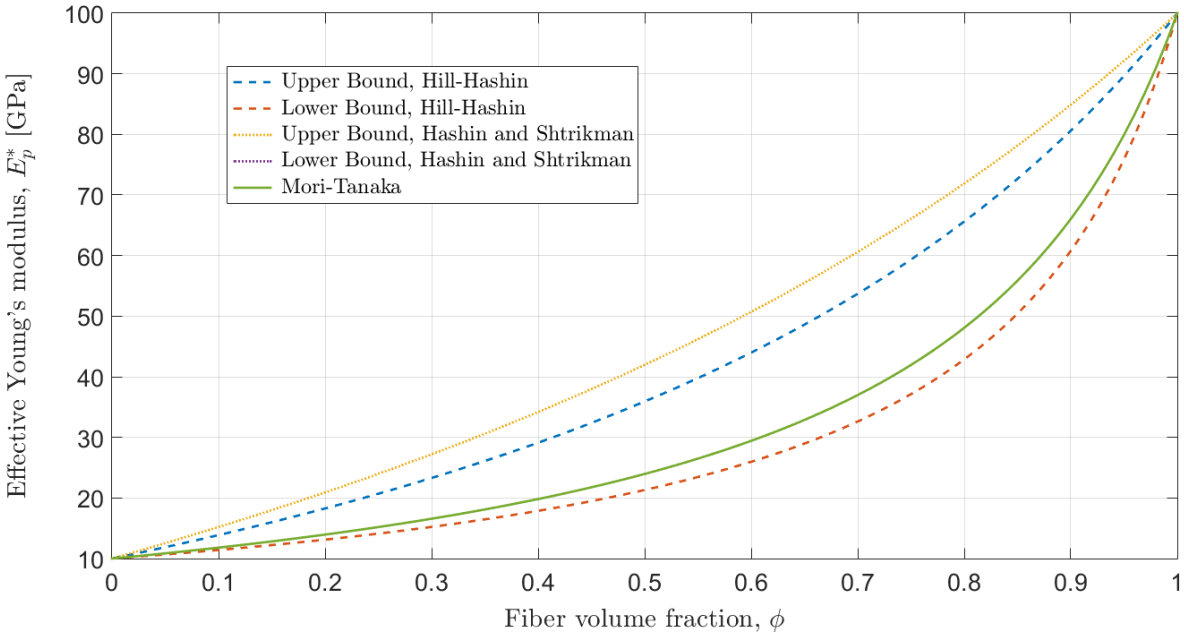

Figure 5.8: Representation of the *Mori-Tanaka* model and comparison with the *Hill-Hashin* and the *Hashin* and *Shtrikman* bounds. Both cases have $E_f = 100$ GPa, $E_m = 10$ GPa and $\nu_m = \nu_f = 0.3$.

5.2.6 Combined Self-Consistent and Mori-Tanaka Approach

Both methods relate to two schemes that may be considered as two limits of the effective properties, since they are based on different concepts. The *Mori-Tanaka* method, though it considers the disturbance in the matrix due to the inclusions, uses the properties of the matrix before any inclusion is added to calculate the effective properties of the composite and, in the conventional *Self-Consistent* method, one considers the matrix properties after the inclusions are added, as a fictitious homogeneous matrix. Therefore, in Peng et al. (2009) a new method that combines both was formulated to better evaluate the effective properties of a composite material.

Consider an RVE with a matrix material and particle inclusions with volume fraction ϕ_c, where the inclusions are considered as spheres with the same size and are randomly distributed. In the next step, these inclusions are separated into two groups:

- Group I - Contains particle inclusions with a volume fraction of $\left(1-\frac{1}{n}\right)\phi_c$ over the RVE;

- Group II - Contains particle inclusions with a volume fraction of $\frac{c}{n}$ over the RVE,

where $n \geq 1$. The combined approach states that the particle inclusions in Group I have already been embedded in the original matrix to form a fictitious matrix and that the elastic properties of this one are obtained with the *Self-Consistent* scheme. Later, the particles of the Group II are further distributed in this fictitious matrix to create the composite material, and the effective elastic properties of this later one are obtained with the *Mori-Tanaka* scheme. The number of inclusions in Group II should be large enough to meet the requirements of the *Mori-Tanaka* method. As it was demonstrated in Peng et al. (2009), Figure 5.9 illustrates the whole process in a visual way.

It can be noticed that if $n = 1$ this combined method is equal to the *Mori-Tanaka* estimate and that if $n \to \infty$ the combined method refers to the *Self-Consistent* scheme (Figure 5.10b).

Briefly, assuming that the volume of the RVE is V_{RVE}, the volume of the original matrix is given by:

$$V_m = (1-\phi_c)V_{RVE}, \tag{5.65}$$

and the volume of particle inclusions in Group I is,

$$V_{c_I} = \left[\left(1-\frac{1}{n}\right)\phi_c\right]V_{RVE}, \tag{5.66}$$

thus, the volume of fictitious matrix, $\hat{V}_m$, and the equivalent volume fraction of the particle

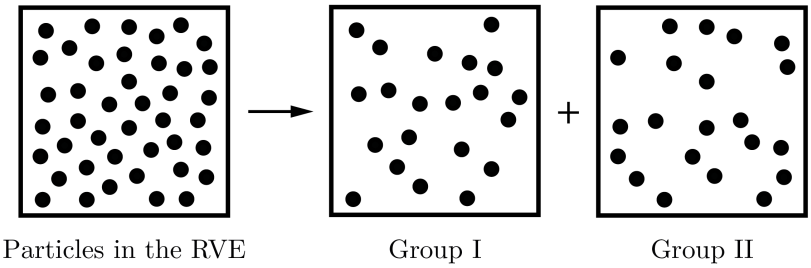

(a) Particles in the original RVE are distributed into Group I and II.

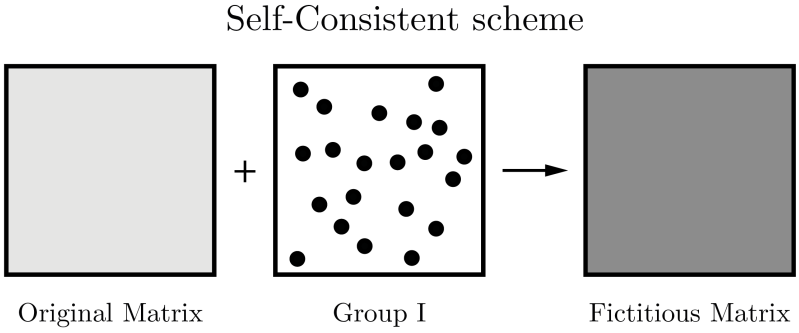

(b) Fictitious matrix formed by the original matrix and the particles of Group I.

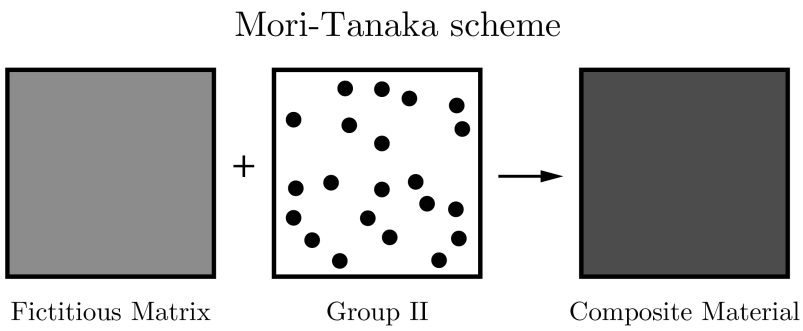

(c) Composite material formed by the fictitious matrix and the particles of Group II.

Figure 5.9: Schematic view of the combined self-consistent and Mori-Tanaka approach.

inclusions in the fictitious matrix, $\hat{\phi}_c$, are denoted as:

$$\hat{V}_m = V_m + \left[\left(1 - \frac{1}{n}\right)\phi_c\right] V_{RVE}, \tag{5.67a}$$

$$\hat{\phi}_c = \frac{n-1}{n-\phi_c}\phi_c. \tag{5.67b}$$

The elasticity tensor of the fictitious matrix, $\hat{\mathbf{L}}_m$, is then determined with the Expression (5.53b) if ϕ_c is replaced by $\hat{\phi}_c$, and this matrix is the one that it is used in the *Mori-Tanaka* model.

Assuming, again, isotropic spherical particle inclusions and isotropic elastic fictitious matrix,

one can write explicit expressions for the bulk and shear moduli,

$$K^* = \hat{K}_m \left[1 + \frac{\frac{\phi_c}{n}\left(\frac{K_c}{\hat{K}_m} - 1\right)}{1 + \alpha\left(1 - \frac{\phi_c}{n}\right)\left(\frac{K_c}{\hat{K}_m} - 1\right)} \right], \tag{5.68a}$$

$$G^* = \hat{G}_m \left[1 + \frac{\frac{\phi_c}{n}\left(\frac{G_c}{\hat{G}_m} - 1\right)}{1 + \beta\left(1 - \frac{\phi_c}{n}\right)\left(\frac{G_c}{\hat{G}_m} - 1\right)} \right], \tag{5.68b}$$

where the effective elastic properties of the fictitious matrix are defined by the *Self-Consistent* method,

$$\frac{1}{\hat{K}_m} = \frac{1}{K_m} + \frac{\hat{\phi}_c\left(1 - \frac{K_c}{K_m}\right)}{\hat{K}_m + \frac{1+\hat{\nu}_m}{3(1-\hat{\nu}_m)}(K_c - \hat{K}_m)}, \tag{5.69a}$$

$$\frac{1}{\hat{G}_m} = \frac{1}{G_m} + \frac{\hat{\phi}_c\left(1 - \frac{G_c}{G_m}\right)}{\hat{G}_m + \frac{2(4-5\hat{\nu}_m)}{15(1-\hat{\nu}_m)}(G_c - \hat{G}_m)}, \tag{5.69b}$$

and,

$$\beta = \frac{2(4-5\hat{\nu}_m)}{15(1-\hat{\nu}_m)}, \tag{5.70a}$$

$$\alpha = \frac{1+\hat{\nu}_m}{3(1-\hat{\nu}_m)}, \tag{5.70b}$$

$$\hat{\nu}_m = \frac{3\hat{K}_m - 2\hat{G}_m}{6\hat{K}_m + 2\hat{G}_m}. \tag{5.70c}$$

where $\hat{\nu}_m$ is the Poisson's ratio of the fictitious matrix.

In Figure 5.10a the representation of the combined method is displayed and it can be noticed that the parameter n has a major role in the results (Figure 5.10b). The *Mori-Tanaka* and the *Self-Consistent* method serve as the lower and upper boundaries, respectively.

5.3 Numerical Methods

The aforementioned methods only take into consideration the properties of the phases that constitute the composite material and the phase volume fractions but the effective elastic properties also depend on the geometrical morphology of the microstructure. As it was demonstrated in

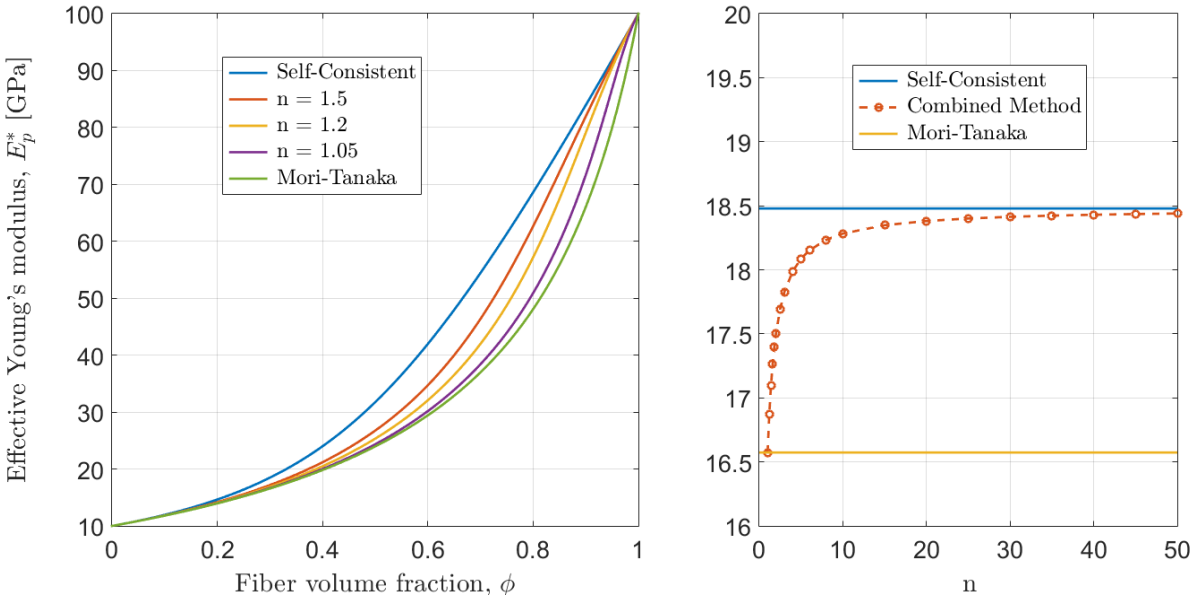

(a) Comparison with the *Self-Consistent* and *Mori-Tanaka* models.

(b) Dependency of E^* regarding the parameter n. In this case, $\phi_c = 0.3$.

Figure 5.10: Representation of the combined *Self-Consistent* and *Mori-Tanaka* approach. In this example, $E_f = 100$ GPa, $E_m = 10$ GPa and $\nu_m = \nu_f = 0.3$.

Chapter 4, using an image of the RVE, which models the microstructure of the material, it is possible to create a finite element mesh that adjusts to the geometry of the singularities. With this, one can perform a *Finite Element Analysis* to obtain the effective elastic properties of the material. Imposing the deformation gradient and the boundary conditions, the program used (MSP) solves the micro-scale problem under the hypothesis of large deformations. As a result, the incremental deformation gradient and the homogenized first Piola-Kirchhoff are obtained for each increment.

As mentioned in Section 2.6.3, the time domain of the problem is discretized to be able to solve problems that are dependent of the deformation history. The main objective of this work is to find the effective elastic properties of the composite material that are representative of the elastic domain and, as shown in the Figure 5.11. Usually in this domain, the stress is a linear function of the strain. Therefore, theoretically, any force increment that stresses the material inside this domain should give the same effective elastic properties (shown in Section 5.4), and so, in order to get the results in a faster way, the values obtained in the first increment are the ones that will be used.

5.3.1 Phase Material Properties

The materials contained in the RVE are considered to be are isotropic and defined through the Young's modulus and the Poisson's ratio. During the digital image analysis, a material is attributed to each pixel. Then, the skeleton of the finite element mesh is created and, in order

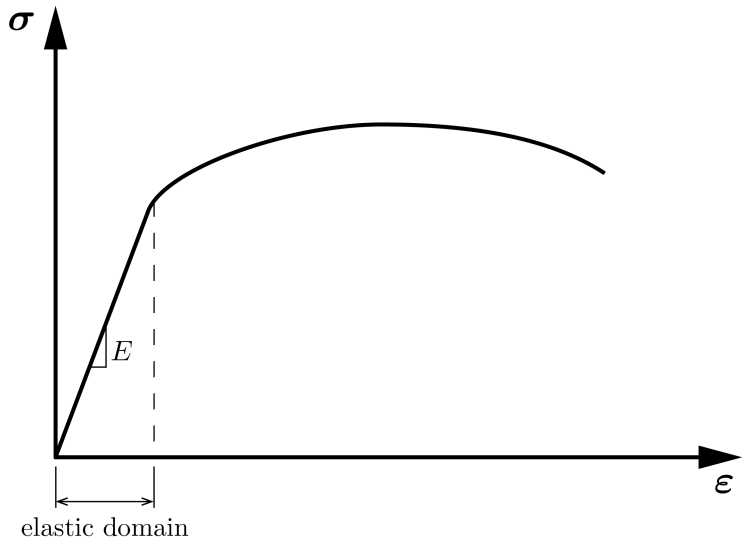

Figure 5.11: Stress - strain curve - Representation of the elastic domain.

to increase the homogeneity of each element, several algorithms are applied to it[1]. When the final result is obtained, the skeleton gives rise to the finite element mesh where each element has a material and a type of element assigned to it.

For each combination of element type and material, a new group is created. Therefore, an element is characterized by three things: its identification number, the group number (that has the information about the material and element type) and the identification number of the nodes that define it. Each identification node is related with its Cartesian coordinates. This data is required by MSP to run the analysis.

5.3.2 Determination of the Homogenized Elastic Properties

To determine the elastic properties of the composite material, the homogenized stress tensor and strain tensor are used. These are obtained through the MSP program that solves the microscale problem, but since the stress tensor obtained is the first Piola-Kirchhoff, this must be converted to the Cauchy stress tensor through the following equation:

$$\boldsymbol{\sigma} = \frac{1}{J}\boldsymbol{P}\boldsymbol{F}^T. \tag{5.71}$$

where $J = \det\boldsymbol{F}$.

In the case of a RVE in 3 dimensions, and for the case of an overall orthotropic composite material, as mentioned in the Section 5.1.1, the constitutive relation is given by the following

[1]Mentioned in Chapter 4.

expression,

$$\begin{Bmatrix} \sigma_{11} \\ \sigma_{22} \\ \sigma_{33} \\ \sigma_{23} \\ \sigma_{13} \\ \sigma_{12} \end{Bmatrix} = \begin{bmatrix} C_{11} & C_{12} & C_{13} & 0 & 0 & 0 \\ C_{12} & C_{22} & C_{23} & 0 & 0 & 0 \\ C_{13} & C_{23} & C_{33} & 0 & 0 & 0 \\ 0 & 0 & 0 & C_{44} & 0 & 0 \\ 0 & 0 & 0 & 0 & C_{55} & 0 \\ 0 & 0 & 0 & 0 & 0 & C_{66} \end{bmatrix} \begin{Bmatrix} \varepsilon_{11} \\ \varepsilon_{22} \\ \varepsilon_{33} \\ \gamma_{23} \\ \gamma_{13} \\ \gamma_{12} \end{Bmatrix}, \tag{5.72}$$

where $\gamma_{23} = 2\varepsilon_{23},\ \gamma_{13} = 2\varepsilon_{13},\ \gamma_{12} = 2\varepsilon_{12}$.

As it can be seen, there are 9 coefficients to determine. To solve this, one should apply a deformation gradient that strains the RVE in particular ways. If only one component of the strain tensor, $\boldsymbol{\varepsilon}$, is non-zero, the correspondent column of the stiffness matrix is obtained. As an example, if $\varepsilon_{11} \neq 0$ and all the other components are null, the following is true:

$$\sigma ii = C_{1i}\ \varepsilon 11, \quad i = 1, 2, 3. \tag{5.73}$$

Once all the elastic coefficients are acquired, the elastic properties can be calculated through Expressions (5.14) and (5.16).

The overall composite material can be isotropic or transversely isotropic but, before the analysis is done, the material is considered as orthotropic to be able to consider the most general case and, if the elastic constants are equal, the particular cases of symmetry can be identified.

This methodology can be used, not only to determine the elastic constants of a material with all kind of inclusions, but also for materials that can contain voids in the microstructure.

2D Plane Strain

Rewriting Expression (5.21), for the case of a two dimensional plane strain problem, the constitutive relation is given by:

$$\begin{Bmatrix} \sigma_{11} \\ \sigma_{22} \\ \sigma_{33} \\ \sigma_{12} \end{Bmatrix} = \begin{bmatrix} C_{11} & C_{12} & C_{13} & 0 \\ C_{12} & C_{22} & C_{23} & 0 \\ C_{13} & C_{23} & C_{33} & 0 \\ 0 & 0 & 0 & C_{44} \end{bmatrix} \begin{Bmatrix} \varepsilon_{11} \\ \varepsilon_{22} \\ 0 \\ \gamma_{12} \end{Bmatrix}, \tag{5.74}$$

and the same methodology used in the 3D case is applied. It is important to note that it is not possible to obtain the third column of the stiffness matrix and so the coefficient C_{33} is not achievable. The coefficients C_{13} and C_{23} are obtained through the first and second column steps.

The elastic constants are given by Expressions (5.14) and (5.16) but, without the value of C_{33}, Θ cannot be calculated and, consequently, the elastic constants cannot be obtained. In order to solve this problem, the homogenized axial Young's modulus is calculated by the *Voigt*

model,

$$E_3^* = \phi_f E_f + (1 - \phi_f) E_m, \tag{5.75}$$

where ϕ_f is the fiber volume fraction and E_m and E_f are the matrix and fiber Young's modulus, respectively. After this, Θ and, consequently, C_{33} can be determined.

Deformation Gradient

To be able to determine each column of the stiffness matrix at a certain time, different types of strains must be enforced to the RVE, ensuring that only one component of the strain tensor, $\boldsymbol{\varepsilon}$, is different from zero. Although the MSP program has for input the deformation gradient, $\boldsymbol{F}$, it is possible to connect both tensors. The procedure hereafter presented is based on the procedure used in Carvalho et al. (2015)

In order to relate both concepts, one must find the deformation gradient that applies a single direction longitudinal or a shear stretch on the RVE. To ensure an easy convergence of the *Newton-Raphson* method, the number of increments chosen will be around 10000, and, since the increment of interest is the first, one can consider the strain of the RVE as a infinitesimal strain, thus it is possible to assume that the *Hencky* tensor, $\boldsymbol{E}$, can be approximated by the infinitesimal strain tensor $\boldsymbol{\varepsilon}$,

$$\boldsymbol{E} = \boldsymbol{\varepsilon} \equiv \frac{1}{2}\left[\nabla_X \boldsymbol{u} + (\nabla_X \boldsymbol{u})^T\right]. \tag{5.76}$$

and, on the other hand,

$$\boldsymbol{E} = \ln[\boldsymbol{U}] \equiv \ln\left[\sqrt{\boldsymbol{F}^T \boldsymbol{F}}\right] = \frac{1}{2}\ln \boldsymbol{F}^T \boldsymbol{F}. \tag{5.77}$$

where $\ln[\cdot]$ denotes the tensor logarithm of $[\cdot]$. With this expression, it is possible to relate both the strain tensor and the deformation tensor. Due to the characteristics of this relation, the spectral decomposition of the *Hencky* tensor [2] has to be taken into consideration,

$$\boldsymbol{E} = \sum_{i=1}^{3} \lambda_i^E \boldsymbol{l}_i^E \otimes \boldsymbol{l}_i^E, \tag{5.78}$$

in which λ_i^E are the eigenvalues and $\boldsymbol{l}_i^E$ are the eigenvectors of $\boldsymbol{E}$. The eigenvalues, in the case of three dimensions and for a generic matrix $\boldsymbol{A}$ with real components, can be calculated through the following equation:

$$\lambda_i^3 - I_1 \lambda_i^2 + I_2 \lambda_i - I_3 = \det(\boldsymbol{A} - \lambda_i \boldsymbol{I}) = 0, \tag{5.79}$$

[2] $\boldsymbol{E}$ is a symmetric tensor, thus admits the spectral decomposition.

where I_i are the invariants and are defined by:

$$I_1 = \mathrm{tr}\boldsymbol{A}, \tag{5.80a}$$

$$I_2 = \frac{1}{2}\left[(\mathrm{tr}\boldsymbol{A})^2 - \mathrm{tr}\boldsymbol{A}^2\right], \tag{5.80b}$$

$$I_3 = \det\boldsymbol{A}. \tag{5.80c}$$

Furthermore, the eigenvectors of this matrix $\boldsymbol{A}$ are calculated by:

$$(\boldsymbol{A} - \lambda_i \boldsymbol{I})\,\boldsymbol{l}_i = \boldsymbol{0}. \tag{5.81}$$

From the definition of the *Hencky* tensor, it is possible to find the following expression:

$$\lambda_i^U = \exp(\lambda_i^E), \tag{5.82}$$

where λ_i^U are the eigenvalues of the right stretch tensor $\boldsymbol{U}$. Furthermore and taking into account,

$$\boldsymbol{U} = \boldsymbol{F}^T\boldsymbol{F} \tag{5.83}$$

it is possible to find the eigenvalues of $\boldsymbol{F}$, λ_i^F, relating them with the previous ones,

$$\lambda_i^F \equiv \sqrt{\lambda_i^U}. \tag{5.84}$$

At the end, the main objective can be accomplished and the deformation gradient, $\boldsymbol{F}$, is defined by its own eigenvalues, λ_i^F, and by the eigenvectors of the imposed *Hencky* tensor, $\boldsymbol{l}_i^E$,

$$\boldsymbol{F} = [\Psi]\begin{bmatrix} \lambda_1^F & 0 & 0 \\ 0 & \lambda_2^F & 0 \\ 0 & 0 & \lambda_3^F \end{bmatrix}[\Psi]^T, \tag{5.85}$$

where $[\Psi]$ is a matrix in where each column i is the normalized vector of the eigenvector $\boldsymbol{l}_i^E$.

In Table 5.1 one can find the deformation gradients that enable this methodology for a three dimensional problem. For a two dimensional plane strain problem, the deformation gradients are presented in Table 5.2.

5.4 Estimate the Homogenized Elastic Properties Based on a Micrograph Information

Since in Chapter 4, the procedure to create a finite element mesh that correctly models the microstructure of a material has been explained and, in Section 5.3, the method to determine the homogenized elastic properties of a material, based on a finite element multi-scale model is also described, the overall strategy is further detailed with an example.

Table 5.1: Deformation gradients imposed to stretch the RVE in particular directions for a three dimensional problem.

$\boldsymbol{\varepsilon}$	$\boldsymbol{F}$
$\begin{bmatrix} 1 & 0 & 0 \\ 0 & 0 & 0 \\ 0 & 0 & 0 \end{bmatrix}$	$\begin{bmatrix} 2.718 & 0 & 0 \\ 0 & 1 & 0 \\ 0 & 0 & 1 \end{bmatrix}$
$\begin{bmatrix} 0 & 0 & 0 \\ 0 & 1 & 0 \\ 0 & 0 & 0 \end{bmatrix}$	$\begin{bmatrix} 1 & 0 & 0 \\ 0 & 2.718 & 0 \\ 0 & 0 & 1 \end{bmatrix}$
$\begin{bmatrix} 0 & 0 & 0 \\ 0 & 0 & 0 \\ 0 & 0 & 1 \end{bmatrix}$	$\begin{bmatrix} 1 & 0 & 0 \\ 0 & 1 & 0 \\ 0 & 0 & 2.718 \end{bmatrix}$
$\begin{bmatrix} 0 & 0 & 0 \\ 0 & 0 & 1 \\ 0 & 1 & 0 \end{bmatrix}$	$\begin{bmatrix} 1 & 0 & 0 \\ 0 & 1.543 & 1.175 \\ 0 & 1.175 & 1.543 \end{bmatrix}$
$\begin{bmatrix} 0 & 0 & 1 \\ 0 & 0 & 0 \\ 1 & 0 & 0 \end{bmatrix}$	$\begin{bmatrix} 1.543 & 0 & 1.175 \\ 0 & 1 & 0 \\ 1.175 & 0 & 1.543 \end{bmatrix}$
$\begin{bmatrix} 0 & 1 & 0 \\ 1 & 0 & 0 \\ 0 & 0 & 0 \end{bmatrix}$	$\begin{bmatrix} 1.543 & 1.175 & 0 \\ 1.175 & 1.543 & 0 \\ 0 & 0 & 1 \end{bmatrix}$

Table 5.2: Deformation gradients imposed to stretch the RVE in particular directions for a two dimensional problem.

$\boldsymbol{\varepsilon}$	$\boldsymbol{F}$
$\begin{bmatrix} 1 & 0 \\ 0 & 0 \end{bmatrix}$	$\begin{bmatrix} 2.718 & 0 \\ 0 & 1 \end{bmatrix}$
$\begin{bmatrix} 0 & 0 \\ 0 & 1 \end{bmatrix}$	$\begin{bmatrix} 1 & 0 \\ 0 & 2.718 \end{bmatrix}$
$\begin{bmatrix} 0 & 1 \\ 1 & 0 \end{bmatrix}$	$\begin{bmatrix} 1.543 & 1.175 \\ 1.175 & 1.543 \end{bmatrix}$

In Figure 4.7, an initial microstructure is presented and the finite element mesh created from it is illustrated in Figure 4.18. For an easier perception of these figures, the initial micrograph and the final result are displayed in Figure 5.12.

As addressed in Section 4.2.5, the mesh information is saved in OOF2 using the format *Abaqus*. A MATLAB® script was developed to extract the mesh data from this file and to rewrite that information with the data needed to run MSP (e.g. deformation gradient, prescribed boundary condition, number of increments). During this process the area of the each element

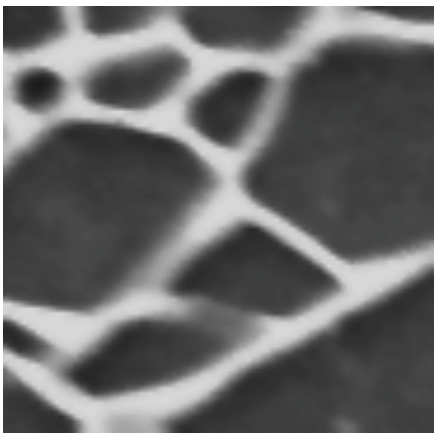

(a) Initial micrograph (Figure 4.7).

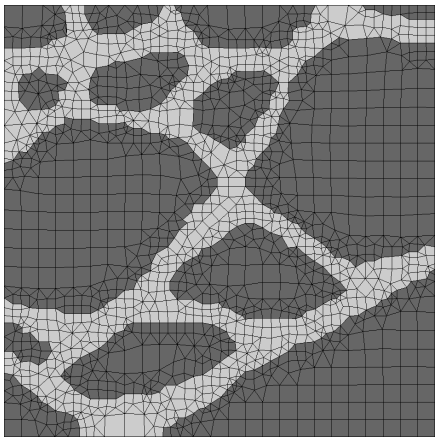

(b) Finite element mesh based on Figure 5.12a.

Figure 5.12: DIB microstructure recognition demonstrated in Section 4.3.

is computed to determine the volume fraction of each constituent.

In this case, the effective elastic properties are determined with the *Mortar Periodic* boundary condition. In order to accomplish it, the deformation gradients presented in Table 5.2 are applied to the RVE (Figure 5.12b). After completing the finite element analysis, the MSP returns the corresponding homogenized first Piola-Kirchhoff stress tensor and the incremental deformation gradient for each case.

Using the following equation, the Cauchy stress tensor is computed:

$$\boldsymbol{\sigma}_i = \frac{1}{\det \boldsymbol{F}_i} \boldsymbol{P}_i \boldsymbol{F}_i^T, \tag{5.86}$$

where i denotes the load increment that is applied to the RVE. The infinitesimal strain tensor is calculated with the next expression:

$$\boldsymbol{\varepsilon}_i \approx \boldsymbol{E}_i = \frac{1}{2} \ln \boldsymbol{F}_i^T \boldsymbol{F}_i. \tag{5.87}$$

Again, another MATLAB® script (described in Appendix D) was created to determine these tensors and the coefficients of the effective constitutive tensor, $\mathbf{C}^*$, presented in Equation (5.74). Finally, using the equations described in (5.14), (5.16) and (5.75), the effective elastic properties are obtained for a two dimensional plane strain problem.

Code Validation

In order to validate this MATLAB® script, the same elastic properties ($E = 100$ GPa and $\nu = 0.3$) are assigned to both phases, generating a RVE that resembles a homogeneous material. As expected and presented in Table 5.3, the overall elastic properties obtained by this procedure are equal to those assigned to each constituent, where, in this case, G_{12} corresponds to the theoretical $G = 38.4615$ GPa given by Equation (5.30).

Table 5.3: Homogenized elastic properties of the material represented in Figure 5.12 when both constituents have the same elastic properties.

E_1^*	E_2^*	E_3^*	G_{12}^*	Unit
99.991	99.991	100.000	38.462	GPa

ν_{12}^*	ν_{21}^*	ν_{13}^*	ν_{31}^*	ν_{23}^*	ν_{32}^*	Unit
0.3000	0.3000	0.3000	0.3000	0.3000	0.3000	-

Increment Load Validation

To prove that the information obtained from the first load increment is enough to determine with accuracy the effective elastic properties of an heterogeneous material[3], these properties are computed for different load increments (only for the *Mortar Periodic* boundary condition) and the results are presented in Table 5.4. The volume fraction of the *Black* material is 69.89%.

Table 5.4: Homogenized elastic properties of the material represented in Figure 5.12 for different load increments. The elastic properties of each constituent are presented in Table 4.3.

Increment	E_1^*	E_2^*	E_3^*	G_{12}^*	2-norm of $\mathbf{C}^*$	**Unit**
1	42.637	36.537	72.905	15.188	106.264	GPa
5	42.601	36.506	72.905	15.188	106.203	GPa
	0.084	0.086	0.000	0.001	0.057	%
10	42.556	36.466	72.905	15.188	106.127	GPa
	0.189	0.194	0.000	0.002	0.129	%

Increment	ν_{12}^*	ν_{21}^*	ν_{13}^*	ν_{31}^*	ν_{23}^*	ν_{32}^*	**Unit**
1	0.3401	0.2914	0.1754	0.3000	0.1503	0.3000	-
5	0.3401	0.2914	0.1753	0.3000	0.1502	0.3000	-
	0.000	0.000	0.057	0.000	0.067	0.000	%
10	0.3400	0.2914	0.1751	0.3000	0.1501	0.3000	-
	0.029	0.000	0.171	0.000	0.133	0.000	%

The scalars E_1^* and E_2^* represent the effective in-plane Young's moduli and E_3^* the effective out-of-plane Young's modulus. The second norm of the constitutive tensor, $\mathbf{C}^*$, is a scalar value that aims to characterize the whole tensor. The numbers in the second row of increment 5 and 10 represent the relative error between the respective and the first increment. It can be noticed that the error is much smaller than 1%, thus, the first increment is the one used to estimate the effective elastic properties.

However, currently there is no way to know if these results are correct. As mentioned in Section 3.1, the size of the RVE is an important factor to take into account. It needs to be large

[3] As mentioned in the introduction of Section 5.3.

enough to be statistically representative of the material's microstructure and small enough to be easily analysed on a computational level. Figure 5.12 is clearly not big enough to correctly represent the microstruscture of the plasma-etched Si_3Na_4, since it only contains a low number of its singularities. To solve this problem, in Chapter 6, the study of the RVE size is presented.

5.5 Conclusions

The majority of the engineering structures are designed to withstand loads that do not stress the material outside the elastic domain and, due to the significant demand that composite materials have nowadays, it is important to be able to estimate the macroscopic elastic properties of materials, even when their microstructure is too complex.

Despite the existence of analytical methods that, resorting to the Eshelby tensor ($\mathbb{S}$), take into consideration the microstructure geometry, their limitations are exposed when the inclusions diverge from simple spherical or ellipsoidal shapes. For those cases, the Digital Image Based microstructure recognition technique presents a new method that, for any given microstructure, is able to correctly model the behaviour of a material at the microscopic level, hence, producing more accurate results than those obtained by the mathematical expressions given by analytical methods.

The procedure to estimate the elastic properties has been presented in this chapter and a simple validation of the code is performed. The use of the first load increment to obtain the effective elastic constants is also justified. It is then important to perform some parametric studies to improve each step of the process and to be certain that the obtained results are correct.

In the next chapter, these parametric studies are presented, such as the optimal RVE size and the finite element size that correctly model its behaviour.

Chapter 6

Parametric Studies on the Homogenized Elastic Properties

Due to high costs associated with the experimental procedures and given the fact that analytical methods are not sufficiently accurate to predict the homogenized elastic properties in complex conditions, the method presented in Chapters 4 and 5 offers a new and more accurate solution to obtain the homogenized properties, enabling the problem to be solved on a computational level while taking into account complex microstructure geometries.

In the case of a 3D RVE, the full stiffness tensor may be obtained through this procedure while, in the case of a 2D RVE, the out-of-plane Young's modulus must set *a priori*, due to the lower number of equations compared with the amount of unknown elasticity constants. However, in order to validate the results achieved by this method, the whole process used to generate the finite element mesh has to be analysed step by step.

First of all, parametric studies are made to define whether the obtained results are valid or not. This include a study on the RVE size to find the optimized value that correctly represents the microstructure and a study on the mesh size also needs to be performed, due to the use of the *Finite Element Method*. During this process, it is noteworthy to mention the influence of the image quality of the representative micrograph on the estimated effective elastic properties. Later, a comparison note between the results obtained and the analytical methods described in Section 5.2 is presented, more precisely with the *Mori-Tanaka* method and with the *Hashin-Hill* boundaries. The influence of the stiffness ratio between the fiber and matrix materials on the RVE size, is also analysed.

With these studies completed, the optimal RVE and correspondent mesh size are defined and the influence of the stiffness ratio on the homogenized elastic properties is determined in the case of a unidirectional fiber composite.

6.1 Studies to Determine the RVE Size

As mentioned in Chapter 3 and in Section 5.4, the size of the RVE that aims to model the microstructure of a material is an important factor when estimating its homogenized elastic properties.

In this section, the main objective is to find the minimum RVE size that is statistically representative of the microstructure. To study the influence of this parameter, a micrograph (Figure 6.1) of a metal matrix composite, whose matrix and fibers are respectively $NiAl_2$ and Cr, is analysed for different sizes of the RVE.

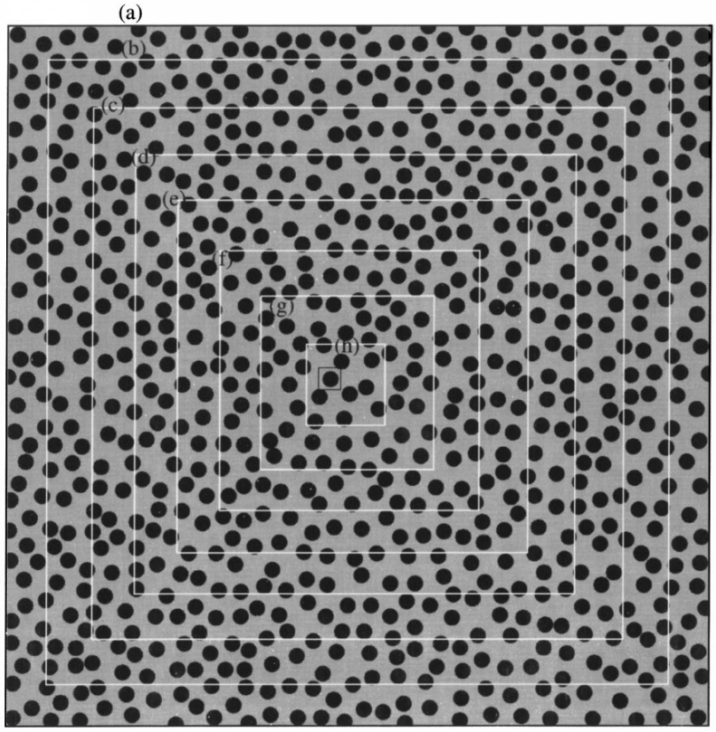

Figure 6.1: Micrograph of a composite material ($NiAl_2$-Cr) with different sizes of RVEs displayed (Terada et al., 2000): (a) 1024×1024 px; (b) 896×896 px; (c) 768×768 px; (d) 640×640 px; (e) 512×512 px; (f) 384×384 px; (g) 256×256 px; (h) 128×128 px. The smallest RVE in the middle with only one fiber has 32×32 px.

6.1.1 Image Treatment

Figure 6.1 does not contain enough quality or resolution, therefore, firstly an image treatment is necessary to improve the quality of the micrograph to later permit faster and better results with the image segmentation step.

Using Adobe Photoshop®, the white square lines that subdivide the whole micrograph in different RVEs are removed, the matrix part (lighter color) is coloured with white and the fibers are painted with black. After this color manipulation, it is easier to select the different pixel groups that belong to the matrix and fiber parts.

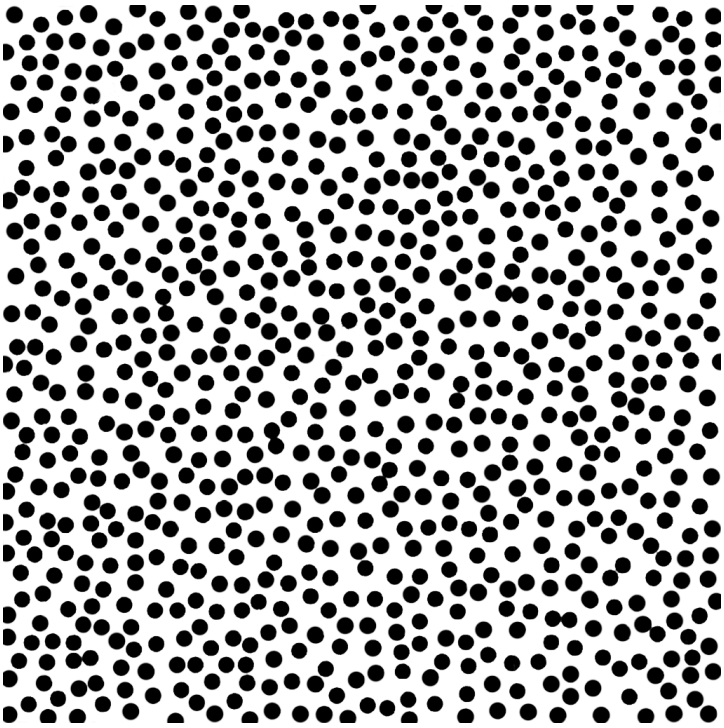

Figure 6.2: Image manipulation of Figure 6.1 to better define the material boundaries.

Considering the sub-divisions displayed in Figure 6.1, this newly treated micrograph illustrated in Figure 6.2 is divided into 8 RVEs of different sizes, presented in Figure 6.3. These RVEs are characterized by their pixel dimensions but, attributing a physical dimension to them, facilitates the process of automatically creating the first version of the skeleton using the automated script[1] of OOF2. In a first order Multi-Scale model, the precise size of the RVE is not important, only the relative size between the constituents and the RVE matter. Therefore, the conversion from pixel to physical dimensions is presented in Table 6.1. The value of 10×10 is random, but not too small to keep the $x-$ and $y-$coordinates admissible, avoiding the numerical errors which arises from extremely small numbers. The other dimensions correctly characterize the scale between RVEs.

Table 6.1: Conversion from pixel to physical dimensions.

Pixel	128×128	256×256	384×384	512×512
Physical	10×10	20×20	30×30	40×40

Pixel	640×640	768×768	896×896	1024×1024
Physical	50×50	60×60	70×70	80×80

Considering the smallest RVE (Figure 6.3a), the procedure to create the finite element mesh is further described. The same steps are followed to generate the meshes for the other RVEs.

[1] Mentioned in Section 4.2.4.

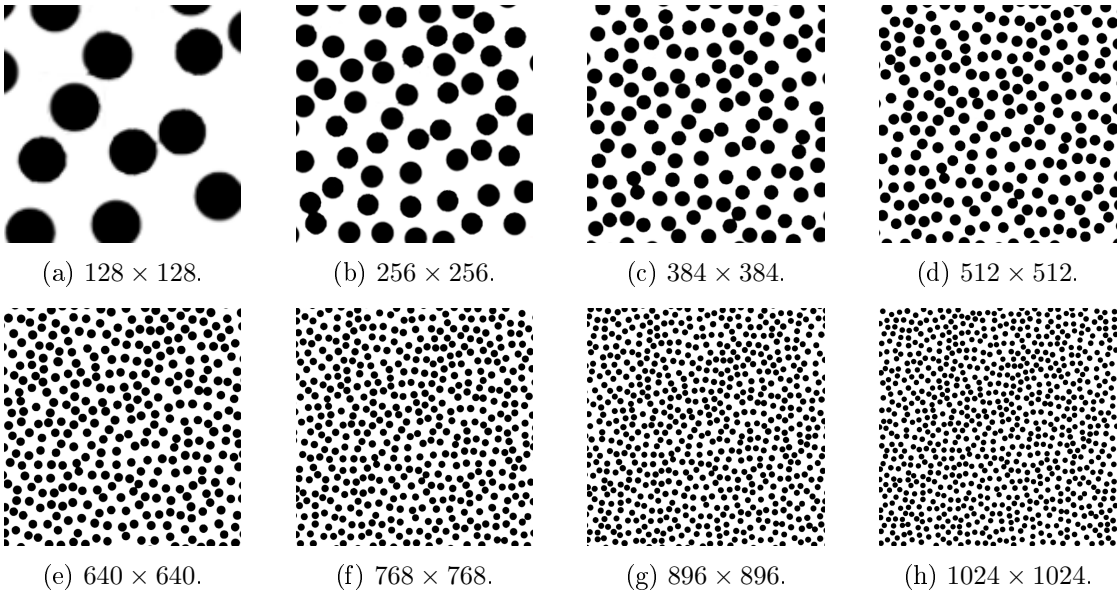

(a) 128×128. (b) 256×256. (c) 384×384. (d) 512×512.

(e) 640×640. (f) 768×768. (g) 896×896. (h) 1024×1024.

Figure 6.3: Subdivision of the whole micrograph and representation of the different RVEs oriented per pixel dimensions.

6.1.2 Image Segmentation

To better understand the concept of image segmentation, the full detailed process is explained in Section 4.2.2 and an example is given in Section 4.3.2.

The pixel selection is done with the *Color* tool of OOF2. The range difference is computed in gray scale values and *delta gray* $= 0.5$. The result is displayed in Figure 6.4 with the material image presented too.

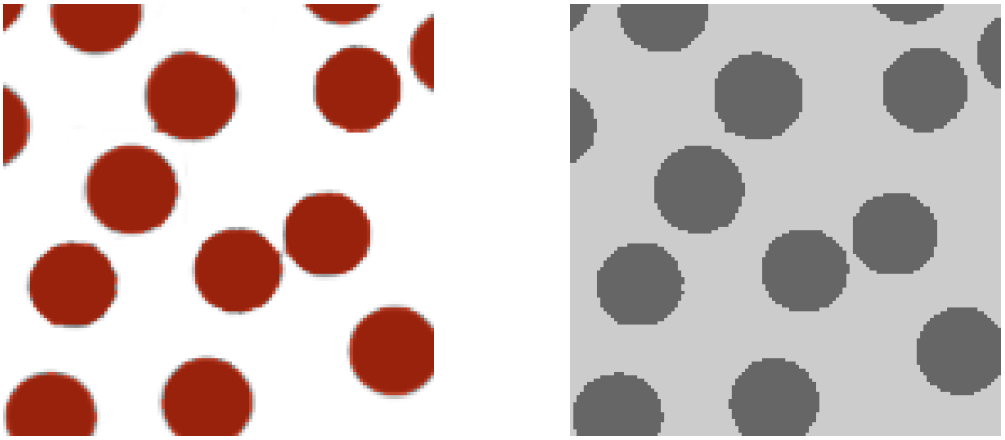

(a) Pixel selection. (b) Material image.

Figure 6.4: Image segmentation of the smallest RVE.

The elastic properties of each constituent are equal to the ones from Terada et al. (2000) and are presented in Table 6.2, where Fiber and Matrix correspond, respectively, to the darker and lighter constituent.

Table 6.2: Elastic properties assigned to each constituent of the RVE.

	Young's Modulus	**Poisson's Ratio**	**Color**
Fiber	100 GPa	0.3	0.8
Matrix	10 GPa	0.3	0.4

6.1.3 Studies to Determine the Mesh Size

As it is well known, while utilizing the *Finite Element Method*, the accuracy of the results is highly dependent on the mesh refinement. Hence, before presenting the results about the RVE size, a study to define the correct mesh size must be performed. During this analysis, only the *Mortar Periodic* boundary condition is utilized.

In the first place, the initial versions of the skeletons are created by the automated script of OOF2, therefore the following parameters[2] must be defined for each case: *maxscale*, *minscale* and *homogeneity threshold*. Later, each skeleton is improved utilizing the *Rationalize*, *Swap Edges*, *Split Quads*, *Merge Triangles*, *Smooth* and/or *Anneal* routines. There is not a correct way to create the perfect skeleton, meaning that these functions should be chosen according with the user's criteria of a well designed skeleton (finite element mesh) that correctly resembles the microstructure's geometry.

Table 6.3 presents the different parameters chosen to create the four different mesh versions, along with the final informations. The final versions are displayed in Figure 6.5.

Table 6.3: Parameters chosen to automatically create the initial skeleton version for each mesh of the 10×10 RVE and respective information. The *homogeneity threshold* is equal to 0.9 in all versions.

Mesh	**1**	**2**	**3**	**4**
Maxscale	0.5	0.3	0.2	0.1
Minscale	0.5	0.3	0.2	0.1
Elements	534	1610	2909	10766
Quadrilateral	341	863	2322	9812
Triangular	193	747	587	954
Nodes	483	1310	2720	10491
Homogeneity	0.967	0.973	0.991	0.996

Finally, the effective elastic properties obtained by each mesh are presented in Table 6.4. The smaller numbers with (%) unit are the relative difference between mesh versions. As it is noticed, from version 1 to 3, this difference is higher than 1% in the majority of the elastic properties but, the difference between version 3 and 4 is lower than 1% and, therefore, version 3 is considered to be refined enough to accurately estimate the effective elastic properties of the composite material.

[2] Addressed in Section 4.2.4

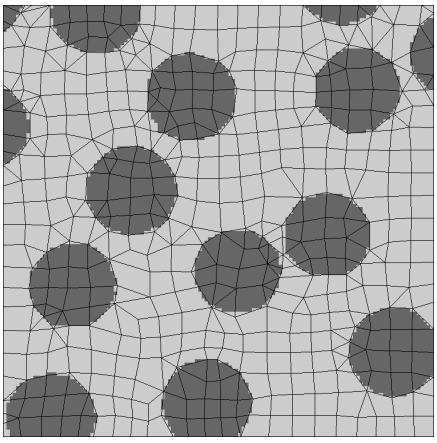

(a) Mesh 1.

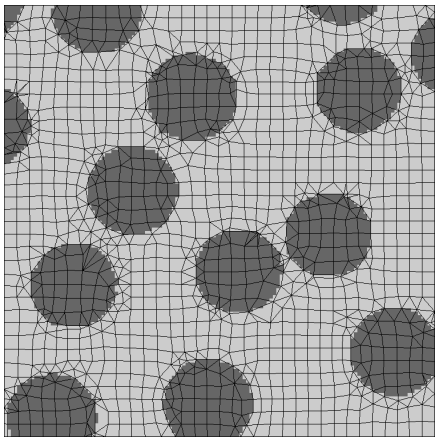

(b) Mesh 2.

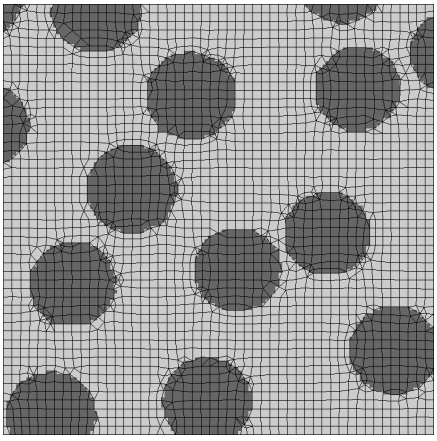

(c) Mesh 3.

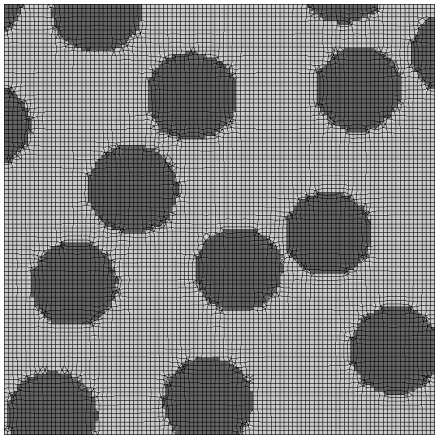

(d) Mesh 4.

Figure 6.5: Representation of the different meshes of the 10×10 RVE.

To be certain that this mesh size is still valid for larger RVEs, the same study is repeated for the 20×20 and 30×30 dimensions. The parameters used to automatically create the skeleton and the respective informations are presented in Table 6.5. Excluding the Poisson's ratio, the results are given in Table 6.6. It can be noticed that, regarding the 20×20 and the 30×30 RVEs, the difference from version 1 and 2 (more refined) is lower than 0.5%, thus, version 1 is the selected one for these cases. As the size of the RVE increases, the relative importance of each fiber decreases, hence, a more coarse mesh may be used to estimate the homogenized elastic properties. Summarizing,

$$\begin{aligned} &\textit{maxscale} = \textit{minscale} = 0.2, && \text{for the } 10 \times 10 \text{ RVE,} \\ &\textit{maxscale} = \textit{minscale} = 0.3, && \text{for RVEs equal and larger than } 20 \times 20. \end{aligned}$$

where the *homogeneity threshold* is equal to 0.9 in every case.

Before presenting the results about the RVE size, an analysis on the image quality of the RVE taken from Terada et al. (2000) is performed.

Table 6.4: Homogenized elastic properties for each mesh version of the 10×10 RVE.

Mesh	E_1^*	E_2^*	E_3^*	G_{12}^*	2-norm of $\mathbf{C}^*$	**Unit**
1	17.741	17.802	39.320	6.838	52.949	GPa
	2.330	1.900	0.050	2.365	0.392	%
2	17.327	17.463	39.340	6.676	52.741	GPa
	2.085	2.268	1.941	2.754	1.919	%
3	16.966	17.068	38.576	6.492	51.729	GPa
	0.740	0.729	0.354	0.509	0.490	%
4	17.092	17.192	38.713	6.525	51.983	GPa

Mesh	ν_{12}^*	ν_{21}^*	ν_{13}^*	ν_{31}^*	ν_{23}^*	ν_{32}^*	**Unit**
1	0.3477	0.3489	0.1354	0.3000	0.1358	0.3000	-
	2.243	2.694	2.437	0.000	1.915	0.000	%
2	0.3555	0.3583	0.1321	0.3000	0.1332	0.3000	-
	0.619	0.419	0.151	0.000	0.375	0.000	%
3	0.3577	0.3598	0.1319	0.3000	0.1327	0.3000	-
	0.196	0.195	0.379	0.000	0.377	0.000	%
4	0.3570	0.3591	0.1324	0.3000	0.1332	0.3000	-

Table 6.5: Parameters chosen to automatically create the initial skeleton version for each mesh of the 20×20 and 30×30 RVEs and respective information. The *homogeneity threshold* is 0.9 in every case.

RVE	**Mesh**	**Maxscale**	**Minscale**	**Elements**	**Nodes**	**Homogeneity**
$\mathbf{20 \times 20}$	**1**	0.3	0.3	5750	5046	0.987
	2	0.2	0.2	11865	10729	0.989
$\mathbf{30 \times 30}$	**1**	0.3	0.3	11867	10595	0.986
	2	0.2	0.2	26610	23998	0.989

Table 6.6: Homogenized elastic properties for each mesh version of the 20×20 and 30×30 RVEs.

RVE	**Mesh**	E_1^*	E_2^*	E_3^*	G_{12}^*	2-norm of $\mathbf{C}^*$	**Unit**
$\mathbf{20 \times 20}$	**1**	17.976	18.022	41.117	6.694	54.461	GPa
		0.217	0.150	0.285	0.344	0.170	%
	2	17.937	17.995	41.234	6.671	54.554	GPa
$\mathbf{30 \times 30}$	**1**	17.918	18.091	41.068	6.646	54.365	GPa
		0.146	0.226	0.327	0.245	0.215	%
	2	17.892	18.050	41.202	6.629	54.482	GPa

Remarks on the Image Quality

Since the DIB microstructure recognition technique relies on a micrograph of the material to generate the finite element mesh that model its behaviour, the quality of the micrograph is an important factor to take into account.

Figure 6.6 illustrates a zoom of the mesh obtained for the 80×80 RVE. As it can be seen, the jagged boundaries of the materials do not correctly represent the real microstructure. Therefore, the skeleton, while trying to reduce the *shape* and *homogeneity energy*[3], attempts to mold to the low quality boundaries illustrated in this image and the final results may be inaccurate.

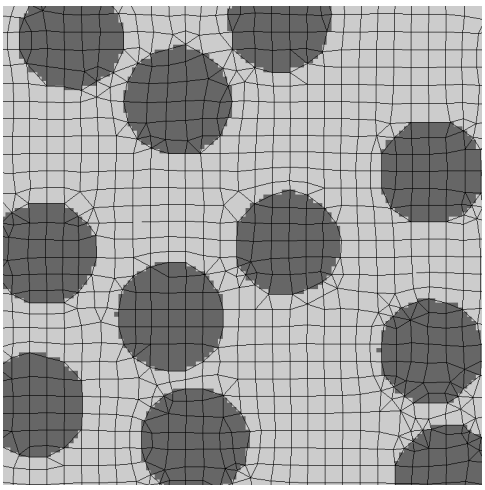

Figure 6.6: Zoom of the 80×80 RVE to illustrate the quality of the mesh.

To solve this problem, the image displayed in Figure 6.2 is vectorized using Adobe Illustrator®, i.e. using the function *Image Trace*, the bitmap image undergoes a raster-to-vector conversion (or vectorization). In a vector image, the edges are represented as a mathematical lines or curves and, unlike the raster image, it can be magnified, theoretically, thousands of times without losing definition. After the image tracing procedure, same parts are not correctly represented and manual corrections are needed, specially when two fibers are connected as illustrated in Figure 6.7.

Nevertheless, after the image tracing procedure has been completed, the image has to be exported from Adobe Illustrator® as a bitmap file again (e.g. .png file extension). The image is exported with a high resolution of 300 PPI (pixels per inch). In Figure 6.8, the difference between the initial and the final 80×80 RVE is presented. As it can be seen in Figure 6.8d, the jagged boundaries of Figure 6.8c have nearly vanished. The initial image had a dimension of 1024×1024 pixels and the new one has 4267×4267 pixels, which means around 17 times more resolution.

[3] Addressed in Section 4.2.3.

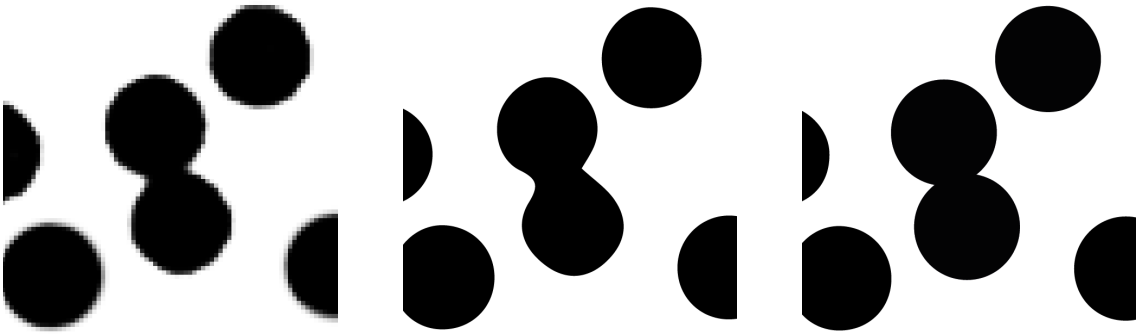

(a) Before the image tracing. (b) After the image tracing. (c) After the manual correction.

Figure 6.7: Example of the two steps needed to complete the image tracing procedure.

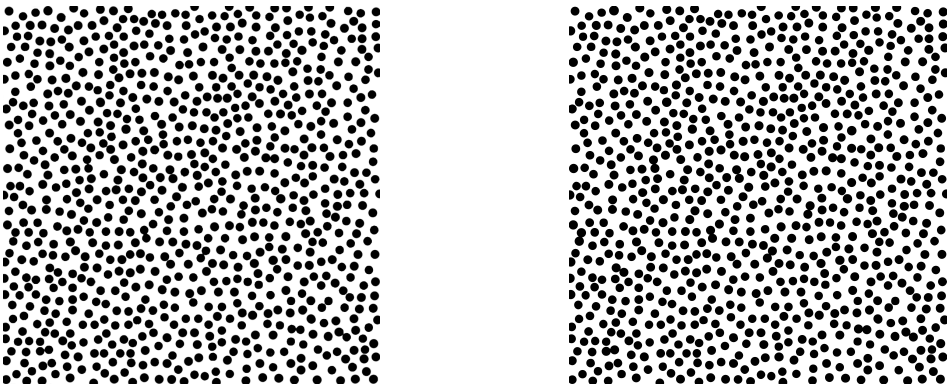

(a) Initial RVE (Figure 6.2). (b) New RVE.

(c) Zoom of Figure 6.8a. (d) Zoom of Figure 6.8b.

Figure 6.8: Difference between the initial image (lower quality) and the new one (higher quality) for the 80×80 RVE.

Repetition of the Mesh Size Study

With the change in the image quality, the study about the mesh size has to be remade. Following the same procedure that was used to generate the finite element meshes presented in Figure 6.5, the new meshes have been created and Table 6.7 presents the parameters chosen to run the automated script of OOF2 for each mesh version and the respective final informations.

Unlike the other versions, comparing version 3 with 4, the *maxscale* is the same but the *minscale* changes to half and it can be noticed that the number of elements doubled but the

Table 6.7: Parameters chosen to automatically create the initial skeleton version to each mesh of the new 10×10 RVE. The *homogeneity threshold* is equal to 0.9 in all versions.

Mesh	**1**	**2**	**3**	**4**	**5**
Maxscale	0.5	0.3	0.2	0.2	0.1
Minscale	0.5	0.3	0.2	0.1	0.1
Elements	667	1193	3009	6478	10734
Quadrilateral	399	1015	2352	3200	9715
Triangular	268	178	657	3278	1019
Nodes	581	1173	2786	4962	10431
Homogeneity	0.993	0.993	0.996	0.997	0.997

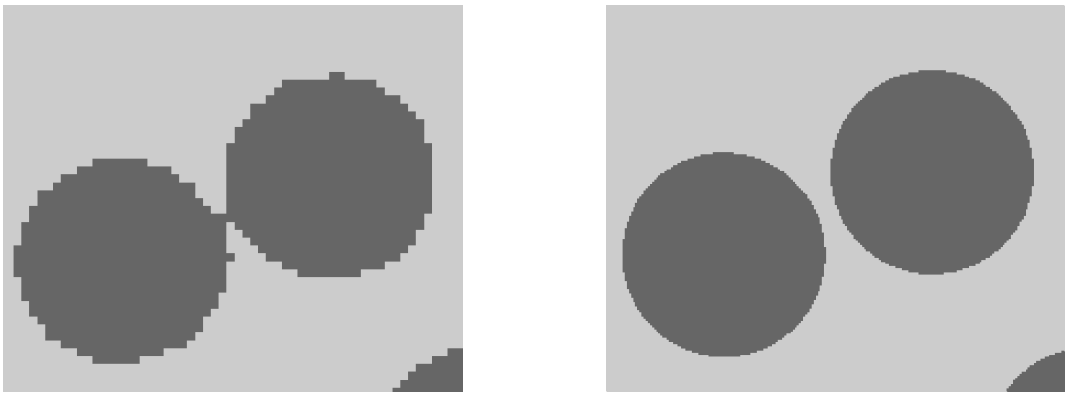

(a) Zoom of the initial material image Figure 6.4b. (b) Zoom of the new material image.

Figure 6.9: Difference between the image segmentation of the initial and new 10×10 RVE.

majority of elements created are triangular (as it can be seen later in Figure 6.10), since it is the type of elements that better fits circular boundaries. Furthermore, it is noteworthy to mention that the *homogeneity* is higher in these meshes than it was in the meshes generated trough the initial image (Table 6.4). This can be explained by the higher resolution image that enables better results in the segmentation process, as illustrated in Figure 6.9.

The homogenized elastic properties for these five versions are presented in Table 6.8. Based on the same criterion as before, the selected version is the number 3 because the relative differences from this version to the next one (version 4) are lower than 0.5%.

The same study is repeated for larger RVEs (20×20, 30×30 and 60×60). The parameters used to automatically create the skeleton and the respective mesh informations are given in Table 6.9. Excluding the Poisson's Ratio, the results are presented in Table 6.10.

Analysing these results, one can notice that for the 20×20 and 30×30 RVE, the selected version is the number 2 because, comparing both versions, there is around 1% of relative error in the G_{12}^* value. However, regarding the 60×60 RVE and comparing the results, the selected version is the number 1, thus, RVEs larger than this should be modelled with the same

Table 6.8: Homogenized elastic properties for each mesh version of the new 10×10 RVE.

Mesh	E_1^*	E_2^*	E_3^*	G_{12}^*	2-norm of $\mathbf{C}^*$	**Unit**
1	18.674	18.765	42.443	7.128	56.353	GPa
	1.187	1.128	0.208	1.756	0.221	%
2	18.452	18.554	42.531	7.003	56.229	GPa
	0.957	1.170	0.135	1.314	0.291	%
3	18.276	18.337	42.473	6.911	56.065	GPa
	0.246	0.293	0.008	0.313	0.044	%
4	18.231	18.283	42.476	6.889	56.041	GPa
	0.200	0.211	0.033	0.274	0.072	%
5	18.194	18.244	42.462	6.870	56.000	GPa

Mesh	ν_{12}^*	ν_{21}^*	ν_{13}^*	ν_{31}^*	ν_{23}^*	ν_{32}^*	**Unit**
1	0.3454	0.3471	0.1320	0.3000	0.1326	0.3000	-
	0.898	0.980	1.364	0.000	1.282	0.000	%
2	0.3485	0.3505	0.1302	0.3000	0.1309	0.3000	-
	1.263	1.027	0.845	0.000	1.070	0.000	%
3	0.3529	0.3541	0.1291	0.3000	0.1295	0.3000	-
	0.340	0.282	0.232	0.000	0.309	0.000	%
4	0.3541	0.3551	0.1288	0.3000	0.1291	0.3000	-
	0.169	0.169	0.233	0.000	0.155	0.000	%
5	0.3547	0.3557	0.1285	0.3000	0.1289	0.3000	-

Table 6.9: Parameters chosen to create the skeleton and information relative to each mesh of the new 20×20, 30×30 and 60×60 RVEs. The *homogeneity threshold* is 0.9 in every case.

RVE	**Mesh**	**Maxscale**	**Minscale**	**Elements**	**Nodes**	**Homogeneity**
$\mathbf{20 \times 20}$	**1**	0.3	0.3	6108	5347	0.995
	2	0.2	0.2	11604	10760	0.996
$\mathbf{30 \times 30}$	**1**	0.3	0.3	13676	11680	0.995
	2	0.2	0.2	27193	24245	0.995
$\mathbf{60 \times 60}$	**1**	0.3	0.3	51633	44707	0.992
	2	0.2	0.2	106640	96668	0.995

parameters of this mesh version. Therefore, the chosen parameters are the following ones:

$$\begin{aligned} &maxscale = minscale = 0.2, && \text{for the } 10 \times 10,\ 20 \times 20,\ \ldots,\ 50 \times 50 \text{ RVEs,} \\ &maxscale = minscale = 0.3, && \text{for RVEs equal and larger than } 60 \times 60. \end{aligned}$$

Table 6.10: Homogenized elastic properties for each mesh version of the new 20×20, 30×30 and 60×60 RVE.

RVE	Mesh	E_1^*	E_2^*	E_3^*	G_{12}^*	2-norm of $\mathbf{C}^*$	Unit
20 × 20	**1**	17.715	17.980	40.737	6.603	53.994	GPa
		0.472	0.571	0.042	0.835	0.097	%
	2	17.631	17.878	40.754	6.548	53.941	GPa
30 × 30	**1**	18.261	18.333	42.078	6.744	55.495	GPa
		0.747	0.793	0.179	0.994	0.294	%
	2	18.125	18.186	42.003	6.677	55.332	GPa
60 × 60	**1**	18.022	18.022	41.395	6.636	54.647	GPa
		0.269	0.307	0.678	0.374	0.436	%
	2	17.974	17.967	41.676	6.612	54.885	GPa

with the *homogeneity threshold* equal to 0.9 in all cases.

As it can be seen from Table 6.9, the number of elements in the 60×60 RVE changes from 106640 to 51633, reflecting a decrease of 52% and, regarding the number of nodes, the reduction is around 54%, meaning that the computational power needed to generate the finite element meshes and to run the analyses is lower. Considering that the values hereafter mentioned depend on the specifications of the computer used, the time taken to complete the analysis of one load increment with a *Mortar Periodic* boundary condition in the case of mesh 1 is around 19 seconds and, in the case of mesh 2, is 73 seconds, meaning that, on a computational level, mesh 2 is almost four times heavier than mesh 1.

Figure 6.10 presents the finite element mesh of version 3 and 4 of the new 10×10 RVE along with version 3 of the initial 10×10 RVE. Comparing Figure 6.10a with Figure 6.10b, one can notice that the improved results obtained during the image segmentation process (Figure 6.9) reflect on a skeleton that better characterizes the microstructure of the material, hence, producing more accurate results.

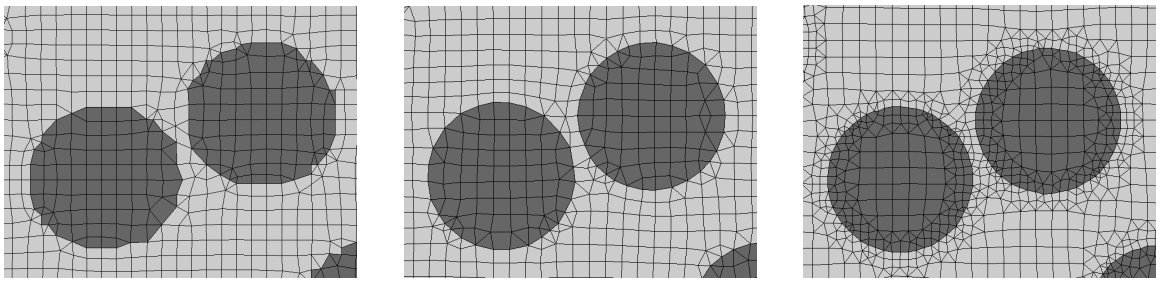

(a) Zoom of the initial mesh 3. (b) Zoom the new mesh 3. (c) Zoom of the new mesh 4.

Figure 6.10: Comparison between the initial and new finite element meshes of the 10×10 RVE.

Furthermore, taking into account the results presented in this section, and considering a RVE of a unidirectional fiber composite, it is possible to define that a value within one third

and one fourth of the fiber radius is a good element's size and so:

$$\frac{1}{4}\,\text{radius}_{\text{fiber}} \leq \textit{minscale} \leq \frac{1}{3}\,\text{radius}_{\text{fiber}}, \tag{6.1}$$

while the *maxscale* parameter should have an approximate value in order to favor the formation of quadrilateral elements.

6.1.4 Results

With the mesh size defined for all RVEs, the steps needed to estimate the effective elastic properties are performed. In this section, the results are presented for the initial RVE (Figure 6.2) and for the new RVE (Figure 6.8b), obtained after the image tracing process. Later, a note on both results is made, along with a comparison with the estimated properties obtained with the *Mori-Tanaka* method and with the *Hashin-Hill* bounds.

Finally, a study on the influence of different stiffness ratios (stiffness of the fiber material over the stiffness of the matrix material) is made to analyse if the RVE size is dependent on this factor.

To enable an easier interpretation of the results, the RVE size is described by a characteristic length, which is the RVE dimensions normalized by the smallest RVE that only contains one fiber (presented in Figure 6.1). In Terada et al. (2000), this model has 32×32 pixels, thus, the characteristic lengths are defined in Table 6.11.

Table 6.11: Conversion from pixel dimensions to characteristic length.

Pixel Dimensions	128×128	256×256	384×384	512×512
Physical Dimensions	10×10	20×20	30×30	40×40
Characteristic Length	4	8	12	16

Pixel Dimensions	640×640	768×768	896×896	1024×1024
Physical Dimensions	50×50	60×60	70×70	80×80
Characteristic Length	20	24	28	32

Initial RVE

In order to achieve these results, the procedure described in Figure 1.1 was followed, excluding the first block "Acquisition of a Micrograph", which was obtained from Terada et al. (2000), as described earlier in this section.

Furthermore, the finite element analyses are computed taking into consideration the three main constraints addressed in Section 3.4 (*Linear*, *Mortar Periodic* and *Uniform Traction* boundary conditions).

With the material properties defined in Table 6.2, the homogenized stiffness tensor is computed for each RVE and the 2-norm of these tensors are presented in Figure 6.11.

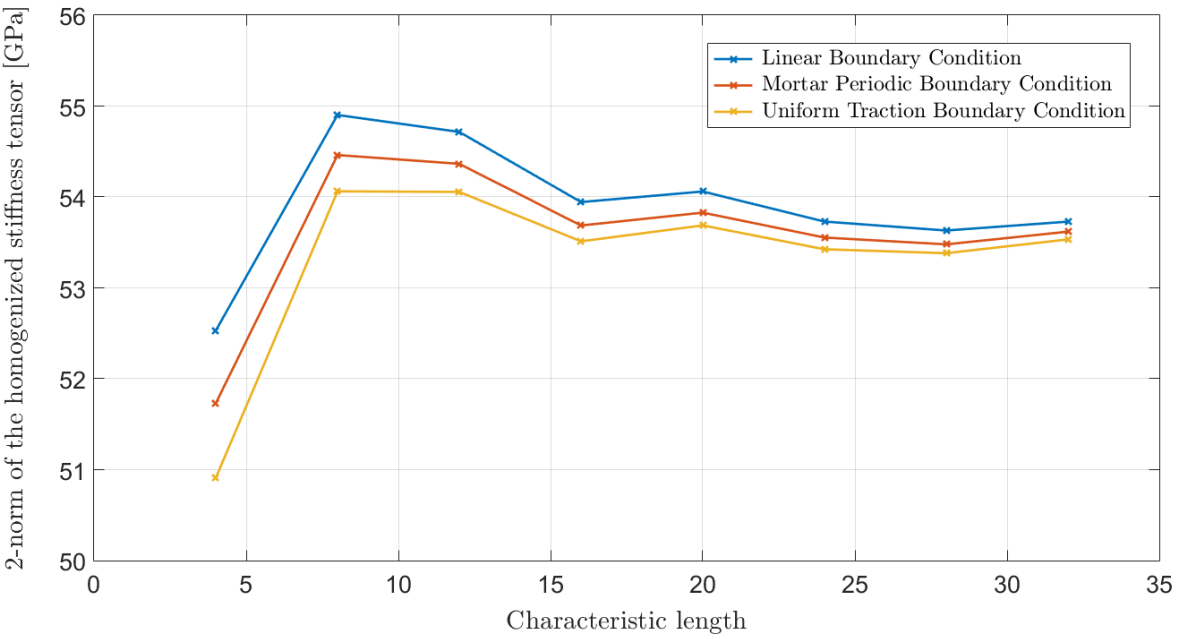

Figure 6.11: Representation of the 2-norm of the homogenized stiffness tensor, $\mathbf{C}^*$, of the initial RVEs.

Looking at these results, it can be seen that the *Linear* and *Uniform Traction* boundary conditions set the upper and lower boundaries for the homogenized elastic properties, as mentioned in Section 3.4.5. Moreover and as it is expected, the different boundary conditions are converging for the same value and the *Mortar Periodic* boundary condition seems to converge faster for the optimal result.

In Figure 6.12, the homogenized in-plane Young's moduli, E_1^* and E_2^*, are illustrated for the three boundary conditions aforementioned. The same conclusions taken for Figure 6.11 can be applied and one can notice that both moduli tend to converge for the same value, meaning that the composite material may be characterized as transversely isotropic[4]. This is explained by the randomness distribution of the fibers that tend to influence both plane directions on the same way, as the RVE increases in size.

Table 6.12: Mesh information of the initial 10×10, 40×40 and 80×80 RVEs.

RVE	Elements	Nodes
10×10	2909	2720
40×40	22001	19311
80×80	91846	77913

[4]Addressed in Section 5.1.2.

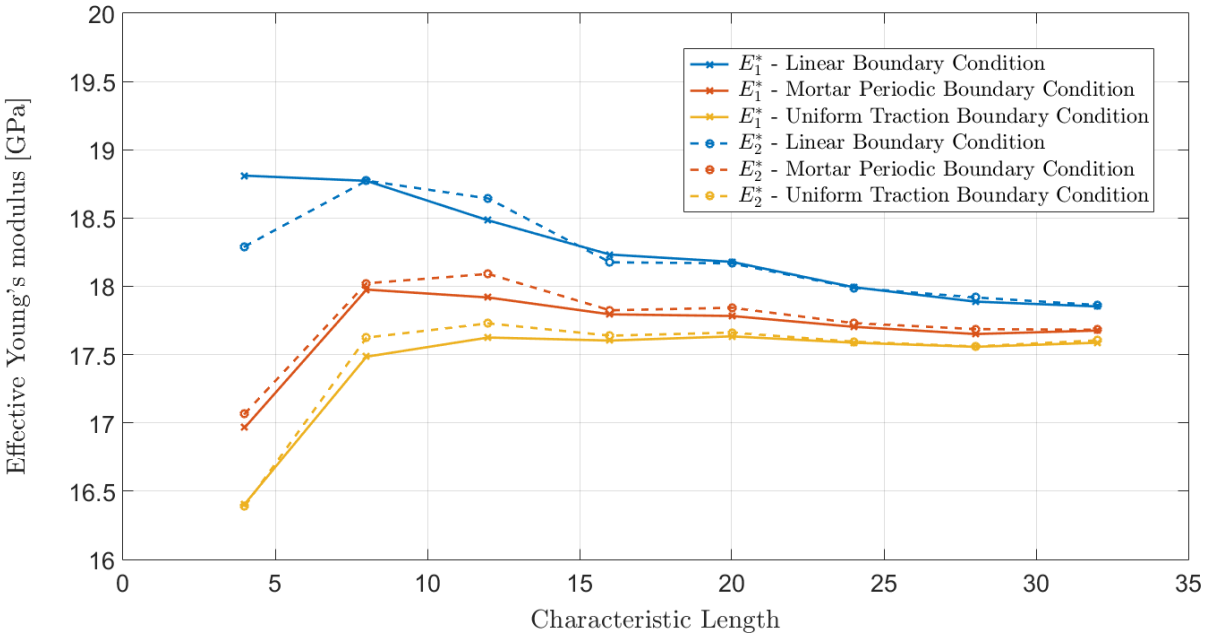

Figure 6.12: Representation of the homogenized in-plane Young's moduli, E_1^* and E_2^*, of the initial RVEs.

In both Figure 6.11 and 6.12, it can be seen that the values of the *Mortar Periodic* boundary condition start to converge for a characteristic length of 16, meaning that the middle RVE (512×512 px or 40×40 in physical dimensions) may be considered large enough to correctly represent the microstructure of this material.

The mesh information relative to this RVE is presented in Table 6.12, along with the information regarding the 10×10 and 80×80 RVEs. The number of elements and nodes necessary to model this microstructure is nearly 25% than those needed to model the largest RVE, meaning that the computational power needed to run the analyses is much lower. For instance, considering the computer used to run the majority of the simulations, in the case of the 40×40 RVE, it takes around 5 seconds to complete the analysis of one load increment for a single deformation gradient and boundary condition (*Mortar Periodic*) and, for the 80×80 RVE, it takes ten times more to complete the same process (≈ 50 seconds). The generation of the finite element mesh is also quicker in the 40×40 RVE, since it not only depends on the amount of nodes and elements that are processed during the OOF2 routines but also on the amount of pixels of the micrograph.

New RVE

Taking into consideration the new RVE generated after the image tracing process (Figure 6.8b), the procedure to obtain the homogenized properties is equal to the one followed in the initial RVE. Therefore, Figure 6.13 illustrates the variation of the 2-norm of the homogenized stiffness tensor.

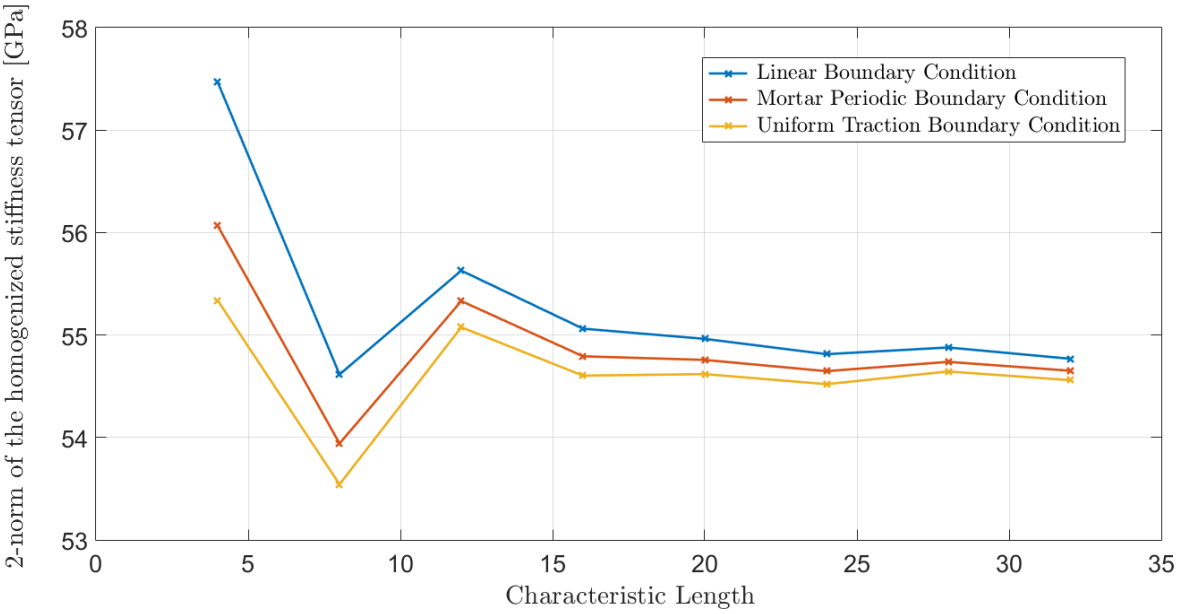

Figure 6.13: Representation of the 2-norm of the homogenized stiffness tensor, $\mathbf{C}^*$, of the new RVEs.

Analysing the results, the same conclusions regarding the upper and lower boundaries can be made, i.e. the *Linear* and *Uniform Traction* boundary conditions represent the upper and lower boundaries of the homogenized elastic properties. One can also conclude that the *Mortar Periodic* boundary condition converges faster to the theoretical value, thus, being the favoured boundary condition when estimating the homogenized elastic properties of a composite material.

It is known that the phases' volume fraction is one of the most important factors concerning composite materials, and, while running the analyses for this studies, it has been noticed that the fiber volume fraction drives the results regarding the other effective properties. Moreover, to be able to compute the different stiffness tensor coefficients, the effective axial Young's modulus, E_3^*, is previous settled by the *Voigt* model[5] (*rule of mixtures*), thus, E_3^* depends linearly on the fiber volume fraction, ϕ_f, as demonstrated in Figure 6.14.

In Figure 6.15, the variations of the effective in-plane Young's moduli are presented and again, E_1^* and E_2^*, converge to the same value (transversely isotropic material). Moreover, the homogenized plane shear modulus, G_{12}^*, presents the same type of dependence on the RVE size, and the upper and lower boundaries remain the same (Figure 6.16).

Furthermore, it is noteworthy to mention that the upper and lower boundaries invert when analysing the homogenized plane Poisson's ratio, ν_{12}^*. This is illustrated in Figure 6.17, and to explain this phenomenon, it is important to remember that the Poisson's ratio reflects the capacity of the material to expand/contract in a specific orientation when loaded on a perpendicular direction. Therefore, the *Uniform Traction* boundary condition, being the less restrictive of the microscopic constraints here applied, tends to give more flexibility to the material during

[5] As expressed in Equation (5.75).

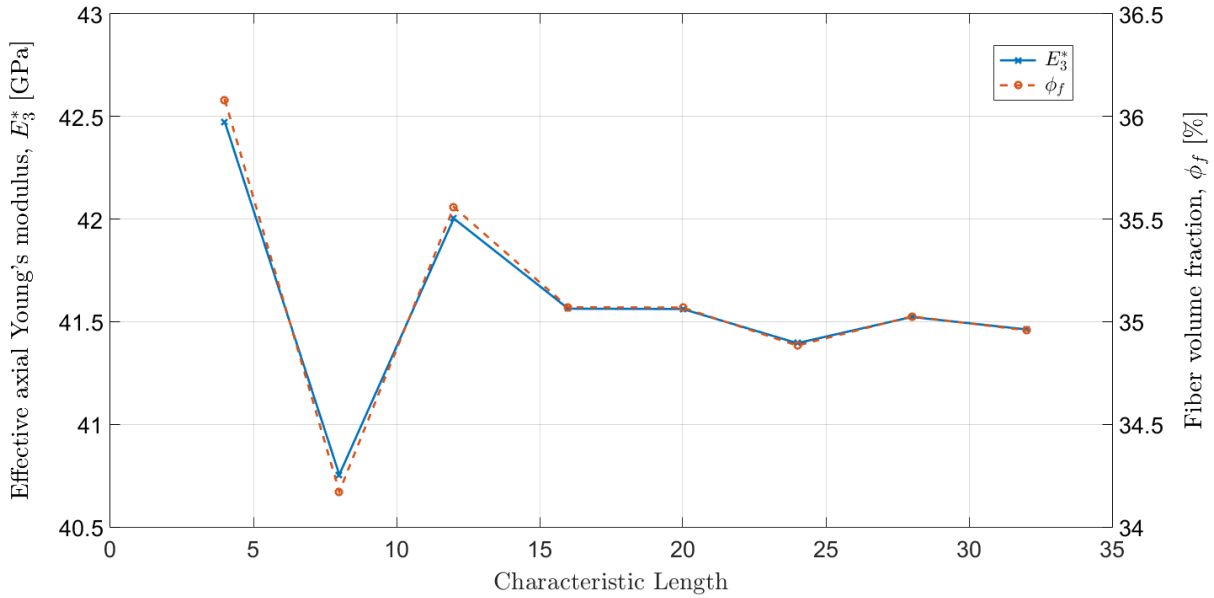

Figure 6.14: Representation of the homogenized axial Young's modulus, E_3^*, and fiber volume fraction, ϕ_f, of the new RVEs.

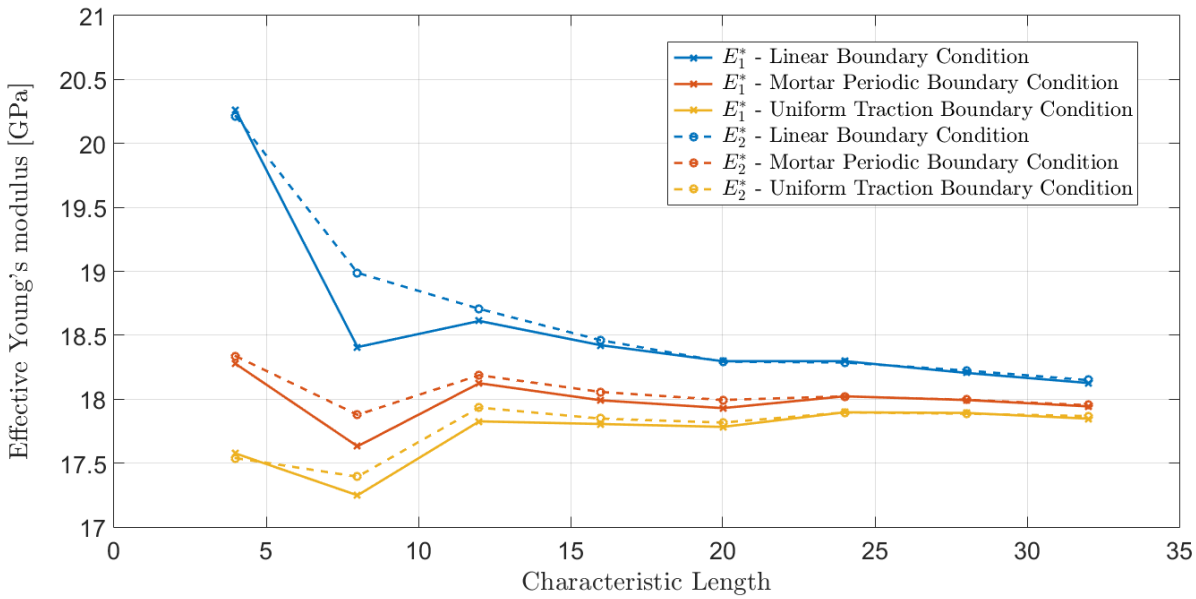

Figure 6.15: Representation of the homogenized in-plane Young's moduli, E_1^* and E_2^*, of the new RVEs.

the deformation process, resulting on a higher Poisson's ratio. Contrariwise, the *Linear* boundary condition, as the most restrictive one, partly prevents the deformation, producing a lower Poisson's ratio.

Finally, with all these results, the 40×40 RVE may be considered as the optimal RVE size to estimate the overall properties, as mentioned during the analyses of the initial RVEs.

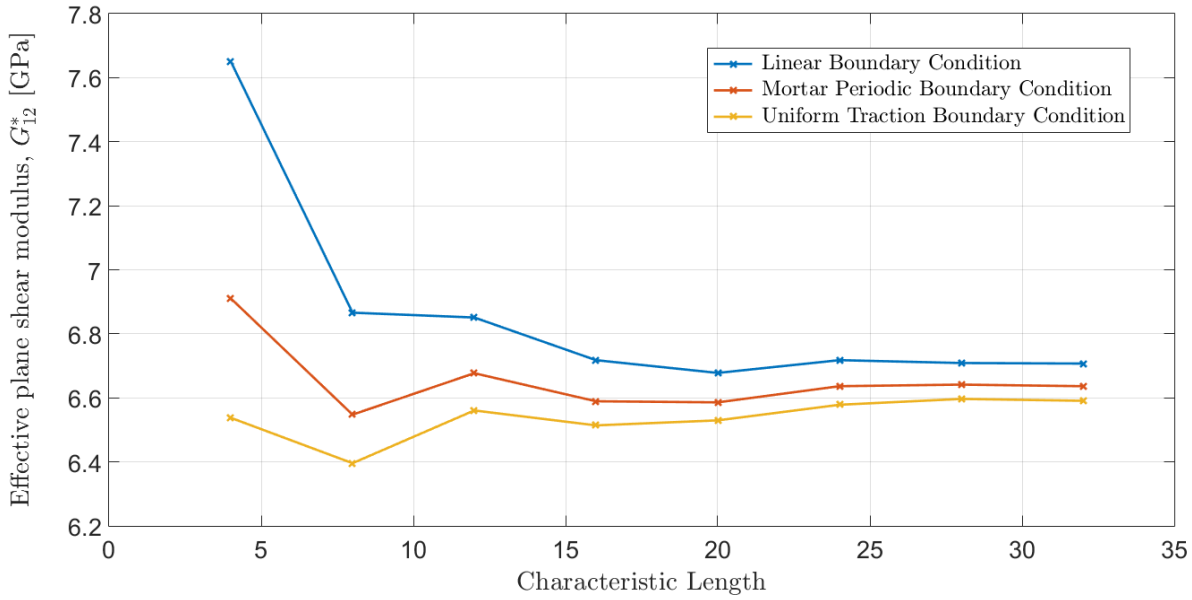

Figure 6.16: Representation of the homogenized plane shear modulus, G_{12}^*, of the new RVEs.

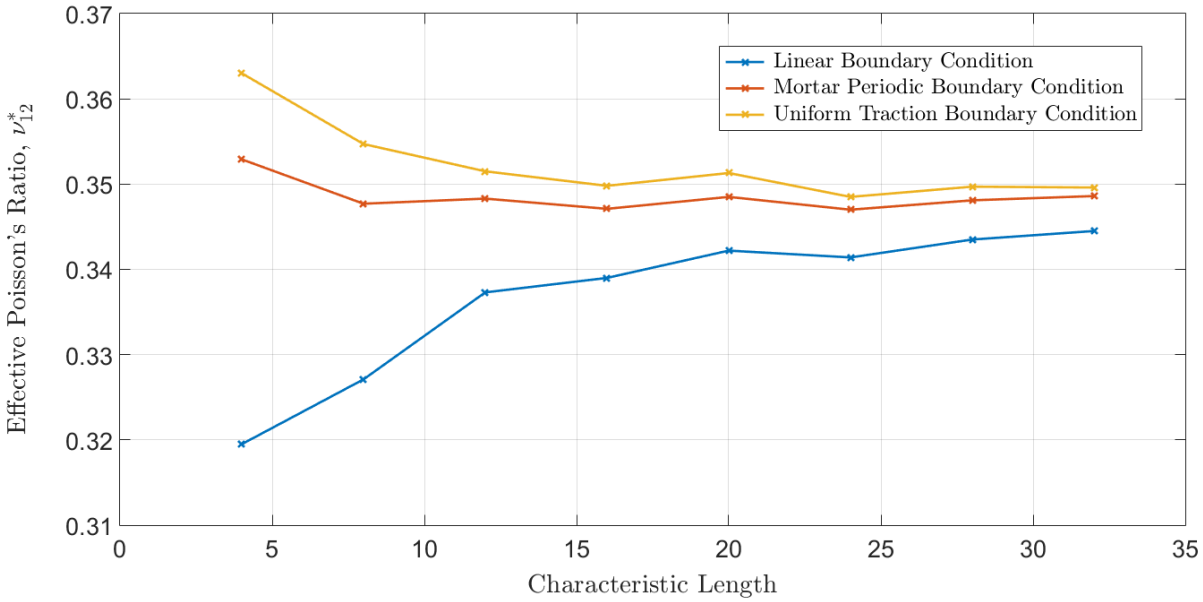

Figure 6.17: Representation of the homogenized Poisson's ratio, ν_{12}^*, of the new RVEs.

Comparison between RVEs

With these different studies completed, the influence of the image processing that converted the initial RVEs into the new ones can be analysed.

As mentioned before and represented in Figure 6.15, 6.16 and 6.17, the homogenized elastic properties are highly dependent on the fiber volume fraction (Figure 6.14). This value is obtained using the MATLAB® script that reads the output file of OOF2 and writes the input

file for MSP. It computes the volume fraction for each constituent from the sum of the finite elements' area assigned to them. Therefore, the fiber volume fractions of the initial and new RVEs are presented in Figure 6.18, and a stabilized difference of 1% for RVEs larger than 30×30 (characteristic length = 12) is noticed. This change in volume fraction is explained by the fact that, after the image tracing process the fibers are better defined (Figure 6.8) and during the segmentation process more pixels are selected generating a smoother shape (Figure 6.9).

In Table 6.13, the results for E_1^* are presented along with the respective relative differences, Δ, obtained by the following expression:

$$\Delta = \frac{\mid E^*_{1_{\text{new}}} - E^*_{1_{\text{initial}}} \mid}{E^*_{1_{\text{new}}}} \times 100 \quad [\%]. \tag{6.2}$$

The change of 1% in the fiber volume fraction results on Δ values between 1% and 2% on the homogenized elastic properties. Neither one of the results can be considered correct since the initial RVEs lack image definition because they are taken directly from an article (Terada et al., 2000), and the new RVEs are generated through an image modification process that may introduce changes in the microstructure. Nonetheless, these analyses aim to show the importance of the image quality on the final results and, since the new RVEs present a better correlation with the microstructure geometry, those are the ones that will be used on the studies presented hereafter.

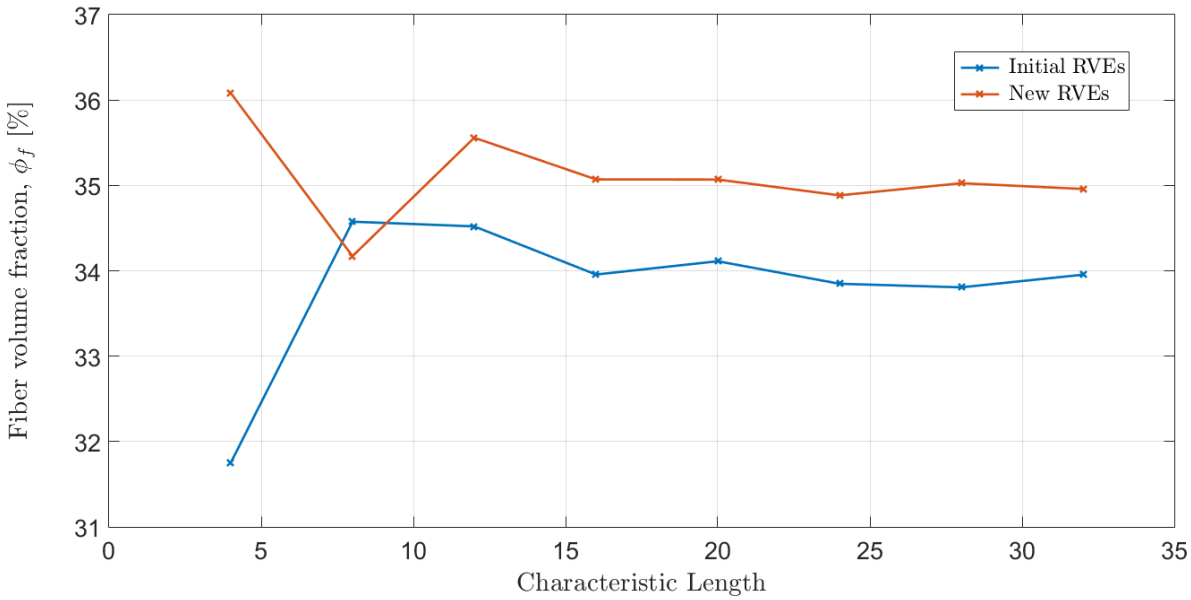

Figure 6.18: Representation of the fiber volume fraction, ϕ_f, of the initial and new RVEs.

Comparison with the Analytical Methods

As mentioned in the beginning of this chapter, the analytical methods presented in Section 5.2, have limitations when estimating the homogenized elastic properties of composite materials. In

Table 6.13: Comparison between the homogenized Young's modulus, E_1^*, of the initial and new RVEs.

RVE	**10 × 10**	**20 × 20**	**30 × 30**	**40 × 40**	**Unit**
Initial	16.966	17.976	17.918	17.795	GPa
New	18.276	17.631	18.125	17.991	GPa
Relative Error	7.165	1.957	1.139	1.090	%

RVE	**50 × 50**	**60 × 60**	**70 × 70**	**80 × 80**	**Unit**
Initial	17.783	17.704	17.651	17.676	GPa
New	17.930	18.022	17.994	17.944	GPa
Relative Error	0.820	1.768	1.905	1.491	%

this section, the results obtained by the DIB microstructure recognition method are compared with one of the most popular analytical models, the *Mori-Tanaka* method (Section 5.2.5).

Since the material may be considered as transversely isotropic, the effective plane Young's modulus, E_p^*, is calculated by the average of both in-plane Young's moduli, E_1^* and E_2^*. In Figure 6.19 the representation of this elasticity constant computed with the three main microscopic constraints is presented along with the effective Young's modulus obtained by the *Mori-Tanaka* model.

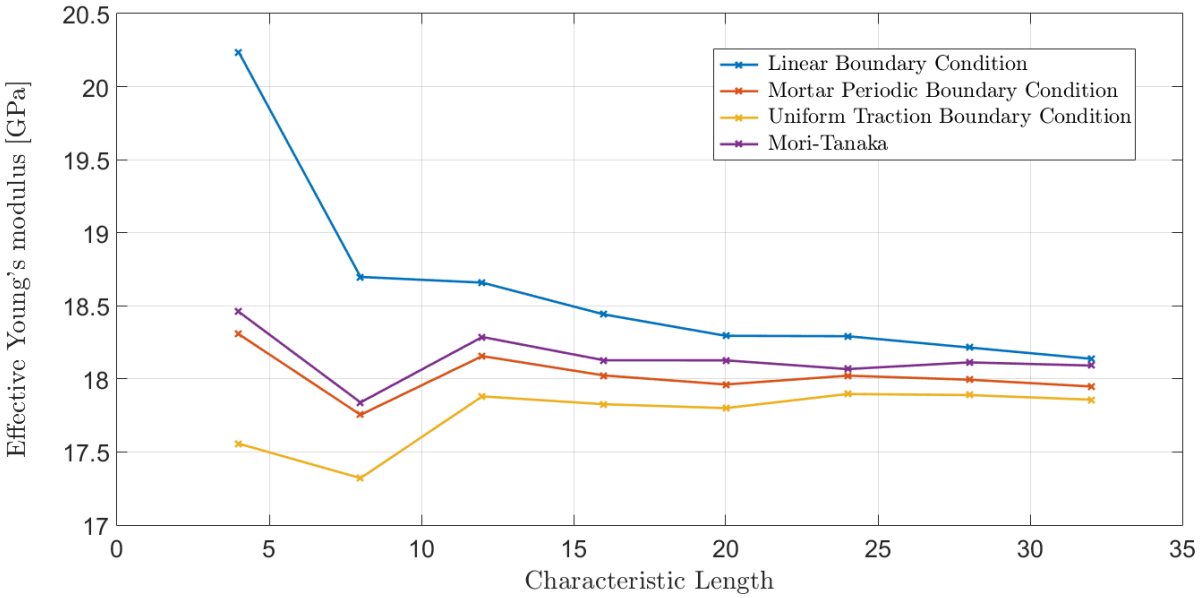

Figure 6.19: Representation of the homogenized plane Young's modulus, E_p^*, obtained by the numerical and the *Mori-Tanaka* models.

Despite the fact that the equation of the *Mori-Tanaka* model presented in Figure 6.19 was obtained assuming an isotropic and elastic matrix and isotropic and elastic spherical inclusions,

the similarities with the numerical DIB microstructure recognition technique are high. Moreover, the results given by the *Mori-Tanaka* method are within the boundaries settled by the *Linear* and *Uniform Traction* boundary conditions. The results and the volume fraction used to compute the analytical values are presented in Table 6.14, along with the relative differences, Δ, calculated by:

$$\Delta = \frac{\mid E^*_{p_{\text{Mori}}} - E^*_{p_{\text{DIB}}} \mid}{E^*_{p_{\text{Mori}}}} \times 100 \quad [\%]. \tag{6.3}$$

Table 6.14: Comparison between the homogenized plane Young's modulus, E^*_p, obtained by the numerical and *Mori-Tanaka* models.

RVE	$\mathbf{10 \times 10}$	$\mathbf{20 \times 20}$	$\mathbf{30 \times 30}$	$\mathbf{40 \times 40}$	**Unit**
Volume Fraction	36.081	34.172	35.559	35.070	%
Numerical*	18.306	17.754	18.156	18.024	GPa
Analytical**	18.459	17.839	18.287	18.128	GPa
Δ	0.829	0.475	0.715	0.574	%

RVE	$\mathbf{50 \times 50}$	$\mathbf{60 \times 60}$	$\mathbf{70 \times 70}$	$\mathbf{80 \times 80}$	**Unit**
Volume Fraction	35.069	34.884	35.026	34.958	%
Numerical*	17.962	18.022	17.995	17.948	GPa
Analytical**	18.127	18.067	18.113	18.091	GPa
Δ	0.911	0.249	0.655	0.790	%

* *Mortar Periodic* boundary condition.
** *Mori-Tanaka* model.

The Δ values are below 1%, and this difference may be partly justified by the fact that the numerical analyses are made with the assumption of a 2D plane strain problem, meaning that it is the same as considering that the microstructure modelled by the RVE (Figure 6.2) is a cross section of a material of length several times bigger than the cross section dimensions. Therefore, the inclusions can be considered as fibers and not spherical particles, contrariwise to the assumptions made during the deduction of the final expressions of the *Mori-Tanaka* model. Furthermore, since the *Mori-Tanaka* method is within the *Hashin-Hill* boundaries (Figure 5.8), that limits the homogenized properties of transversely isotropic composite materials composed by isotropic constituents, the numerical results are also between those limits. However, the *Hashin-Hill* boundaries are not represented in Figure 6.19 because the values do not match the appropriate range for the accurate plotting of the results.

Results Discussion

In summary, the variance in the image quality usually tends to produce slightly different segmentation outcomes, which culminates in different phases' volume fractions. Being the volume

fraction one of the most important factors and the variable that drives the homogenized properties, it is important to take this into consideration when trying to improve the image resolution of a micrograph. Even so, in this case, the image after the vectorization process better characterized the materials microstructure.

In addition, the homogenized elastic properties started to converge for dimensions greater than the 40×40 RVE. Thus, this can be defined as the optimal RVE size to predict the effective elastic properties of a microstructure of this type. The 40×40 RVE is defined by a characteristic length of 16, hence, one can conclude that, for a unidirectional fiber composite material, its microstructure can be modelled by a RVE 15-20 times larger than a single fiber (inclusion). This leads to a shorter use of computational power than the necessary to analyse the 80×80 RVE.

Furthermore, the numerical model with the *Mortar Periodic* boundary constraint and the analytical *Mori-Tanaka* model seem to produce similar results regarding the homogenized plane Young's modulus, E_p^*, with a relative difference below 1%, validating the results obtained with the numerical method. However, the numerical method is not limited to simple shapes, like spherical or ellipsoidal inclusions, and can model any given microstructure. In addition, the values obtained with both methods are within the theoretical upper and lower boundaries of *Hashin -Hill* and the numerical upper and lower limits produced by the *Linear* and *Uniform Traction* boundary conditions (Figure 6.19). Also, it is important to mention that the numerical boundary conditions invert when referring to the effective plane Poisson's ratio, ν_{12}^*, due to the nature of this elastic constant (Figure 6.17).

6.1.5 Influence of the Stiffness Ratio on the RVE Size

With the RVE size study completed for a stiffness ratio of 10, other stiffness ratios may be attributed to the constituents properties to test the impact of this parameter on the minimal size of the RVE that statistically represents the microstructure.

To do so, the Young's modulus of the fiber material is changed while keeping the Young's modulus of the matrix material constant and equal to 10 GPa. In Figure 6.20, the normalized effective plane Young's modulus, $\bar{E_p^*}$, given by:

$$\bar{E_p^*} = \frac{E_p^*}{E_m}, \tag{6.4}$$

is presented for different stiffness ratios. Focusing on the values of the middle RVEs, the relative differences are presented in Table 6.15 for comparison and a small influence can be noticed since this value increases. However, as shown in Figure 6.20, the 40×40 RVE (characteristic length = 16) still correctly represents the microstructure since it is near the average value obtained with larger RVEs.

In Figure 6.21, the estimated properties for the case where the stiffness ratio is 100 are presented, and it is noticed that the *Linear* boundary condition tends to depart from the values given by the *Mortar Periodic* and the *Uniform Traction* boundary conditions, meaning that

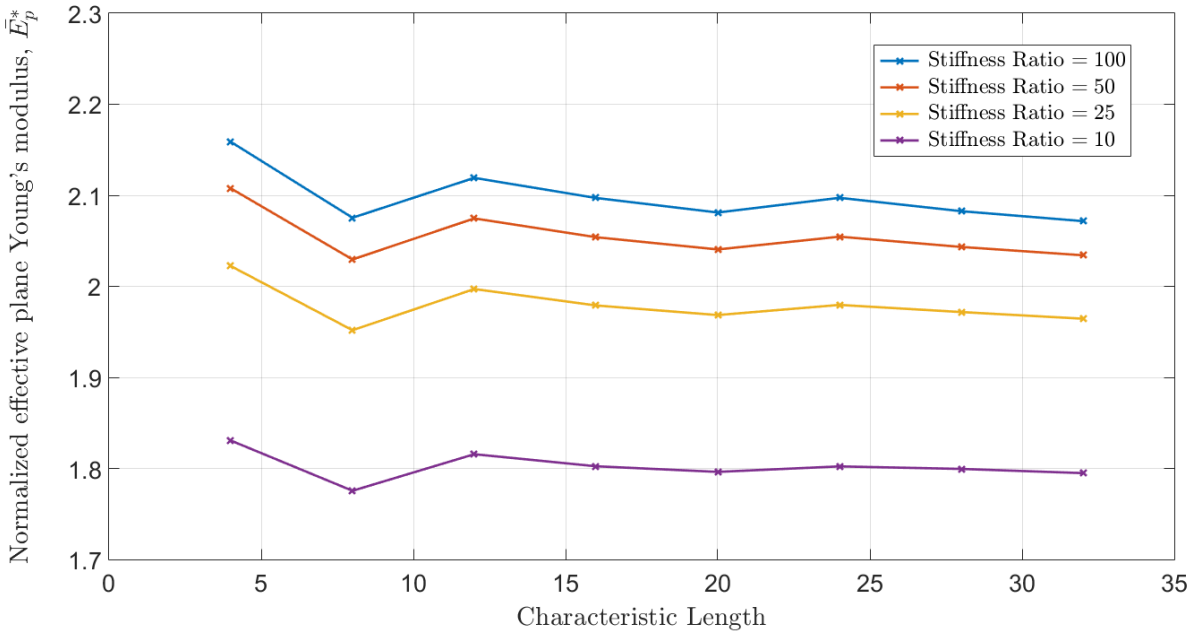

Figure 6.20: Representation of the normalized effective plane Young's modulus, $\bar{E}_p^*$, for different stiffness ratios.

this constraint loses accuracy as the stiffness ratio increases. Either so, the *Mortar Periodic* constraint continues to lie within the other two boundaries.

Furthermore, even with the increasing difference in the fiber/matrix properties, the analytical *Mori-Tanaka* model remains a good approximation to the numerical values achieved with the *Mortar Periodic* boundary condition, as illustrated in Figure 6.22. However, as seen in Figure 6.19, the *Mori-Tanaka* model gave results higher than those obtained with the numerical method and, in this case, the estimated values are lower. This means that with an increase in the stiffness ratio, the *Mori-Tanaka* model tends to underestimate the effective Young's modulus (as shown in Figure 6.20). Moreover, for the 60×60 RVE, the analytical values are even below the lower boundary settled by the *Uniform Traction* constraint.

Table 6.15: Comparison between the homogenized plane Young's modulus, E_p^*, for different stiffness ratios.

Stiffness Ratio	**10**	**25**	**50**	**100**	**Unit**
30 × 30	18.156	19.970	20.746	21.192	GPa
	0.730	0.903	0.994	1.042	%
40 × 40	18.024	19.790	20.540	20.971	GPa
	0.343	0.534	0.655	0.762	%
50 × 50	17.962	19.684	20.405	20.811	GPa

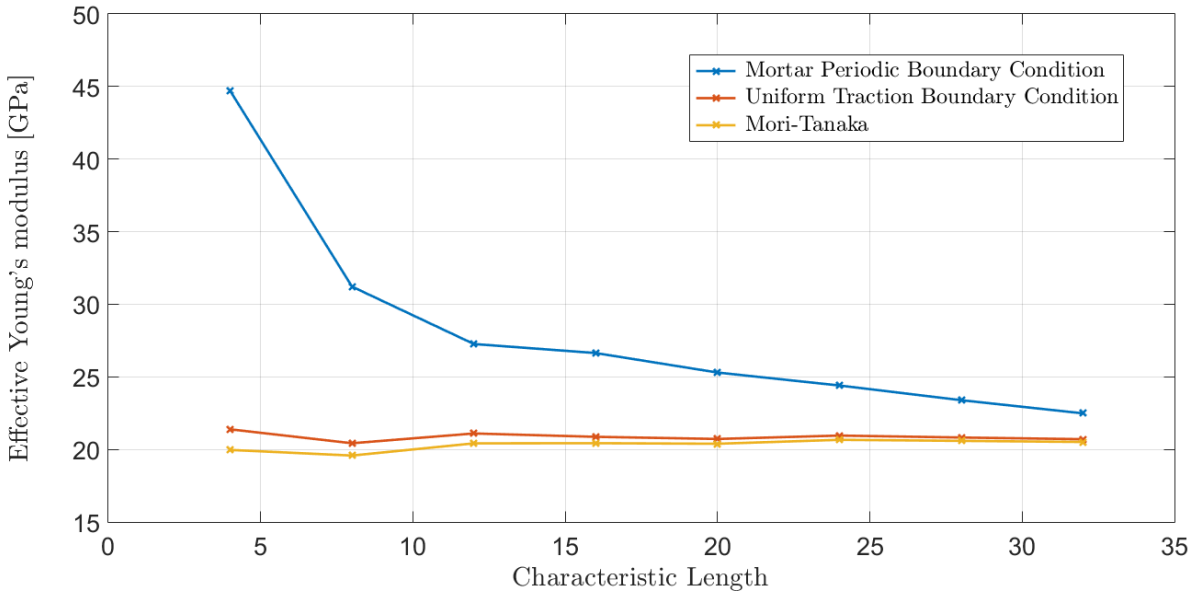

Figure 6.21: Representation of the homogenized Young's modulus, E_1^*, for a stiffness ratio of 100.

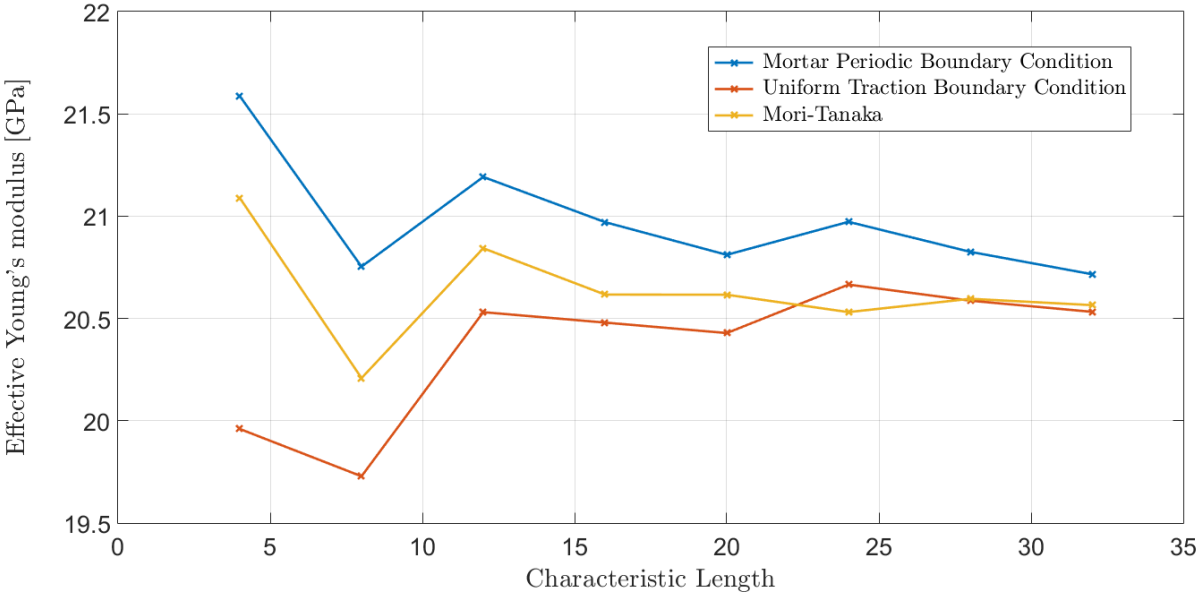

Figure 6.22: Representation of the homogenized plane Young's modulus, E_p^*, obtained by the numerical and the *Mori-Tanaka* models.

Note: In the MSP program, the standard criterion set to finish the *Newton-Raphson* iterative process[6] is that the relative residual norm, $\frac{\| \mathbf{r} \|}{\| \mathbf{f}^{\text{ext}} \|}$, has to be lower than 10^{-6}. Due to the high stiffness ratio, the interfacial fiber/matrix zone presents high stress concentration factors and the convergence to this tolerance value has revealed extremely difficult, thus, for stiffness ratios

[6] Addressed in Section 2.6.4.

higher than 50, the tolerance was set to 10^{-5} and, for stiffness ratios higher than 70, this value decreased to 10^{-4}. However, the results obtained with both tolerances are not distinguishable.

6.2 Influence of the Stiffness Ratio on the Homogenized Elastic Properties

Analysing Figure 6.20 and comparing the increase in the effective plane Young's modulus with a stiffness ratio of 10 to 25, and with a stiffness ratio of 50 to 100, it can be noticed that, as the stiffness ratio between fiber and matrix materials increases, the influence of the fiber material diminish.

With the results obtained in the previous studies, it is possible to conclude that the new 40×40 RVE modelled with elements of size near 0.3, is capable of correctly characterizing the microstructure of this unidirectional fiber composite. Therefore, the following studies are performed using only this RVE.

Different stiffness ratios were analysed, from 5 to 100 with a step of 5 and the results for the homogenized plane Young's modulus, E_p^* (average of the E_1^* and E_2^* moduli), are presented in Figure 6.20.

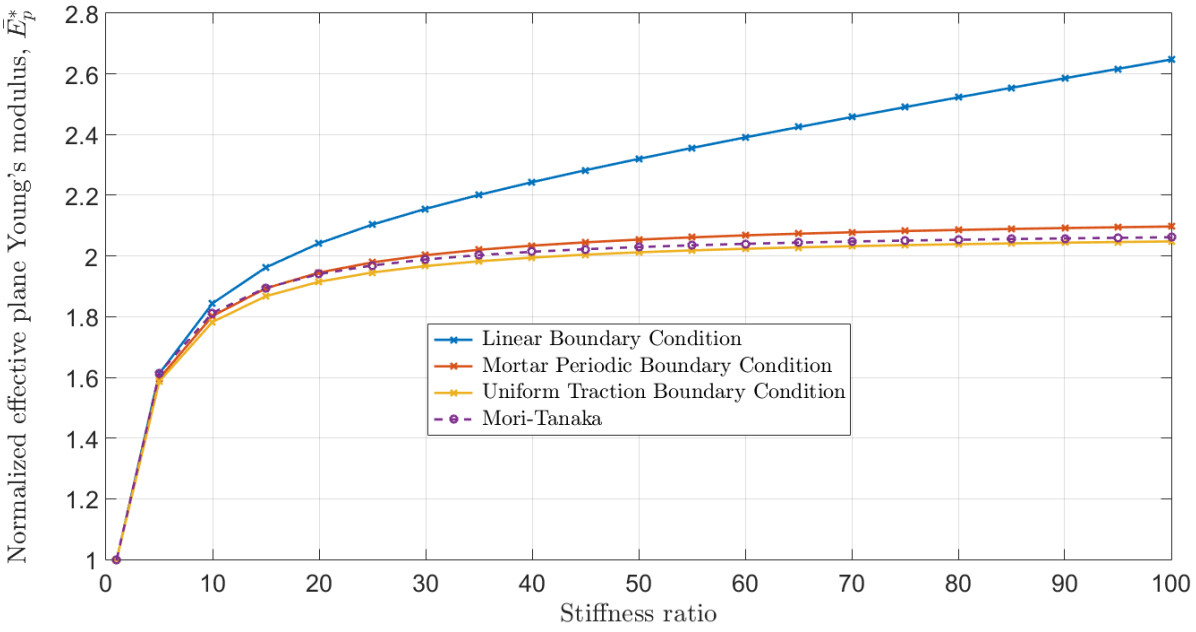

Figure 6.23: Influence of the stiffness ratio on the normalized effective plane Young's modulus, $\bar{E}_p^*$, obtained by the numerical and the *Mori-Tanaka* models.

As mentioned in Section 6.1.5 and illustrated in Figure 6.20, the impact of the fiber material tends to decrease as the stiffness ratio increases. For lower ratios the influence of the fiber elastic properties is accentuated but it starts to stabilize as the Young's modulus of the fiber material

becomes higher. For instance, for a ratio of 5, the effective plane Young's modulus is 1.6 times higher than that of the matrix but, for a ratio of 100, it only is 2.1 times higher.

Also noteworthy to mention is the fact that the *Linear* boundary condition completely diverges from the other results as the stiffness ratio increases, showing a linear relation for ratios higher than 30.

In the case of the effective axial Young's modulus, E_3^*, with the assumption of the *rule of mixtures*, its value increases linearly with the stiffness ratio, being this the main function of the fiber material in unidirectional fiber composites, designed to withstand high traction loads in the axial direction.

Note: All of these studies have been performed for $\nu_m = \nu_f = 0.3$, while changing one parameter at a time. In Table 6.16, the influence of the Poisson's ratio is demonstrated to indicate that a change on its value may lead to different results than those here obtained. Material 1 has $\nu_m = \nu_f = 0.3$ while material 2 has $\nu_m = 0.4$ and $\nu_f = 0.3$. Both have a stiffness ratio of 10 and $E_m = 10$ GPa.

Table 6.16: Comparison between the homogenized elastic properties of two materials, while changing the Poisson's ratio of the matrix.

Material	E_1^*	E_2^*	E_3^*	G_{12}^*	2-norm of $\mathbf{C}^*$	Unit
1	17.991	18.056	41.563	6.589	54.792	GPa
	4.020	3.959	0.000	4.648	13.051	%
2	17.268	17.341	41.563	6.896	47.641	GPa

Material	ν_{12}^*	ν_{21}^*	ν_{13}^*	ν_{31}^*	ν_{23}^*	ν_{32}^*	Unit
1	0.3471	0.3484	0.1299	0.3000	0.1303	0.3000	-
	30.913	30.855	21.247	17.900	21.028	17.800	%
2	0.2398	0.2409	0.1023	0.2463	0.1029	0.2466	-

The relative differences of the Young's and shear moduli are around 5% but, when considering the Poisson's ratio, these values increase as expected. Nonetheless, the overall qualitative conclusions attained when considering $\nu_m = \nu_f$ are still valid.

6.3 Homogenized Elastic Properties obtained with 3D RVEs

Since all the analyses here presented are performed with the assumption of a two dimensional plane strain problem, which considers the 2D RVE as cross section of an equally extruded microstructure, it is important to find for which axial (out-of-plane) length this assumption starts to produce accurate results.

Therefore, using the open-source program OOF3D, several finite element meshes were created in order to estimate the overall elastic properties, while increasing the axial dimension of

the RVE. The main goal was to find a relation between the length of the RVE and the respective cross section dimensions and to conclude that for higher values it was valid to replace the three dimensional problem by a two dimensional plane strain analysis, aiming to reduce the complexity of the whole procedure.

However, as mentioned in Section 4.4, the open-source program OOF3D revealed some errors while creating the output file that contained the finite element mesh data. Therefore, this program could not be used to generate meshes for 3D RVEs and a different approach was carried out.

Using the image of the 40×40 RVE obtained after the image tracing process, and using the Autodesk AutoCAD® program, a ".dwg" file was created with the information of the microstructure. Two ".dxf" files were exported from AutoCAD®, representing the matrix and fiber material, illustrated in Figure 6.24a and 6.24b, respectively.

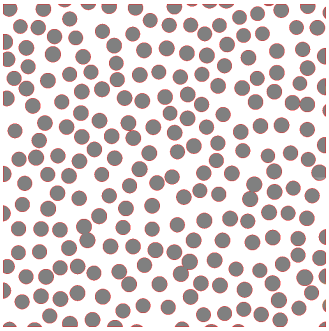

(a) 2D fibers representation.

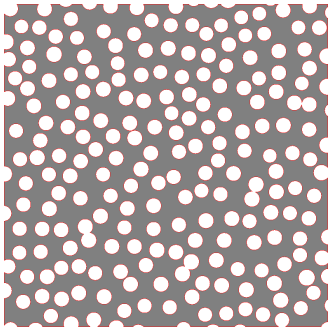

(b) 2D matrix representation.

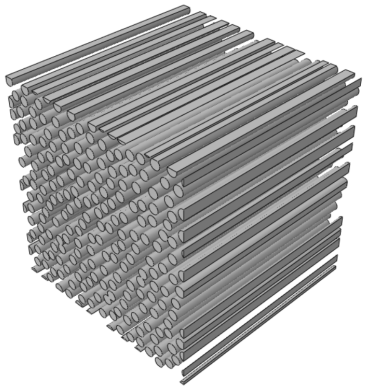

(c) 3D fibers part.

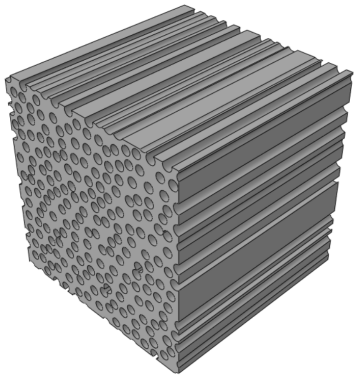

(d) 3D matrix part.

Figure 6.24: Representation of the 2D files exported by Autocad® and the respective 3D parts generated by Abaqus®

These two ".dxf" files were loaded on Abaqus® to create the parts that modelled both constituents: the matrix and the fibers that are displayed in Figure 6.24c and 6.24d, respectively. Those parts were assembled into a unique 3D RVE and a finite element mesh was generated using this program[7] and the final result is presented in Figure 6.25.

[7]The GiD® mesh generator was also tested but Abaqus® produced meshes with higher quality.

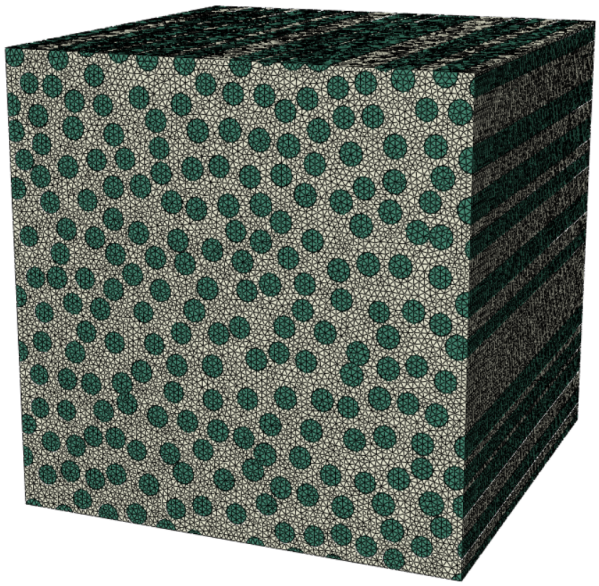

Figure 6.25: Representation of the 3D RVE and the finite element mesh generated by Abaqus®.

With the finite element mesh generated, a *Job* was created in Abaqus® and a ".inp" file, that contained the mesh data, was exported. Again, a MATLAB® script (described in Appendix E) was created to convert the mesh data into a readable file for MSP.

While creating the finite element meshes with Abaqus®, the type of elements chosen were tetrahedrons and a large amount of nodes and elements were generated to model the behaviour of a cubic 3D RVE, which lead to a high demand of computational power to perform the finite element analysis.

The input data files were generated but the MSP program could not finish the analysis due to lack of memory. Therefore, in order to overcome this obstacle, a computer cluster was used to run the MSP algorithm. However, the system of equations that results from the large number of nodes/elements was too big for the solver included in the program (PARDISO 5.00 (Kuzmin et al., 2013; Schenk et al., 2008, 2007)) to compute, and the analysis failed once again. Even with a more coarse mesh, the problem continued to occur.

To summarize, different approaches were tested to estimate the effective elastic properties of 3D RVEs but, due to computational limitations, the procedures were not successful. One way to solve the problem given by the current solver (categorized as a direct solver), is to use iterative solvers that may need fewer memory to complete the analysis.

6.4 Conclusions

Several numerical studies have been performed to determine, for the material under study, the statistically representative RVE size. These studies included the influence of the image quality that represents the microstructure of the material together with the appropriate treatment for

generating a finite element mesh and the impact of mesh parameters such as type of element employed and mesh density on the solution.

The numerical results obtained with the strategy proposed in this work were systematically compared and validated against analytical solutions available in the literature.

More over, the influence of the constituents' properties on the homogenized response was analysed in detail for several cases by comparing analytical and numerical solutions.

Chapter 7

Influence of the Interface Material on the Effective Elastic Properties

Until this section, the homogenized properties were obtained considering composite materials with only two phases. Because the properties of both constituents can be too different, micro-damaging nucleation mechanisms (cracking of particles, debonding or even fracture of the matrix due to strong inclusions) may be observed during the deformation process (Chen et al., 2003), weakening the overall behaviour of the material.

However, several studies have been made to understand the influence of a third interface material between the inclusions and matrix. If the interface material is not strong enough, the debonding may occur and, on the opposite, if the strength of the interface material is high, the probability of debonding decreases and the microcracks start to happen in the matrix material (Zhang and Chen, 2012).

Now that the influence of the stiffness ratio on the homogenized properties of a second-phase composite material has been studied, it is important to understand the effect of the interface material on the homogenized elastic properties of the composite.

Therefore, some parametric studies are made while changing the stiffness of not only the fiber material, but also of the interface. At the end, a mathematical function with good approximation with the results is found, allowing the use of this analytical function to extrapolate the homogenized elastic properties without the need for numerical simulation. This study has been made for specific fiber volume fraction and two interfacial widths. Hence, any change on these values would result on the need of different parameters to attain the same good agreement with the results.

7.1 Image Processing

First of all, and since the easiest way to recognize different materials in OOF2 is through different color values, the image that represents the 40×40 RVE has to be modified to include

the interface material. In the previous chapter, the higher resolution of the RVE created after the image tracing process proved to be an asset, since it improves the material boundaries enabling better results in the segmentation process, as such this will be the RVE used.

Since the image modification presented in Section 6.1.3 was done with Adobe Illustrator®, the same program is used to create the interface material. After the image tracing process, the fibers are represented by vector graphics and it is possible to modify them individually or as a group. Therefore, all fibers are selected (Figure 7.1) and a border is created with a specific width. This border must be aligned to the outside of the selected fibers to keep the same fiber volume fraction from the initial RVE.

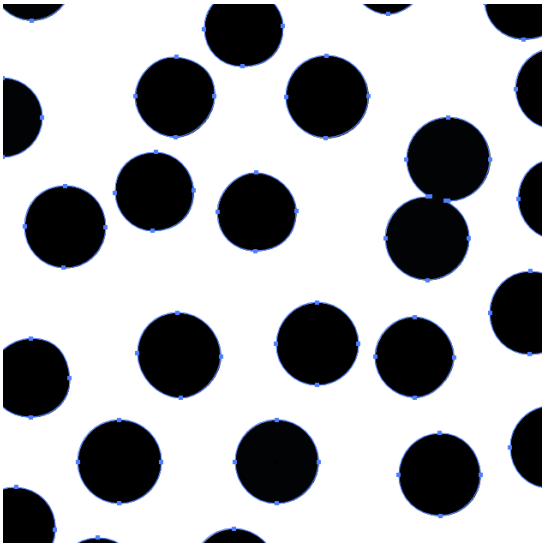

Figure 7.1: Zoom on selected fibers represented as vector graphics in the 40×40 RVE.

Using the *Measure Tool*, the average diameter of a fiber is gauged as 24 pixels. The representation of the initial RVE with a interface material of width equal to 10% of the fiber radius (weight stroke = 1.2 points)[1] is presented in Figure 7.2. The rasterized image, exported with high quality (300 PPI) has a width and height of 2133×2133 pixels.

In a black and white image, the presence of a material represented by a red color makes it difficult to identify the different materials using the *Color* method[2] set to a range of gray values. Thus, the red color (that illustrates the interface material in Figure 7.2) is replaced by a gray color, characterized by the 0.4 value in the gray scale (Figure 7.3a). To better understand, Figure 7.3b illustrates a single fiber surrounded by the interface material.

While selecting the fiber material (black color), it is important that a similar fiber volume fraction is obtained when comparing it with the initial 40×40 RVE. For that reason, after some experiments, the value of 0.4 in the gray scale is chosen to represent the interface material.

[1] Dimension used in Adobe Illustrator®.
[2] Described in Section 4.2.2.

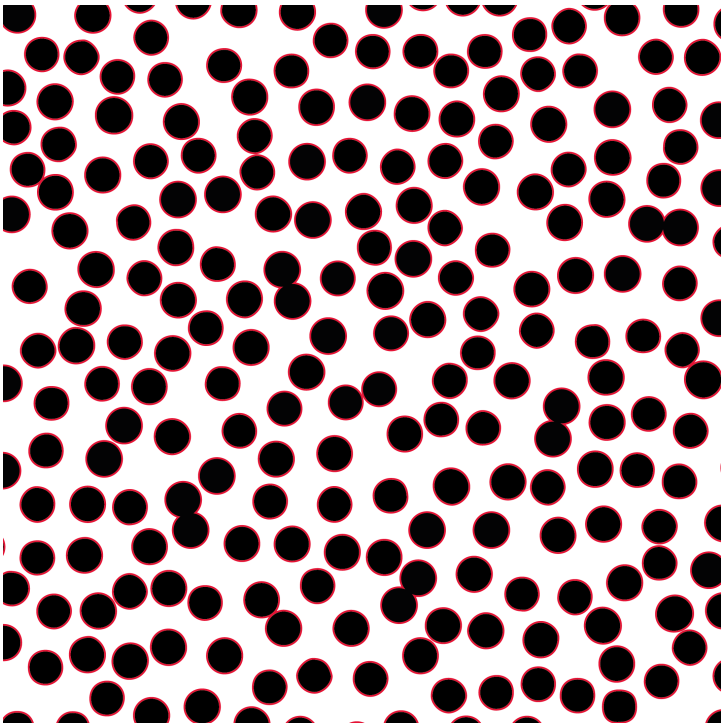

Figure 7.2: Representation of the 40×40 RVE with an interface material (red color) of width equal to 10% of the fiber radius.

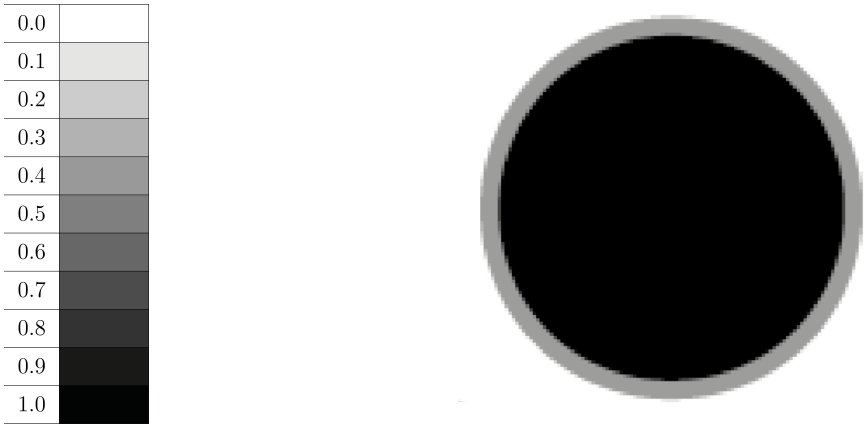

(a) Gray scale.

(b) Single fiber with interface material.

Figure 7.3: New color values of the 40×40 RVE.

7.2 Image Segmentation

The pixel selection process is done with the *Color* tool of OOF2. Considering the color of the fibers and matrix as 1.0 and 0.0, respectively, the selection of the pixels assigned to the fiber material is made with any black pixel targeted while the *delta gray* parameter is set to 0.55. Moreover, to select the matrix material, *delta gray* $= 0.1$ and a white pixel is targeted. Finally, both fiber and matrix materials are elected simultaneously and, by inverting it, the interface material is highlighted (Figure 7.4a).

To study the influence of the interface material on the homogenized elastic properties of the unidirectional fiber composite material, different Young's modulus are assigned to this material. Two different cases are identified: the interface is tougher than the matrix but softer than the fiber or the interface is the toughest material.

To take this into account, the stiffness ratio between the fiber and matrix material is set to 10 and the Young's modulus of the interface material ranges from the matrix Young's modulus to values higher than those of the fiber properties. For that purpose, a parameter q is created and denotes the interface Young's modulus, E_{inter}, normalized between the other two constituents' properties:

$$q = \frac{E_{inter} - E_m}{E_f - E_m}, \tag{7.1}$$

where E_f and E_m is the fiber and matrix Young's moduli, respectively. By changing the value of q, the Young's modulus of the interface varies and if $q = 0$, the interface is equal to the matrix material and, on the contrary, if $q = 1$, the interface and the fiber materials share the same properties. The elastic properties of these constituents are presented in Table 7.1.

Table 7.1: Elastic properties assigned to each constituent of the RVE.

	Young's Modulus	**Poisson's Ratio**	**Gray Color**
Fiber	100 GPa	0.3	0.6
Matrix	10 GPa	0.3	0.2
Interface	-	0.3	RGB*

*Red = 0.85, Green = 0.00, Blue = 0.00

7.3 Finite Element Mesh Generation

With the image segmentation completed, the finite element mesh has to be generated. Similar to the process followed in Section 6.1.3, the initial skeleton is generated through the automated script of OOF2, and further improved to lower the two elemental functionals: *homogeneity* and *shape energy*, while correctly characterizing the microstructure's geometry.

7.3.1 Mesh Size

With the insertion of a new material, the ideal element size must be defined again, and studies similar to the ones carried in Section 6.1.3 are performed. The width of the interface equals 10% of the radius of the fibers and, due to this extremely small dimension, the mesh has to be more refined in those parts. Therefore, the parameters used to generate the skeleton (*maxscale*, *minscale* and *homogeneity threshold*) have to change to correctly fit and model the microstructure.

The *maxscale* value is the same and equal to 0.2, since this is the biggest element size that can be used to model the matrix and fiber materials for the 40×40 RVE as mentioned in

Section 6.1.3. Moreover, the *homogeneity threshold* is equal to 0.9 to avoid the refinement of elements that already have low *homogeneity energy*, preventing the generation of a large number of unneeded nodes and elements, making the finite element analysis heavier. Finally, the only specification that has to be changed is the *minscale* parameter, being the one that sets the smallest element dimension.

Due to the difference in material properties and to the small width of the interface, high stress distributions develop in the interfacial part. Hence, a finer mesh should be made to correctly characterize this phenomenon. The *minscale* parameter is then defined as 0.1 to enable the formation of smaller elements in this part. In Table 7.2, the information of two different mesh versions for the 40×40 RVE are presented. The first one is simply created through the automated script of OOF2 and then improved to lower the *shape energy*. The second version is created through the same procedure (with the same parameters), however, it is further refined in the parts of interest. Using the *Refine* routine (with $\alpha = 0.9$) targeted in an expanded selection of the interface elements and with the condition that it only refines elements that have area bigger than 0.01, the number of nodes and elements that define the interfacial part of the microstructure increases. After the *Refine* tool has been applied, the *Split Quads* and the *Swap Edges* routines are used in the elements with homogeneity lower than 0.9 and the *Merge Triangles* and *Rationalize* routines are applied to lower the *shape energy*, that was high because of the application of the *Refine* tool with $\alpha = 0.9$. To finalize, the *Smooth* method is applied ($\alpha = 0.15$) for 10 iterations with the internal boundary nodes pinned.

In Table 7.3, values for an interface material softer than the fiber ($q = 0.5$) and tougher than the fiber ($q = 1.2$) are analysed and only the Young's moduli, shear modulus and 2-norm of $\mathbf{C}^*$ are presented, along with the respective relative differences between both versions.

Table 7.2: Final information of both mesh versions of the 40×40 RVE.

Mesh	**Nodes**	**Elements**	**Homogeneity**
1	93081	138377	0.992
2	107259	159781	0.993

Table 7.3: Comparison between both mesh versions for the 40×40 RVE.

q	**Mesh**	E_1^*	E_2^*	E_3^*	G_{12}^*	2-norm of $\mathbf{C}^*$	**Unit**
0.5	**1**	20.388	20.480	45.051	7.486	60.411	GPa
		0.011	0.011	0.007	0.030	0.010	%
	2	20.386	20.477	45.054	7.483	60.417	GPa
1.2	**1**	20.941	21.039	49.877	7.671	64.594	GPa
		0.020	0.014	0.053	0.048	0.037	%
	2	20.937	21.036	49.904	7.667	64.618	GPa

With these results it can be noticed that a more refined mesh in the interface part is not

needed and the version 1 is good enough to correctly characterize the microstructure behaviour, when estimating the homogenized elastic properties of the composite material. Figure 7.4 presents the procedure from the image segmentation step until the generation of the finite element mesh.

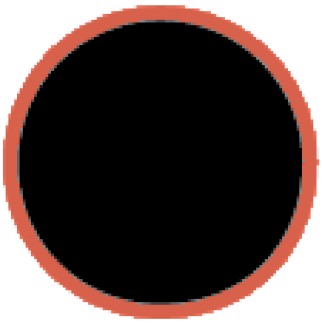

(a) Pixel selection of the interface material.

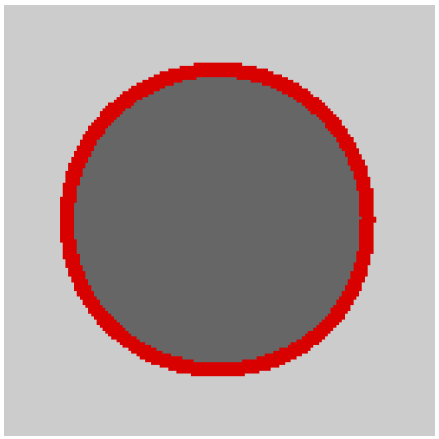

(b) Material map.

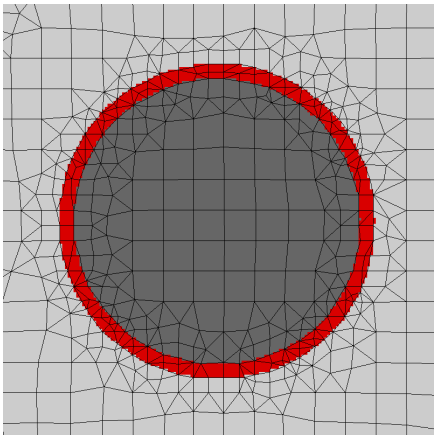

(c) Skeleton geometry.

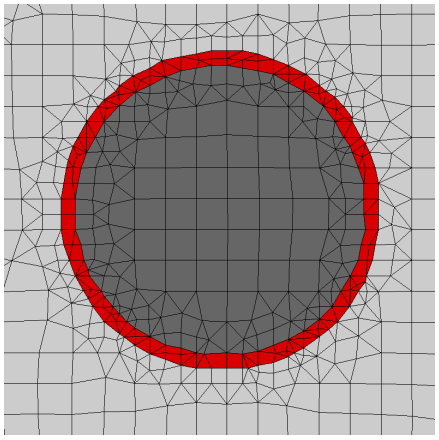

(d) Finite element mesh.

Figure 7.4: Image segmentation and finite element mesh generation for the RVE with the interface material of width equal to 10% of the fiber radius.

7.4 RVE Size

Due to the insertion of a different material in the microstructure, the RVE size that correctly represents it may change and, to validate the 40×40 RVE, deemed as the optimal RVE size in the previous chapter, the estimated elastic properties obtained with this RVE are compared with those obtained with the 50×50 RVE.

The stiffness ratio is 10, $E_m = 10$ GPa and $q = 0.5$, meaning that $E_{\text{inter}} = 55$ GPa. The numerical results obtained for each RVE and the relative difference between these are given in Table 7.4.

Table 7.4: Homogenized elastic properties for the 40×40 and 50×50 RVEs.

RVE	E_1^*	E_2^*	E_3^*	G_{12}^*	2-norm of $\mathbf{C}^*$	**Unit**
$\mathbf{40 \times 40}$	20.388	20.479	45.051	7.486	60.411	GPa
	0.108	0.085	0.142	0.315	0.100	%
$\mathbf{50 \times 50}$	20.366	20.462	45.115	7.509	60.471	GPa

RVE	ν_{12}^*	ν_{21}^*	ν_{13}^*	ν_{31}^*	ν_{23}^*	ν_{32}^*	**Unit**
$\mathbf{40 \times 40}$	0.3399	0.3414	0.1358	0.3000	0.1364	0.3000	-
	0.294	0.322	0.295	0.000	0.220	0.000	%
$\mathbf{50 \times 50}$	0.3409	0.3425	0.1354	0.3000	0.1361	0.3000	-

The values obtained are extremely similar, with relative differences around 0.2%. Thus, the 40×40 RVE is still capable of characterizing the microstructure behaviour of this particular material.

7.5 Results

In this section the influence of the interface material is analysed for a width of 5%, 10% and 15% of the fiber radius (hereafter denominated only by 5%, 10% and 15%). However, to make sure that the values obtained are correct, it is important to validate the results first.

Validation

As mentioned in Section 7.1 and 7.2, during the image manipulation and segmentation, it was important to secure a similar fiber volume fraction in both RVEs to have consistency in the results. The gray color attributed to the interface material and the *delta gray* parameters were defined with this purpose and the results are presented in Table 7.5. As it can be seen, the fiber volume fraction is practically the same.

Table 7.5: Volume fraction of each constituent of the 40×40 RVEs without and with interface material of various widths.

RVE	**Fiber**	**Matrix**	**Interface**	**Unit**
No Interface	35.07	64.93	-	%
Interface - 5%	34.98	61.07	3.95	%
Interface - 10%	35.12	57.22	7.66	%
Interface - 15%	34.92	53.31	11.77	%

With this information, if one considers that the interface material is equal to the matrix material ($q = 0$), these new RVEs may be considered the same as the one used in the last chapter. Therefore, a comparison can be made between the results already obtained (from the

RVE without interface and analysed in Chapter 6) and the values attained from these RVEs, with $q = 0$, and computed with the *Mortar Periodic* boundary condition. The results are obtained for a stiffness ratio of 10 and presented in Table 7.6, where the values located in the second rows of the 5%, 10% and 15% RVEs are the relative differences between the respective and the RVE with no interface.

Table 7.6: Comparison between the results obtained from the 40×40 RVEs without and with interface material of various widths. In the RVEs with interface, the parameter $q = 0$.

RVE	E_1^*	E_2^*	E_3^*	G_{12}^*	2-norm of $\mathbf{C}^*$	**Unit**
No interface	17.991	18.056	41.563	6.589	54.792	GPa
Interface - 5%	17.919	17.982	41.484	6.559	54.683	GPa
	0.401	0.413	0.190	0.466	0.200	%
Interface - 10%	17.948	18.015	41.604	6.572	54.816	GPa
	0.238	0.277	0.097	0.264	0.042	%
Interface - 15%	17.883	17.947	41.431	6.548	54.608	GPa
	0.597	0.604	0.318	0.627	0.335	%

RVE	ν_{12}^*	ν_{21}^*	ν_{13}^*	ν_{31}^*	ν_{23}^*	ν_{32}^*	**Unit**
No interface	0.3471	0.3484	0.1299	0.3000	0.1303	0.3000	-
Interface - 5%	0.3484	0.3497	0.1296	0.3000	0.1300	0.3000	-
	0.375	0.373	0.231	0.000	0.230	0.000	%
Interface - 10%	0.3485	0.3498	0.1294	0.3000	0.1299	0.3000	-
	0.403	0.402	0.385	0.000	0.307	0.000	%
Interface - 15%	0.3487	0.3500	0.1295	0.3000	0.1300	0.3000	-
	0.479	0.460	0.313	0.000	0.266	0.000	%

The majority of the relative differences are all smaller than 0.5%. Therefore, the RVEs may be compared with each other when $q = 0$.

7.5.1 Stiffness Ratio = 10

Now that the validation of the results has been performed, the values obtained with an interface material of width equal to 5%, 10% and 15% of the fiber radius, while the parameter q increases, are analysed. The stiffness ratio between fiber and matrix is set to 10 and the values of the homogenized plane Young's modulus, E_p^*, are illustrated in Figure 7.5 for both interfacial widths. There is a higher discretization of the parameter q between the 0.0 and 0.2 to better define that range.

The dependency is similar to the one found in Figure 6.23, that relates the homogenized plane Young's modulus with the stiffness ratio of the fiber and matrix materials, i.e. the stiffness of the interface material becomes less important as it increases. Furthermore, and as expected,

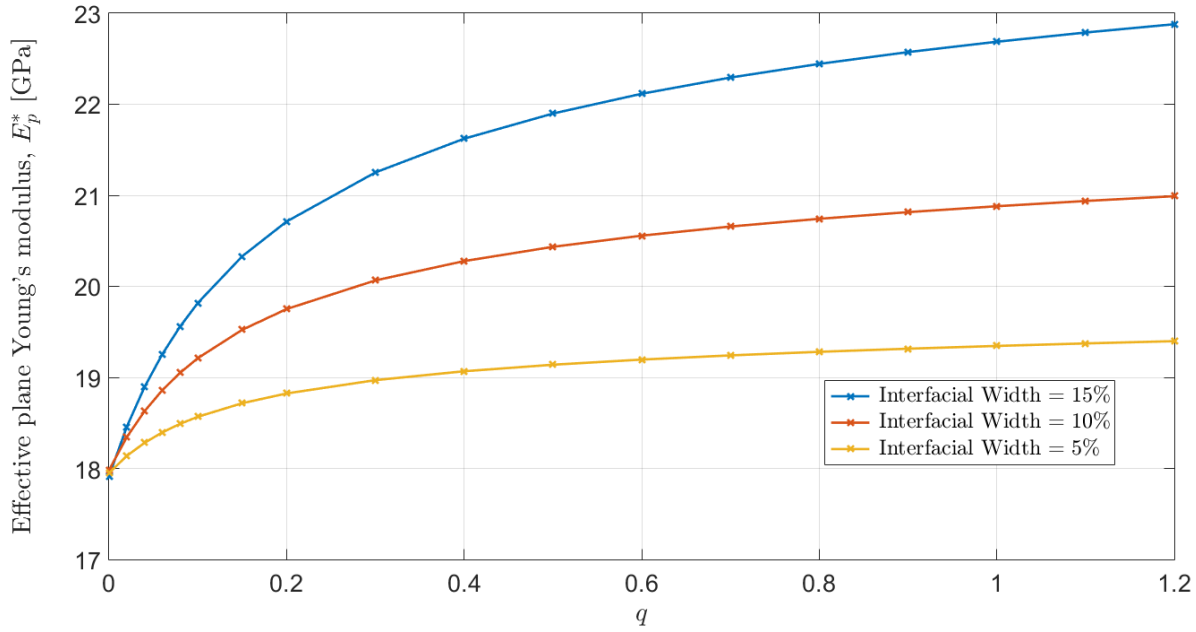

Figure 7.5: Influence of the interface material with different widths on the homogenized plane Young's modulus, E_p^*.

the width of this material is a major factor regarding the overall properties of the composite material. The slope in the stabilized part ($q > 0.6$) is higher for higher widths.

In Figure 7.6, the results for the shear modulus are presented and one can notice that, both effective plane Young's and shear moduli have the same trend.

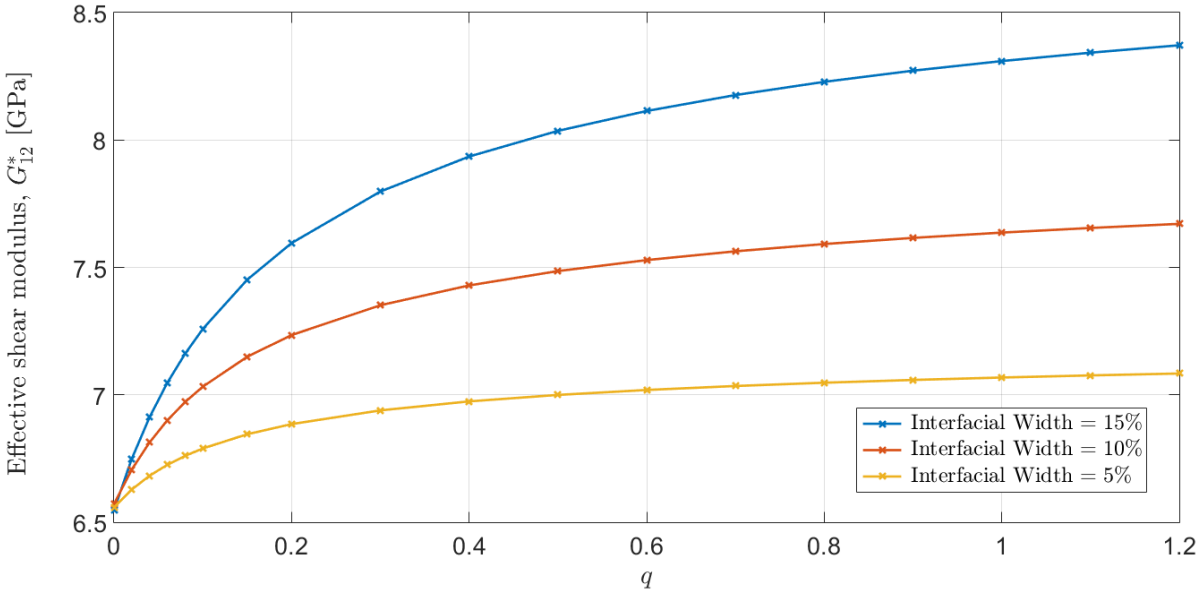

Figure 7.6: Influence of the interface material with different widths on the homogenized plane shear modulus, G_{12}^*.

7.5.2 Different Stiffness Ratios

The results obtained in the last section were computed for a stiffness ratio of 10. In this section, different stiffness ratios are tested to analyse if this parameter has any influence on the way the homogenized properties depend on the interface material.

Figure 7.7 illustrates the same as Figure 7.5 but for a stiffness ratio of 10, 35 an 70. The different interfacial widths are also presented in this figure and the homogenized plane Young's modulus is normalized dividing the result by the Young's modulus of the matrix material.

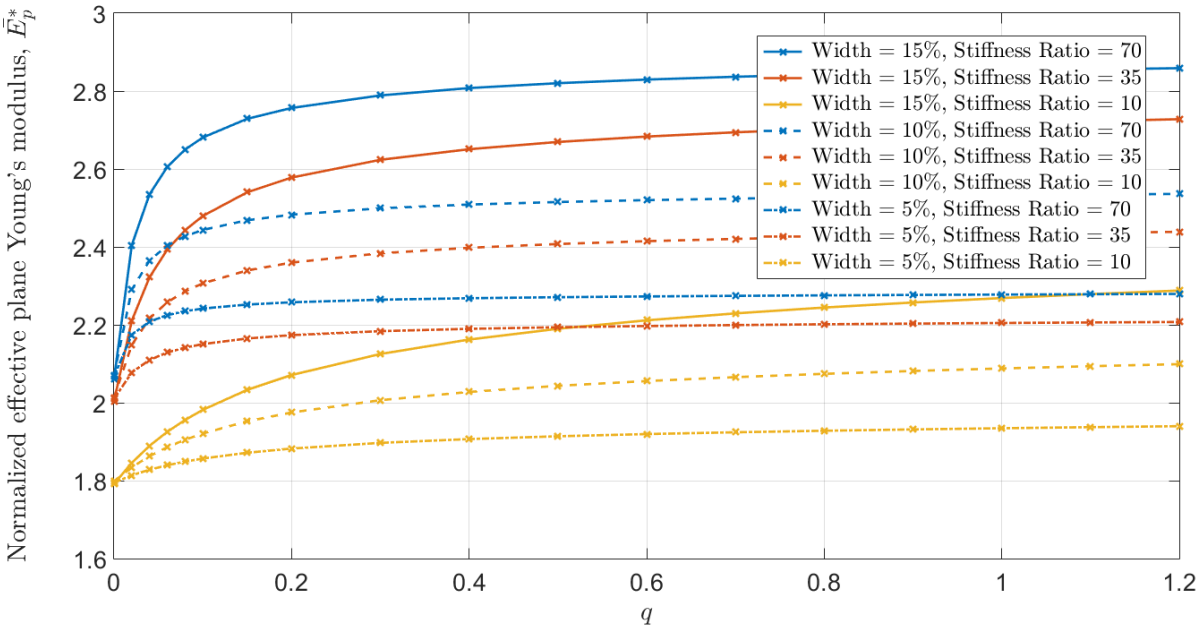

Figure 7.7: Influence of the interface material with different widths on the normalized effective plane Young's modulus, $\bar{E}_p^*$, for different stiffness ratios of the fiber/matrix materials.

Analysing these results, it is possible to verify that the conclusion withdrawn in Section 6.2 is admissible, i.e. increasing the stiffness ratio between the fiber/matrix materials does not have a big impact for values higher than 20/30. For instance, the difference in the homogenized properties while increasing the stiffness ratio from 10 to 35 is large, but from 35 to 70 this difference sharply decreases. Having a unidirectional fiber composite material characterized by a stiffness ratio of 35 and with a width of 10% of the fiber radius produces, for a $q > 0.04$, better results than a composite with a stiffness ratio of 70 and with a width of 5%. Even more, if one considers interfaces tougher than the fiber material, a composite with stiffness ratio of 10 and width of 15% has the same plane Young's modulus than one with stiffness ratio of 70 and width of 5%.

The same type of dependency is found in the three different stiffness ratios tested. Moreover, the slope at the beginning increases with the stiffness ratio.

7.5.3 Analytical Expressions

Since, for different stiffness ratios, the homogenized plane Young's modulus seems to be approximated by the same type of mathematical expression, a curve fitting is performed. The MATLAB® *Curve Fitting Tool* is used for this purpose.

Interfacial Width = 10%

All the results presented in this section are obtained considering that the width of the interface material is 10% of the fiber radius. Therefore, using the curve fitting tool, it is possible to fit the values obtained for a stiffness ratio of 10 to a sum of two exponential functions, denoted by:

$$\bar{E_p^*} = a \ \exp(b \cdot q) + c \ \exp(d \cdot q), \tag{7.2}$$

where a, b, c and d are constants that characterize the mathematical expression. In the case of a stiffness ratio of 10, these parameters are:

$$a = 2.0146, \tag{7.3a}$$

$$b = 0.0355, \tag{7.3b}$$

$$c = -0.2035, \tag{7.3c}$$

$$d = -6.8207, \tag{7.3d}$$

and the curve fitting is demonstrated in Figure 7.8. In this figure, along with the values obtained for the stiffness ratio of 10, two other different stiffness ratios are presented with the respective exponential curve fittings. The approximations are made with an expression equal to Equation (7.2), but with different parameters. Thus, increasing the discretization of the stiffness ratio, Table 7.7 presents the respective a, b, c and d parameters for all cases, along with the respective coefficient of determination, R^2, of the curve fittings to the numerical results.

The values shown in Table 7.7, demonstrate that, despite the fact that the coefficient of determination (characterized by R^2) worsens as the stiffness ratio increases, the curve fittings are excellent approximations to the results obtained by the numerical method. The exponential curve fittings were made with the fit option robust "Bisquare" selected. It enabled a better approximation for all points except for $q = 0$ that, as the stiffness ratio increases, is not correctly expressed by Equation (7.2). Furthermore, the parameters seem to have a correspondence with the stiffness ratio.

Therefore, a curve fitting is made to relate the constants presented in Table 7.7. The following equations are the ones that better express the dependency of these parameters:

$$a = m_1 \cdot r^{\,n_1} + p_1, \tag{7.4a}$$

$$b = \frac{m_2 \cdot r + n_2}{r + p_2}, \tag{7.4b}$$

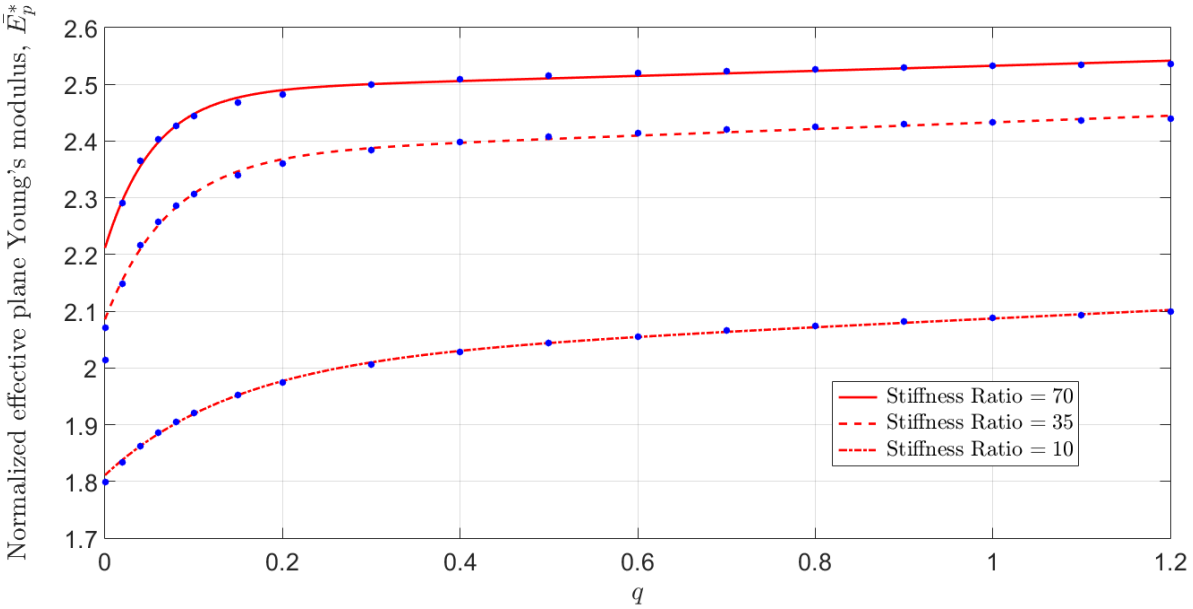

Figure 7.8: Exponential curve fitting of the normalized effective plane Young's modulus, $\bar{E}_p^*$, for different stiffness ratios of the fiber/matrix materials. The interfacial width is equal to 10% of the fiber radius.

Table 7.7: Parameters that characterize the curve fitting for different stiffness ratios and respective coefficient of determination, R^2.

Stiffness Ratio	a	b	c	d	R^2
5	1.7212	0.0378	-0.1248	-4.4461	0.9998
10	2.0146	0.0355	-0.2035	-6.8207	0.9992
15	2.1565	0.0323	-0.2434	-8.7108	0.9984
20	2.2423	0.0296	-0.2657	-10.2605	0.9977
25	2.3005	0.0274	-0.2786	-11.5768	0.9970
30	2.3428	0.0256	-0.2858	-12.7146	0.9964
35	2.3752	0.0241	-0.2894	-13.7065	0.9958
40	2.4009	0.0228	-0.2907	-14.5803	0.9954
45	2.4219	0.0216	-0.2903	-15.3567	0.9950
50	2.4390	0.0209	-0.2887	-16.0920	0.9948
55	2.4539	0.0201	-0.2856	-16.6607	0.9945
60	2.4673	0.0191	-0.2835	-17.2161	0.9942
65	2.4786	0.0183	-0.2803	-17.6976	0.9940
70	2.4884	0.0177	-0.2767	-18.1471	0.9939

$$c = \frac{m_3 \cdot r + n_3}{r^2 + p_3 \cdot r + k_3}, \tag{7.4c}$$

$$d = \frac{m_4 \cdot r + n_4}{r + p_4}, \tag{7.4d}$$

where r denotes the stiffness ratio between fiber and matrix and the parameter a is expressed by a power function of two terms, the parameters b and d are approximated by a rational function of degree 1 in both the numerator and denominator and the parameter c is given by a rational function of degree 1 in the numerator and 2 in the denominator. For a width of 10%, the constants that defined these functions are expressed in Table 7.8 and the respective curve fittings are presented in Figure 7.9.

Table 7.8: Constants that define the expressions for the parameters a, b, c and d (Equations (7.4)) for an interfacial width of 10%.

	1	**2**	**3**	**4**
m_i	-2.3299	0.0048	-72.32	-27.6514
n_i	-0.4772	1.5139	80.66	-63.7359
p_i	2.7989	34.5089	167.3	40.1317
k_i	-	-	1389	-

Now that the 5 expressions that characterize the normalized effective plane Young's modulus, $\bar{E_p^*}$, are presented, these equations are programmed in Microsoft Excel® to analyse the error induced by them. Since the values are normalized by the Young's modulus of the matrix material ($E_m = 10$ GPa during the simulations that produced these results), the homogenized properties can be determined for different Young's modulus of the matrix material.

In Table 7.9, several tests are presented along with the relative error between the results given by MSP, $E^*_{p_{\text{MSP}}}$ (average of E_1^* and E_2^*), and the analytical expressions, E_p^* determined in this section.

Table 7.9: Relative errors between numerical results and analytical results obtained by Expression (7.2) for a width of 10%.

E_m [GPa]	**Stiffness Ratio**	q	E_p^* [GPa]	$E^*_{p_{\text{MSP}}}$ [GPa]	**Relative Error** [%]
10	17.85	0.83	22.666	22.698	0.141
15	14.6	0.64	32.918	32.925	0.021
15	14.6	1.5	33.860	33.605	0.757
20	47	0.05	45.961	46.143	0.394
20	47	0.15	48.159	48.020	0.290
20	47	0.3	48.816	48.784	0.065
20	47	1.5	50.137	49.845	0.586

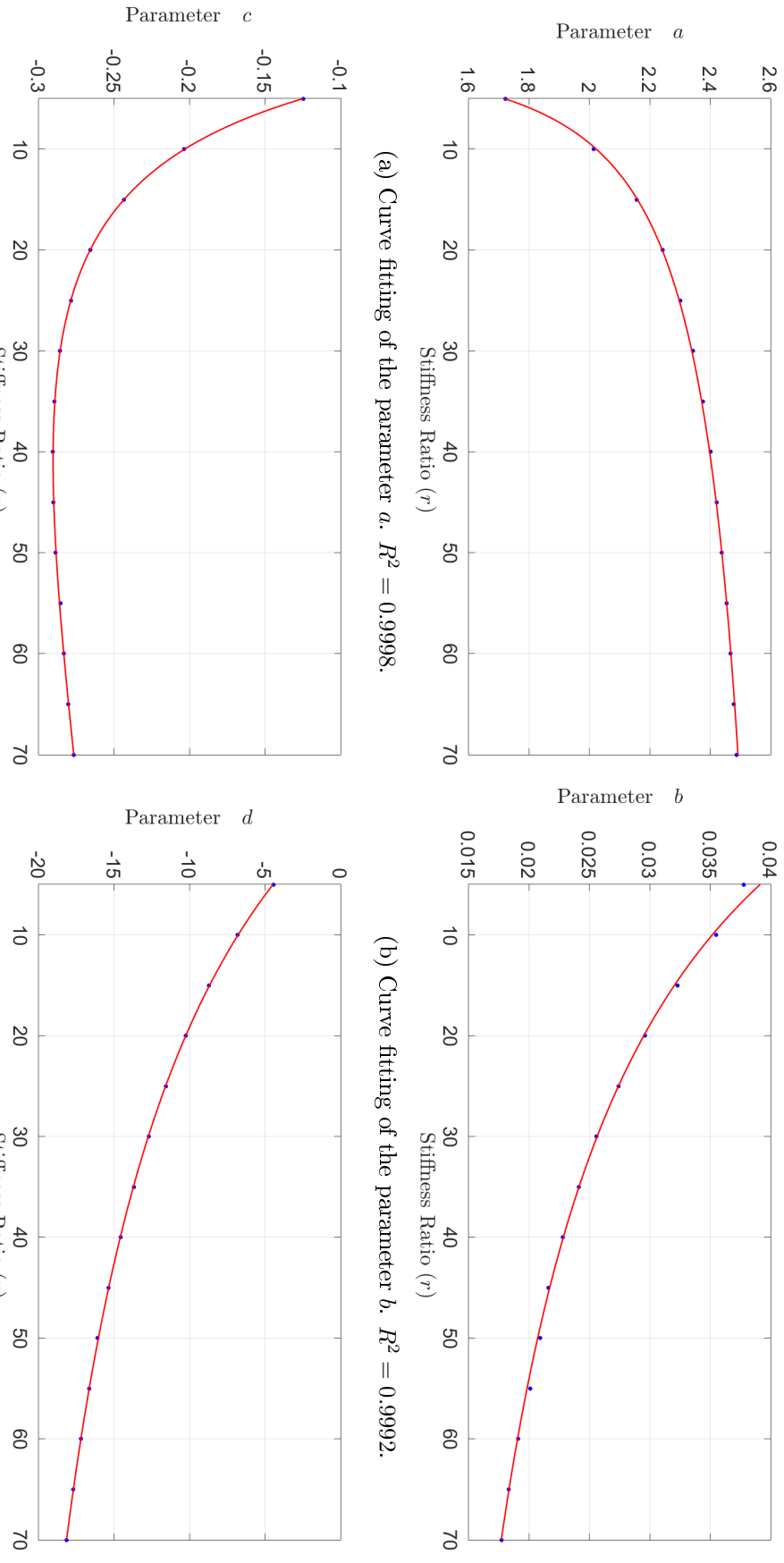

(a) Curve fitting of the parameter a. $R^2 = 0.9998$.

(b) Curve fitting of the parameter b. $R^2 = 0.9992$.

(c) Curve fitting of the parameter c. $R^2 = 1.0000$.

(d) Curve fitting of the parameter d. $R^2 = 1.0000$.

Figure 7.9: Curve fittings for the parameters that define Equation (7.2) for an interfacial width of 10%.

Different Interfacial Widths

The same procedure is followed for the RVEs that model different interface material widths and the constants m, n, p and k that characterize Equations (7.4) are determined and presented in Table 7.10. It is possible to note a relation between these constants as the width of the interface increases.

Table 7.10: Constants that define the expressions for the parameters a, b, c and d (Equations (7.4)) for different interfacial widths.

Width	Parameter	1	2	3	4
5%	m_i	-1.9424	0.0004	-27.11	-29.0250
	n_i	-0.5550	0.8221	30.79	-61.2528
	p_i	2.4466	35.6782	134	38.3728
	k_i	-	-	1037	-
10%	m_i	-2.3299	0.0048	-72.32	-27.6514
	n_i	-0.4772	1.5139	80.66	-63.7359
	p_i	2.7989	34.5089	167.3	40.1317
	k_i	-	-	1389	-
15%	m_i	-2.8851	0.0277	-163.2	-26.5907
	n_i	-0.3943	2.2693	184.8	-93.1313
	p_i	3.3180	33.1444	224	46.8829
	k_i	-	-	1971.4	-

7.6 Conclusions

In this chapter, the impact of different interface properties between the fiber and matrix material was analysed. Using Adobe Illustrator®, the micrograph was modified and a new color was inserted around the fiber inclusions, to be later interpreted as a new material by OOF2.

To extract valid results, in the first place it was verified that the RVE size is not influenced by the insertion of this new material, thus, the 40×40 RVE continues to correctly characterize the microstructure behaviour.

The study was carried for the overall in-plane properties of the composite material, more specifically the effective plane Young's modulus, E_p^*. Analysing the results, it can be concluded that the influence of the elastic properties of the interface material on this homogenized properties are high. Not only the elastic properties but also the width of the interface material plays a major role on the overall properties of the composite material. There are cases where having a larger width is better than increasing the stiffness ratio between fiber/matrix materials.

Furthermore, since the dependency of the homogenized plane Young's modulus over the Young's modulus of the interface material (represented by the parameter q) seemed to be

similar for different stiffness ratios, a curve fitting was made using the *Curve Fitting Tool* of MATLAB®. It was revealed that the results can be expressed by a sum of two exponential functions characterized by four parameters (a, b, c and d) and that these parameters depend on the stiffness ratio of the fiber/matrix materials. Thus, the homogenized plane Young's modulus is approximated (with a high coefficient of determination - R^2) by a mathematical expression that is defined by more four mathematical functions. Moreover, for a specific volume fraction, it only depends on the stiffness ratio, on the parameter q and on the interfacial width. The errors presented in Table 7.9 are small, meaning that the mathematical approximation is successful.

To summarize, by using a program to manipulate the micrograph of the material, a new RVE was created and new conclusions were withdrawn by analysing it. The DIB microstructure recognition technique is extremely flexible, enabling a minimal change on a RVE to be translated into new outcomes and conclusions.

Chapter 8

Conclusions and Future Works

A methodology based on image acquisition and recognition has been proposed to model the behaviour of heterogeneous materials at the microscale. It is not based on assumptions or simplifications, as it considers the microstructure geometry given by real micrographs. At the beginning of the document the goals are settled, being analysed hereafter.

As mentioned in the introductory chapter, two initial chapters of bibliographic references are presented, were concepts such as *Continuum Mechanics*, *Micromechanics* and *Multi-Scale* models are introduced as the foundations that support the next chapters. With *Continuum Mechanics*, the assumption that solids may be modelled as a continuum medium, facilitates the understanding of their overall behaviour while loaded or deformed. *Micromechanics* enables the study of heterogeneous materials by analysing them at the microscale level, thus, considering the influence of each constituent (considered as continuum) to model the overall behaviour of the material. Finally, *Multi-Scale* models create the bridge between both macro and microscale and introduce a new and reliable method to simulate the behaviour of multi-phase materials. Furthermore, to characterize the microstructure of the material, the concept of *Representative Volume Element* (RVE) is introduced in Section 3.1.

The main aspect of this thesis is the use of real micrographs to create RVEs that model the concerned material. Hence, the *Digital Image Based* (DIB) microstructure recognition technique is introduced and described in Chapter 4, with the support of two Linux® open-source programs: OOF2 and OOF3D. Usually, *Multi-Scale* models use simplified RVEs to predict the impact of singularities with different characteristics in the microstructure of the material. In this case, with the use of real micrographs, the method becomes more general, modelling heterogeneous materials of any complexity, being it metallic, ceramic, polymeric or composites.

The programs used to perform the image recognition and generate the finite element mesh have yet several limitations. In OOF2, minor bugs add a degree of difficulty when analysing images of high quality that need to be modelled by a large amount of nodes and elements. Moreover, OOF3D presents errors that prevent its usage during this thesis, since the output

file cannot be saved in the format needed. Nonetheless, other methods were tested such as, using the GiD® and the Abaqus® programs to generate the finite element meshes for 3D RVEs that had 2D micrographs as cross section. However, these attempts created a number of nodes/elements that could not be analysed by the *Micro-Scale Problem* (MSP), due to a limitation on the amount of memory that the direct solver (PARDISO 5.0.0) can allocate.

The main goal of this thesis was to use the aforementioned DIB microstructure recognition and *Multi-Scale* models to estimate the homogenized elastic properties of heterogeneous materials. In Chapter 5, other than introducing the numerical methodology used to obtain these properties from finite element analyses, also presented several analytical expressions that aim to estimate these values through *mean field approaches*.

The ideal size of RVE that should be used was the first parametric study performed in this thesis, as it is one the most important factors to take into account when using *Multi-Scale* models. It was proved that RVEs smaller than this optimal size are likely to give wrong results and that, for a unidirectional fiber composite, the smallest RVE size that still is statistically representative of the microstructure should be around 15/20 times larger than the size of a single fiber (inclusion). Moreover, the refinement of the finite element mesh was also studied *a priori*, since the results obtained with the *Finite Element Method* are highly dependent on this aspect. For the analysed case, an element size of approximately one fourth of the fiber radius enabled accurate results. In addition, the image quality of the micrograph plays a major role on the results, since higher quality enables a better characterization of the microstructure. However, due to the fact that the phases' volume fraction may change, one should be careful when manipulating a micrograph. After all, this parameter drives the whole homogenized elastic properties.

Furthermore, all results obtained in Chapter 6 were consistent with the literature. The *Mortar Periodic* boundary condition converged faster to the theoretical value and was always enclosed by the *Linear* and *Uniform Traction* boundary conditions, that define the upper and lower bounds, respectively. Also, the results achieved with the numerical method were similar to the ones predicted by the *Mori-Tanaka* analytical model. This is, the numerical method, based on the combination of *Multi-Scale* models and DIB microstructure recognition techniques, produced results with extremely small relative differences, for cases that could be compared with known results. Therefore, these results indicate that this numerical model is accurate enough to predict the mechanical behaviour of heterogeneous materials of higher complexity, for which the analytical methods, mentioned in the literature, are not able to provide results.

In Chapter 7, the influence of an interface material on the homogenized properties was analysed. The RVE size remained the same and a study on the mesh size was also carried out, leading to the conclusion that for the purpose of this thesis, a mesh of similar size continued to be refined enough. The impact of the interface on the homogenized properties is high and seems to increase linearly with larger widths. Furthermore, mathematical expressions were deduced to obtain the homogenized plane Young's modulus, while taking into consideration the stiffness ratio between fiber/matrix materials, the Young's modulus of the interface material

and its width. The average coefficient of determination (R^2) of these equations with the numerical results is above 0.995, which means that the homogenized plane Young's modulus can be accurately estimated by them.

Despite the fact that throughout this work, only heterogeneous materials up to three different constituents have been analysed, the proposed methodology does not have any limitation regarding this aspect.

To summarize, different MATLAB® scripts were created to connect the different programs used throughout the thesis and the final results are extremely satisfactory. Apart from the use of OOF3D to estimate the homogenized properties from 3D RVEs due to computational limitations, all goals were completed. The results presented in this thesis are considered as a good starting point in the use of this methodology to model the microscopic behaviour of materials that are becoming progressively more complex.

8.1 Future Works

Relying on the work earlier presented, further developments and validations could be done with a combined effort of experimental and numerical procedures. For instance, comparing the elastic properties of a heterogeneous material obtained through experimental methods with those obtained by the DIB microstructure recognition technique (using a real micrograph of the concerned material).

Since there are no analytical methods to estimate the elastic properties of highly complex materials (e.g. materials with a large number of constituents or with singularities with unusual shapes), this type of approach could add more credibility to the presented methodology. In addition, it could support the study of 3D RVEs (with an upgraded version of OOF3D or with a different open-source or commercial program).

Furthermore, since in this thesis only the elastic domain was addressed, new studies about non-elasticity or fracture damage could be developed. The current knowledge in this areas is limited, and through this procedure, the impact of singularites of higher complexity could be studied.

Interface Materials

In Chapter 7, analytical equations were proposed to obtain the homogenized plane Young's modulus of unidirectional fiber composites. This study can be extended to other elasticity constants (e.g. plane shear modulus or Poisson's ratio).

Moreover, only three different widths were analysed and a relation could be identified between this parameter and the homogenized property. Therefore, by increasing the discretization of the interfacial width, a new mathematical equation that would depend on two arguments (parameter q and interfacial width) may be identified, as illustrated in Figure 8.1 (this representation is purely figurative, since it was created solely based on three different widths). This 3D

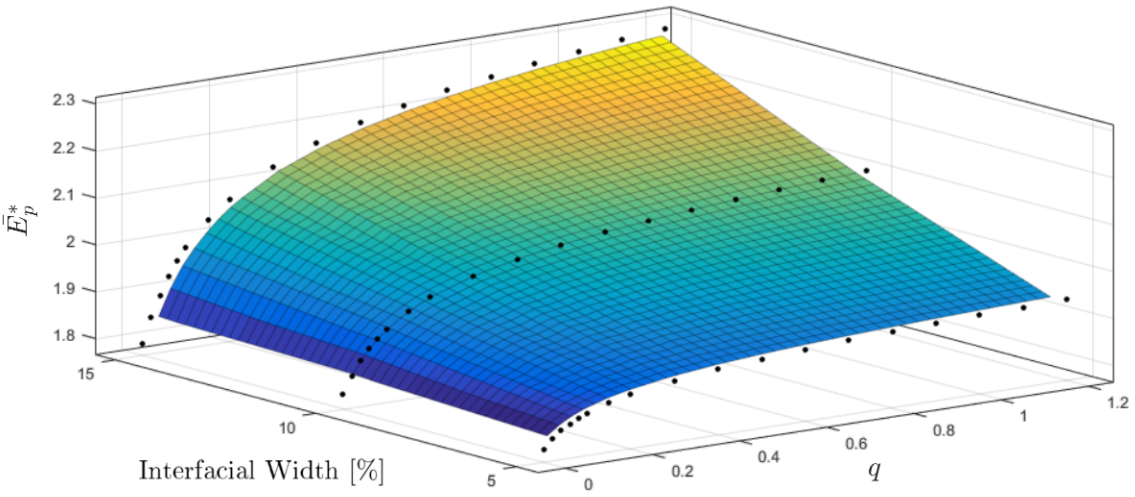

Figure 8.1: 3D representation of and extended version of Equation (7.2).

surface would depend on the stiffness ratio between fiber/matrix and on the width and Young's modulus of the interface material.

In addition, and with the purpose of creating a more general empiric expression, the fiber volume fraction can also be changed, making Equations (7.4) dependent of not only the stiffness ratio but also on the fiber volume fraction. This would make the whole assembly of equations ((7.2); (7.4)) as 3D surface mathematical expressions, leading to a model that would be able to characterize the plane Young's modulus of any unidirectional fiber composite (with $\nu_m = \nu_f = 0.3$).

Appendix A

Relations between Elastic Constants

The stiffness and compliance tensors, C and S, respectively, are characterized by elasticity constants. In Table A.1, the relations between the most common constants are presented, where E, G and ν represent the Young's modulus, the Shear modulus and the Poisson's ratio and K and λ denote the Bulk modulus and the Lamé's first parameter, respectively.

Table A.1: Relations between elastic constants.

	λ	G	E	ν	K
λ , G	λ	G	$\frac{G(3\lambda+2G)}{\lambda+G}$	$\frac{\lambda}{2(\lambda+G)}$	$\lambda+\frac{2}{3}G$
λ , E	λ	$\frac{E-3\lambda+r}{4}$	E	$\frac{2\lambda}{E+\lambda+r}$	$\frac{E+3\lambda+r}{6}$
λ , ν	λ	$\frac{\lambda(1-2\nu}{2\nu}$	$\frac{\lambda(1+\nu)(1-2\nu)}{\nu}$	ν	$\frac{\lambda(1+\nu)}{3\nu}$
λ , K	λ	$\frac{3}{2}(K-\lambda)$	$\frac{9K(K-\lambda}{3K-\lambda}$	$\frac{\lambda}{3K-\lambda}$	K
G , E	$\frac{G(E-2G)}{3G-E}$	G	E	$\frac{E-2G}{2G}$	$\frac{GE}{3(3G-E)}$
G , ν	$\frac{2\nu G}{1-2\nu}$	G	$2G(1+\nu)$	ν	$\frac{2G(1+\nu)}{3(1-2\nu)}$
G , K	$K-\frac{2}{3}G$	G	$\frac{9KG}{3K+G}$	$\frac{3K-2G}{6K+2G}$	K
E , ν	$\frac{E\nu}{(1+\nu)(1-2\nu)}$	$\frac{E}{2(1+\upsilon)}$	E	ν	$\frac{E}{3(1-2\nu)}$
E , K	$\frac{3K(3K-E)}{9K-E}$	$\frac{3KE}{9K-E}$	E	$\frac{3K-E}{6K}$	K
ν , K	$\frac{3K\nu}{1+\nu}$	$\frac{3K(1-2\nu)}{2(1+\nu)}$	$3K(1-2\nu)$	ν	K

$r=\sqrt{E^2+9\lambda^2+2E\lambda}$

Appendix B

MATLAB® Script for the Interface of OOF2-MSP

Appendix B contains the code developed to connect OOF2 with MSP. The scripts were all developed in MATLAB® and can be found on the attached CD.

The purpose of these scripts is to read the ".mesh" file given by OOF2 (saved in *Abaqus* format), interpret the data contained on it and write an output ".dat" file with the whole problem information described. This file is later loaded on MSP to perform the finite element analysis.

The program contains a data file where the information needed (e.g. type of problem, prescribed deformation gradient, boundary condition, material properties, number of increments) is introduced. It can work with any number of materials and it is fully automatic, once the data file is correctly defined and, if the parameters do not present the correct format, the program issues warning messages.

While transcribing the nodes and elements data, a script computes the area of each element to determine the volume fraction of each material. This is important, since E_3^*, in the case of 2D plane strain problems, is calculated by the *Voigt* model.

In addition, the data file contains a couple of options, enabling the writing of multiple files at once (e.g. different boundary conditions with a set of prescribed deformation gradients for each).

Appendix C

Demonstration of the Equality between the Mori-Tanaka model and the Lower Bound of Hashin-Shtrikman for a Particular Case

The following appendix contains the mathematical derivation that leads to the conclusion that Equations (5.63) are equal to Equations (5.42a) and (5.43a). Let us consider that the constituent 1 is the matrix material and that 2 is the inclusion. Therefore, the expressions of the bulk modulus for the *Mori-Tanaka* method and for the lower bound of *Hashin* and *Shtrikman* are presented below, respectively:

$$K^* = K_m \left[1 + \frac{\phi_c \left(\frac{K_c}{K_m} - 1 \right)}{1 + \alpha \left(1 - \phi_c\right) \left(\frac{K_c}{K_m} - 1 \right)} \right] \tag{C.1a}$$

$$K_L^* = K_m + \frac{\phi_c}{\frac{1}{K_c - K_m} + \frac{3\left(1 - \phi_c\right)}{3K_m + 4G_m}} \tag{C.1b}$$

where,

$$\alpha = \frac{1 + \nu_m}{3\left(1 - \nu_m\right)}, \tag{C.2a}$$

$$\nu_m = \frac{3K_m - 2G_m}{6K_m + 2G_m}, \tag{C.2b}$$

and ν_m is the Poisson's ratio of the matrix phase. The first step was to simplify Equation (C.1a):

$$K^* = K_m \left[1 + \frac{\phi_c \left(\frac{K_c}{K_m} - 1 \right)}{1 + \alpha \left(1 - \phi_c\right) \left(\frac{K_c}{K_m} - 1 \right)} \right]$$

$$= K_m + \frac{\phi_c \left(K_c - K_m\right)}{1 + \alpha \left(1 - \phi_c\right) \left(\frac{K_c}{K_m} - 1 \right)}$$

$$= K_m + \frac{\phi_c}{\frac{1}{K_c - K_m} + \frac{\alpha \left(1 - \phi_c\right) \left(\frac{K_c}{K_m} - 1 \right)}{K_c - K_m}} \tag{C.3}$$

Comparing Equation (C.1b) and (C.3), we can conclude that they are very similar and, as such, only the part of the denominator where they are distinct is addressed. The premise is then:

$$\frac{\alpha \left(1 - \phi_c\right) \left(\frac{K_c}{K_m} - 1 \right)}{K_c - K_m} = \frac{3 \left(1 - \phi_c\right)}{3K_m + 4G_m} \tag{C.4}$$

By replacing Equation (C.2a) in the first term of Equation (C.4) the following is obtained:

$$\frac{\alpha \left(1 - \phi_c\right) \left(\frac{K_c}{K_m} - 1 \right)}{K_c - K_m} = \frac{\frac{1 + \nu_m}{3 \left(1 - \nu_m\right)} \left(1 - \phi_c\right) \left(\frac{K_c}{K_m} - 1 \right)}{K_c - Km} \tag{C.5}$$

In addition, Equation (C.2b) is substituted on $\frac{1 + \nu_m}{3 \left(1 - \nu_m\right)}$ and simple algebra is used to simplify this expression.

$$\frac{1 + \nu_m}{3 \left(1 - \nu_m\right)} = \frac{1 + \nu_m + \nu_m - \nu_m}{3 \left(1 - \nu_m\right)}$$

$$= \frac{1}{3} + \frac{2\nu_m}{3 \left(1 - \nu_m\right)}$$

$$= \frac{1}{3} + \frac{2 \frac{3K_m - 2G_m}{6K_m + 2G_m}}{3 \left(1 - \frac{3K_m - 2G_m}{6K_m + 2G_m} \right)}$$

$$= \frac{1}{3} + \frac{2 \frac{3K_m - 2G_m}{6K_m + 2G_m}}{3 \frac{3K_m + 4G_m}{6K_m + 2G_m}}$$

$$
\begin{aligned}
&= \frac{1}{3} + \frac{2\left(3K_m - 2G_m\right)}{3\left(3K_m + 4G_m\right)} \\
&= \frac{3K_m + 4G_m + 6G_m - 4G_m}{9K_m + 12G_m} \\
&= \frac{9K_m}{9K_m + 12G_m} \\
&= \frac{3K_m}{3K_m + 4G_m} \qquad \text{(C.6)}
\end{aligned}
$$

Plugging Equation (C.6) back into Equation (C.5), we get:

$$
\begin{aligned}
\frac{\alpha\left(1-\phi_c\right)\left(\dfrac{K_c}{K_m} - 1\right)}{K_c - K_m} &= \frac{\dfrac{3K_m}{3K_m + 4G_m}\left(1-\phi_c\right)\dfrac{1}{K_m}\left(K_c - K_m\right)}{K_c - K_m} \\
&= \frac{3\left(1-\phi_c\right)}{3K_m + 4G_m}, \qquad \text{(C.7)}
\end{aligned}
$$

thus concluding that Equations (C.1a) and (C.1b) are in fact equal.

The process to prove that Equation (5.63b) and (5.43a) are also equal is very similar to the method described above, therefore will not be demonstrated.

Appendix D

MATLAB® Script for Post-Processing

Appendix D contains the code developed to obtain the full stiffness tensor of heterogeneous materials under analysis. The scripts were developed in MATLAB® and can be found on the attached CD.

It reads the output file of MSP that contains the first *Piola-Kirchhoff* stress tensor and the deformation gradient for each increment. With that information, the procedure described in Section 5.3.2 is performed and a data file is written with the respective stiffness tensor, individual elastic properties and 2-norm of the stiffness tensor presented.

At the beginning of the script, a couple of options can be defined. For example, the user can choose to input the information about the directory that contains the MSP output files trough graphical user interface or through a ".txt" file (that can contain several directories at once). After these options are defined, the program is fully automatic and can even save all the information in Microsoft Excel® spreadsheet.

Appendix E

MATLAB® Script for the Interface of Abaqus®-MSP

Appendix E contains the code developed to connect Abaqus® with MSP. The scripts were all developed in MATLAB® and can be found on the attached CD.

It reads the ".inp" file exported in Abaqus, extracts the data contained on it and writes an output ".dat" file that is then loaded on MSP. This data file has all the information needed to perform the finite element analysis.

The program is similar to the one described in Appendix B. However, the way Abaqus® allocates the nodes and elements information is different from OOF2, hence, a distinct approach has to be pursued while reading and treating this data.

It is only developed for two different parts (e.g. fibers and matrix), but it can be further extended based on the same methodology.

References

A.Langer, S., Fuller, E. R., and Carter, W. (2001). OOF: An Image-Based Finite-Element Analysis of Material Microstructures. *Computing in Science & Engineering*, pages 15–23.

Benveniste, Y. (1987). A new approach to the application of Mori-Tanaka's theory in composite materials. *Mechanics of Materials*, 6(2):147–157.

Bergen (2016). Phoenix nanome|x. http://www.bergengroupindia.com/product_description.php?product_name=Phoenix nanome|x&product_id=85&pbv_id=3&category_id=18#prettyPhoto, Last accessed on 2016-07-25.

Berryman, J. G. (2004). Bounds and self-consistent estimates for elastic constants of polycrystals composed of orthorhombics or crystals with higher symmetries. *Journal of the Mechanics and Physics of Solids*.

Böhm, H. (2016). A Short Introduction To Basic Aspects of Continuum Micromechanics. Technical report, Institute of Lightweight and Structural Biomechanics (ILSB), Vienna University of Technology.

Bower, A. (2010). *Applied Mechanics of Solids*. CRC Press, Boca Raton, Florida.

Budiansky, B. (1965). On the elastic moduli of some heterogeneous materials. *Journal of the Mechanics and Physics of Solids*, 13(4):223–227.

Carvalho, R. P., Francisco, P., and Andrade, M. (2015). *Análise do Comportamento Elasto-plástico de Materiais Dúcteis baseada em Homogeneização Computacional*. PhD thesis, Faculty of Engineering of the University of Porto.

Chen, J. K., Huang, Z. P., and Mai, Y. W. (2003). Constitutive relation of particulate-reinforced viscoelastic composite materials with debonded microvoids. *Acta Materialia*, 51(12):3375–3384.

Coenen, E. W. C., Kouznetsova, V. G., and Geers, M. G. D. (2012). Novel boundary conditions for strain localization analyses in microstructural volume elements. *International Journal for Numerical Methods in Engineering*, 90(1):1–21.

Eshelby, J. D. (1957). The Determination of the Elastic Field of an Ellipsoidal Inclusion, and Related Problems. *Proceedings of the Royal Society A: Mathematical, Physical and Engineering Sciences*, 241(1226):376–396.

Gitman, I. M., Askes, H., and Sluys, L. J. (2007). Representative volume: Existence and size determination. *Engineering Fracture Mechanics*, 74(16):2518–2534.

Haboussa, D. (2012). Anisotropic elasticity Code _ Aster. Technical report.

Hashin, Z. (1962). The Elastic Moduli of Heterogeneous Materials. *Journal of Applied Mechanics*, 29(1):143–150.

Hashin, Z. (1965). On elastic behaviour of fibre reinforced materials of arbitrary transverse phase geometry. *Journal of the Mechanics and Physics of Solids*, 13(3):119–134.

Hashin, Z. (1983). Analysis of composite materials - A survey. *Journal of Applied Mechanics*, 50(3):481–505.

Hashin, Z. and Shtrikman, S. (1963). A variational approach to the theory of the elastic behaviour of multiphase materials. *Journal of the Mechanics and Physics of Solids*, 11(2):127–140.

Hill, R. (1952). The Elastic Behaviour of a Crystalline Aggregate. *Proceedings of the Physical Society. Section A*, 65(5):349–354.

Hill, R. (1963). Elastic properties of reinforced solids: Some theoretical principles. *Journal of the Mechanics and Physics of Solids*, 11(5):357–372.

Hill, R. (1964). Theory of Mechanical Properties of Fibre-Strengthened Materials: I. Elastic Behaviour. *Journal of the Mechanics and Physics of Solids*, 12(4):213–218.

Hill, R. R. (1965). A Self-Consistent Mechanics of Composite Materials. *Journal of the Mechanics and Physics of Solids*, 13(March 1962):213–222.

Hitachi (2016). SU8030. http://www.mrfn.org/instruments/electron-probe-instrumentation-center-epic/hitachi-su8030, Last accessed on 2016-07-25.

Hwu, C. (2010). *Anisotropic Elastic Plates*. Springer, Tainan City, Taiwan.

Kanit, T., Forest, S., Galliet, I., Mounoury, V., and Jeulin, D. (2003). Determination of the size of the representative volume element for random composites: Statistical and numerical approach. *International Journal of Solids and Structures*, 40(13-14):3647–3679.

Kuzmin, A., Luisier, M., and Schenk, O. (2013). Fast methods for computing selected elements of the greens function in massively parallel nanoelectronic device simulations. In Wolf, F., Mohr, B., and Mey, D., editors, *Euro-Par 2013 Parallel Processing*, volume 8097 of *Lecture Notes in Computer Science*, pages 533–544. Springer Berlin Heidelberg.

Lai, M., Krempl, E., and Ruben, D. (2010). *Introduction to Continuum Mechanics*. Butterworth–Heinemann, fourth edition.

Li, L. X. and Wang, T. J. (2005). A Unified Approach to Predict Overall Properties of Composite Materials. *Materials Characterization*, 54(1):49–62.

Mori, T. and Tanaka, K. (1973). Average stress in matrix and average elastic energy of materials with misfitting inclusions. *Acta Metallurgica*, 21(5):571–574.

Nakamura, T., Wang, T., and Sampath, S. (2000). Determination of Properties of Graded Materials by Inverse Analysis and Instrumented Indentation. *Acta Materialia*, 48:4293–4306.

Nemat-Nasser, S., Hori, M., In, N.-h. S., Achenbach, J. D., Budiansky, B., Lauwerier, H. a., Wijngaarden, L. V. a. N., and Willis, J. R. (1993). *Applied mathematics and mechanics*, volume 37.

Neto, S., Peric, D., and Owen, D. R. J. (2008). *Computational Methods for Plasticity*, volume 55.

Peng, X., Hu, N., Zheng, H., and Fukunaga, H. (2009). Evaluation of Mechanical Properties of Particulate Composites with a Combined Self-Consistent and Mori – Tanaka Approach. *Mechanics of Materials*, 41(12):1288–1297.

Reid, A. C. E., Langer, S. A., Lua, R. C., Coffman, V. R., Haan, S. I., and García, R. E. (2008). Image-based finite element mesh construction for material microstructures. *Computational Materials Science*, 43(4):989–999.

Reis, F. J. P. (2014). Multi-Scale Modelling and Analysis of Heterogeneous Solids at Finite Strains. (January).

Reis, F. J. P. and Andrade Pires, F. M. (2014). A mortar based approach for the enforcement of periodic boundary conditions on arbitrarily generated meshes. *Computer Methods in Applied Mechanics and Engineering*, 274:168–191.

Rodrigues Lopes, I. (2016). Computational Strategies for the Solution of Coupled Multi-Scale Problems. Technical Report March.

Schenk, O., Bollhöfer, M., and Römer, R. A. (2008). On large-scale diagonalization techniques for the anderson model of localization. *SIAM Rev.*, 50(1):91–112.

Schenk, O., Wächter, A., and Hagemann, M. (2007). Matching-based preprocessing algorithms to the solution of saddle-point problems in large-scale nonconvex interior-point optimization. *Computational Optimization and Applications*, 36(2-3):321–341.

Sharma, N. K., Pandit, S. N., and Vaish, R. (2012). Microstructural Modeling of Ni-Al2O3 Composites Using Object-Oriented Finite-Element Method. *ISRN Ceramics*, 2012:1–6.

Sharma, N. K., Pandit, S. N., Vaish, R., and Srivastava, V. (2014). Effective Young's Modulus of Ni-Al2O3 composites with particulate and interpenetrating phase structures: A multi-scale analysis using object oriented finite element method. *Computational Materials Science*, 82:320–324.

Technology, N. (2016). OOF2. http://www.ctcms.nist.gov/oof/oof2/, Last accessed on 2016-08-31.

Terada, K., Hori, M., Kyoya, T., and Kikuchi, N. (2000). Simulation of the multi-scale convergence in computational homogenization approaches. *International Journal of Solids and Structures*, 37(16):2285–2311.

Voigt, W. (1889). Ueber die Beziehung zwischen den beiden Elasticitätsconstanten isotroper Körper. *Annalen der Physik*, 274(12):573–587.

Waters, C., Salih, M., and Ajinola, S. (2015). Porosity comparative analysis of porous copper and OOF modelling. *Journal of Porous Materials*, 22(4):989–995.

Weng, G. J. (1984). Some elastic properties of reinforced solids, with special reference to isotropic ones containing spherical inclusions. *International Journal of Engineering Science*, 22(7):845–856.

Zhang, M. H. and Chen, J. K. (2012). Analysis of interfacial fracture strength of an inclusion in a polymeric composite considering cohesive force. *Computational Materials Science*, 61:6–11.